LAPPEENRANAN TEKNILLINEN KORKEAKOULU
LAPPEENRANTA UNIVERSITY OF TECHNOLOGY

Tieteellisiä Julkaisuja
Research Papers
34

Zhiliang Zhang

A Practical Micro-Mechanical Model-Based Local Approach Methodology for the Analysis of Ductile Fracture of Welded T-Joints

Lappeenranta, Finland
3.1994

A Practical Micro-Mechanical Model-Based Local Approach Methodology for the Analysis of Ductile Fracture of Welded T-Joints

UDK 539.42 : 624.078.45 : 519.64

Zhiliang Zhang

ABSTRACT

This thesis concentrates on developing a practical local approach methodology based on micro-mechanical models for the analysis of ductile fracture of welded joints. Two major problems involved in the local approach, namely the dilational constitutive relation reflecting the softening behaviour of material, and the failure criterion associated with the constitutive equation, have been studied in detail.

Firstly, considerable efforts were made on the numerical integration and computer implementation for the non-trivial dilational Gurson-Tvergaard model. Considering the weaknesses of the widely used Euler forward integration algorithms, a family of generalized mid-point algorithms is proposed for the Gurson-Tvergaard model. Correspondingly, based on the decomposition of stresses into hydrostatic and deviatoric parts, an explicit seven-parameter expression for the consistent tangent moduli of the algorithms is presented. This explicit formula avoids any matrix inversion during numerical iteration and thus greatly facilitates the computer implementation of the algorithms and increase the efficiency of the code. The accuracy of the proposed algorithms and other conventional algorithms has been assessed in a systematic manner in order to highlight the best algorithm for this study. The accurate and efficient performance of present finite element implementation of the proposed algorithms has been demonstrated by various numerical examples. It has been found that the true mid-point algorithm ($\alpha = 0.5$) is the most accurate one when the deviatoric strain increment is radial to the yield surface and it is very important to use the consistent tangent moduli in the Newton iteration procedure.

Secondly, an assessment of the consistency of current local failure criteria for ductile fracture, the critical void growth criterion, the constant critical void volume fraction criterion and Thomason's plastic limit-load failure criterion, has been made. Significant differences in the predictions of ductility by the three criteria were found. By assuming the void grows spherically and using the void volume fraction from the Gurson-

Tvergaard model to calculate the current void-matrix geometry, Thomason's failure criterion has been modified and a new failure criterion for the Gurson-Tvergaard model is presented. Comparison with Koplik and Needleman's finite element results shows that the new failure criterion is fairly accurate indeed. A novel feature of the new failure criterion is that a mechanism for void coalescence is incorporated into the constitutive model. Hence the material failure is a natural result of the development of macroscopic plastic flow and the microscopic internal necking mechanism. By the new failure criterion, the critical void volume fraction is not a material constant and the initial void volume fraction and/or void nucleation parameters essentially control the material failure. This feature is very desirable and makes the numerical calibration of void nucleation parameters(s) possible and physically sound.

Thirdly, a local approach methodology based on the above two major contributions has been built up in ABAQUS via the user material subroutine UMAT and applied to welded T-joints. By using the void nucleation parameters calibrated from simple smooth and notched specimens, it was found that the fracture behaviour of the welded T-joints can be well predicted using present methodology. This application has shown how the damage parameters of both base material and heat affected zone (HAZ) material can be obtained in a step-by-step manner and how useful and capable the local approach methodology is in the analysis of fracture behaviour and crack development as well as structural integrity assessment of practical problems where non-homogeneous materials are involved. Finally, a procedure for the possible engineering application of the present methodology is suggested and discussed.

PREFACE

This thesis work was initiated in the beginning of 1991 and was carried out in the Department of Mechanical Engineering at Lappeenranta University of Technology, Lappeenranta, Finland, between October 1991 and March 1994. From January to September 1991 I had the opportunity to practice fracture mechanics as a research engineer in the structural mechanics group at Nuclear Engineering Laboratory, Technical Research Centre of Finland (VTT).

I am especially grateful to my supervisor, Professor Erkki Niemi, Head of the Section of Steel Structures, for his valuable discussions, supportive guidance, continuous encouragement, and kind help. In particular, I appreciate the freedom I have had in pursuing my research interests. I would like to express my thanks to the two official pre-examiners of this dissertation, Professor Wolfgang Brocks, Fraunhofer-Institut für Werkstoff Mechanik (FhG-IWM), Germany and Professor Viggo Tvergaard, The Technical University of Denmark, Denmark for their valuable corrections and comments. I also want to thank Dr. Dietmar Klingbeil, Bundesanstalt für Materialforschung und -prüfung (BAM), Germany for reading this thesis and his valuable comments.

The nine month period in VTT was a professionally important experience in learning fracture mechanics. I graduated with a M.Sc. in civil engineering and had a very limited knowledge of the application of fracture mechanics. I wish to express my gratitude to my former colleagues in VTT, particularly, Mr. Kari Ikonen, Mrs. Heli Talja and Dr. Timo Mikkola for their support, many stimulating discussions and friendship.

Dr. Dong-Zhi Sun, FhG-IWM, Germany, is gratefully acknowledged for sending me his interesting articles in the initiation period of my thesis and for his helpful discussions and comments about my work I received later. His articles influenced greatly the choice of my thesis topic. I want to thank Professor Alan Needleman, Brown University, U.S.A. for reading one article related to the thesis (Chapter 6) and his valuable comments on the conditions of the new failure criterion. My appreciation is extended to Mr. Andreas Hönig, FhG-IWM, Germany for reproducing the data in Figs. 6.10-6.12 and pointing out a small inconsistency in the initial manuscript, which otherwise might have gone unnoticed.

One copy of the ABAQUS User Material Subroutine (UMAT) program developed in this thesis has been sold to ABB STAL AB, Finspång, Sweden. I express my gratitude to Mr. Björn Sjödin, ABB STAL AB for his interest in the work concerning the computer implementation of the Gurson-Tvergarrd model as well as its failure criterion.

The experimental work of the thesis was carried out in the Steel Structures Laboratory of the department. I wish to thank the personnel in the laboratory, particularly Mr. Timo

Björk for his help in arranging the experiments, and Mr. Olli Pynnönen and Mr. Vesa Järvinen for their assistance with the experiments.

Many people have helped me in the material aspect. I want to thank Mr. Esko Reinikainen in the welding Laboratory for taking the micrographic photos. I am indebted to Mr. Kari Uimonen and other staff in Rautaruukki Oy for making chemical composition and inclusion analysis. Thanks are due to Dr. Jukka Martikainen in the Welding Laboratory for determining the heat-affected-zone (HAZ) material simulation parameters and Mr. Juha Seppälä, University of Oulu, for carrying out the HAZ simulation.

I am grateful to Mr. Simo Nikula, Mr. Matti Koskimäki and Mr. Teuvo Partanen and other colleagues in the department for their computational assistance as well as much kind help I received during the years. It is also my pleasure to thank my long time roommate and friend Mr. Jukka Karhula for his patience in teaching me the Finnish culture, language and for his willingness to help.

The financial support from the Finnish Ministry of Education, Rautaruukki Oy and Lappeenranta University of Technology is gratefully acknowledged. I would also like to thank the personnel of the Computing Centre of this university for their help in using main-frame computers and e-mail.

Acknowledgment is due to Mr. Peter Jones for correcting the English text.

I have no words to describe the patience of my wife Shunying and my daughter Dixie and the "global" support and encouragement given to me by them during the course when I was heavily involved with my "local" approach.

Zhiliang Zhang

March, 1994
Lappeenranta, Finland

NOMENCLATURE

1(2)(3)D	one(two)(three) dimensional.
CDM	continuum damage mechanics.
CGHAZ	Coarse grained heat affected zone.
C(T)OD	crack (tip) opening displacement.
COTM	continuum tangent moduli.
CTM	consistent tangent moduli.
DM	damage mechanics.
EPFM	elastic-plastic fracture mechanics.
Fc	failure criterion using constant critical void volume fraction.
FEM	finite element method.
GMPA	generalized mid-point algorithms.
G-T	Gurson-Tvergaard (model).
HAZ	heat affected zone.
HRR	Hutchinson, Rice and Rosengren field.
LEFM	linear elastic fracture mechanics.
NSc	new failure criterion proposed in this thesis study.
Rc	critical void growth criterion.
Sc	failure criterion by Thomason's plastic limit load theory.
SIF	stress intensity factors.
UMAT	user material subroutine in ABAQUS.
VWP	virtual work principal.
a_0	initial length of one finite element
A	void nucleation intensity in a strain-controlled nucleation model.
A_n	net void area fraction.
$\mathbf{D}$	tangent moduli.
E	Young's modulus.
f	void volume fraction.
f_N	volume fraction of void nucleation particles.
f_0	initial void volume fraction.
f_c	critical void volume fraction at void coalescence.
f_c^*	real critical void volume fraction observed either experimentally or numerically.
f_F	void volume fraction at final failure.
f_u^*	$1/q_1$, no physical meaning.
$\mathbf{f}$	body force.
g	flow potential; plastic constraint factor.
G	shear modulus.
$\mathbf{H}$	internal variable vector.

$\mathbf{I}$ second order unit tensor.
J *J*-integral.
J_R *J*-resistance.
K Bulk modulus; stress intensity factor.
K_F amplification coefficient for accelerated void coalescence.
K_{Ic} material toughness.
n, n+1 time intervals.
$\mathbf{n}$ unit vector in the deviatoric space normal to the yield surface.
$\mathbf{n}_r \mathbf{n}_t$ unit radial and tangential vectors in the deviatoric plane.
N power exponent.
p pressure.
P intermediate scalar variable; current applied load in *R*6 method.
q von Mises equivalent stress.
q_1, q_2 Tvergaard's parameters.
Q intermediate scalar variable.
R_0, R_x R_y, initial void radius, current void radii in x and y directions.
R_{mean} mean void radius.
S_N standard deviation.
$\mathbf{S}$ deviatoric stress tensor.
T stress triaxility.
$\mathbf{t}$ applied surface traction.
$\mathbf{u}$ incremental displacement field.
V state of material.
w^e elastic strain potential.
α algorimetric parameter.
$\boldsymbol{\beta}$ centre of the yield surface in a kinematic hardening model.
$\sigma_m, \overline{\sigma}_m$ mean normal stress and macroscopic flow stress.
$\overline{\sigma}_0, \overline{\sigma}$ the initial yield and current flow stresses of the matrix material.
σ_y, σ_z stress components in y, z axes.
σ_1^{weak} applied maximum principal stress on the current stable yield surface.
σ_1^{strong} virtual maximum principal stress to initiate the localized internal necking of intervoid matrix material
σ_n mean stress required to initiate the internal necking in the intervoid matrix of a porous solid.
$\boldsymbol{\sigma}$ Cauchy stress tensor.
$\overline{\sigma}'$ radius of the yield surface in a kinematic hardening model
$\overline{\varepsilon}^p$ equivalent plastic strain.
ε_N mean strain for void nucleation.
$\boldsymbol{\varepsilon}, \boldsymbol{\varepsilon}^e, \boldsymbol{\varepsilon}^p$ total, elastic and plastic strain tensor.
$d\boldsymbol{\varepsilon}^p$ plastic strain increment.
$\overline{\varepsilon}_D^T$ equivalent trial strain in the deviatorc plane.

$\boldsymbol{\varepsilon}_D^T$	deviatoric trial strain tensor.
$\bar{\varepsilon}_0$	initial yield strain
ε_v	logarithmic volumetric strain.
ε_n , ε_c	strains at void nucleation and at coalescence.
$\Delta\varepsilon_p, \Delta\varepsilon_q$	intermediate variables corresponding to volumetric and deviatoric plastic strain increments.
ρ_p and ρ_q	corrections of $\Delta\varepsilon_p$ and $\Delta\varepsilon_q$.
ν	poisson's ratio.
ϕ	yield function.
ω_m	normalized volumetric strain increment.
ω_r, ω_t	normalized radial and tangential strain increments in the deviatoric plane.
$d\lambda, \partial\lambda$	positive scalar.
δ	Kronecker delta.

CONTENTS

List of Publications as a result of the PhD study

International Journal papers:

1. Z. L. Zhang* and E. Niemi, Analyzing ductile fracture by using dual dilatational constitutive equations, *Fatigue Fracture Engineering Materials Structures* 17 (1994) 695-707.

2. Z. L. Zhang* and E. Niemi, Studies on the ductility predictions by different local failure criteria, *Engineering Fracture Mechanics* 48 (1994) 529-540.

3. Z. L. Zhang* and E. Niemi, A new failure criterion for the Gurson-Tvergaard dilatational constitutive model, *International J. Fracture* 70 (1995) 321-334.

4. Z. L. Zhang*, Explicit consistent tangent moduli with a return mapping algorithm for pressure-dependent elastoplasticity models, *Computer Methods Applied Mechanics Engineering* 121 (1995) 29-44.

5. Z. L. Zhang*, On the accuracies of numerical integration algorithms for Gurson pressure-dependent elastoplastic constitutive models, *Computer Methods Applied Mechanics Engineering* 121 (1995) 15-28.

6. Z. L. Zhang* and E. Niemi, A class of generalized mid-point algorithms for Gurson-Tvergaard continuum damage material model, *International J. Numerical Methods Engineering* 38 (1995) 2033-53.

Conference papers:

7. Z. L. Zhang and E. Niemi, Assessment of ductile crack development in welded (tubular) joins, *Proceedings of the 6th International Symposium on Tubular Structures*, Melbourne, Australia. *Tubular Structures* VI, edited by P. Grundy, A. Holgate & B. Wong, p.671-676. 1994 -– Best paper award.
8. Z. L. Zhang and E. Niemi, Studies of the behaviour of RHS gap K-joints by nonlinear FEM, *Proceedings of the 5th International Symposium on Tubular Structures, Nottingham,* Nottingham, *UK. Tubular Structures V*, edited by M. G. Coutie & G. Davies p364-372, 1993.

Chapter I

INTRODUCTION

This chapter begins with an introduction of the applications of fracture mechanics to welded (tubular) joints. In the second section, a non-exhaustive review of the main approaches to ductile fracture problem is presented. The section ends with a comparison between the two branches of the modern local approaches in order to highlight the most promising approach for this thesis study. The objective, problems and outline of this thesis study is given at the end of this chapter.

1.1 Welded (Tubular) Joints and Fracture Mechanics

Both circular and rectangular hollow sections are widely used in the offshore and building construction industries. Tubular members are generally connected through the use of some form of welded joint. The performance of the welded joint is vital to the reliability of a welded structure. Usually there are three kinds of mechanical failure in structural components and welded (tubular) joints:

- buckling or instability
- plastic collapse
- fracture (brittle and ductile).

In recent years, significant achievements have been made on the application of non-linear theories involving large elastoplastic deformations, and modern non-linear finite element methods (FEM) have been found to be very effective in tackling the first two problems. Linear elastic fracture mechanics (LEFM) has proved to be a very promising technique for assessing the brittle fracture behaviour and fatigue crack propagation life of 2D as well as 3D welded joints. Many successful applications of this technique to the prediction of the fatigue life of welded (tubular) joints have been reported [30,45-46,59,91,102-103,145]. The key part in the application of LEFM is the computation of stress intensity factors (SIF). A review of various methods and techniques for acquiring SIF now available in the literature has been made by Atulri and Nishioka [6]. Recently, methods based on Bueckner's fundamental fields [17-18] have been developed for efficiently calculating SIF and weight functions [8-10,113-114,149]. A brief review of the fracture mechanics models for tubular joints has been given by Haswell and Hopkins [46]. In general, although the application of LEFM to 2D welded joints is fruitful [45], how to acquire the SIF efficiently for general 3D (tubular) joints still remains a difficult and tedious task.

On the other hand, both our recent experiments [123] and other experimental results [19,27] have shown that ductile fracture is a very important failure mechanism for tension or bending loaded welded joints. Welded joints are usually made of tough, ductile materials that exhibit considerable strength even when containing cracks. The ductile properties ensure that significant amounts of crack growth occur prior to final failure. Consequently large scale plasticity will undergo in the crack tip region prior to catastrophic fracture. With the advance of engineering design method, for example, the load and resistance factor design method, there is an increasingly stringent demand for more accurate prediction and realistic modelling of the behaviour of structural components and welded joints. Therefore, the computational simulation of crack initiation and stable crack growth has become an important aspect of structural integrity assessment. However, it should be noted that, besides the theoretical difficulties in treating ductile fracture problems which will be addressed in the following section, there are various complexities in the assessment of welded joints, by the presence of defects and residual stress. In addition, the mechanical properties, both strength and toughness, of the weld metal as well as heat effected zone (HAZ) material may be different from parent material. This difference may have a significant influence on the assessment of welded joints. When these complications are taken together with practical thickness and toughness levels for structural weldments, it is found that LEFM is no longer adequate in dealing with the fracture of welded joints, and perhaps the elastic-plastic fracture mechanics (EPFM) for the assessment of ductile fracture failure must be adopted [19].

In the conventional EPFM, it is assumed that a crack or cracks must exist in the engineering components and the complicated triaxial local stress and strain field near crack tip is reduced to one global physical quantity characterizing the loading "intensity", which is defined as *J*-integral or CTOD [57]. Therefore, fracture analysis means the evaluation of the loading "intensity" and comparison with a critical value of this quantity, i.e. fracture resistance. However, it will be seen in the next section that, the conventional EPFM is not problem-free and there is an increasing awareness of more versatile tools, such as local approaches, to ductile fracture. Furthermore, in real engineering structures and components, finding the crack initiation location and the time itself is an important and not an easy matter. Recently there has been a growing world-wide interest in developing continuum damage models or micro-mechanical models for ductile fracture and other problems. Some applications of continuum damage mechanics to real three-dimensional tubular joints have already appeared in literature [27,55].

The main objective of this thesis study is to develop and implement a realistic tool that can be used to treat the ductile fracture and ultimate failure problems of welded (tubular) joints. In the following section, a brief review of the main approaches to ductile fracture is given first.

1.2 Review of the Methods for Ductile Fracture

In this review, methods for ductile fracture are classified as non-fracture mechanics methods, classical fracture mechanics methods and modern fracture mechanics methods. The non-fracture mechanics methods are mainly developed for the assessment of ultimate capacity problems. The methods addressed in classical methods are the two popular approaches, the *R*6 and *J*-integral approaches. An introduction to other classical methods can be found in a recent review by Francois [36]. In modern fracture mechanics methods, which are the main concern of this study, continuum damage mechanics and micro-mechanical model based approaches are discussed and compared.

1.2.1 Non-Fracture Mechanics Methods

The non-fracture mechanics methods here mean the methods for ductile fracture [13,38, 58,66-67], where no common sense fracture or damage parameter is involved, except equivalent stress and/or strain. The methods are also defined as the macroscopic approaches in which the whole structural system is analyzed to predict the load-displacement history up to the ultimate fracture failure load [38]. The main idea of these methods is the normal elastoplastic finite element analysis plus a failure criterion. The failure criterion employed in these methods is very simple, either ultimate stress or ultimate (fracture) strain. So the typical strategy is to evaluate the effective or equivalent stress or strain in every increment of finite element analysis. If the evaluated effective stress or strain in the element integration point is greater than or equal to the ultimate stress or strain of the material as obtained from the uniaxial stress-strain curve, then the material at the integration point is said to have fractured [38]. Various techniques have been developed to redistribute the strain energy of the fractured element to the remaining unfractured elements [38,58,66]. The non-fracture mechanics methods have been applied to the predictions of ultimate fracture failure load of 2D plane stress [13,38,67], 3D [58] problems and more complicated problems such as a tubular T-joint [66]. However, the weaknesses of these methods are obvious, because of the fact that no fracture or damage parameters are dealt with. Results in [38] show that mesh size effect is especially strong in these methods. More importantly, stress triaxility, which plays a decisive role in fracture mechanics [75], is difficult to take into account in these methods.

1.2.2 Classical Fracture Mechanics Methods

LEFM & EPFM

Much work has been done during the past decades in an effort to find fracture characterizing material properties for engineering materials. In LEFM, it is assumed that the remote strains are smaller than the yield strain, and the plastic zone size at the crack tip is much smaller than the crack length or body dimensions. Under the so-called "small scale yielding" condition, the load-displacement curve of the body is elastic and reversible in a global sense. The linear-elastic solution for a cracked body leads to a stress field surrounding the crack tip that is characterized by a single parameter called the

stress intensity factor (*K* field). Elastic fracture occurs when *K* reaches a critical value. When the inelastic deformation region is not small, as in the case of ductile material, the concept of EPFM using global criteria like *J*-integral or CTOD is necessary to describe the fracture process. In EPFM, the size of the overall plastic zone at the onset of crack extension is larger than the *K*-field and the work of remote flow is comparable in magnitude to other components of the total external work, i.e. the reversible elastic strain energy and the irreversible work of fracture. The strain remote from crack may be of the same order of magnitude as the yield strain [57].

R6 Approach

*R*6 and J-integral approaches are usually referred to as "classical approaches" for ductile fracture [79]. *R*6 approach is an engineering safety assessment method, developed mainly in Great Britain, which considers brittle fracture together with plastic collapse mechanics. The result of R6 assessment is either safe or not safe. There are two limiting cases. One is in small scale yielding where LEFM applies: $K_R<1$, safe; $K_R\geq 1$, not safe, where $K_R = K / K_{IC}$ is the loading factor, *K* is the current stress intensity factor of the structural component and K_{IC} is the toughness of the material. The other limiting case is in complete yielding where load is limited by the limit load of the component. The loading factor in this case is defined as: $L_R = P / P_L$, where *P* is current applied load and P_L is the limit load. A set of systematic failure assessment diagrams is available in *R*6 approach. In a general loading case, the combination of loading factors (K_R, L_R) should lie inside the failure assessment diagram, otherwise the structure or the component is not safe. In the safe situation, the *R*6 procedure allows the evaluation of the reserve factor in terms of the applied load for a given condition. The reserve factor is defined through the ratio between the load corresponding to limit conditions and the actual applied load. The reserve factor can be seen as an estimation of the structural integrity reduction induced by the presence of flaws. Very recently Burdekin et al. [34-35] have successfully applied *R*6/revised PD6493 approach to the assessment of welded tubular joints. The assessment has taken into account the effects of residual stresses on the significance of defects in various types of welded joint [32-33]. Although being easy to use, there are, however, some weaknesses involved in the *R*6 approach. Firstly, *R*6 assessment can only give "Yes" or "No" options. It cannot characterize the appreciable stable crack growth which usually can be observed in a material of high toughness prior to catastrophic failure. Secondly, for engineering material which usually displays strain hardening behaviour, it is not easy to define the limit load of the structural component.

J-Integral Approach

J-integral was introduced by Rice [104] in 1968 as a characterization parameter for EPFM. For deformation plasticity (nonlinear elastic behaviour) the *J*-integral is path-independent. Because of this non-trivial property, *J* has been taken as a crack tip characterization parameter for the intensity of stress or strain singularity near the crack tip. For a power-law hardening nonlinear elastic material, Hutchison, Rice and Rosengren (HRR) [52,105] have derived a famous asymptotic solution of stress-strain field at the crack tip, called HRR field, where the stress and strain near the crack tip can be evaluated

based on the state of stress and strain far from the crack tip, as represented by *J*. Taking *J* as a characterizing parameter, the so-called *J*-approach has been developed [57]. It has been found that *J* could be a more general fracture parameter than *K*. Unlike *K*, which can only characterize the crack initiation, *J* can also be used to characterize the stable crack growth using the so-called *J* resistance (J_R) curve which is considered as a material property. According to *J* approach, by comparing the applied *J* and material J_R curve, the crack initiation, the *J*-controlled stable and/or unstable crack growth could be calculated. Considerable efforts [2,39,57] in the past decades or so have been made to develop methods of characterizing crack growth in terms of the variation of the *J*-integral parameter with the increase in crack length. However, behind the nice idea of *J* approach, there are various difficulties, both theoretical and experimental, in its application. Experimentally it is difficult to define J_{1c}, the critical *J* at crack initiation, which seems to depend on geometry [79]. It is also becoming increasingly clear that the methods of *J*-controlled crack growth give an inadequate description of the critical conditions for unstable crack growth following extensive sub-critical crack growth. Although it is argued that large deformation in cracked bodies is generally limited to a small region surrounding the crack tip and that large deformation therefore may have no effect or only a slight effect on the global behaviour of the body, various studies, both experimental and theoretical, [2,7,64,124] have shown that the global fracture mechanics concepts fail in their prediction of the structural behaviour when the triaxility of the stress state varies considerably or is different from that in the specimens used to measure critical material values of the parameters employed. The problem with the *J* approach lies in its formulation in terms of a deformation theory of plasticity [104]. It is also a known fact that severe non-proportional loading and elastic unloading always accompany the stable crack extension. These effects greatly complicate the development of global fracture criteria. Bakker [7] concluded that the global fracture parameters such as *J*-integral and CTOD may well be used to predict crack growth initiation in structures based on critical material values determined on standard specimens. For stable tearing the constraint influences may be substantial and a correct description may only be obtained from a local fracture criterion.

1.2.3 Modern Fracture Mechanics Methods - Local Approaches

The true reason for the failure of conventional fracture mechanics is that they completely neglect the presence of the microfracturing process in the heavy stressed region. In recent years, as a remedy to the conventional fracture mechanics methods, local approaches using either

- continuum damage mechanics (CDM) models or
- micro-mechanical models

have emerged as a viable model capable of characterizing creep rupture, fatigue, brittle and ductile fracture. These two branches will be addressed in this section separately. One significant advantage of local approaches is that it is not necessary to assume that a crack or cracks pre-exist in engineering components.

Micro-mechanical models

Critical Void Growth Model by Rice and Tracey [106] During the last 20 years, many research efforts have been devoted to the study of the ductile fracture of metals. It has long been recognized that ductile fracture occurs in plastically deforming metals through the nucleation, growth and coalescence of small internal voids or cavities at the sites of inclusions and second-phase particles. It was natural to develop a fracture criterion based on critical void growth ratio: void coalescence will occur, when the void growth ratio exceeds a critical value, which is assumed to be a material constant and can be determined by experiments

$$(R / R_0) > (R / R_0)_c \tag{1.1}$$

where $R, R_0, ()_c$ are the current void radius, initial void radius and critical void growth ratio. Several researchers have devoted great attention to void growth models, for a detailed review see [108]. Among them, McClintock [76] developed a void growth model based on his analysis of cylindrical void in an infinite matrix subject to axial and transverse stresses. An exponential dependence of the void growth rate on biaxial stress was obtained. The most successful and versatile model for void growth in a plastic flow field was developed by Rice and Tracey [106] for the case of a spherical void of radius R_0 in a remote uniform strain-rate field (infinite matrix). It leads to the following expression for the ratio between the deformed void radius R and its initial radius R_0:

$$\int_{void\_initiation} 0.283 \exp\left(\frac{3\sigma_m}{2\bar{\sigma}}\right) d\bar{\varepsilon}^p = \ln(R / R_0) \tag{1.2}$$

where $\sigma_m, \bar{\sigma}, \bar{\varepsilon}^p$ are mean normal stress, flow stress and equivalent plastic strain, respectively. Clearly equation (1.2) shows a strong dependence of the void growth on stress triaxility, $\sigma_m / \bar{\sigma}$. Given the growth rate in equation (1.2), analytical or numerical integration methods can be applied to predict approximately the void growth history under any stress field. Although this model does not account for the feed-back of the void growth to the constitutive behaviour of the material, it has nevertheless been proved to give a fairly accurate description of ductile fracture process in a number of applications [7, 28,127]. It is essential to note that the void growth models are not coupled with the damage or softening of material. At most, they can only be taken as fracture criteria.

Micro-mechanical Model by Gurson [43-44] The void growth stage of ductile fracture contains stable expansion of voids within a material undergoing tensile plastic deformation. There are two aspects of this stage that must be considered: (I) the void expansion and change in shape during deformation; (II) the degradation in the material's load-carrying capacity due to the presence of the voids. The critical void growth model by Rice and Tracey [106] has only considered the first aspect of the stable void expansion stage. Dilational constitutive functions which can take account of the degradation of load-carrying capacity by the presence of porosity are therefore a desirable component of a mathematical model of the ductile fracture process [44].

In contrast to developing a single void growth model as Rice and Tracy [106], Gurson [43-44] has proposed a yield function for a porous solid with a randomly distributed volume fraction f of voids. This function was obtained based on an approximate analysis of spherical voids ($q_1 = 1,\ q_2 = 1$):

$$\phi(\boldsymbol{\sigma}, f, \bar{\sigma}) = \frac{q^2}{\bar{\sigma}^2} + 2q_1 f \cosh\left(\frac{3q_2\sigma_m}{2\bar{\sigma}}\right) - 1 - (q_1 f)^2 = 0 \qquad (1.3)$$

where $\bar{\sigma}$ is flow stress of the matrix material and q is the von Mises equivalent stress. Tvergaard [136-137] has investigated the macroscopic shear band instability behaviour, based on a numerical model which fully accounts for the non uniform stress field around each void and also for the interaction between neighbouring voids. Good qualitative agreement was found between the predictions of the full numerical model and Gurson model for the onset of localization. Based on this comparison, for both plane strain [136] and axisymmetric [137] conditions, Tvergaard suggested $q_1 = 1.5$ should be used in equation (1.3). The modified Gurson model is sometimes called the Gurson-Tvergaard model [31], which is abbreviated as G-T model in this study.

According to Tvergaard's modification, the material loses load carrying capacity, if f reaches the limit $1/q_1$, because all the stress components have to vanish in order to satisfy equation (1.3). It is clear that the aim of Tvergaard's modification is merely to decrease the critical void volume fraction to a reasonable extent, at which the material will lose the load carrying capacity. The advantage of the Gurson-based model is that fracture could arise as a natural outcome of the deformation process [84]. One thing that should be taken into consideration is that the stress singularity will totally disappear ahead of the new crack front when using this advantage for the modelling of crack propagation [140]. It should be noted that $1/q_1$ is usually too big as a critical void volume fraction at which the material loses load-carrying capacity. Therefore, an extra criterion in G-T model is needed to model the material failure, typically by void coalescence.

Due to the relative versatility of the G-T model, it has been implemented into the commercial finite element programs ADINA [127-129] and ABAQUS [62,144]. The G-T model has been applied to study the shear localization behaviour [111,136-138] of solids and some practical problems [83,126-128,144] as well.

Finally, it must be noted that, like other models, the Gurson-based model is only an approximate model. Three-dimensional finite element studies[49-50] of the void growth in elastic-plastic materials, in which the full three-dimensional interactions between voids were accounted for, show that neither the Gurson model nor the modified Gurson model by Tvergaard reproduces all the aspects of the stress-strain behaviour of the cubic array.

Plastic Limit-load Model by Thomason [134] After making the mechanical and physical analysis of ductile fracture by nucleation, growth and coalescence of voids, a critical condition which leads to the intervention of ductile fracture, by a localized mode of internal microscopic necking in a previously homogeneous plastic flow state of a solid,

was introduced by Thomason [131-134]. Two different responses of a plastically deformed solid were defined by Thomason [134]. One called "weak" response is the isotropic dilational plastic response of a homogeneous macroscopic flow field, resulting from the presence of micro-voids, which can be modelled by any dilational plastic yield function. Thomason himself [134] employed the von Mises yield model and a "law of mixture" to account approximately for the dilational effect of voids. Correspondingly, a virtual mode of incipient void coalescence, by localized internal necking or plastic limit load failure across a sheet of micro-voids, represents a "strong" dilational plastic response.

It must be emphasized that the "strong" response which is characterized by the plastic limit-load stress σ^{1c} is a virtual mode, even though it is present from the very beginning of yielding. The plastic limit load stress σ^{1c} is determined by the zero stress boundary conditions on the void surfaces and the relative velocity of the rigid regions above and below the incipient fracture surface, either by upper-bound solution or slip-line field solution for the inter-void matrix.

According to Thomason's theory [134], in the beginning of deformation, the stress level required to initiate the "strong" but unstable response is higher than the actual stress which controls the "weak" but stable response. In other words, the deformation and stress are not large enough to change the material response from stable to unstable. During the deformation, the "weak" response is terminated once the actual stress level reaches the plastic limit-load stress level which could initiate the "strong" response. Until now, 2D plane strain and 3D approximate equations for the evaluation of plastic limit-load stress have been presented by Thomason [134].

One important feature of the Thomason's model for ductile fracture described above is that it emphasizes the necessity of modelling the ductile fracture process in terms of "dual" plastic constitutive responses for a void-containing solid. Thomason [134] noted that the full effect of the actual presence of micro-voids in a plastic continuum model can only be accounted for by incorporating a second and "strong" dilational plastic responses to model the possible plastic limit load failure of the inter-void matrix [134]. If a dual constitutive response is not used in modelling the ductile fracture process, then the primary mechanism of ductile fracture by internal microscopic necking of inter-void matrix has effectively been excluded as a controlling mechanism of fracture.

Continuum damage mechanics (CDM) approaches

Another branch of local approach is the CDM approach. In CDM, "**damage**" is defined [69,74] as the progressive deterioration of the material behaviour prior to failure. From the physical point of view, damage is related to the process of initiation and growth of micro-voids and cavities [72]. On the micro-scale, the damage variable can be understood to be a measure of the density of voids in a material volume or the intersection of these voids with a certain plane [56].

The damage effect is incorporated into the stress-strain constitutive equation usually through the concept of hypothesis of effective stress and strain equivalence. Doing so, two states should be considered. One is the damaged state acted upon by the actual stress and the other is a hypothetical undamaged state acted upon by an effective stress. The stress vector taken as the density of forces with regard to the effective area is called the effective stress vector. By the hypothesis of strain equivalence, the actual stress is replaced by the effective stress (as a function damage variable) in the constitutive law. Thus we get the coupled relation between stress-strain and damage variables.

According to the principals of thermodynamics, the deformation process in ductile materials is usually accompanied by two major dissipative mechanisms: plasticity and damage. In a coupled analysis, two dissipation potentials must be adopted [22,141]. The plastic dissipation potential can be taken as the von-Mises yield criterion with the effective stress used instead of the actual stress.

In modelling of ductile fracture, initiation is defined by the first time when damage has reached its critical value (material constant) in one point of the structure and propagation corresponds to the extension of a more or less localized completely damaged zone which is the volume where the damage has reached its maximum value. However, the hydrostatic stress has a significant effect on the initiation of fracture [129]. It has been found necessary by Coffer [26] to incorporate an extra criterion, for example, maximum strain limit [72,55], to account for this effect.

CDM has now developed to a state which can be incorporated into finite element formulation [15,23] and allows practical engineering applications [69,55]. Due to the fact that real evolution of damage is an anisotropic process, a second-order tensorial form of damage variables has recently been widely adopted, for example, by [22,24,55,69,80].

Within the CDM based local approaches, the model by Rousselier [11,109] has obtained much attention. This is because it is one of the simplest which may be derived from the principles of generalized continuum mechanics [14]. By comparison, Rousselier [109] has shown that the Rousselier model is in some way very similar to the Gurson model, even though the damage laws are different. However, Perrin and Leblond [98] recently commented that Rousselier theory fails to meet a consistency criterion derived by considering a single void population model as the limit one with two populations of voids.

Comparison between CDM and micro-mechanical models

As discussed above, CDM models and micro-mechanical models are two different branches in local approach. It is interesting to make a comparison between these two branches. Basically, both approaches take into account the effect of damage in the form of void nucleation, growth and coalescence on the overall response behaviour of the material, both are endowed with a yield surface, a flow rule and a measure of damage and a law for damage evaluation, and further, in the absence of voids, both reduce to the Prandtl-Reuss plasticity theory in relation to the von Mises yield condition [21].

However, despite these similarities, there are some major differences which are highlighted in Table 1.1, where the micro-mechanical model is typically represented by the G-T model.

Table 1.1 Comparison between CDM and G-T model

	CDM	G-T model
General	CDM is phenomenological in nature. It ignores the fine details of microscopic distributions and geometries and the mode shape with regard to the microscopic damage growth.	G-T model studies the micromechanics of void nucleation, growth and coalescence which leads to the final fracture of material.
Damage parameters	Parameters are related to macroscopic material behaviour. For 1D case, it is the fraction of damaged area. For 3D anisotropical damage case, damage is described by a 6×6 tensor.	Void volume fraction, a scalar parameter, given by the material geometry on the micro-scale [139].
Failure criterion	Critical damage parameter and fracture strain [26-27,55]	Critical void volume fraction corresponding void coalescence
Advantages and disadvantages	Relatively easy to determine the damage parameters. No microscopic measurements are needed. It can be well applied to the characterization of crack initiation. Damage evaluation law is difficult to handle.	Microscopic measurements may be needed. Damage and triaxial stress effects are explicitly coupled in a yield function. It can characterize both crack initiation, growth and plasticity localization. It describes the microscopic nature of fracture more accurately than CDM.
Merits	In CDM, effective stress and strain are calculated as a function of actual macroscopic stress and damage. By substituting the effective stress and the strain into classical von Mises yield model, new tangent moduli for the actual stress and strain increment are thus obtained.	In G-T model, the macroscopic stress is directly and explicitly coupled with damage and triaxial stress to form a pressure-dependent yield function. The stress is updated according this yield function.

1.3 Objectives, Problems and Outline of the Study

The driving force of this study arises from our previous experimental studies [123] on the fracture behaviour of gapped rectangular hollow section K-joints, which revealed the importance of ductile fracture in tubular joints. The main objective of this thesis is to develop a realistic tool for the analysis of ductile fracture of welded joints. Because a real K-joint [123] is too complicated to tackle in this first investigation stage, a simple welded T-joint (see chapter 7) suggested by Niemi [90] is adopted in this study for testing the methodology.

Various methods for ductile fracture have been introduced in the previous section. It should be mentioned that ductile fracture is an extremely difficult problem, and currently there is no accepted way of treating the problem [110]. Of the methods introduced, the local approaches seem to be the most promising ones. Based on the comparison between CDM, and the G-T model, it is realized that the micro-mechanical model based approaches might be more accurate in a sense that they describe the ductile fracture process in more detail. Furthermore, considering the fact that within the micro-mechanical models, the G-T model has been applied more than any other for the studies of the failure of ductile metals [53,77], hence, the G-T model was chosen as the basis of this study.

There are usually two important aspects involved in the application of local approach to ductile fracture, one is a constitutive relation which must reflect the softening or deteriorating behaviour of the material, the other one is a failure criterion. Here the G-T model is taken as the dilational constitutive equation. Two immediate difficulties were encountered in the application of the G-T model.

The first difficulty encountered is the computer implementation, in other words, how to integrate the material model and implement the model into computer efficiently and accurately. Currently, numerical integration algorithm, which is the most important part of any numerical scheme employed for the analysis of elastoplastic problems, is still an active research area even for a trivial material model, for example the von Mises model [40,119]. Explicit integration algorithms, represented by the Euler forward algorithms were widely used for the G-T model as well as the von Mises model. It is well known that the Euler forward algorithm is accurate only when the increment size is very small. Recently implicit integration algorithms classified as generalized mid-point rules and generalized trapezoidal rules [94] have become more and more popular. When the Newton's method is used in the global iteration, it has also been found that the consistency of constitutive tangent moduli with the numerical integration algorithm is crucial in preserving the quadratic rate of convergence [121]. For the non-trivial G-T model which is pressure-dependent and is coupled with damage problems have been reported by Worswick and Pick [144] that an extremely small increment step size is needed when the Euler forward algorithm is used in the finite element program ABAQUS, in order to avoid numerical instability.

The second difficulty is that, as we have discussed in the review, there is no well built-in failure criterion in the G-T model and an extra one should be employed. In the literature, in line with convenience, a criterion using constant critical void volume fraction is widely used. The constant value of the critical void volume fraction was either determined from

the simulation of crack initiation of a smooth round tension specimen [126-128] or from cell model analysis [63]. However, the problems are that whether the critical void volume fraction is a material constant, is questionable and that the value of the critical void volume fraction is closely related to the void nucleation parameters which are very difficult to monitor in practice. Furthermore, even if the void nucleation is absent, there are still difficulties in determining the constant value of the critical void volume fraction.

Based on the above analysis, it was decided that the main efforts in this thesis are to be spent on overcoming these two main problems. Firstly, considering the weakness of the Euler forward algorithm and the fact that the accuracy of numerical algorithms has been widely assessed for von Mises [40,94,122] and modified von Mises models [70] and no such assessment is available for the non-trivial G-T model, a class of generalized mid-point algorithms have been presented in order to give evidence for the choice of an accurate numerical algorithm for the G-T model for this study. The accuracy of various algorithms, including the Euler forward and Euler backward algorithms, has been systematically assessed. Furthermore, by linearization of the algorithms and decomposition of the stresses into hydrostatic and deviatoric parts, the tangent moduli consistent with the generalized mid-point algorithms are derived and an explicit expression, with seven-constants, of the consistent tangent moduli (CTM) is obtained. The explicit formula greatly facilitates the computer implementation of the algorithms. The efficiency, especially the quadratic convergence performance using the CTM derived, and accuracy of the adopted algorithm are demonstrated in numerical examples.

Secondly, three local failure criteria: the critical void growth criterion, the constant critical void volume fraction criterion and the Thomason plastic limit-load criterion, are studied and compared against the ductility prediction as a function of stress triaxility. By assuming the void grows spherically and using the void volume fraction from G-T model to calculate the void-matrix geometry, and using the G-T model to represent the weak dilational response as once suggested by Thomason [134], Thomason's plastic limit-load failure model [134] is modified as a new failure criterion for the G-T model. Comparison with finite element results by Koplik and Needleman [63] shows that the new failure criterion is not only very accurate but also more versatile than the widely known criterion using the constant void volume fraction. The significant advantages of the new failure criterion is that the critical void volume fraction is not necessarily a material constant and need not be fitted beforehand. Furthermore, after the initial void volume fraction is selected, the void nucleation parameter(s) could be numerically fitted from experimental results through the use of this new failure criterion.

After the two problems have been solved, a micro-mechanical model based methodology is built up and this methodology is implemented into ABAQUS via user material subroutine UMAT. So, the third part of this thesis is the study of the fracture behaviour of welded T-joint by application of the methodology developed. Because the crack in welded joints usually initiates at the heat affected zone (HAZ), both base and simulated HAZ materials are studied.

This thesis is divided into eight chapters. The second chapter is a compact introduction to the G-T as well as other constitutive models. The third and fourth chapters deal with the

numerical integration problem and CTM of the G-T model. The failure criteria problem is presented in chapters five and six. The seventh chapter presents the results of the application of the methodology developed to the practical problems of welded joints. A summary of the work and a proposed procedure for the possible practical application of present methodology finish this thesis and are presented in the last chapter, chapter 8.

Chapter 2

CONSTITUTIVE RELATIONS FOR POROUS DUCTILE SOLIDS

The purpose of this chapter is to present the background for the G-T constitutive model which is the main concern of the thesis. Some other constitutive models for porous material are also introduced for comparison purposes.

2.1 Introduction

In normal elastoplastic analysis, it is commonly assumed that hydrostatic stress has no effect on plastic yield and plastic deformation is incompressible. This assumption is based on physical considerations and is experimentally well verified, except for conditions close to ductile fracture. This fact resulted in the idea of developing constitutive relations which take into consideration the void effect. When micro-voids are present in ductile material, studies [76,106] have indicated that the hydrostatic component of stress can cause macroscopic dilation through the mechanism of void growth. Over the years, several plasticity theories for void containing solids have been developed to model the void growth under hydrostatic tension.

The outstanding difference between classical plasticity yield equations, for example, von Mises model, and micro-mechanical void containing elastic-plastic yield models, for example, the G-T model [43-44,136-137] is that the stress triaxility has been incorporated into the latter ones. In other words, such models have become pressure-dependent. In this chapter, the most widely known and well-defined G-T model which is the main concern of this study, is introduced. Then the lower bound model presented by Sun [130] and other models will be briefly mentioned for comparison purposes.

The Gurson model is based on the observation that the nucleation and growth of voids in ductile porous metal may macroscopically be described by extending classical plasticity to cover effects of plastic dilatancy and pressure sensitivity of plastic flow. Crude approximations inherent in the Gurson model such as the assumption of spherical voids and lack of their coalescence, inconsistencies in postulating the evolution law for the void volume fraction or evident inaccuracy in describing volumetric compression have not prevented its surprising popularity [61]. The model has already been extensively and

successfully applied to the analysis of plastic localization problems [60,86,111,136,140, 146] and also some practical problems [83,126-128].

2.2 Gurson-Tvergaard (G-T) Model

For a ductile porous material containing a certain volume fraction *f* of voids, Gurson [43] has suggested the use of an approximate yield condition of the form $\phi(\boldsymbol{\sigma}, f, \bar{\sigma})=0$. Here, $\boldsymbol{\sigma}$ is the average macroscopic Cauchy stress, and $\bar{\sigma}$ is the flow stress representing the actual microscopic stress-state in the matrix material. Gurson's theory is endowed with a yield condition, a flow law, a measure of void volume fraction, a rule for nucleating voids, and a law for evolution of the voids [53]. The approximate yield locus is obtained by the following procedures [43]:

(1) von Mises condition is used to characterize the yield and flow of the matrix material (itself incompressible)
(2) A rigid-plastic model is assumed valid because of the large strain involved in ductile fracture.
(3) A form is then assumed for the velocity in the aggregate, which allows the voids to grow but requires incompressibility in the matrix. This velocity field must also meet kinematic boundary conditions corresponding to deformation rates on the surfaces of the unit cube.

Based on the above rigid-plastic upper-bound analysis of spherical voids, Gurson [43] obtained the following yield function ($q_1 = q_2 = 1$):

$$\phi(\boldsymbol{\sigma}, f, \bar{\sigma}) = \frac{q^2}{\bar{\sigma}^2} + 2q_1 f\cosh\left(\frac{3q_2\sigma_m}{2\bar{\sigma}}\right) - 1 - (q_1 f)^2 = 0 \qquad (2.1)$$

where σ_m, q are the mean normal of the average macroscopic Cauchy stress $\boldsymbol{\sigma}$ and the von Mises equivalent stress. Constants q_1 and q_2 are introduced by Tvergaard [136-137] to bring predictions of the model into closer agreement with full numerical analyses of a periodic array of voids. The implication of the Gurson model is that the voids are assumed to be randomly distributed, so that the macroscopic response is isotropic. It is easy to see that if $f \equiv 0$, this constitutive relation reduces to the classical isotropic hardening plasticity. The yield surface was extended to hardening materials by regarding $\bar{\sigma}$ as a measure of the effective (in an appropriate average sense) flow stress of the matrix material in the current state. Due to the presence of microvoids, the plastic flow (2.1) is dilational and pressure sensitive. Furthermore, although the matrix material continues to harden, the aggregate can soften.

Void Nucleation and Growth

During plastic yielding, the void volume fraction increases, partly due to void growth and partly due to the nucleation of new voids. The nucleation and growth of microvoids play a central role in the ductile fracture of metals. Void nucleation and growth are, however, two separate mechanisms. The increase of void volume fraction is written in the form

$$df = df_{growth} + df_{nucleation} \tag{2.2}$$

The void growth law is described by,

$$df_{growth} = (1-f)d\boldsymbol{\varepsilon}^{p} : \mathbf{I} \tag{2.3}$$

which is an outcome of the plastic incompressibility of the matrix material. In (2.3), $d\boldsymbol{\varepsilon}^{p}$ and $\mathbf{I}$ are the plastic strain increment tensor and the second-order unit tensor, respectively. Experimental investigations show that the nucleation of new voids occurs mainly at second phase particles by decohesion of the particle-matrix interface or particle fracture [134]. In reality, accurate modelling of void nucleation is very complicated and difficult. However, nucleation can be related to an increment of deformation when the proper boundary conditions are given. In general, nucleation can be classified into two categories, namely strain-controlled and stress-controlled. Various nucleation models have been discussed by Gurson [43]. Although the choice of a nucleation model depends on the problem, because it is easy to handle and it adds no extra term to the asymmetry of tangent moduli (see section 7.6), strain-controlled nucleation model is widely used in the literature:

$$df_{nucleation} = Ad\bar{\varepsilon}^{p} \tag{2.4}$$

where $\bar{\varepsilon}^{p}$ is the equivalent plastic strain in the matrix material. Void nucleation intensity A depends on the void nucleation model used. Two strain-controlled void nucleation models have been seen in the literature. One is the continuous nucleation model by Le Roy et al. [68] and Gurland [42] with a linear relation to equivalent plastic strain (A is kept constant). Another was proposed by Chu and Needleman [25] where the void nucleation is assumed to follow a normal distribution as suggested:

$$A_1 = \frac{f_N}{S_N\sqrt{2\pi}}\exp\left[-\frac{1}{2}\left(\frac{\bar{\varepsilon}^{p}-\varepsilon_N}{S_N}\right)^2\right] \tag{2.5}$$

with f_N = volume fraction of void nucleating particles, ε_N = mean strain for void nucleation, S_N = corresponding standard deviation. In a more general case, for example the case in [47], these two strain-controlled nucleation models can be combined together. The coefficient A in (2.4) can then be written

$$A = A_0 + A_1 \tag{2.6}$$

where A_0 is the constant or void nucleation intensity of the continuous void nucleation model. It should be mentioned that the non-zero value of A is only used if the equivalent plastic strain exceeds its current maximum in the increments considered; otherwise A=0.

It must be noted that in the Chu and Needleman nucleation model (2.5), there are three parameters which should be determined for a specific material. Generally speaking, these three parameters depend on the material properties and loading conditions (geometry and stress status). Because of the lack of experimental procedure and difficulties in determining the parameters, the values except f_N, used by Tvergaard and Needleman [140] are widely used for almost any other applications of the G-T model [62,83,126-128].

The equivalence of the overall rate of plastic work and that in the matrix material leads to

$$\boldsymbol{\sigma}: d\boldsymbol{\varepsilon}^p = (1-f)\bar{\sigma} d\bar{\varepsilon}^p \tag{2.7}$$

or equivalently

$$d\bar{\varepsilon}^p = \frac{\boldsymbol{\sigma}: d\boldsymbol{\varepsilon}^p}{(1-f)\bar{\sigma}} \tag{2.8}$$

For application to porous metals, the flow rule is usually assumed to obey macroscopic normality [89], so that,

$$d\varepsilon_{ij}^p = d\lambda \frac{\partial \phi}{\partial \sigma_{ij}}. \tag{2.9}$$

Void Coalescence Simulation

It can be seen that, although the G-T model demonstrates the softening effect of the material, the model itself does not constitute a fracture criterion. It is also easy to see that the material loses the load carrying capacity, if f reaches the limit $1/q_1$, because all the stress components have to vanish in order to satisfy equation (2.1). However, even if q_1 = 1.5 as proposed by Tvergaard [136-137], the void volume fraction, f = 1/1.5, is still too large to be realistic in practice to simulate the final material failure. Therefore, a critical parameter, namely the critical void volume fraction has to be used to simulate the material failure. It should be noted that, in order to avoid numerical difficulties, once fracture (void coalescence) has been determined to appear according to a specific criterion (see chapter 5 and 6), numerically it is preferred to simulate the material

separation gradually, rather than suddenly. Therefore, a modification using the following f^* to replace f in (2.1) in order to account for the void coalescence effect on final failure has been proposed by Tvergaard and Needleman [140] and applied in this study:

$$f^* = \begin{cases} f & for \quad f \le f_c \\ f_c + K_F(f - f_c) & for \quad f > f_c \end{cases}. \tag{2.10}$$

Here, f_c is the critical void volume fraction at which voids coalesce, which in the present study was determined by a new failure criterion (see chapter 6), and K is a constant determined from the void volume fraction, f_F, at final failure of the material:

$$K_F = \frac{f_u^* - f_c}{f_F - f_c} \tag{2.11}$$

where f_u^*=1/q_1.

It should be noted that the value of the ultimate void volume fraction f_u^* has no physical meaning but the product $q_1 f_u^*$ in practical application may not be equal to 1, in order to keep numerical stability.

An alternative approach has been suggested by Kleiber [61] to simulate the post void coalescence behaviour: assume for a number of incremental steps (10 was used by Kleiber) a proportional increase in f from f_c up to f_u^* from which the material carrying capacity at that point is effectively zero. Clearly the evolution equation (2.2) for f is not used during the process from f_c to f_u^*.

In present investigation, approach (2.10) proposed by Tvergaard and Needleman [140] is expected to be more suitable for the present numerical algorithms proposed, because it was understood that the convergence is much better if the stress drop is controlled by constitutive equations [125]

Kinematic Hardening

It has been found that the predictions of plastic flow localization are very sensitive to the formation of a vertex on subsequent yield surfaces [88,139]. In order to account for the effect of increased yield surface curvature during ductile fracture, Mear and Hutchinson [78] have suggested a kinematic hardening model for a porous ductile material. The corresponding yield function ($q_1 = q_2 = 1$):

$$\phi(\boldsymbol{\sigma}', f, \overline{\sigma}) = \frac{q'^2}{\overline{\sigma}'^2} + 2q_1 f \cosh\left(\frac{3q_2\sigma'_m}{2\overline{\sigma}'}\right) - 1 - (q_1 f)^2 = 0 \tag{2.12}$$

where

$$\boldsymbol{\sigma}' = \boldsymbol{\sigma} - \boldsymbol{\beta} \tag{2.13}$$

$$\bar{\sigma}' = (1-b)\bar{\sigma}_0 + b\bar{\sigma} \tag{2.14}$$

Here $\boldsymbol{\beta}$ defines the centre of the yield surface, $\bar{\sigma}'$ is the radius of the yield surface, $\bar{\sigma}_0$ is the initial and $\bar{\sigma}$ the current flow stresses for the matrix material. The model is formulated in such a manner that for *b*=1, it reduces to the Gurson model with isotropic hardening and for *b*=0, purely kinematic hardening results.

The model has subsequently been extended by Tvergaard [138] to account for void nucleation. Although the kinematic hardening has not been considered in the present investigation, it could be readily incorporated into the methodology developed in this study.

Calibration of the G-T model with FEM results

It should be noted again that, despite its popularity, the G-T model is an approximate model in nature. Many finite element analyses have been performed to verify the G-T model. Koplik and Needleman [63] have conducted a cell model analysis to compare the numerical results with predictions by the G-T model. Very good agreement has been observed between the finite element results and the predictions using the values of $q_1 = 1.25$ and $q_2 = 1.0$ for Tvergaard's parameters. Becker et al. [12] have used the same cell model formulations as Koplik and Needleman [63] but with an experimentally determined matrix uniaxial stress-strain curve and found good agreement between the cell model response and the G-T constitutive relation prediction for $q_1 = 1.25$ and $q_2 = 0.95$. Mear [77] has compared the stress-strain response of spherical shell model analysis, where void interaction effects were taken into account, and the predictions by the G-T model. It was found that the agreement is in line with *q* values between $q_1 = 1.0$ and 1.5. Hom and McMeeking [49] compared predictions of void-growth plasticity theories by G-T model with results obtained from three-dimensional finite element models of unit cells containing discrete voids and incompressible matrix material. Although Hom and McMeeking showed that none of the continuum void growth models exactly agreed with the 3D finite element results, the predictions were generally good in uniaxial tension, hydrostatic tension, and pure shear stress fields. Very recently, Richelsen and Tvergaard [107] have performed unit cell model analyses to obtain a more complete understanding of the effect of different stress states and void shapes on the growth of voids to coalescence. Both 2D plane strain and 3D analyses using non-hardening elastic-plastic material containing small voids were conducted. They have shown that the FE predictions are well represented by the G-T model. They concluded that by using the function in (2.10), with appropriate values of q_1, q_2, f_c and f_F, the G-T model gives a rather good description of the ductile failure process, including both the initial growth of voids and the final failure by void coalescence. Hence, from the

calibration efforts made by various researchers, it appears that G-T models capture the essential aspects of the effect of void growth on the macroscopic constitutive behaviour.

2.3 Other constitutive models

Several alternative models for porous material have been presented in the literature [41,81,99,117,130,147]. For a detailed review, please see the recent work by Riedel [108]. Here two new models, the lower-bound model by Sun [130] and the anisotropic model by Nagaki et al. [81] are briefly introduced. It is known that the Gurson model was obtained from upper-bound analysis by assuming a velocity field in the void model which satisfies the velocity boundary conditions and strain rate and velocity compatibility conditions. A theory parallel to the Gurson theory for porous materials, based on lower-bound analysis, has been established by Sun [130]. In the lower-bound theory, the yield surface is derived from solutions to problems for a volume element of the idealized-elastic-plastic material containing a void (a thick spherical shell). Moreover, it is extended to strain hardening materials under assumption of the isotropic hardening. Recently, the Sun model has been extended, as Mear and Hutchinson [78] for the Gurson model, to include yield surface changes by incorporating the kinematic hardening, in the analysis of local necking in biaxially stretched sheets in porous materials [147].

Using the same assumptions as Gurson [43], Sun [130] obtained the following initial yield function for porous materials based on the lower-bound approach of plasticity:

$$\phi(\boldsymbol{\sigma}, f, \bar{\sigma}) = \frac{q^2}{\bar{\sigma}^2} + f\beta_1 \cosh\left(\frac{3\sigma_m}{2\bar{\sigma}}\right) - \beta_2 = 0 \tag{2.15}$$

where

$$\beta_1 = 2 - \tfrac{1}{2}\ln f \tag{2.16}$$

$$\beta_2 = 1 + f(1 + \ln f). \tag{2.17}$$

Comparison of Sun model and Gurson model shown in Fig. 2.1 indicates that there is a distinct difference between these two models. What role the lower-bound model will have in the ductile fracture remains to be seen. In this study we are not going to compare the predictions by the lower-bound model, however, if it is necessary, it can be readily incorporated into the local approach methodology.

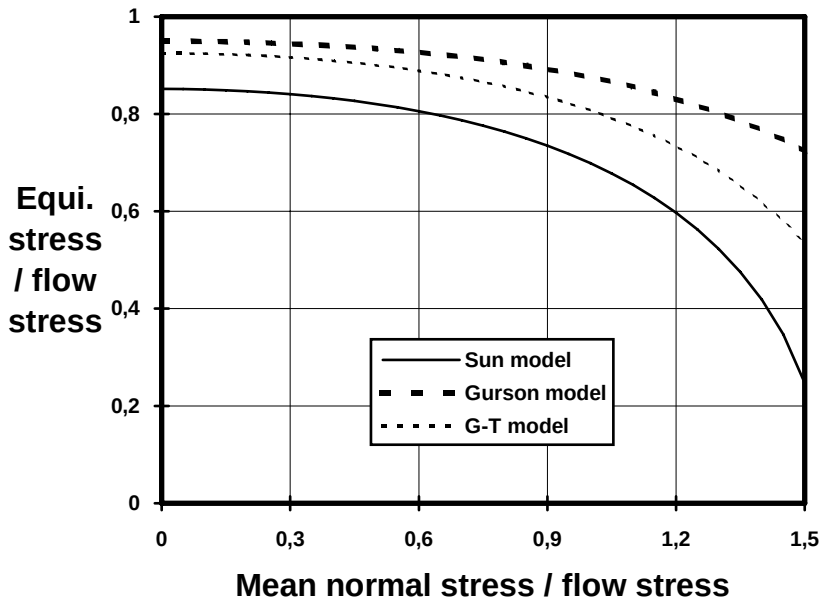

Fig. 2.1 Comparison of three models for the case f=0.05. In G-T model $q_1 = 1.5$ *and* $q_2 = 1.0$ *were used.*

Most of the yield models which have been proposed for porous materials are isotropic, in the sense that voids are introduced as a volume fraction, i.e. a scalar parameter, independent of the shape and spatial distribution of voids. In real materials the voids are not necessarily spherical, and their initial distribution (and resulting growth due to plastic deformation) is likely to be irregular. Hence, initial and subsequent anisotropy can be anticipated in porous metals. Therefore, it would be desirable to incorporate some features of the microstructure into the constitutive relations. Recently, Nagaki [81] et al. have extended the Gurson model by allowing for the influence of void spacing on the anisotropic behaviour of porous materials. In their examples, they have demonstrated that void distribution can exert a very strong influence on the anisotropy of the aggregate. It should be noted, although anisotropic models are promising and may narrow the difference between experimental results and the predictions by the G-T model as discussed by Mear [77], they are not well defined yet and further research efforts is needed.

Finally, one word from professor Tvergaard [139] is borrowed here to end this chapter. "Although there is a need for further developments to make the (constitutive) descriptions more realistic in some respects, the material models in their current form (G-T model) appear to be quite powerful".

Chapter 3

NUMERICAL INTEGRATION FOR G-T TYPE MODELS

(I) Algorithms and accuracy

The accuracy of numerical integration algorithms for the G-T type model is not well-known to the G-T model community. In this chapter, after an introduction, the one-step Euler forward and the Euler backward algorithms are briefly addressed. Then, a class of generalized mid-point algorithms is proposed and formulated for the G-T type models. The accuracy of all the algorithms mentioned is then assessed in a systematic manner by varying the size and direction of strain increments in order to give evidence for the choice of the best algorithm for this investigation. The assessment results are shown by means of iso-error maps. It is found that the conventional one-step Euler forward algorithm has the poorest accuracy and the true mid-point algorithm is the most accurate one when the deviatoric strain increment is radial to the yield surface. The Euler backward algorithm gives moderate accuracy in all the cases assessed.

3.1 Introduction

Finite element method (FEM) nowadays is a general and powerful tool for the numerical solution of elastoplastic problems, for example, the ductile fracture problems. In the finite element method, the constitutive equations of an elastoplastic material model are usually given in rate form. Typically, the solution of the nonlinear problem is performed incrementally and numerical integration of the nonlinear constutive equations eventually becomes necessary. More importantly, numerical algorithms for the integration of constitutive relations play a central role in finite element methods. The importance of understanding and controlling this source of numerical error has motivated a number of studies and several methods for the integration of elastoplastic constitutive equations have been proposed in the literature [3-5,16,40,65,70-71,82,92-97,100-101,110,118-122,148]. Many computer analyses have been carried out and a number of general purpose computer programs for non-linear as well as elastic problems have been developed. In spite of these advances, however, the scope of the methodology heretofore proposed has been mostly restricted to simple plasticity models, such as von Mises

model. Nevertheless, the choice for an efficient, accurate and economical numerical algorithm to solve elastoplastic problems, especially when a new material model appears, becomes very important and is still a challenging task.

One important aspect in an overall numerical procedure is the nature of the integration scheme: whether it is explicit or implicit. Most of the early finite element methods for non-linear problems were predominantly based on explicit integration of the constitutive relations. The stress change due to plastic deformation is taken as tangential to the yield surface in somewhat arbitrary fashion. Usually the explicit algorithm gives a stress state which does not lie on the yield surface and an additional correction is then needed to bring the stresses back to the yield surface. A number of procedures including sub-incrementation technique to ensure plastic admissibility have been suggested in the literature [92,96]. For a perfectly plastic von Mises yield model, Krieg and Krieg [65] have found that for small increment steps the explicit algorithm based on the traditional Euler forward integration scheme is the most inaccurate. Schreyer et al. [112] presented similar results including hardening. Similar results have also been shown by Lee [70] for pressure-modified von Mises yield model. The stability properties of both explicit and implicit schemes were discussed by Nagtegaal and De Jong [82] who showed that the explicit Euler forward algorithm or "tangent modulus" algorithm for the integration of elastoplastic equations is conditional stable and that implicit algorithms such as "mean normal" algorithm are to be preferred. Another limitation of explicit algorithms is the convergence deterioration when the Newton method, such as the method used in ABAQUS [1], is used for global iteration. Detailed discussion on the convergence is presented in next chapter. Probably for these reasons, algorithms based on implicit integration have gained popularity in recent years [3,16,40,93,95,120-122].

Implicit algorithms have been generalized by Ortiz and Popov [94] to two families, the generalized trapezoidal and generalized mid-point algorithms in a manner that facilitate satisfaction of the plastic consistency condition. The accuracy and stability of a number of integration algorithms have been widely assessed for the classical pressure-independent problems [40,65,82,94-95]. For perfectly plastic von Mises model, Ortiz and Popov [94] found that for both generalized trapezoidal and mid-point algorithms, the true mid-point algorithm results are second order accurate for small increment steps, whereas for large increment steps the Euler backward algorithm leads to better accuracy. They also observed that the stability properties of the generalized mid-point algorithms are better than those of the generalized trapezoidal algorithms. Recently Gratacos et. al. [40] have investigated the generalized mid-point algorithms in detail for the case of von Mises criterion with isotropic work-hardening rule. They concluded that, in most cases, first order accurate Euler backward algorithm should be preferred to second order accurate true mid-point algorithm for realistic time steps.

As to the non-trivial G-T model concerned in this study, which is much more complicated that the von Mises model in that the plasticity evolution law is coupled with the damage evolution law as well as that the yield criterion is pressure dependent, the performance of numerical algorithms is not well-known to the G-T model community. The return mapping algorithm has been proved to be effective, robust and

unconditionally stable, and it is at present perhaps one of the most widely used integration procedures for plane strain and 3D classical J_2 elastoplasticity [122]. However, due to the laborious task of obtaining the tangent moduli consistent (see next chapter) with the return mapping algorithms, Euler forward algorithms based on the use of elastoplastic tangent moduli are overwhelmingly used [111,126-128,137,144]. While the accuracy of the Euler forward algorithm for the G-T model remains widely unknown, the convergence problem of the Euler forward algorithms when used in ABAQUS has been reported by Worswick and Pick [144] as that very small time steps are required in the solution in order to avoid numerical instability. An Euler backward integration algorithm for G-T type models has been presented by Aravas [3]. However, no assessment concerning the accuracy and efficiency has been made.

Upon recognizing the importance and ever-increasing applications of the G-T model in ductile fracture, it was understood that it is necessary and very important to study the accuracy of integration algorithms for the G-T and G-T type models and to make the best choice for FEM implementation in this study. For this purpose, a class of generalized mid-point algorithms for G-T type models was thus proposed and formulated. In the following, the numerical algorithms including the classical Euler forward algorithm, Euler backward algorithm and a class of generalized mid-point algorithms for G-T type model, will be described first. Then the accuracy of the algorithms is assessed in a systematic way by means of iso-error maps. This chapter is closed with some conclusions.

Here and subsequently, following the standard practice, we shall use bold-face symbols for variables of tensorial character; the symbol (:) signifies a doubly-contracted tensor product, e.g. $(\mathbf{D}:\boldsymbol{\varepsilon})_{ij} = D_{ijkl}\,\varepsilon_{kl}$, $(\mathbf{S}:\mathbf{S}) = S_{ij}S_{ij}$; the symbol ($\otimes$) indicates the tensor product of two tensors, e.g. $(\mathbf{I}\otimes\mathbf{n})_{ijkl} = I_{ij}n_{kl}$.

3.2 Generalization of Elastoplastic Constitutive Relations

In this study, the assumption of small elastic strain is made, although, finite plastic deformations are allowed. The class of G-T type constitutive equations governing the behaviour of an elastoplastic solid considered here may be generalized in the form

$$\boldsymbol{\varepsilon} = \boldsymbol{\varepsilon}^e + \boldsymbol{\varepsilon}^p \tag{3.1}$$

$$d\boldsymbol{\varepsilon} = d\boldsymbol{\varepsilon}^e + d\boldsymbol{\varepsilon}^p \tag{3.2}$$

$$\boldsymbol{\sigma} = \mathbf{D}^e:\boldsymbol{\varepsilon}^e \tag{3.3}$$

$$\phi(\boldsymbol{\sigma},\mathbf{H}) = \phi(p,q,\mathbf{H}) = 0 \tag{3.4}$$

$$d\boldsymbol{\varepsilon}^p = d\lambda\frac{\partial g}{\partial \boldsymbol{\sigma}} \tag{3.5}$$

$$d\mathbf{H} = \mathbf{h}(d\boldsymbol{\varepsilon}^p,\boldsymbol{\sigma},\mathbf{H}) = \mathbf{h}(d\boldsymbol{\varepsilon}^p,p,q,\mathbf{H}) \tag{3.6}$$

where, following standard notation, $\boldsymbol{\varepsilon}, \boldsymbol{\varepsilon}^e$ and $\boldsymbol{\varepsilon}^p$ denote the total, elastic and plastic strain tensors, respectively. $\boldsymbol{\sigma}$ is the Cauchy stress tensor and $\mathbf{H}$ signifies some internal state

variables, for example in present G-T type models, the void volume fraction and equivalent plastic strain. In (3.3), the existence of an elastic strain potential W^e, such that, $\boldsymbol{\sigma} = \partial W^e / \partial \boldsymbol{\varepsilon}$, is assumed. This has the effect of rendering the elastic tangent moduli symmetric, i.e. $D^e_{ijkl} = D^e_{klij}$. In this study, linear isotropic elasticity is assumed:

$$D^e_{ijkl} = (K - \tfrac{2}{3}G)\delta_{ij}\delta_{kl} + 2G\delta_{ik}\delta_{jl} \tag{3.7}$$

where δs are the Kronecker deltas, and G and K are the shear and bulk moduli, respectively. In the general yield function (3.4), the pressure p and the equivalent stress q can be calculated, respectively:

$$p = -\tfrac{1}{3}\boldsymbol{\sigma}:\mathbf{I} \tag{3.8}$$

$$q = \sqrt{\tfrac{3}{2}\mathbf{S}:\mathbf{S}}\,. \tag{3.9}$$

I and **S** are the second-order unit tensor and deviatoric stress, respectively.

The plastic flow rule is given by (3.5), where $d\lambda$ is a positive scalar and g is the flow potential. In the literature, the associated flow rule is commonly applied to porous solids [89]. Here, the associated flow rule alone is used, which means $g = \phi$. However, there are no difficulties in applying the method to the non-associated flow rule. Equation (3.6) expresses the general internal state variable evolution rule, which could include both plasticity and damage evolution rules. For rate-independent materials, **h** must be homogeneous of degree one in $d\varepsilon^p$.

3.3 Euler Forward Algorithm

In an explicit integration algorithm such as the Euler forward algorithm, the governing equations are satisfied at the beginning of the increment. This implies that the plastic stress increment can be calculated explicitly by using the consistency condition that upon yielding the stress point must remain on the yield surface if no unloading occurs.

For the G-T type constitutive model considered here, we may rewrite the continuum increment equations as follows

$$\Delta\boldsymbol{\sigma} = \mathbf{D}^e:(\Delta\boldsymbol{\varepsilon} - \Delta\boldsymbol{\varepsilon}^p) \tag{3.10}$$

$$\Delta\boldsymbol{\varepsilon}^p = \Delta\lambda\frac{\partial\phi}{\partial\boldsymbol{\sigma}} \tag{3.11}$$

Without losing generality, the general internal variable evolution rules can be written

$$\Delta\mathbf{H} = \Delta\lambda\mathbf{d} \tag{3.12}$$

where **d** can be derived from (3.6). By enforcing the yield consistency condition we obtain

$$\Delta\lambda = \frac{\partial\phi}{\partial \mathrm{s}} : \mathrm{D}^e : \Delta \mathrm{e} / \left(\frac{\partial\phi}{\partial \mathrm{s}} : \mathrm{D}^e : \frac{\partial\phi}{\partial \mathrm{s}} - \frac{\partial\phi}{\partial \mathrm{H}} : \mathrm{d} \right). \tag{3.13}$$

So for any given strain increment $\Delta\boldsymbol{\varepsilon}$, the plastic stress increment can be calculated by

$$\Delta\boldsymbol{\sigma} = \mathbf{D}^e : (\Delta\boldsymbol{\varepsilon} - \Delta\lambda \frac{\partial\phi}{\partial\boldsymbol{\sigma}}). \tag{3.14}$$

It should be noted that, in (3.14), $\partial\phi/\partial\boldsymbol{\sigma}$, $\partial\phi/\partial\mathbf{H}$ and **d** are evaluated at the beginning of the time increment, and therefore, they are known in advance. From (3.14) we can see that for a given state in the beginning of the increment, the stress increment is a linear function of the strain increment.

After the increment, the updated stress usually lies outside the yield surface and an additional radial return correction [20] is necessary in the Euler forward algorithm.

3.4 A Class of Generalized Mid-point Algorithms

General formulae

In the context of displacement finite element analysis using isoparametric elements, stress updates take place at the Gaussian integration points when the total and incremental strains are given. The problem is to update the known state variables $\boldsymbol{\varepsilon}_n, \boldsymbol{\varepsilon}_n^p, \boldsymbol{\sigma}_n$ and $\mathbf{H}_n$ associated with an converged solution at time t_n into their corresponding values $\boldsymbol{\varepsilon}_{n+1}, \boldsymbol{\varepsilon}_{n+1}^p, \boldsymbol{\sigma}_{n+1}$ and $\mathbf{H}_{n+1}$ on the updated solution at time t_{n+1}. We shall as usual suppose that the strain rate remains constant in the following formulations. Here and subsequently, the subindices n and n+1 are used to identify the value of the various state variables at time t_n and t_{n+1}.

By applying the elastic-plastic splitting methodology, Ortiz and Popov[94] formulated a class of generalized mid-point algorithms which in the present context for the G-T type model takes the form:

$$\boldsymbol{\varepsilon}_{n+1} = \boldsymbol{\varepsilon}_n + \Delta\boldsymbol{\varepsilon}_{n+1} \tag{3.15}$$
$$\boldsymbol{\sigma}_{n+1}^e = \mathbf{D}^e : (\boldsymbol{\varepsilon}_n^e + \Delta\boldsymbol{\varepsilon}_{n+1}) \tag{3.16}$$
$$\boldsymbol{\sigma}_{n+1} = \boldsymbol{\sigma}_{n+1}^e - \mathbf{D}^e : \Delta\boldsymbol{\varepsilon}_{n+1}^p \tag{3.17}$$
$$\Delta\boldsymbol{\varepsilon}_{n+1}^p = \Delta\lambda \mathbf{r}_{n+\alpha} \tag{3.18}$$
$$\mathbf{H}_{n+1} = \mathbf{H}_n + \Delta\mathbf{H}_{n+1} \tag{3.19}$$
$$\Delta\mathbf{H}_{n+1} = \mathbf{h}_{n+\alpha} \tag{3.20}$$
$$\phi_{n+1} = 0 \tag{3.21}$$

where one writes

$$\mathbf{r}_{n+\alpha} = (\frac{\partial \phi}{\partial \boldsymbol{\sigma}})_{n+\alpha} = \mathbf{r}(\boldsymbol{\sigma}_{n+\alpha}, \mathbf{H}_{n+\alpha}) \tag{3.22}$$

$$\mathbf{h}_{n+\alpha} = \mathbf{h}(\boldsymbol{\sigma}_{n+\alpha}, \mathbf{H}_{n+\alpha}) \tag{3.23}$$

$$\boldsymbol{\sigma}_{n+\alpha} = (1-\alpha)\boldsymbol{\sigma}_n + \alpha\boldsymbol{\sigma}_{n+1} \tag{3.24}$$

$$\mathbf{H}_{n+\alpha} = (1-\alpha)\mathbf{H}_n + \alpha\mathbf{H}_{n+1} \tag{3.25}$$

and the algorithmic parameter α takes values in the interval [0,1]. It must be noted that in the above formulations, the equilibrium equations are satisfied exactly at the end of the time increment in a full implicit way regardless of the value of α. For $\alpha = 1$, one recovers the closest point return mapping algorithm or Euler backward algorithm [3], whereby the elastic predictor is relaxed onto the closest point on the updated yield surface. On the other hand, if one takes $\alpha = 0$, one obtains a semi-implicit algorithm in the sense that the plastic flow direction is known before the increment, only the value needs to be solved implicitly. A theoretical analysis given by Ortiz and Popov [94] shows that for small increment steps, the algorithm is second-order accurate for α=0.5 and unconditionally stable for $\alpha \geq 0.5$ regardless of the shape of the yield surface. Fig. 3.1 depicts a geometric interpretation of the algorithm (3.15)-(3.21).

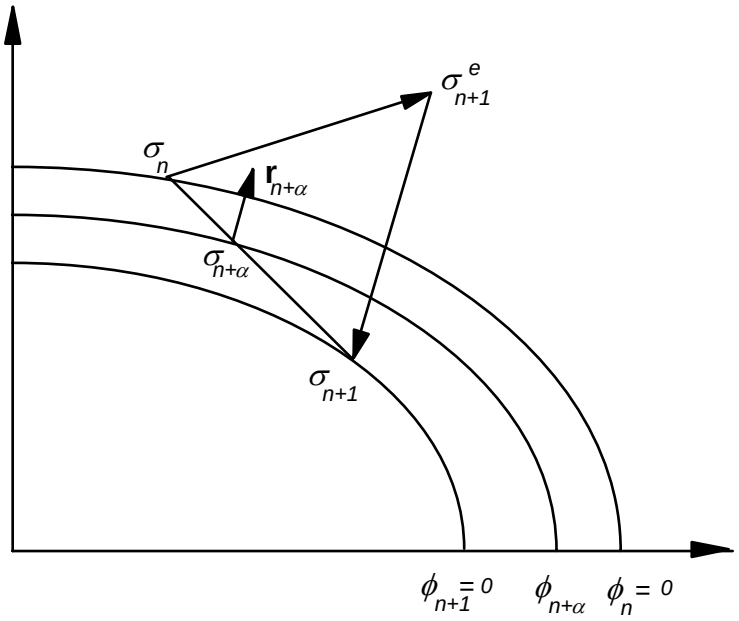

Fig. 3.1 Geometric interpretation of the generalized midpoint algorithms

Formulations for G-T type models

For a general pressure-dependent constitutive model, we can separate any stress tensor into its deviatoric and hydrostatic components as was done by Aravas [3]:

$$\boldsymbol{\sigma}_{n+1} = -p_{n+1}\mathbf{I} + \mathbf{S}_{n+1} = -p_{n+1}\mathbf{I} + \tfrac{2}{3}q\mathbf{n}_{n+1} \tag{3.26}$$

where

$$\mathbf{n}_{n+1} = \frac{3}{2q}\mathbf{S}_{n+1} \tag{3.27}$$

is the unit vector in the deviatoric space normal to the yield surface and **S** is the deviatoric stress. Likewise, the plastic strain increment can be decoupled into volumetric ($\Delta\boldsymbol{\varepsilon}_V^p$) and deviatoric ($\Delta\boldsymbol{\varepsilon}_D^p$) parts:

$$\Delta\square^p = \Delta\square_V^p + \Delta\square_D^p = \Delta\lambda\left[-\left(\frac{\partial\phi}{\partial p}\right)_{n+\alpha}\tfrac{1}{3}\mathsf{I} + \left(\frac{\partial\phi}{\partial q}\right)_{n+\alpha}\tfrac{3}{2}\frac{\mathsf{S}_{n+\alpha}}{q_{n+\alpha}}\right] \tag{3.28}$$

where the subscript n+1 of $\Delta\boldsymbol{\varepsilon}^p$ is omitted for convenience. The above equation with α=1 was used by Aravas [3] in the Euler backward algorithm formulations. After preliminary trials, it was realized that direct application of the above equation to the generalized midpoint algorithms will cause serious difficulties, which will be indicated later. It is found that using the following rearrangement of (3.28) will bypass these difficulties:

$$\Delta\square^p = \Delta\lambda\left[-\left(\frac{\partial\phi}{\partial p}\right)_{n+\alpha}\tfrac{1}{3}\mathsf{I} + \left(\frac{\partial\phi}{\partial q}\right)_{n+\alpha}\frac{q^e_{n+1}}{q_{n+\alpha}}\tfrac{3}{2}\frac{\mathsf{S}_{n+\alpha}}{q^e_{n+1}}\right] = \tfrac{1}{3}\Delta\varepsilon_p\mathsf{I} + \Delta\varepsilon_q\tfrac{3}{2}\frac{\mathsf{S}_{n+\alpha}}{q^e_{n+1}} \tag{3.29}$$

where

$$\Delta\varepsilon_p = -\Delta\lambda\left(\frac{\partial\phi}{\partial p}\right)_{n+\alpha} \tag{3.30}$$

$$\Delta\varepsilon_q = \Delta\lambda\frac{q^e_{n+1}}{q_{n+\alpha}}\left(\frac{\partial\phi}{\partial q}\right)_{n+\alpha} \tag{3.31}$$

By eliminating $\Delta\lambda$ from the above two equations one obtains

$$\Delta\varepsilon_p\left[\frac{q^e_{n+1}}{q_{n+\alpha}}\left(\frac{\partial\phi}{\partial q}\right)_{n+\alpha}\right] + \Delta\varepsilon_q\left(\frac{\partial\phi}{\partial p}\right)_{n+\alpha} = 0 \tag{3.32}$$

or more simply

$$\Delta\varepsilon_p P + \Delta\varepsilon_q Q = 0 \tag{3.33}$$

where

$$P = \frac{q^e_{n+1}}{q_{n+\alpha}} \left(\frac{\partial \phi}{\partial q} \right)_{n+\alpha} \tag{3.34}$$

$$Q = \left(\frac{\partial \phi}{\partial p} \right)_{n+\alpha} \tag{3.35}$$

Substitution (3.29) into (3.17) yields

$$\boldsymbol{\sigma}_{n+1} = \boldsymbol{\sigma}^e_{n+1} - K \Delta \varepsilon_p \mathbf{I} - 3G \Delta \varepsilon_q \frac{\mathbf{S}_{n+\alpha}}{q^e_{n+1}}. \tag{3.36}$$

By separating $\boldsymbol{\sigma}_{n+1}$ and $\boldsymbol{\sigma}^e_{n+1}$ into deviatoric and hydrostatic components according to (3.26) and using the mid-point rule for $\mathbf{S}_{n+\alpha}$, we obtain

$$p_{n+1} = p^e_{n+1} + K \Delta \varepsilon_p \tag{3.37}$$

$$\mathbf{S}_{n+1} = \mathbf{S}^e_{n+1} - 3G \Delta \varepsilon_q \frac{\mathbf{S}_{n+\alpha}}{q^e_{n+1}}. \tag{3.38}$$

After obtaining $\mathbf{S}_{n+1}$, q_{n+1} can be computed through (3.9). It should be pointed out that, due to the important arrangement of (3.29), current $\mathbf{S}_{n+1}$ is only a simple function of one unknown, the $\Delta \varepsilon_q$. Otherwise, if (3.28) is used, $\mathbf{S}_{n+1}$ is not only a function of $\Delta \varepsilon_q$ but also a function of itself. This would make the present generalized mid-point algorithms impossible.

In the present mid-point algorithms the general internal state variable evolution rules (3.6) can be written more specifically

$$\Delta \mathbf{H}_{n+1} = \mathbf{h}_{n+\alpha} (\Delta \varepsilon_p, \Delta \varepsilon_q, p_{n+\alpha}, q(\mathbf{S})_{n+\alpha}, \mathbf{H}_{n+\alpha}). \tag{3.39}$$

Through the above preliminary work, the integration problem of the elastoplastic equations for G-T type models can be reduced to the solution of the following nonlinear equations

$$\Delta \varepsilon_p P + \Delta \varepsilon_q Q = 0 \tag{3.40}$$

$$\phi_{n+1} = \phi(p_{n+1}, q(\mathbf{S})_{n+1}, \mathbf{H}_{n+1}) = 0 \tag{3.41}$$

$$p_{n+1} = p^e_{n+1} + K \Delta \varepsilon_p \tag{3.42}$$

$$\mathbf{S}_{n+1} = \mathbf{S}^e_{n+1} - 3G \Delta \varepsilon_q \mathbf{S}_{n+\alpha} / q^e_{n+1} \tag{3.43}$$

$$\Delta \mathbf{H}_{n+1} = \mathbf{h}_{n+\alpha} (\Delta \varepsilon_p, \Delta \varepsilon_q, p_{n+\alpha}, q(\mathbf{S})_{n+\alpha}, \mathbf{H}_{n+\alpha}). \tag{3.44}$$

By choosing $\Delta\varepsilon_p$ and $\Delta\varepsilon_q$ as the primary unknowns, these equations can be solved by Newton's method. Using ρ_p and ρ_q as the corrections for $\Delta\varepsilon_p$ and $\Delta\varepsilon_q$ and treating (3.40) and (3.41) as the two basic equations in which p, **S** and Δ**H** are updated using (3.42) - (3.44), we obtain the following scalar Newton equations:

$$\begin{aligned} A_{11}\rho_p + A_{12}\rho_q &= b_1 \\ A_{21}\rho_p + A_{22}\rho_q &= b_2 \end{aligned} \tag{3.45}$$

where the constants A_{ij} and b_i are given in the Appendix *A* at the end of this thesis. Taking $\Delta\varepsilon_p$ and $\Delta\varepsilon_q$ as zero in the beginning of the solution, these equations are solved for ρ_p and ρ_q; and the values of $\Delta\varepsilon_p$ and $\Delta\varepsilon_q$ are updated by

$$\begin{aligned} \Delta\varepsilon_p &= \Delta\varepsilon_p + \rho_p \\ \Delta\varepsilon_q &= \Delta\varepsilon_q + \rho_q \end{aligned}. \tag{3.46}$$

Then, the values p, **S** and Δ**H** are updated using (3.42)-(3.44). The iteration is continued until the solution converges. In the numerical problem presented here, the convergence is controlled by the requirement, $\left|\phi_{n+1}\right| \leq$ 1E-7.

As stated previously, for $\alpha = 1$ the formulation recovers the Euler backward algorithm [3]. It should be noted that the constants in (3.45) with $\alpha = 1$ are not the same as those given by Aravas [3], because of the difference between (3.28) which was used by Aravas [3] and (3.29) adopted here. The same applied to $\Delta\varepsilon_q$ in (3.46). However, despite these differences, the calculated plastic strain increment (3.18) is exactly the same in both formulations. Therefore, using either (3.28) or (3.29) for the Euler backward algorithm has no effect on final results.

3.5 Assessment of the Accuracy of the Algorithms

In this section, a systematic assessment of the accuracies of the one-step Euler forward algorithm and the proposed generalized mid-point algorithms including the Euler backward algorithm for the G-T constitutive model have been performed.

In the present context, iso-error maps have been used to display the numerical results. Without losing generality, the initial location of the stress shown in Fig. 3.2a is assumed to lie on the G-T yield surface with a hydrostatic stress equal to the initial yield stress of the matrix material. The matrix material used here is von Mises isotropic hardening material with the flow stress in the matrix material, $\overline{\sigma}$, assumed to be

$$\frac{\bar{\sigma}}{\bar{\sigma}_0} = \left(\frac{\bar{\sigma}}{\bar{\sigma}_0} + \frac{3G}{\bar{\sigma}_0} \bar{\varepsilon}^p \right)^N \tag{3.47}$$

where $\bar{\sigma}_0$ is the initial tensile yield stress of the matrix and $\bar{\varepsilon}^p$ is the equivalent plastic strain in the matrix material. This material has been used by Aravas [3]. The constants of the elastic-plastic properties of the matrix material are: N=0.1, $E/\bar{\sigma}_0$ =300, ν = 0.3, where E is the Young's modulus and ν is the Poisson's ratio. Tvergaard's constants in equation (2.1) are q_1=1.5 and q_2=1.0. The strain-controlled void nucleation model (2.5) by Chu and Needleman [25] is used here. The nucleation parameters in (2.5) are f_N = 0.04, ε_N = 0.3 and S_N =0.1. The initial void volume fraction in the beginning of the increment is 0.03.

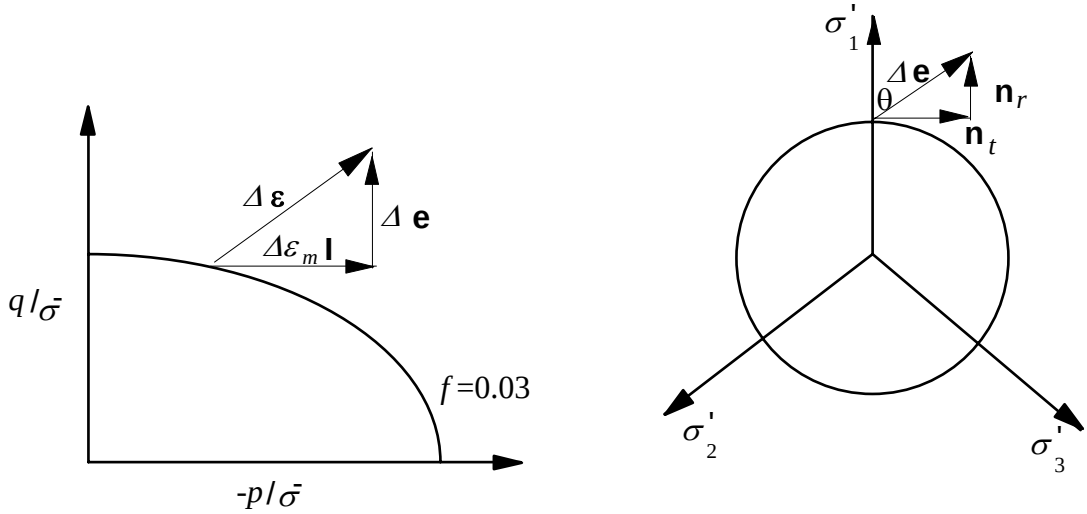

Fig. 3.2 Strain increment decomposition (a) Meridian section; (b) Deviatoric plane.

For the convenience of illustration, the strain increment $\Delta\boldsymbol{\varepsilon}$ is first decomposed into its deviatoric component, $\Delta\mathbf{e}$, and volumetric component, $\Delta\varepsilon_m$ (see Fig. 3.2a), i.e. $\Delta\boldsymbol{\varepsilon}=\Delta\varepsilon_m\mathbf{I}+\Delta\mathbf{e}$. Furthermore, the deviatoric strain increment $\Delta\mathbf{e}$ is resolved into its radial component, Δe_r, and tangential components, Δe_t (see Fig. 3.2), i.e. $\Delta\mathbf{e}=\Delta e_r\,\mathbf{n}_r+\Delta e_t\,\mathbf{n}_t$, where $\mathbf{n}_r$ and $\mathbf{n}_t$ are the unit vectors in the radial and tangential directions, respectively. For the deviatoric component the ranges for both radial and tangential directions are

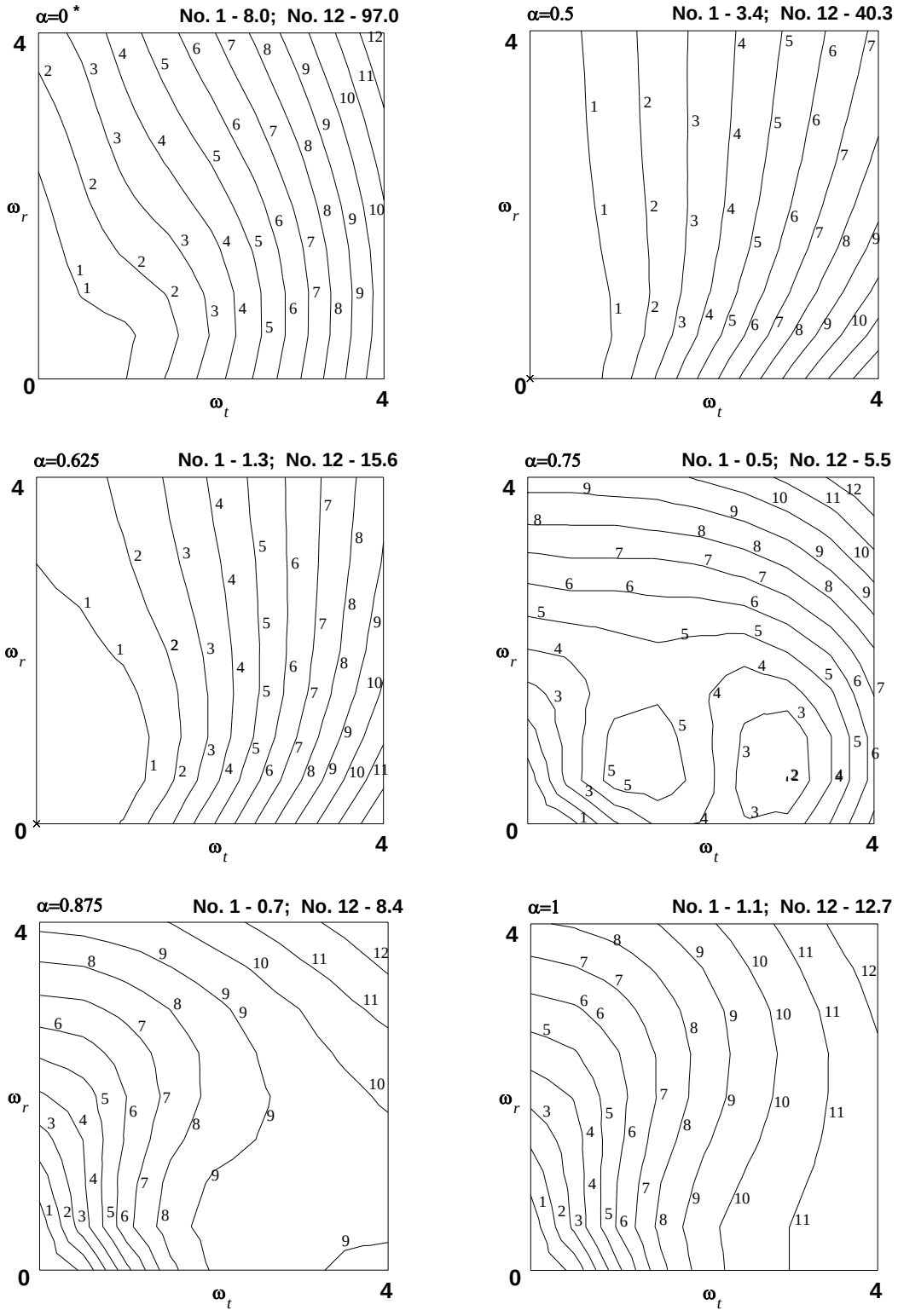

Fig. 3.3 Iso-error maps as a function of α for the case ω_m=0. $\alpha = 0^*$ denotes the one-step Euler forward algorithm.

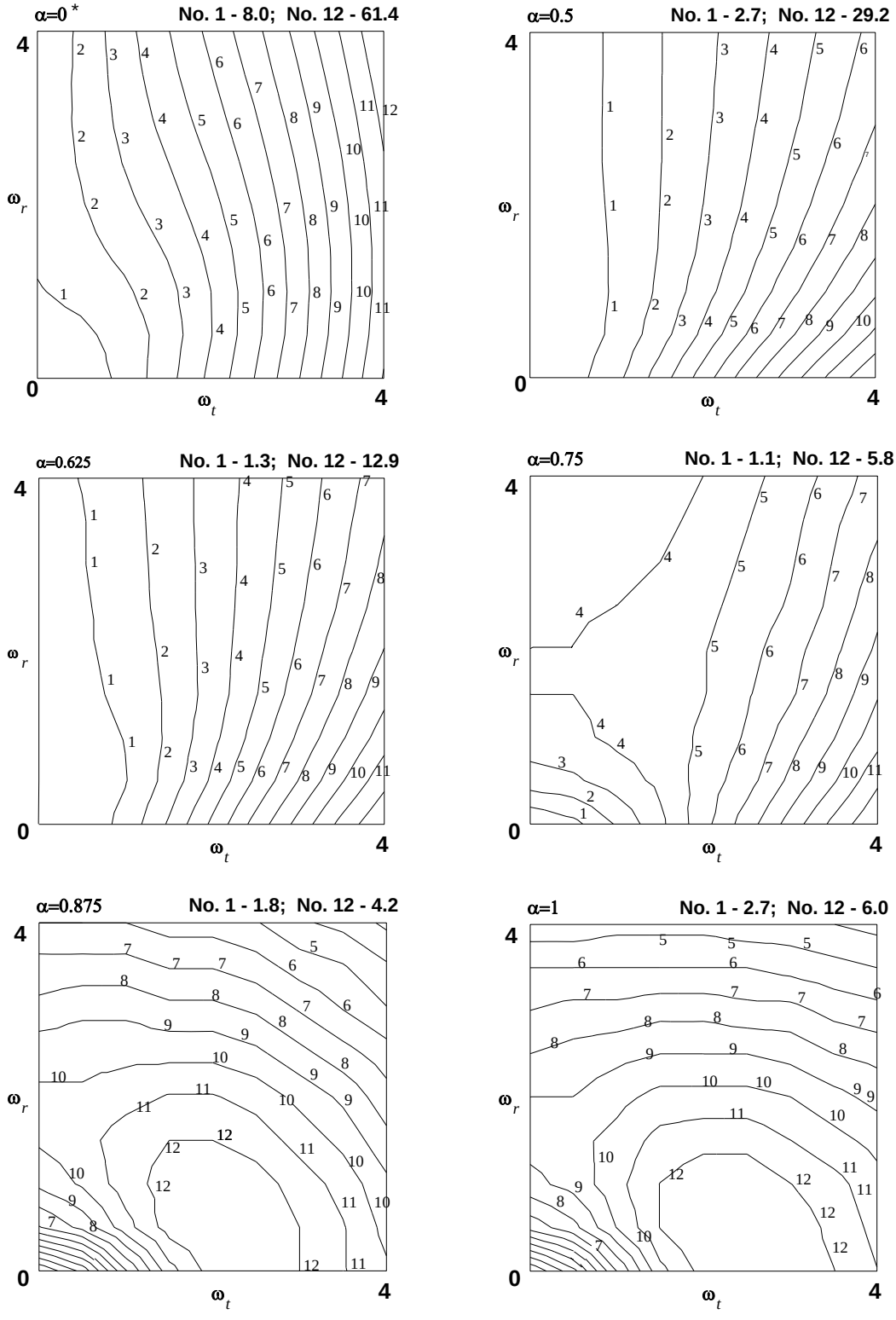

Fig. 3.4 Iso-error maps as a function of α for the case ω_m=1. $\alpha = 0^*$ denotes the one-step Euler forward algorithm.

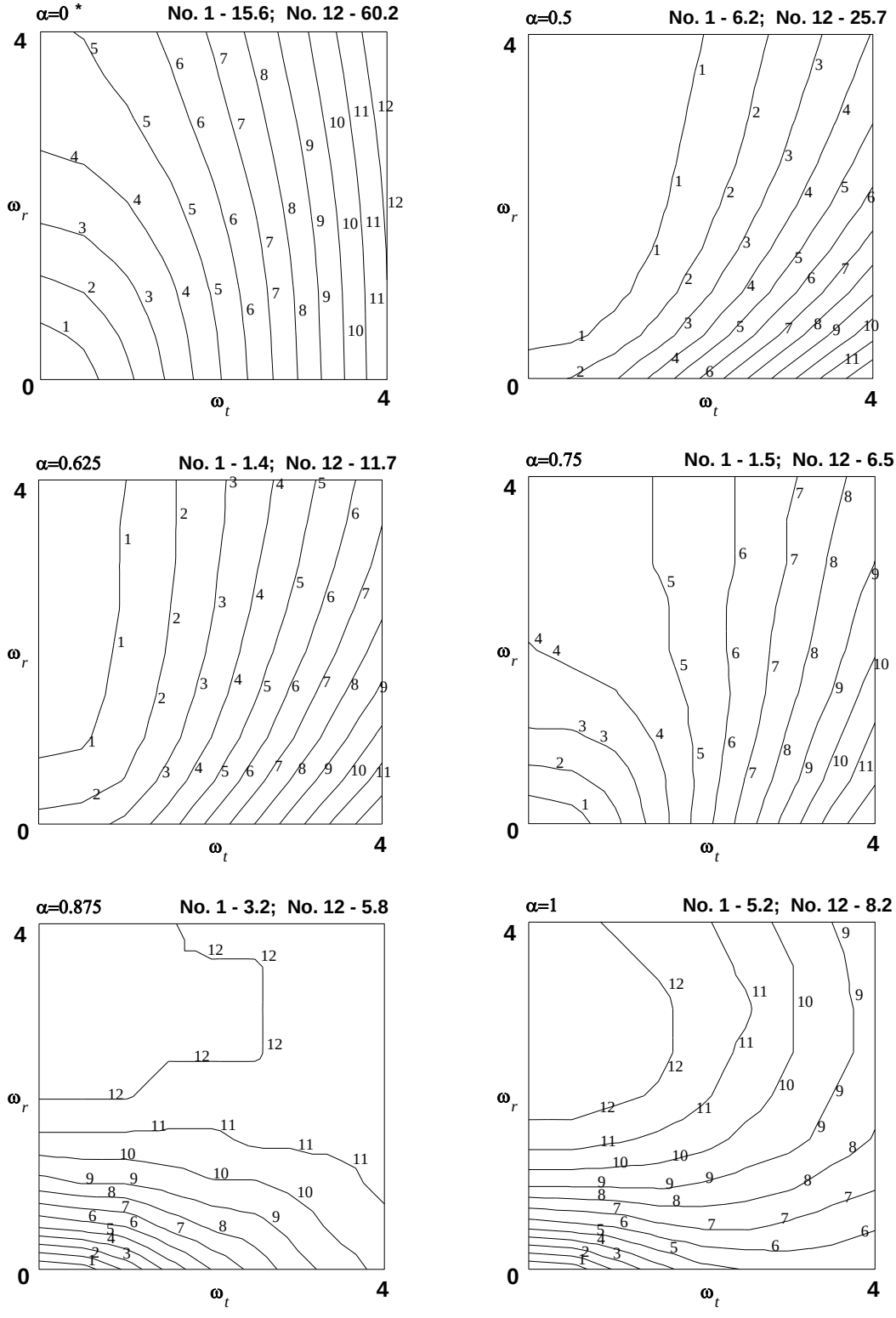

Fig. 3.5 Iso-error maps as a function of α for the case ω_m=2. $\alpha = 0^*$ denotes the one-step Euler forward algorithm.

$$0 \le \omega_r \le 4 \text{ and } 0 \le \omega_t \le 4 \tag{3.48}$$

where $\omega_r = \dfrac{2G\Delta e_r}{\bar{\sigma}_0}$ and $\omega_t = \dfrac{2G\Delta e_t}{\bar{\sigma}_0}$. For the volumetric component, three values of $\Delta\varepsilon_m$ have been used in the assessment: ω_m=0,1,2, where $\omega_m = 3K\Delta\varepsilon_m / \bar{\sigma}_0$.

Figs. 3.3-3.5 show the iso-error maps for the computed stress as a function of the prescribed volumetric and deviatoric strain increments and the algorithmic parameter α. In Figs. 3.3-3.5 $\alpha = 0^*$ denotes the one-step Euler forward algorithm in which the radial return correction [20] mentioned before was made after the increment is finished. Results are reported in terms of the relative root mean square of the error between the exact and computed results, which is obtained according to the expression

$$error = \frac{\sqrt{(\boldsymbol{\sigma} - \boldsymbol{\sigma}^*) : (\boldsymbol{\sigma} - \boldsymbol{\sigma}^*)}}{\sqrt{\boldsymbol{\sigma}^* : \boldsymbol{\sigma}^*}} \times 100 \tag{3.49}$$

Here $\boldsymbol{\sigma}$ is the result obtained by the application of the algorithms, whereas $\boldsymbol{\sigma}^*$ is the "exact" solution corresponding to the specified strain increment. The exact solution is obtained for the given strain increment by repeated application of the Euler forward algorithm with equal strain sub-increments of 1/1000 of the initial yield strain in order to ensure high accuracy. In each iso-error map, 12 iso-error curves have been used, with the lowest error denoted by curve No. 1 and the highest error denoted by curve No. 12. These two values are shown on the top of each iso-error map.

Effect of α on the accuracy of the algorithms

Nine values of α from 0 to 1, with an increment 0.125 have been used in the assessment. It has been shown by Ortiz and Popov [94] that, when $\alpha \ge 0.5$, the generalized mid-point algorithms are unconditionally stable. Therefore, only the results of these unconditional stable algorithms are presented in Figs. 3.3-3.5.

In general, Figs. 3.3-3.5 show that, the errors are not excessive for the generalized mid-point algorithms with $\alpha > 0.5$, for both small and large time steps. For small deviatoric strain increments, say in the region (1,1), all the generalized mid-point algorithms gave the error less than or near 5%. Fig. 3.6 shows the errors as a function of α for several strain increment steps. Clearly, the true mid-point algorithm demonstrated the second-order accuracy [94] for zero or very small tangential strain increments (less than 0.5). It is worth noting that in the small tangential strain increment range, the second-order accuracy is not sensitive to radial increment size. However, when the tangential strain increment size is equal to or larger than 0.5, the second-order accuracy with the true mid-point algorithm disappears. Fig. 3.6b shows that in the pure tangential strain increment case, the second order accuracy moved from the algorithm $\alpha = 0.5$ to 0.625 and 0.75. Moreover, the true mid-point algorithm gave a very poor solution for reasonably large tangential strain increment steps compared with other members of the generalized mid-

point algorithms with $\alpha > 0.5$. For large tangential strain increments in the case $\omega_m = 0$, the true mid-point algorithm gave a maximum error as high as 40%, which is almost 8 times the maximum error given by the algorithm with $\alpha = 0.75$. The algorithm with $\alpha = 1$ which recovers the Euler backward algorithm of Aravas [3], gave moderate accuracy in all the cases. The error is smaller when the volumetric strain increment, ω_m, is positive than in the case where ω_m is zero.

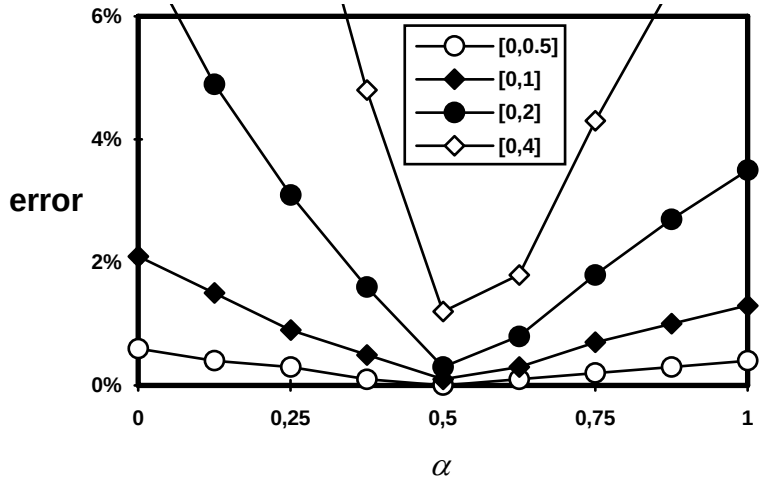

(a) Increments in radial direction

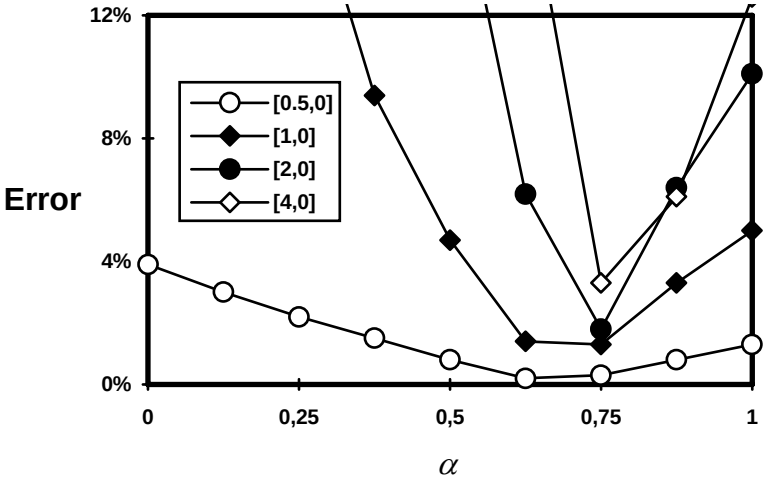

(b) Increments in tangential direction

Fig. 3.6 Range of the second-order accuracy of the algorithms for the case $\omega_m = 0$. The numbers in the legend denote the normalized step size in the tangential and radial directions, respectively.

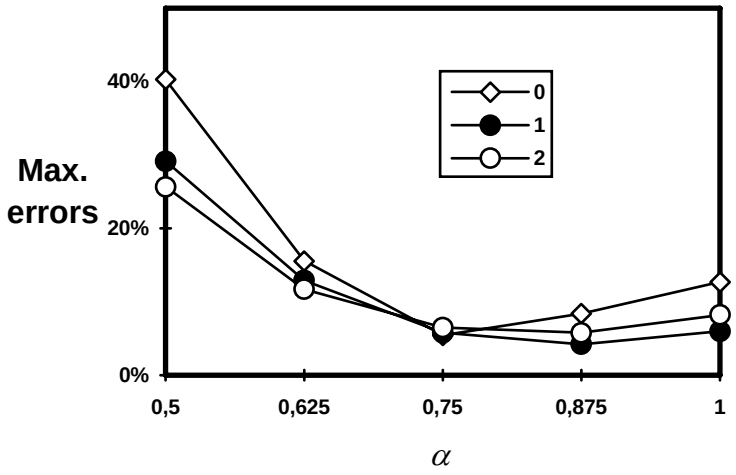

(a)

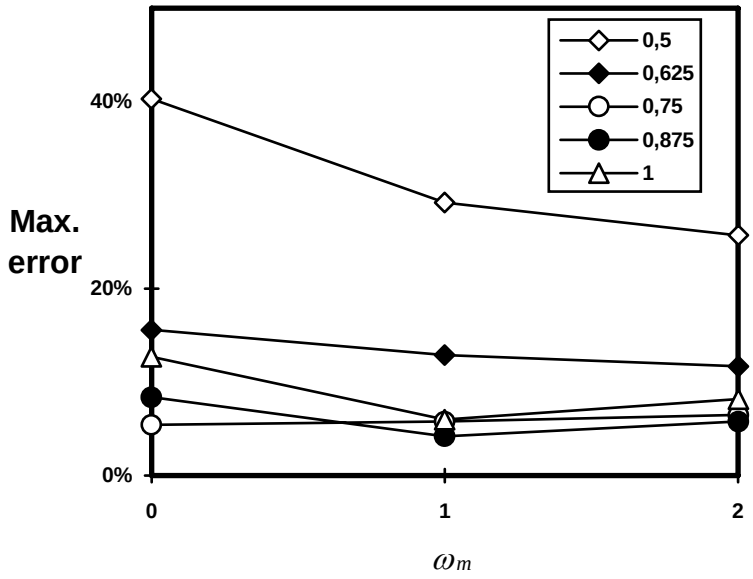

(b)

Fig. 3.7 (a) Maximum errors as a function of α. The numbers 0, 1, 2 in the legend correspond to the values of ω_m. (b) Maximum errors as a function of $\Delta\varepsilon_m$. The numbers in the legend imply the values of ###.

The maximum errors of the generalized mid-point algorithms in all the increment schemes assessed is plotted in Fig. 3.7a as a function of α. It shows that in the present case, the optimal value of α which gave the lowest maximum error was between 0.75 and 0.875. For elastic perfectly-plastic model, Gratacos et. al. [40] computed two points in the ($\Delta\mathbf{e}_r$, $\Delta\mathbf{e}_t$) space, point (1) is almost tangential, point (2) includes both components. They found the optimal values of α corresponding to those two points were $\alpha = 0.75$ and α
=0.83. Although the problems are different, the present results for the optimal values of α in terms of maximum errors coincide with Gratacos et al.'s results [40]. This finding

suggests that unlike the pressure-modified von Mises model [70], where it was found that for both large and small time steps, the algorithm with $\alpha = 0.5$ is the most accurate one, the true mid-point algorithm and the Euler backward algorithm are not the most accurate ones for the G-T material model considered.

Ortiz and Popov [94] have studied the accuracy of the generalized mid-point algorithms for perfectly plastic von Mises model with six values of α
, from 0.5 to 1.0. It is interesting to note that the shapes of present results with $\omega_m = 0$ (Fig. 3.3) are similar to their results, with the exception of the cases $\alpha \geq 0.875$ and ω_r, ω_t, > 3. Ortiz and Popov only gave results within the range $3 \geq \omega_t$, $\omega_r \geq 0$.

Effect of volumetric strain increments on the accuracy

Figs. 3.3-3.5 show that the shapes of the iso-error maps of the generalized mid-point algorithms with $0.625 \geq \alpha \geq 0.5$ and the one-step Euler forward algorithm are not very sensitive to the volumetric strain increments. Furthermore, these iso-error curves are not sensitive to the radial strain increment size. However, it can be observed from Figs. 3.3-3.5 that for the generalized mid-point algorithms with $\alpha \geq 0.825$, the shapes of the iso-error maps are very sensitive to the volumetric strain increments.

The maximum errors as a function of ω_m are shown in Fig. 3.7b. For the three values of volumetric strain increments considered, no significant effect on the accuracy can be observed. The general trend is that, in the presence of non-zero volumetric strain increments, all the algorithms gave smaller maximum errors than in the cases where ω_m is zero, except the algorithm $\alpha = 0.75$.

Accuracy of the one-step Euler forward algorithm

In all the increment cases assessed, the one-step Euler algorithm gave the worst accuracy. For the case where ω_m is zero, it gave the maximum error nearly as high as 100%. The shapes of the iso-error maps are very insensitive to the volumetric strain increment size. When the tangential strain increment size is large, they are also not sensitive to the radial strain increment size. In other words, the error of the increment scheme (4,4) is near, for example, to that of the increment (4,0) for the case $\omega_m \neq 0$. The comparison of the errors between the one-step Euler forward algorithm and the algorithm with $\alpha = 0.75$ and 1 is shown in Table 1 for the case ω_m=2.0. Tangential and radial strain increments are considered separately in Table 1. Table 1 shows that for both radial and tangential increments, the errors of the Euler forward algorithm are more than 8 times those of the algorithm with $\alpha = 0.75$.

As was mentioned in the section (3.1), up to now, Euler forward algorithms are still widely used for the G-T model. Present results show that, in order to get reasonable accuracy, the increment size for the Euler forward algorithms should be kept very small.

Table 1 Comparison of the errors between different algorithms

		Radial increments				Tangential increment			
(ω_t, ω_r)	(0,0)	(0,1)	(0,2)	(0,3)	(0,4)	(1,0)	(2,0)	(3,0)	(4,0)
$\frac{\alpha=0^{\bullet}}{\alpha=0.75}$	11.6	8.0	8.9	9.7	10.4	10.4	8.8	8.4	8.7
$\frac{\alpha=0^{\bullet}}{\alpha=1}$	2.4	2.4	3.0	3.4	3.8	3.4	5.0	6.9	9.5

3.6 A Brief Summary

In this chapter, the accuracy of different numerical integration algorithms has been assessed in a systematic way. The numerical results demonstrated that, from the point of view of accuracy, the one-step Euler forward algorithm is the worst one. For the generalized mid-point algorithms, we may conclude that the optimal choice of α for the G-T model may depend on the nature of the problem under consideration. When the deviatoric strain increments are given in the radial direction, the true mid-point algorithm gives the best accuracy and is second-order accurate, no matter how large the increment size is. Furthermore, it may be concluded that for the G-T model the standard Euler backward algorithm is not the most accurate ones for reasonably large time steps. For the cases assessed, in terms of maximum errors, the optimal choice of α is between 0.75 and 0.875.

Chapter 4

NUMERICAL INTEGRATION FOR G-T TYPE MODELS

(II) FE implementation, efficiency and performance

In the finite element implementation of any numerical algorithm, the calculation of consistent tangent moduli (CTM) by linearization of the involved field equations is very important and crucial to the convergence behaviour, or efficiency. In this chapter, the global iterative methods are discussed first. Then, by linearization of the integration algorithms proposed in the preceding chapter and by decomposition of the stresses into hydrostatic and deviatoric parts, the CTM for the generalized mid-point algorithms are derived and an explicit expression, with seven-constants, for the CTM is presented. The explicit formula greatly facilitates the computer implementation of the algorithms, because no matrix inversion is involved in the formula. Finally, the efficiency and performance of the present finite element implementation is widely assessed by various numerical examples.

4.1 Global Iterative Methods

Stress update algorithms and the accuracy of the algorithms for the G-T model have been explored in the previous chapter. In addition to the accuracy, the involved numerical approximations must be stable and efficient. In this chapter, these problems in the FE implementation of the proposed numerical algorithms are addressed.

An important step in the solution of non-linear deformation problems using a Newton type of iterative scheme is the calculation of CTM by linearization of the involved field equations. It has been emphasized by Simo and Taylor [121] that for rate-independent elastoplastic problems, the consistency between the tangent moduli and the integration algorithms employed in the solution of incremental problem plays a crucial role in preserving the quadratic rate of asymptotic convergence of iterative solution schemes based on Newton's method.

In finite element methods, the virtual work principal (VWP) is usually used to express the equilibrium at the end of the increment (t_{n+1}). Due to the extreme non-linearity associated with VWP for large deformation elastoplastic problems, it must be solved iteratively. Consequently, two distinct phases must be considered when developing a computational procedure for non-linear problems: the numerical algorithm for accurate state determination of the material and the numerical global iterative method to solve the system of nonlinear equations. The former is considered in the previous chapter and this chapter deals with the second phase.

Newton method is widely used to solve the set of nonlinear equations for the incremental displacement field $\mathbf{u}(\mathbf{X}_n, t_{n+1})$, and it requires the linearization of the governing equations at the present guess of the solution. In order to obtain the linearized form, VWP must be written referring to a fixed state so that all integrations are carried out and all gradients are taken in this state. The equilibrium statement can be written in terms of incremental virtual displacement $\bar{\mathbf{u}}(\mathbf{X}_n)$ in updated Lagrangian form as follows:

$$\Phi(\mathsf{u}_{n+1}, \bar{\mathsf{u}}(\mathsf{X}_n)) = \int_{V_n} \mathsf{t}^c : \delta \bar{\mathsf{e}}\, dV_n - \int_{\partial V_{n+1}} \mathsf{t}^T \cdot \delta \bar{\mathsf{u}}\, ds - \int_{V_{n+1}} \mathsf{f}^T \cdot \delta \bar{\mathsf{u}}\, dV \tag{4.1}$$

where V_n and V_{n+1} are the volume at the beginning of the increment and current volume; $\mathbf{t}$ and $\mathbf{f}$ are the applied surface traction and body force; $\boldsymbol{\tau}^c$ and $\bar{\boldsymbol{\varepsilon}}$ are any conjugate pairing of material stress and strain measures. Within the context of finite element analysis, the solution of problem (4.1) is accomplished by an iterative scheme such as the Newton method. Typically, one solves a sequence of linearized problems defined as

$$\Phi(\mathbf{u}_{n+1}, \bar{\mathbf{u}}(\mathbf{X}_n)) + \left.\frac{\partial \Phi}{\partial \mathbf{u}}\right|_{n+1} \cdot \Delta \mathbf{u}_{\mathbf{n+1}} = 0 \tag{4.2}$$

until the residual $\Phi(\mathbf{u}_{n+1}, \bar{\mathbf{u}}(\mathbf{X}_n))$ vanishes to within a prescribed tolerance. In (4.2) $\left.\frac{\partial \Phi}{\partial \mathbf{u}}\right|_{n+1} \equiv \mathbf{J}_{global}$ is known as the tangent operator or global Jacobian matrix. A closed form of the complete Jacobian matrix is given in the ABAQUS Theory Manual V5.1 [1]:

$$\mathsf{J}_{global} = \int_{V_n} \mathsf{B}_M : \mathsf{D}^{ep}_{cons.} : \mathsf{B}_N\, dV_n + \mathsf{J}_1 \tag{4.3}$$

$\mathbf{B}_M$ and $\mathbf{B}_N$ are matrixes which depend, in general, on the current position of the material point being considered; $\mathbf{J}_1$ is the left term of the global Jacobian matrix which is described in [1]; $\mathbf{D}^{ep}_{cons.}$ are the so-called consistent tangent moduli (CTM) of the material which should be derived by consistent linearization of the update procedure, in order to achieve the asymptotic rate of quadratic convergence characteristic of the Newton method [121]. In (4.3), $\mathbf{D}^{ep}_{cons.}$ is defined as

$$\mathbf{D}^{ep}_{cons.} = \left.\frac{\partial \boldsymbol{\sigma}}{\partial \boldsymbol{\varepsilon}}\right|_{n+1}. \tag{4.4}$$

The convergence of (4.2) is essentially governed by the choice of the CTM, $\mathbf{D}^{ep}_{cons.}$, which depends in turn on the iteration scheme adopted. Based on the choice of the reference state for successive iterations (V_{ref}), two different procedures may be used [4,120]:

(a) During one increment, the reference state is kept fixed to the configuration at the beginning of an increment, i.e. $V_{ref} = V_n$. Thus, all the physical quantities are referred to a mechanical permissible configuration at the beginning of the increment. After the equilibrium is achieved at the end of the increment, the reference state is updated to the solution configuration.

(b) The reference state is updated after each iteration *i* within the increment ($V_{ref} = V^i_{n+1}$) whether it is in equilibrium with the prescribed loading or not.

Both of the above solution procedures can be developed maintaining consistency with the integration scheme to update stress and other state variables. However, scheme (b) introduces a "history dependence" of the converged values on the intermediate non-converged iterations. As far as elastoplastic problems are concerned, which are path-dependent, the intermediate, non converged solutions obtained during the iteration process are usually not on the actual solution path and it is preferred with large increment steps that the iteration process always refers to a physically permissible state. This is what is done in ABAQUS [1].

4.2 CTM for Euler Forward Algorithm - Continuum Tangent Moduli

If scheme (b) is adopted, stress is added from the previous iteration of the same increment:

$$\boldsymbol{\sigma}^{i+1}_{n+1} = \boldsymbol{\sigma}^{i}_{n+1} + \Delta\boldsymbol{\sigma}^{i+1}_{n+1} \tag{4.5}$$

where *i* is the number of iterations within increment *n*+1. It is expected that the changes of stresses between iterations is rather small compared with the changes between increments, consequently, the Euler forward algorithm is often associated in this case. Thus, the incremental response of the Euler forward algorithm (see the previous chapter) can be rewritten as

$$\boldsymbol{\sigma}^{i+1} = \mathbf{D}^{e} : (\boldsymbol{\varepsilon}^{i+1} - \boldsymbol{\varepsilon}^{p}) \tag{4.6}$$

where the subscripts n+1 have been omitted for convenience. Because in the Euler forward algorithm, the plastic strain increment direction is known beforehand, the differentiation of the plastic strain can be written as

$$\partial\boldsymbol{\varepsilon}^p = \partial\lambda \mathbf{r}^i = \partial\lambda \left.\frac{\partial\phi}{\partial\boldsymbol{\sigma}}\right|^i . \tag{4.7}$$

Therefore, by linearization of the stress update procedure (4.6), we obtain:

$$\partial\boldsymbol{\sigma} = \mathbf{D}^e : (\partial\boldsymbol{\varepsilon} - \partial\boldsymbol{\varepsilon}^p) = \mathbf{D}^e : (\partial\boldsymbol{\varepsilon} - \partial\lambda \frac{\partial\phi}{\partial\boldsymbol{\sigma}}) \tag{4.8}$$

where the superscripts are also omitted for convenience. The only unknown in (4.8) is $\partial\lambda$ which can be easily determined, by enforcement of the consistency condition that upon yielding the stress point must remain on the yield surface if no unloading occurs [20,121]. After solving $\partial\lambda$, the CTM of (4.4) can be obtained.

For the G-T yield model described in chapter 2, $\mathbf{D}^{ep}_{cons.}$ of (4.4) can be written:

$$D^{ep}_{cons.}\big|_{ijkl} = \frac{E}{1+\nu}\left[\delta_{ik}\delta_{jl} + \frac{\nu}{1+\nu}\delta_{ij}\delta_{kl} - \frac{P_{ij}P_{kl}}{\overline{E}}\right] \tag{4.9}$$

where

$$P_{ij} = \tfrac{3}{2}\frac{S_{ij}}{\overline{\sigma}} + \eta\frac{1+\nu}{1-2\nu}\delta_{ij}$$

$$\overline{E} = (1+\nu)\frac{\overline{H}}{E} + \tfrac{3}{2}\frac{q^2}{\overline{\sigma}^2} + 3\eta^2\frac{1+\nu}{1-2\nu}$$

$$\overline{H} = -\frac{\overline{\sigma}}{2}\left[3\eta(1-f)\frac{\partial\phi}{\partial f} + \left(\frac{\partial\phi}{\partial\overline{\sigma}} + A\overline{h}\frac{\partial\phi}{\partial f}\right)\left(\frac{q^2}{\overline{\sigma}^2} - \eta\frac{3p}{\overline{\sigma}}\right)\frac{\overline{h}}{1-f}\right]$$

$$\frac{\partial\phi}{\partial f} = 2q_1\cosh\left(-\frac{3q_2 p}{2\overline{\sigma}}\right) - 2q_1^2 f$$

$$\frac{\partial\phi}{\partial\overline{\sigma}} = -\frac{2q^2}{\overline{\sigma}^3} + \frac{3q_1 q_2 fp}{\overline{\sigma}^2}q_1\sinh\left(-\frac{3q_2 p}{2\overline{\sigma}}\right)$$

$$\eta = \frac{f}{2}q_1 q_2\sinh\left(-\frac{3q_2 p}{2\overline{\sigma}}\right)$$

$$\overline{h} = \frac{d\overline{\sigma}}{d\overline{\varepsilon}_p}$$

It should be noted that the current CTM for the Euler forward algorithm (4.9) coincide with the classical elastoplastic tangent moduli, which is sometimes called "continuum tangent moduli (COTM)" [121]. As introduced in section (3.1), in the Euler forward scheme, after the iteration, the updated stresses usually lie outside the yield surface, an additional correction is then needed to bring the stress back to the yield surface [20].

It should be mentioned that the COTM is derived based on the scheme (b), which essentially means that the COTM is the CTM only when update procedure (b), where the change of stress in every iteration is very small, is adopted. However, in line with pure mathematical convenience, COTM is widely used in ABAQUS where update (a) is used. It will be shown in the next section that using the COTM in ABAQUS will strongly affect the convergence behaviour of the Newton method.

4.3 CTM for Proposed Numerical Algorithms

If the update scheme (a) is adopted, large increment steps where implicit algorithms are essential to the accuracy, can be used. For the generalized mid-point algorithms (3.15-3.25) proposed in the previous chapter, we no longer have the simple form (4.7) since the stress increment corresponding to any given strain increment must be computed iteratively, but rather

$$\partial \boldsymbol{\varepsilon}^{p}_{n+1} = \partial\lambda \mathbf{r}_{n+\alpha} + \Delta\lambda \partial \mathbf{r}_{n+\alpha} \tag{4.10}$$

The last term of the right hand side of (4.10) makes the derivation of CTM much more difficult than that of the classical COTM, especially for non-trivial material models such as the G-T model considered in this study. For simple yield models such as von Mises model using nonlinear isotropic and kinematic-hardening rules, Simo and Taylor [121] and reference [1] have a closed form ready for use. In general, however, the task of evaluating the consistent tangent moduli in closed form may prove to be exceedingly laborious.

For the G-T model, an expression of (4.4) consistent with a Euler backward algorithm was given by Aravas [3]. However, according to that scheme, two matrix inversions (6×6 for 3D problem) with at least one asymmetric matrix must be performed to obtain the CTM. Furthermore, for perfectly plastic matrix material, the numerical inversion is impossible. In this chapter, we shall focus on the possibility of deriving an explicit expression for the CTM consistent with the generalized mid-point algorithms as well as the Euler backward algorithm. An important strategy in deriving the explicit CTM we are going to use is the decomposition of the stress and strain increments into hydrostatic (volumetric) and deviatoric components.

CTM for Euler backward algorithm

Euler backward algorithm is a member ($\alpha = 1$) of the generalized mid-point algorithm family (3.15-3.25). So, specially the decomposition of the plastic strain increments (3.29) in chapter 3 can be written as:

$$\Delta \boldsymbol{\varepsilon}^p = \Delta \boldsymbol{\varepsilon}_V^p + \Delta \boldsymbol{\varepsilon}_D^p = \tfrac{1}{3}\Delta\varepsilon_p \mathbf{I} + \Delta\varepsilon_q \mathbf{n}_{n+1} \tag{4.11}$$

where

$$\begin{aligned} \Delta\varepsilon_p &= -\Delta\lambda\left(\frac{\partial\phi}{\partial p}\right)_{n+1} \\ \Delta\varepsilon_q &= \Delta\lambda\left(\frac{\partial\phi}{\partial q}\right)_{n+1} \end{aligned} \tag{4.12}$$

By eliminating $\Delta\lambda$ from the above two equations one obtains an equation which is similar to (3.33)

$$\Delta\varepsilon_p P + \Delta\varepsilon_q Q = 0 \tag{4.13}$$

where

$$\begin{aligned} P &= \left(\frac{\partial\phi}{\partial q}\right)_{n+1} \\ Q &= \left(\frac{\partial\phi}{\partial p}\right)_{n+1} \end{aligned} \tag{4.14}$$

Now we can rewrite the plastic relaxation equations of (3.36) by using (4.11) and (3.7) as

$$\boldsymbol{\sigma}_{n+1} = \boldsymbol{\sigma}_{n+1}^e - K\Delta\varepsilon_p \mathbf{I} - 2G\Delta\varepsilon_q \mathbf{n}_{n+1}. \tag{4.15}$$

By comparing equation (4.15) and equation (3.26) in chapter 3 we observe that in the deviatoric stress plane the return to the yield surface is along $\mathbf{n}_{n+1}$, which implies $\mathbf{n}_{n+1}$ can be simply determined from the elastic stress predictor $\boldsymbol{\sigma}_{n+1}^e$ [3,121] as

$$\mathbf{n}_{n+1} = \frac{3}{2q}\mathbf{S}_{n+1} = \frac{3}{2q^e}\mathbf{S}_{n+1}^e \tag{4.16}$$

where $\mathbf{S}_{n+1}^e$ is the deviatoric part of $\boldsymbol{\sigma}_{n+1}^e$. By projecting the plastic relaxation equation onto $\mathbf{I}$ and $\mathbf{n}_{n+1}$, and using (3.26), we find two scalar return mapping equations

$$p = p^e + K\Delta\varepsilon_p$$
$$q = q^e - 3G\Delta\varepsilon_q \tag{4.17}$$

where p^e and q^e are calculated from $\boldsymbol{\sigma}^e_{n+1}$. By choosing η_p and η_q as the primary unknowns, Aravas [3] has presented a detailed procedure for updating the state variables by the Newton method.

Based on the decomposition of the return mapping process described above, we shall derive the CTM for the G-T type models from the hydrostatic and deviatoric components separately. First we consider the deviatoric stress plane in which we have

$$\mathbf{S}_{n+1} = 2G(\boldsymbol{\varepsilon}_D\Big|_n + \Delta\boldsymbol{\varepsilon}_D\Big|_{n+1} - \Delta\boldsymbol{\varepsilon}^p_D) = 2G(\boldsymbol{\varepsilon}^T_D - \Delta\boldsymbol{\varepsilon}^p_D) \tag{4.18}$$

where $\boldsymbol{\varepsilon}^T_D = \boldsymbol{\varepsilon}_D\Big|_n + \Delta\boldsymbol{\varepsilon}_D\Big|_{n+1}$, and $\boldsymbol{\varepsilon}_D\Big|_n$, $\Delta\boldsymbol{\varepsilon}_D\Big|_{n+1}$ are the deviatoric parts of $\boldsymbol{\varepsilon}_n$, $\Delta\boldsymbol{\varepsilon}_{n+1}$ respectively. By substituting (4.11) and (4.16) into (4.18) and rearranging we obtain

$$(1+\frac{3G}{q}\Delta\varepsilon_q)\mathbf{S}_{n+1} = 2G\,\boldsymbol{\varepsilon}^T_D = \mathbf{S}^e_{n+1}. \tag{4.19}$$

The inner product of this equation with itself gives

$$q + 3G\Delta\varepsilon_q = 2G\bar{\varepsilon}^T_D = q^e \tag{4.20}$$

where

$$\bar{\varepsilon}^T_D = \sqrt{\tfrac{2}{3}\boldsymbol{\varepsilon}^T_D : \boldsymbol{\varepsilon}^T_D} \tag{4.21}$$

Differentiation of (4.20) yields

$$\partial q = \partial q^e - 3G\partial\Delta\varepsilon_q \tag{4.22}$$

From the definition of $\bar{\varepsilon}^T_D$ and (4.20) we obtain

$$\partial q = 3G(\frac{\mathbf{S}^e_{n+1}}{q^e}\partial\boldsymbol{\varepsilon}^T_D - \partial\varepsilon_q). \tag{4.23}$$

By taking the variation of (4.19) with respect to all quantities at the end of the increment we obtain

$$(1+\frac{3G}{q}\partial\Delta\varepsilon_q)\partial\mathbf{S}_{n+1}+\mathbf{S}_{n+1}\frac{3G}{q}(\partial\Delta\varepsilon_q-\frac{\Delta\varepsilon_q}{q}\partial q)=2G\partial\boldsymbol{\varepsilon}_D^T. \tag{4.24}$$

By substituting (4.23) into (4.24) and rearranging we find

$$\partial\mathbf{S}_{n+1}=2G\frac{q}{q^e}\partial\mathbf{e}_D^T+\left[\frac{9G^2}{q(q^e)^2}\Delta\varepsilon_q\mathbf{S}_{n+1}\otimes\mathbf{S}_{n+1}^e\right]:\partial\mathbf{e}_D^e-\frac{3G}{q}\mathbf{S}_{n+1}\partial\Delta\varepsilon_q\,. \tag{4.25}$$

Alternatively this can be written

$$\partial\mathbf{S}_{n+1}=\left[2G\frac{q}{q^e}\mathbf{J}+\frac{4G^2}{q^e}\Delta\varepsilon_q\mathbf{n}_{n+1}\otimes\mathbf{n}_{n+1}\right]:\partial\mathbf{e}_D^T-2G\mathbf{n}_{n+1}\partial\varepsilon_q \qquad \text{s} \tag{4.26}$$

where **J** is the fourth-order unit tensor. For all the cases in which three direct strains are defined by the kinematic solution we have

$$\partial\boldsymbol{\varepsilon}_D^T=\left[\mathbf{J}-\tfrac{1}{3}\mathbf{I}\otimes\mathbf{I}\right]:\partial\boldsymbol{\varepsilon}_{n+1} \tag{4.27}$$

and

$$\partial p=-K\mathbf{I}\partial\boldsymbol{\varepsilon}_{n+1}+K\partial\varepsilon_p. \tag{4.28}$$

Differentiation of (4.15) with respect to the strain, and using (4.26) and (4.27) gives

$$\partial\boldsymbol{\sigma}_{n+1}=\mathbf{Z}:\partial\boldsymbol{\varepsilon}_{n+1}-K\mathbf{I}\partial\varepsilon_p-2G\mathbf{n}_{n+1}\partial\varepsilon_q \tag{4.29}$$

where

$$\mathbf{Z}=2G\frac{q}{q^e}\mathbf{J}+(K-\frac{2G}{3}\frac{q}{q^e})\mathbf{I}\otimes\mathbf{I}+\frac{4G^2}{q^e}\partial\varepsilon_q\mathbf{n}_{n+1}\otimes\mathbf{n}_{n+1} \tag{4.30}$$

For the general pressure-dependent elastoplasticity model, by linearization of the flow (equation 4.13) and yield (equation 3.41) conditions at the end of the time step, Aravas [3] obtained the following equations:

$$A_{11}\partial\varepsilon_p+A_{12}\partial\varepsilon_q=(B_{11}\mathbf{I}+B_{12}\mathbf{n}_{n+1}):\partial\boldsymbol{\sigma}_{n+1} \tag{4.31a}$$

$$A_{21}\partial\varepsilon_p+A_{22}\partial\varepsilon_q=(B_{21}\mathbf{I}+B_{22}\mathbf{n}_{n+1}):\partial\boldsymbol{\sigma}_{n+1} \tag{4.31b}$$

where the constants A_{ij} and B_{ij} are given in the Appendix II of [3] and can be reproduced from Appendix *D* in the end of this thesis by using the definitions in (4.12) and (4.14) and $\alpha=1$. Substitution of (4.29) into (4.31) gives

$$\partial\varepsilon_p = (C_{11}\mathbf{I} + C_{12}\mathbf{n}_{n+1}) : \mathbf{Z} : \partial\varepsilon_{n+1} \tag{4.32a}$$

$$\partial\varepsilon_q = (C_{21}\mathbf{I} + C_{22}\mathbf{n}_{n+1}) : \mathbf{Z} : \partial\varepsilon_{n+1} \tag{4.32b}$$

where the constants C_{ij} are given in the Appendix *B* of this thesis.

Substitution of (4.32) into (4.29), yields an expression for the tangent moduli consistent with the Euler backward algorithm:

$$\partial\boldsymbol{\sigma}_{n+1} = \mathbf{M} : \mathbf{Z} : \partial\boldsymbol{\varepsilon}_{n+1} \tag{4.33}$$

where

$$\mathbf{M} = \mathbf{J} - \mathbf{M}^{\mathbf{I}} - \mathbf{M}^{\mathbf{n}} \tag{4.34a}$$

$$\mathbf{M}^{\mathbf{I}} = K(C_{11}\mathbf{I} \otimes \mathbf{I} + C_{12}\mathbf{I} \otimes \mathbf{n}) \tag{4.34b}$$

$$\mathbf{M}^{\mathbf{n}} = 2G(C_{21}\mathbf{n}_{n+1} \otimes \mathbf{I} + C_{22}\mathbf{n}_{n+1} \otimes \mathbf{n}_{n+1}) \tag{4.34c}$$

Finally, by multiplying **M** and **Z** and using the relationship between **I** and $\mathbf{n}_{n+1}$, we obtain the following explicit expression for the CTM:

$$\mathbf{D}^{ep}_{cons.} = d_0\mathbf{J} + d_1\mathbf{I} \otimes \mathbf{I} + d_2\mathbf{n}_{n+1} \otimes \mathbf{n}_{n+1} + d_3\mathbf{I} \otimes \mathbf{n}_{n+1} + d_4\mathbf{n}_{n+1} \otimes \mathbf{I} \tag{4.35}$$

where the five constants are given by

$$d_0 = 2G\frac{q}{q^e} \tag{4.36a}$$

$$d_1 = K - \frac{2G}{3}\frac{q}{q^e} - 3K^2C_{11} \tag{4.36b}$$

$$d_2 = \frac{4G^2}{q^e}\Delta\varepsilon_q - 4G^2C_{22} \tag{4.36c}$$

$$d_3 = -2GKC_{12} \tag{4.36d}$$

$$d_4 = -6GKC_{21} \tag{4.36e}$$

It should be noted that no matrix inversion is involved in the present CTM (4.35). Clearly, $\mathbf{D}^{ep}_{cons.}$ is symmetric if $C_{12} = 3C_{21}$.

For the classical J_2 model associated with an isotropic hardening rule,

$$\phi = \phi(q, \bar{\varepsilon}^p) = q - k(\bar{\varepsilon}^p) = 0 \tag{4.37}$$

where $\mathcal{M}$ is the equivalent plastic strain and *k* the isotropic hardening rule. We can easily obtain the following constants

$$A_{11}=1, A_{12}=0, A_{21}=0, A_{22}=-k' \tag{4.38a}$$

$$B_{11}=0, B_{12}=0, B_{21}=0, B_{22}=-1 \tag{4.38b}$$

$$C_{11}=0, C_{12}=0, C_{21}=0, C_{22}=1/(3G+k') \tag{4.38c}$$

$$d_1=K-\frac{2G}{3}\frac{q}{q^e}\,,\ d_2=-\frac{4G}{3}\left[\frac{1}{1+\dfrac{k'}{3G}}-(1-\frac{q}{q^e})\right],\ d_3=d_4=0\,. \tag{4.38d}$$

s

Substitution of d_0, d_1, d_2, d_3 and d_4 into (4.35), indicates that the present CTM for the classical J_2 problem with an isotropic hardening rule are exactly the same as (4.12) of [121] and equation shown on page 5.4.2-6 of ABAQUS Theory manual (V4.9).

CTM for the generalized mid-point algorithms

An important aspect in the derivation of CTM for the generalized mid-point algorithms is the decomposition of stress and strain into hydrostatic and deviatoric components. In chapter 3, it has been found that direct application of equation (3.28) to the generalized mid-point algorithms will cause serious difficulties. Therefore, in order to bypass the difficulties, equation (3.29) was introduced in the formulations of the generalized mid-point algorithms. However, we realized later that one still faces difficulties when applying (3.29) to derive the corresponding consistent explicit tangent moduli. In this study, we found that using the following equation guarantees the derivation of the explicit consistent tangent moduli:

$$\Delta\square^p=\Delta\lambda\left[-\left(\frac{\partial\phi}{\partial p}\right)_{n+\alpha}\tfrac{1}{3}\mathbf{I}+\left(\frac{\partial\phi}{\partial q}\right)_{n+\alpha}\frac{q_n}{q_{n+\alpha}}\tfrac{3}{2}\frac{\mathbf{S}_{n+\alpha}}{q_n}\right]=\tfrac{1}{3}\Delta\varepsilon_p\mathbf{I}+\tfrac{3}{2}\Delta\varepsilon_q\frac{\mathbf{S}_{n+\alpha}}{q_n} \tag{4.39}$$

where

$$\begin{aligned}\Delta\varepsilon_p&=-\Delta\lambda(\frac{\partial\phi}{\partial p})_{n+\alpha}\\ \Delta\varepsilon_q&=\Delta\lambda\frac{q_n}{q_{n+\alpha}}(\frac{\partial\phi}{\partial q})_{n+\alpha}\end{aligned} \tag{4.40}$$

Please note the differences between (3.28), (3.29) and (4.39). With (3.28), we have no simple equation (3.38) so that $\partial q_{n+1}/\partial\Delta\varepsilon_q$ can be directly solved. This makes the generalized mid-point algorithms impossible. Secondly, using (3.29) instead of (4.39), equation (4.46) in the following wouldn't be available and the deriving of the explicit consistent tangent moduli would be extremely difficult, if not impossible.

By eliminating $\Delta\lambda$ from the above two equations one obtains

$$\Delta\varepsilon_p P + \Delta\varepsilon_q Q = 0 \tag{4.41}$$

where

$$\begin{aligned} P &= \frac{q_n}{q_{n+\alpha}}\left(\frac{\partial\phi}{\partial q}\right)_{n+\alpha} \\ Q &= \left(\frac{\partial\phi}{\partial p}\right)_{n+\alpha} \end{aligned} \tag{4.42}$$

Substituting (4.39) into (3.17) yields

$$\boldsymbol{\sigma}_{n+1} = \boldsymbol{\sigma}^e_{n+1} - K\Delta\varepsilon_p \mathbf{I} - 3G\Delta\varepsilon_q \frac{\mathbf{S}_{n+\alpha}}{q_n}. \tag{4.43}$$

By separating $\boldsymbol{\sigma}_{n+1}$ and $\boldsymbol{\sigma}^e_{n+1}$ into deviatoric and hydrostatic components according to (3.26) and using the mid-point rule for $\mathbf{S}_{n+\alpha}$, we obtain

$$p_{n+1} = p^e_{n+1} + K\Delta\varepsilon_p \tag{4.44a}$$

$$\mathbf{S}_{n+1} = \mathbf{S}^e_{n+1} - 3G\Delta\varepsilon_q \frac{\mathbf{S}_{n+\alpha}}{q_n}. \tag{4.44b}$$

Please be aware the slight difference between equations (4.43)-(4.44) and (3.36)-(3.38).

Based on the new decomposition of the return mapping process described above, we will derive the consistent tangent moduli separately from both the hydrostatic and deviatoric components. First we consider the deviatoric stress plane. By differentiating the equation (4.44b) and rearranging we obtain

$$\left(1 + \frac{3G\alpha\Delta\varepsilon_q}{q_n}\right)\partial\mathbf{S}_{n+1} = \partial\mathbf{S}^e_{n+1} - 3G\frac{\mathbf{S}_{n+\alpha}}{q_n}\partial\Delta\varepsilon_q. \tag{4.45}$$

By substituting $\partial\mathbf{S}^e_{n+1} = 2G\partial\boldsymbol{\varepsilon}^T_D$ into last equation gives

$$\partial\mathbf{S}_{n+1} = \frac{2G}{1+3G\alpha\Delta\varepsilon_q/q_n}\left[\partial\boldsymbol{\varepsilon}^T_D - \tfrac{3}{2}\frac{\mathbf{S}_{n+\alpha}}{q_n}\partial\Delta\varepsilon_q\right]. \tag{4.46}$$

For all the cases in which three direct strains are defined by the kinematic solution we have

$$\partial\boldsymbol{\varepsilon}^T_D = \left[\mathbf{J} - \tfrac{1}{3}\mathbf{I}\otimes\mathbf{I}\right]:\partial\boldsymbol{\varepsilon}_{n+1} \tag{4.27}$$

$$\partial p_{n+1} = -K\mathbf{I}:\partial\boldsymbol{\varepsilon}_{n+1} + K\partial\varepsilon_p. \tag{4.28}$$

By substituting $\partial\mathbf{S}_{n+1}$ and ∂p_{n+1} into equation (3.26) in the previous chapter and rearranging we obtain:

$$\partial\boldsymbol{\sigma}_{n+1} = \mathbf{Z}:\partial\boldsymbol{\varepsilon}_{n+1} - K\mathbf{I}\partial\Delta\varepsilon_p - \frac{2G}{1+3G\alpha\Delta\varepsilon_q/q_n}\frac{q_{n+\alpha}}{q_n}\mathbf{n}_{n+\alpha}\partial\Delta\varepsilon_q \tag{4.47}$$

where

$$\mathbf{Z} = \frac{2G}{1+3G\alpha\Delta\varepsilon_q/q_n}\mathbf{J} + (K - \frac{2G}{3}\frac{1}{1+3G\alpha\Delta\varepsilon_q/q_n})\mathbf{I}\otimes\mathbf{I}. \tag{4.48}$$

For the present pressure-dependent elastoplasticity model, using the same method as Aravas [3], by linearization of the flow and yield conditions, we obtain the following equations for the generalized mid-point algorithms:

$$\begin{aligned} A_{11}\partial\Delta\varepsilon_p + A_{12}\partial\Delta\varepsilon_q &= (B_{11}\mathsf{I} + B_{12}\mathsf{n}_{n+\alpha}):\partial\boldsymbol{\sigma}_{n+1} \\ A_{21}\partial\Delta\varepsilon_p + A_{22}\partial\Delta\varepsilon_q &= (B_{21}\mathsf{I} + B_{22}\mathsf{n}_{n+1}):\partial\boldsymbol{\sigma}_{n+1} \end{aligned} \tag{4.49}$$

where the constants A_{ij} and B_{ij} are shown in Appendix *C* at the end of the thesis. Substitution of (4.47) into (4.49) gives

$$\begin{aligned} \partial\Delta\varepsilon_p &= (D_{11}\mathbf{I} + D_{12}\mathbf{n}_{n+\alpha} + D_{13}\mathbf{n}_{n+1}):\mathbf{Z}:\partial\boldsymbol{\varepsilon}_{n+1} \\ \partial\Delta\varepsilon_q &= (D_{21}\mathbf{I} + D_{22}\mathbf{n}_{n+\alpha} + D_{23}\mathbf{n}_{n+1}):\mathbf{Z}:\partial\boldsymbol{\varepsilon}_{n+1} \end{aligned} \tag{4.50}$$

where the constants D_{ij} are given in Appendix *D*.

By substituting (4.50) into (4.47), we obtain an expression for the CTM with the generalized mid-point algorithms:

$$\partial\boldsymbol{\sigma}_{n+1} = \mathbf{M}:\mathbf{Z}:\partial\boldsymbol{\varepsilon}_{n+1} \tag{4.51}$$

where

$$\begin{aligned} \mathsf{M} &= \mathsf{J} - \mathsf{M}^{\mathrm{I}} - \mathsf{M}^{\mathrm{n}} \\ \mathsf{M}^{\mathrm{I}} &= K(D_{11}\mathsf{I}\otimes\mathsf{I} + D_{12}\mathsf{I}\otimes\mathsf{n}_{n+\alpha} + D_{13}\mathsf{I}\otimes\mathsf{n}_{n+1}) \\ \mathsf{M}^{\mathrm{n}} &= \frac{2G}{(1+3G\alpha\Delta\varepsilon_q/q_n)}\frac{q_{n+\alpha}}{q_n}(D_{21}\mathsf{n}_{n+\alpha}\otimes\mathsf{I} + D_{22}\mathsf{n}_{n+\alpha}\otimes\mathsf{n}_{n+\alpha} + D_{23}\mathsf{n}_{n+\alpha}\otimes\mathsf{n}_{n+1}) \end{aligned} \quad . \tag{4.52}$$

Finally, by multiplying **M** and **Z** and using the relationship between **I** and **n**, we obtain the following explicit expression for the CTM:

$$\mathbf{D}^{consis.} = d_0\mathbf{J} + d_1\mathbf{I}\otimes\mathbf{I} + \mathbf{n}_{n+\alpha}\otimes(d_2\mathbf{n}_{n+\alpha} + d_3\mathbf{n}_{n+1}) + d_4\mathbf{n}_{n+\alpha}\otimes\mathbf{I} + \mathbf{I}\otimes(d_5\mathbf{n}_{n+\alpha} + d_6\mathbf{n}_{n+1}) \quad (4.53)$$

where the seven constants are given by

$$\begin{aligned}
d_0 &= \frac{2G}{1+3G\alpha\Delta\varepsilon_q / q_n} \\
d_1 &= K - \frac{d_0}{3} - 3K^2 D_{11} \\
d_2 &= -d_0^2 \frac{q_{n+\alpha}}{q_n} D_{22} \\
d_3 &= -d_0^2 \frac{q_{n+\alpha}}{q_n} D_{23} \\
d_4 &= -3d_0 K D_{21} \frac{q_{n+\alpha}}{q_n} \\
d_5 &= -d_0 K D_{12} \\
d_6 &= -d_0 K D_{13}
\end{aligned} \quad (4.54)$$

It should be noted that no matrix inversion is involved in the present CTM (4.53). Equation (4.53) represents a general form of the CTM. It can be seen that there are two parts which make the CTM non-symmetric. The first part is attributed to the algorithm used and is represented by the third and last term of (4.53). Obviously, if and only if $\alpha = 1$, then the third term makes no contribution to the non-symmetry of (4.53). Similar results for ideal-plastic von Mises model found by Simo and Taylor [122] and Ortiz and Martin [93] show that only the fully implicit or the classical Euler backward algorithm preserves symmetry of the CTM. It is easy to see that if we enforce the plasticity consistency condition (3.21) in chapter 3 not at the end of increment, but at some mid-point time $t_{n+\alpha}$, i.e. $\phi_{n+\alpha} = 0$, as suggested by Simo and Taylor [122] and Simo and Govindjee [119], then the third part of (4.53) is symmetric. However, it needs special formulations in real finite element implementation to enforce $\phi_{n+\alpha} = 0$, because, by doing so, the momentum balance should also be enforced for the mid-point value stress $\boldsymbol{\sigma}_{n+\alpha}$. On the other hand, even for the algorithm where the consistency is enforced at time $t_{n+\alpha}$, i.e. $\phi_{n+\alpha} = 0$, for example, the Euler backward algorithm ($\alpha = 1$), there is still one part represented by the last two terms of (4.53) which makes the CTM possibly non-symmetric ($d_4 \neq d_5 + d_6$). The values of the last two terms of (4.53) depend on the material constitutive model. For von Mises model with a classical Euler backward algorithm ($\alpha = 1$), it can be proved in equation (4.53) that $d_4 = d_5 + d_6 = 0$. For the present pressure-dependent G-T material model, the non-symmetry of the CTM for the Euler backward algorithm has been demonstrated in numerical tests. However, as pointed out by Aravas [3], the lack of symmetry is not expected to degrade the convergence of the Newton iterations for equilibrium if we approximate $\mathbf{D}^{ep}_{cons.}$ with its symmetric part. Our numerical results have also proved this observation.

CTM for an Euler backward algorithm with mixed hardening rule

After the completion of the above work, Dr. Klingbeil made the author aware of the work by Lee and Zhang [71]. Following the same idea of Aravas [3] for a Euler backward algorithm with isotropic hardening rule, Lee and Zhang [71] have recently presented an Euler backward algorithm for the G-T model with mixed hardening rule. Furthermore, they also derived the CTM for the algorithm in an explicit way, though no closed-forms for the constants as those presented in the above were available in their CTM formula, due to the nature of mixed hardening. It is interesting to note that both the work by Lee and Zhang [71] and the present work used the same strategy in explicitly deriving the CTM. From the present work and the work in [71] it may be concluded that the CTM for the generalized mid-point algorithms for a general pressure-dependent material model can always be derived in an explicit way, no matter if the isotropic or mixed hardening rule is associated, although the application of the generalized mid-point algorithms to the mixed hardening rule remains to be done and needs further clarification.

Relationship between CTM and continuum tangent moduli

The relationship between the CTM and the COTM for a simple 1D problem is shown schematically in Fig. 4.1. As pointed out by Simo and Taylor [121], when the time step $\Delta t \to 0$, the CTM reduces to the COTM. However, we can see from Fig. 4.1 that for large time steps, the consistent tangent moduli may differ significantly from the COTM.

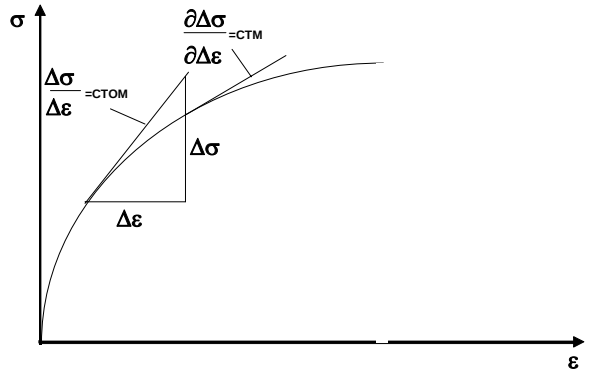

Fig 4.1. The COTM and CTM for 1-D problem

4.4 Efficiency of Present FE Implementation

Both the Euler forward algorithm and the proposed generalized mid-point algorithms formulated in chapter 3 together with their corresponding CTM derived in this chapter have been implemented into finite element ABAQUS via the user material subroutine UMAT. In the computer implementation, equation (4.39) has been used in both the numerical algorithm and CTM formulations. In this section we shall assess the efficiency of the present FE implementation of the Euler backward algorithm ($\alpha = 1$).

Convergence behaviour

Here we shall present a numerical example to illustrate the practical importance and efficiency of CTM in a Newton solution procedure. Our objective is to show the significant loss in the rate of convergence that occurs when the COTM is used in place of CTM.

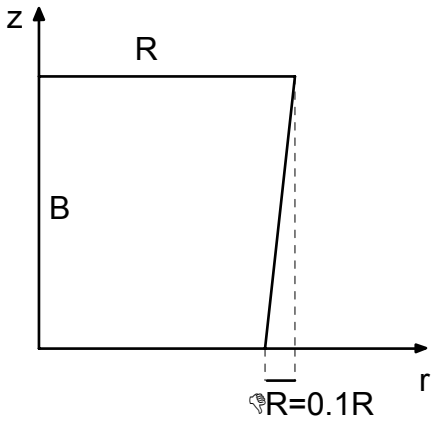

Fig. 4.2 Geometry for an axisymmetric tensile specimen simulated by one element. Uniform axial displacement was applied at the top of the element.

The tension problem of an axi-symmetric tensile specimen with initial geometrical inhomogeneity in the neck is simulated by one 8-node axi-symmetrical element (CAX8R) with reduced integration. The finite element and the geometric imperfection used are shown in Fig. 4.2, with R/B = 1.0. ABAQUS uses Newton's method to solve the overall discretized equilibrium equations. It provides the state at the beginning of the increment with all vectors and tensors properly rotated and the kinematic solution for the increments; the user must update the stress and the state variables and provide the CTM.

The same material as studied in chapter 3 is used here, with an initial void volume fraction 0.003. Displacement control at the upper end of the element was applied with equal increment displacement such that ⊿### = 0.005. Here ABAQUS (V 4.9) was used. The force tolerance (PTOL) was set to be about 1.0E-7 of the initial yield load of the bar. Table 4.1 shows the iterations needed for each step for both procedures using the COTM and the CTM. The convergence behaviour at step No. 1 of both procedures using COTM and CTM are shown in Table 4.2 which demonstrates the excellent convergence of the procedure using CTM. From this simple example, we may conclude that, from the point of view of efficiency, it is important to use the CTM associated with proper numerical procedure.

Table 4.1 Iterations required for both procedures

Increment No.	COTM ($\alpha = 0^{*}$)	CTM ($\alpha = 1$)
1	15	5
2	18	4
3	17	3
4	16	3
5	15	3
6	15	4
7	15	4
8	15	4
9	15	4
10	15	4
11	15	4
12	15	4
13	15	4
14	15	4
15	15	4
16	15	4
17	15	5
18	15	5
19	15	5
20	15	5

Table 4.2 Convergence behaviours for step No. 1

	COTM ($\alpha = 0^{*}$)		CTM ($\alpha = 1$)
Iteration No.	Absolute Maximum PTOL	Iteration No.	Absolute Maximum PTOL
1	5.979E+5	1	5.979E+5
2	2.798E+4	2	5.180E+3
3	9.249E+3	3	57.9
4	3.174E+3	4	0.473
5	1.101E+3	5	2.752E-3
6	384.0		
7	135.0		
8	47.6		
9	16.9		
10	6.02		
11	2.22		
12	0.835		
13	0.314		
14	0.118		
15	4.438E-2		

Present FE implementation and normal ABAQUS runs

For the same algorithm, for example, the Euler backward algorithm, it is impossible to compare the efficiency of present implementation for the G-T model with other implementations because there was no commercial program for the G-T model. However, it is possible to compare the efficiency of present implementation with the normal ABAQUS (V5.2) runs for the conventional von Mises material model. For von Mises material, ABAQUS, by default, uses the Euler backward algorithm for the numerical integration. Two cases have been analysed and compared by using normal ABAQUS (V5.2) (no UMAT) and present implementation (with UMAT). The first case is a notched plane strain tension simulated by one 8-node plane strain element with reduced integration (CPE8R). The geometry is the same as the one shown in Fig. 4.2, except $\Delta R = 0.2R$. Linear elastoplastic stress-strain relation, with Young's modulus 2.06E5 MPa, initial yield stress 400 MPa and ultimate stress 500 MPa at an equivalent plastic strain 0.2, was used. 80 equal displacement increments were applied in the analysis for a top deformation of 1.71828B. Both runs used the same output request. It was found that the analysis results as well as the total iteration numbers and the iteration numbers per increment were exactly the same in both analyses, except the CPU time. The comparison of the CPU time used in both analyses performed in a CONVEX 3420 computer at Lappeenranta University of Technology is shown in Table 4.3.

Table 4.3 Comparison of the CPU time (seconds) used for simple notched plane strain tension problem by normal ABAQUS and present implementation.

	At the end of input processing		At the end of the analysis	
	Present implementation with UMAT	Normal ABAQUS without UMAT	Present implementation with UMAT	Normal ABAQUS without UMAT
User time	0.6552	0.4811	4.2174	4.5298
System time	0.6036	0.5617	0.6048	0.6637
Total time	1.2588	1.0428	4.8222	5.1935

Table 4.4 Comparison of the CPU time (seconds) used for the notched axisymmetric tension by normal ABAQUS and present implementation.

	At the end of input processing		At the end of the analysis	
	Present implementation with UMAT	Normal ABAQUS without UMAT	Present implementation with UMAT	Normal ABAQUS without UMAT
User time	3.0924	3.0089	63.771	63.496
System time	0.62674	0.76908	1.6972	2.1753
Total time	3.7191	3.7780	65.469	65.672

The second case is a real notched axisymmetric tension problem. The FE mesh is shown in Fig. 4.3, with 303 nodes and 88 8-node axisymmetric elements (CAX8R). The same material as the simple notched tension case was used in the axisymmetric tension problem. The direct displacement increment scheme in ABAQUS was used for a total displacement at the top of the model equal to 0.025 of the length of model shown in Fig. 4.3. Both the analysis with and without UMAT used the same output request. As can

expected, the analysis results as well as the total iteration numbers and the iteration numbers per increment were exactly the same in both runs. The CPU time used are compared in Table 4.4.

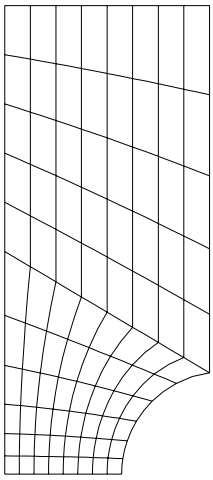

Fig. 4.3 Finite element mesh for a notched axisymmetric tension specimen

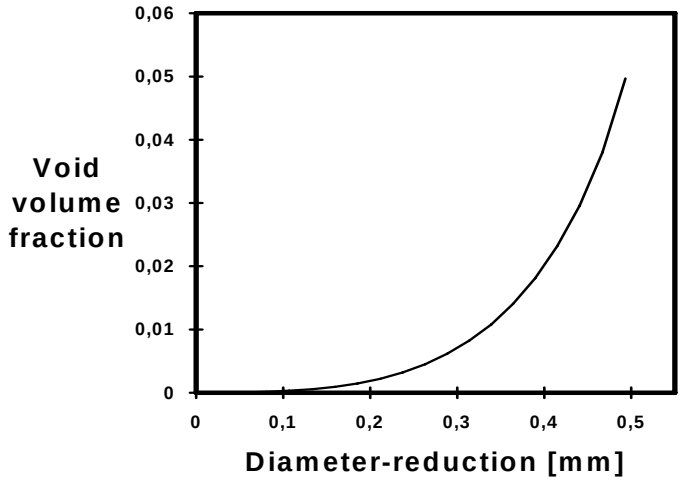

Fig. 4.4 Void volume fraction at the integration point nearest to the centre of notch section, as a function of diameter-reduction.

Table 4.3 and 4.4 indicate that for von Mises material, the analysis using present implementation is at least as efficient as, and sometimes is even slightly more efficient than normal ABAQUS run without UMAT.

Finally the notched tension case shown in Fig. 4.3 was re-analyzed using the G-T material and compared with normal ABAQUS (V5.2) analysis using von Mises material. The elastic-plastic material constants were the same as in the previous analyses. In the G-T model analysis, the void volume fraction was assumed zero at the beginning and the following void nucleation parameters in equation (2.5) were used: $f_N = 0.04, S_N = 0.1$ and $\varepsilon_N = 0.3$. In both analyses, 40 equal displacement increments were performed for a top displacement equal to 0.025 of the model length shown in Fig. 4.3. The void volume

fraction at the notch section near the centre as a function of the diameter-reduction from the analysis using the G-T model is shown in Fig. 4.4. Because the analysis results can not be compared, only the total iteration numbers, iteration numbers per each increment and the CPU time are compared in Table 4.5. Table 4.5 shows that the convergence behaviour using the G-T material in the present FE implementation is very similar to the normal ABAQUS analysis using von Mises material. This observation further proves that present implementation for G-T model could be nearly as efficient as normal ABAQUS run using conventional material model.

Table 4.5 Comparison of iteration numbers and CPU time

Increment no.	G-T material, use UMAT	Mises material, without UMAT
1	2	2
2	3	3
3	3	3
4	3	3
5	2	2
6	2	2
7	2	2
8	1	1
9-29	1	1
30	1	1
31	2	1
32	2	1
33	2	2
34	2	2
35	1	2
36	1	1
37	2	1
38	1	1
39	2	1
40	2	1
CPU time (seconds) at the end of analysis		
User time	147.52	133.51
System time	4.1363	3.7824
Total time	151.65	137.30

4.5 General Performance of Present FE Implementation

In this section, the general performance of the generalized mid-point algorithms is assessed for two problems, the plane strain tension and hydrostatic tension problems.

Plane strain tension problem

In order to compare the numerical results using present implementation, we shall first derive the theoretical solution of the G-T model to the plane strain tension problem. Fig. 4.5 shows an element under plane strain tension with a Cartesian co-ordinate system (x, y, z) defined in such a way that y is the tensile axis. In Fig. 4.5, a_0 is the initial length of the element. The only unknown stress for the problem is σ_y, since σ_z is a function of σ_y. Using the equations described in chapter 2 and enforcing the consistency condition to determine $d\lambda$ in equation (2.9), we obtain, after some algebraic manipulations, the following equations describing the problem:

$$\frac{d\varepsilon_y^p}{d\varepsilon_y} = \omega\frac{3(\sigma_y - \sigma_z)}{\bar{\sigma}^2} \tag{4.55}$$

$$\frac{d\sigma_y}{d\varepsilon_y} = \frac{E}{1-\nu^2}\left[1 - \omega\frac{3(\sigma_y - \sigma_z)}{\bar{\sigma}^2}\right] \tag{4.56}$$

$$\frac{df}{d\varepsilon_y} = \Lambda_f\omega \tag{4.57}$$

$$\frac{d\bar{\varepsilon}^p}{d\varepsilon_y} = \Lambda_{\bar{\varepsilon}}\omega \tag{4.58}$$

where

$$\omega = \frac{E\phi_{\sigma_y}}{1-\nu^2}\Bigg/\left[\frac{E\phi_{\sigma_y}}{1-\nu^2}\frac{3(\sigma_y-\sigma_z)}{\bar{\sigma}^2} - \phi_f\Box_f - \phi_{\bar{\sigma}}\frac{d\bar{\sigma}}{d\bar{\varepsilon}^p}\Box_{\bar{\varepsilon}}\right]$$

$$\phi_{\sigma_y} = \frac{q_1 q_2 f}{\bar{\sigma}}\sinh\left(-\frac{3q_2 p}{2\bar{\sigma}}\right) + \frac{2\sigma_y - \sigma_z}{\bar{\sigma}^2}$$

$$\phi_f = 2q_1\cosh\left(-\frac{3q_2 p}{2\bar{\sigma}}\right) - 2q_1^2 f$$

$$\phi_{\bar{\sigma}} = -\frac{2q^2}{\bar{\sigma}^3} + \frac{3q_1 q_2 fp}{\bar{\sigma}^2}\sinh\left(-\frac{3q_2 p}{2\bar{\sigma}}\right)$$

$$\Lambda_{\bar{\varepsilon}} = \frac{3\sigma_y(\sigma_y - \sigma_z)}{(1-f)\bar{\sigma}^3}$$

$$\Lambda_f = \frac{3(1-f)(\sigma_y - 2\sigma_z)}{\bar{\sigma}^2} + A\Lambda_{\bar{\varepsilon}}$$

$$q = \sqrt{\sigma_y^2 + \sigma_z^2 - \sigma_y\sigma_z}$$

$$p = -\frac{\sigma_y + \sigma_z}{3}$$

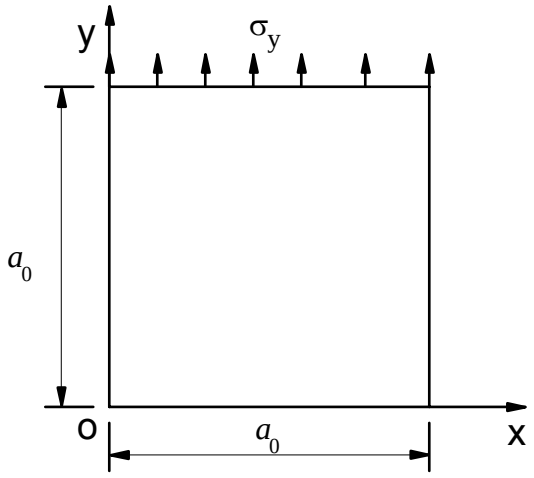

Fig. 4.5 Plane strain tension problem with displacement-controlled loading at the top of the model. x and y are the symmetric axes.

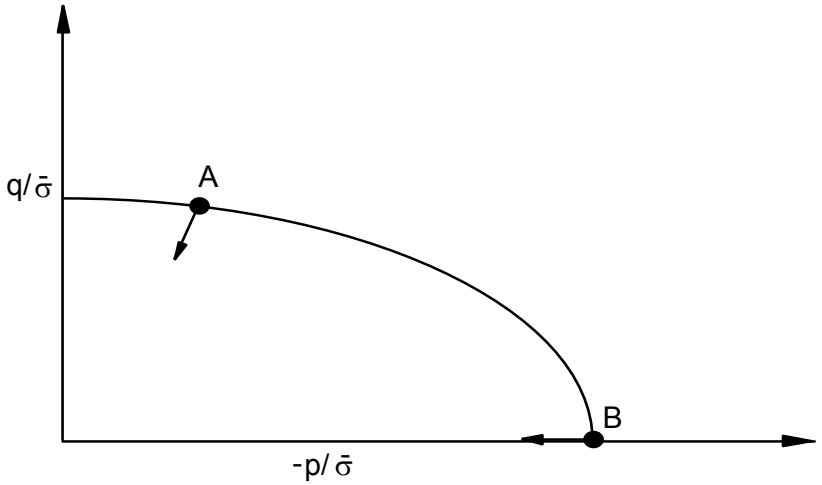

Fig. 4.6 Locations on the yield surface. A-plane strain tension problem, B-hydrostatic tension problem.

and A is the void nucleation intensity in equation (2.4), E, ν are Young's modulus and Poisson ratio; ε_y and ε_y^p are the strain and plastic strain in y-direction. After obtaining σ_y, σ_z can be solved by the equation of plane strain condition:

$$2\sigma_z - \sigma_y = -q_1 q_2 f \bar{\sigma} \sinh\left(\frac{q_2(\sigma_y + \sigma_z)}{2\bar{\sigma}}\right). \tag{4.59}$$

One 8-node parabolic element with reduced integration (CPE8R) in ABAQUS was used for the finite element analysis. The problem was solved with zero initial void volume fraction. Other material constants and Tvergaard's parameters were the same as those used in chapter 3. The exact solution of the problem was numerically obtained by integrating the set of equations (4.55-4.58), using a Euler forward scheme with 200,000 increments performed from the initial yield strain to a strain of 1.0. The initial yield point in the loading path can be easily determined by using the analytical equations derived.

There is no need to find the transition point between the elastic to the elastoplastic deformation in the present finite element implementation, because the implicit algorithms can find it automatically. In order to test the performance of the generalized mid-point algorithms, three values of α were chosen, 0.5, 0.75 and 1. Two displacement increment sizes were tested in the finite element analysis. The comparison of the stresses between the finite element results of both increment sizes and the numerically obtained exact results are shown in Table 4.6 as a function of the logarithmic strain $\varepsilon_y = \ln(1+u/a_0)$, where u is the prescribed y-direction displacement, and a_0 is the initial element length. In Table 4.6, the results are compared at ten steps only, which cut the whole displacement history equally into ten. In the analysis using 80 increments, a negative system eigenvalue problem in the global Newton iteration appeared at increment 51 in the true mid-point algorithm ($\alpha = 0.5$) which discontinued the analysis. The symbol * in Table 4.6 indicates that these values were not available because of the problem encountered.

It can be seen that even for the very large increment size (40 increments) applied, $\Delta\varepsilon_y(average) = 0.025 = 7.5\bar{\varepsilon}_0$ ($\bar{\varepsilon}_0$ is the initial yield strain), the errors are not excessive for all the algorithms considered. It must be noted that, in the present finite element solution, the increment was controlled by displacement. Therefore, it was difficult to obtain equal strain increments by displacement controlled loading in large displacement non-linear analysis. Table 4.6 shows that for the plane strain tension problem the true mid-point algorithm ($\alpha = 0.5$) is the most accurate one in both small and large increment sizes, except at the beginning of the analysis. It can be seen that the second-order accuracy of the true mid-point algorithm is not sensitive to the increment size in the present plane strain tension problem. By contrast, in present analysis the Euler backward algorithm gives the poorest accuracy, although the errors are not at all excessive. In general, the accuracy of an algorithm depends on the nature of the problem. In chapter 3, the accuracy of the generalized mid-point algorithms has been assessed by using different strain increment sizes and directions. In that assessment the initial stress location on the G-T yield surface with f=0.03 was fixed at a point where the hydrostatic stress is equal to the initial yield stress. It was found that the second-order accuracy of the true mid-point has a limited range. In terms of the maximum error, in all the increment sizes assessed it was found that the optimal value of α is observed between 0.5 and 1. When the deviatoric strain increment is radial to the yield surface, the true mid-point algorithm is usually the most accurate one, no matter how large the increment size. However, when the deviatoric strain increment is tangential to the yield surface, the second-order accuracy disappears once the strain increment size increases. For present plane strain tension problem, the stress increases or decrease almost proportionally ($p/q \approx -0.55$, see point A in Fig. 4.6) and the deviatoric strain increment is almost radial to the yield surface. Therefore, the strain increment scheme in the plane strain tension problem lies in the second-order accuracy range of the true mid-point algorithm observed in chapter 3. The second-order accuracy of the true mid-point algorithm demonstrated by this plane strain tension problem has further proved the findings in chapter 3. These findings could lead to some general conclusions which will be stated later.

Table 4.6 Comparison of the stress σ_y between the FE results and the exact results for plane strain tension problem. 40 and 80 equal displacement increments were applied in FE solution.

Exact values			UMAT-40 increments			UMAT-80 increments		
ε_y	Exact stress σ_y	Exact f	$\alpha=0.5$ error (%)	$\alpha=0.75$ error (%)	$\alpha=1$ error (%)	$\alpha=0.5$ error (%)	$\alpha=0.75$ error (%)	$\alpha=1$ error (%)
0.159	172.9	0.0048	-0.87	-0.58	-0.52	-0.35	-0.29	-0.29
0.295	174.2	0.0307	0.23	-0.52	-1.32	0.17	-0.23	-0.69
0.416	170.8	0.0553	0.23	-0.59	-1.46	0.12	-0.29	-0.70
0.523	168.6	0.0714	0.24	-0.71	-1.72	0.12	-0.36	-0.83
0.620	165.7	0.0868	0.36	-0.84	-2.11	0.18	-0.42	-1.03
0.709	161.9	0.1027	0.49	-0.93	-2.47	0.25	-0.43	-1.17
0.790	157.6	0.1191	0.63	-1.02	-2.79	*	-0.51	-1.40
0.865	152.9	0.1358	0.78	-1.11	-3.14	*	-0.59	-1.50
0.935	148.1	0.1526	0.81	-1.28	-3.51	*	-0.68	-1.76
1.000	143.1	0.1693	0.98	-1.33	-3.77	*	-0.70	-1.89

Figs. 4.7 and 4.8 show the comparisons between the stress and void volume fraction results by Euler backward algorithm ($\alpha=1$) and the exact results. Although the Euler backward algorithm is not the most accurate one in the plane strain tension problem, good accuracy has been demonstrated in the global behaviour, especially when the increment size is small.

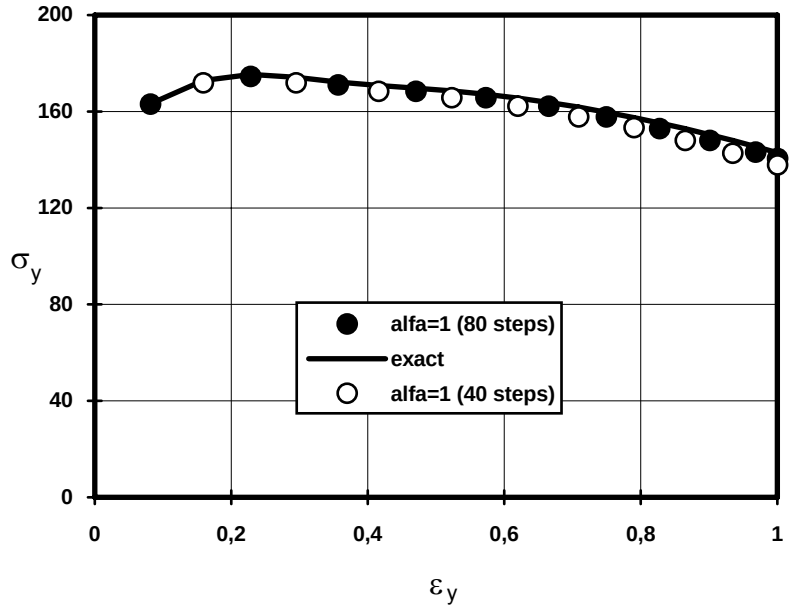

Fig. 4.7 Plane strain tension stress-strain curves

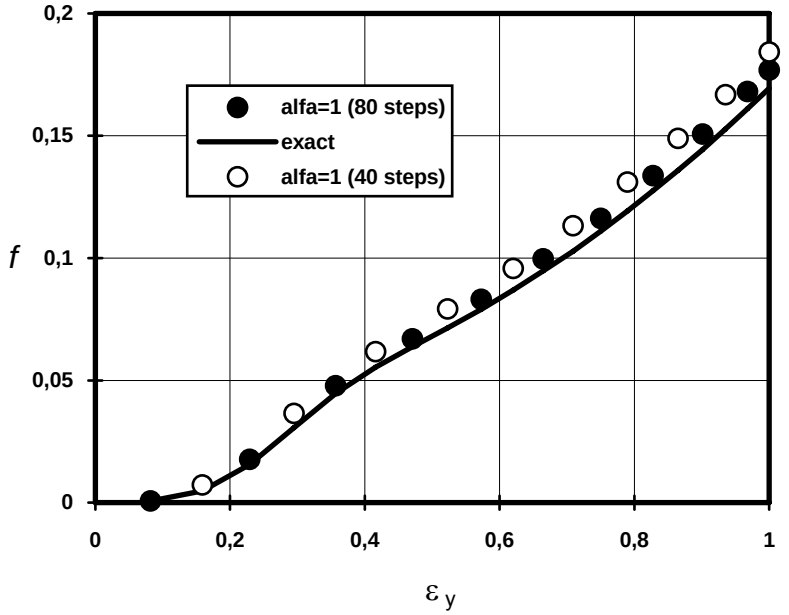

Fig. 4.8 Plane strain tension: porosity as a function strain

In the above analyses using UMAT in ABAQUS, we always used the symmetric part of the CTM for global iteration. Despite this the convergence behaviour of all the algorithms assessed is very good. Table 4.7 shows the number of global iterations used in the large increment size (40 increments) analysis. It is seen that on average less than two iterations for each increment were needed and the true mid-point algorithm is the fastest one to converge and is much faster than the Euler backward algorithm. In the 80 increments analysis, there is no big difference in the convergence behaviour of the three algorithms, because the increment size is relatively small.

Table 4.7 Number of iterations in the 40-increment analysis

Algorithms	$\alpha = 0.5$	$\alpha = 0.75$	$\alpha = 1$
No. of iterations	43	61	65

Hydrostatic tension problem

This problem has been solved by Aravas [3]. Figure 4.9 shows the element dimensions, where a_0 is the initial dimension of the cube. The derivation of the equations is simpler than in the plane strain case. We can easily obtain the following equations describing the problem, which can be integrated numerically

$$\frac{d\sigma_x}{d\varepsilon_v} = \frac{K\Lambda}{\Lambda + 9\beta^2 K} \tag{4.60}$$

$$\frac{d\bar{\varepsilon}^p}{d\varepsilon_v} = \frac{3\beta^2 K}{\Lambda + 9\beta^2 K}\frac{\varpi}{1-f} \tag{4.61}$$

$$\frac{df}{d\varepsilon_v} = \left[3(1-f) + \frac{A\varpi}{1-f}\right] \frac{3\beta^2 K}{\mathrm{A} + 9\beta^2 K} \tag{4.62}$$

where K is the bulk modulus; ε_v is the logarithmic volumetric strain, $\varepsilon_v = 3\ln(1+u/a_0)$; u is prescribed displacement and

$$\varpi = \frac{3\sigma_x}{\bar{\sigma}}$$

$$\mathrm{A} = \frac{\beta\varpi}{1-f}\left[\frac{d\bar{\sigma}}{d\bar{\varepsilon}^p}\beta\varpi - A\frac{\phi_f}{2}\bar{\sigma}\right] - 3\bar{\sigma}\beta\frac{\phi_f}{2}(1-f)$$

$$\beta = \tfrac{1}{2} q_1 q_2 f \sinh(\tfrac{1}{2} q_2 \varpi).$$

$$\phi_f = 2q_1 \cosh(\tfrac{1}{2} q_2 \varpi) - 2q_1^2 f$$

where A is the void volume fraction intensity in equation (2.4). A small error in reference [3] has been corrected in the expression of Λ.

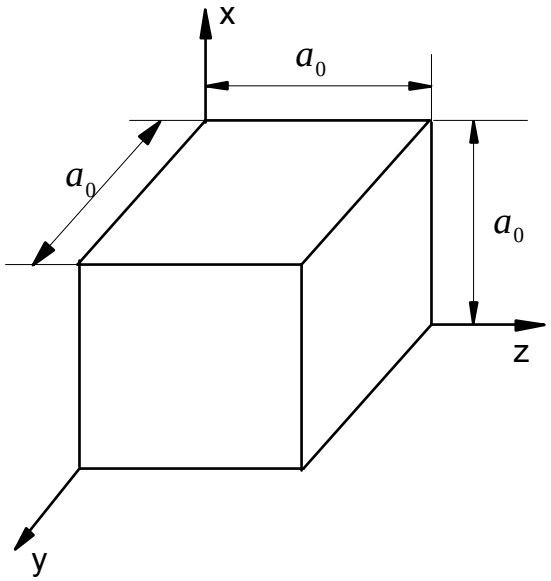

Fig. 4.9 Hydrostatic tension case. Planes x=0, y=0 and z=0 are fixed in x, y and z directions, respectively. Equal displacement increments are applied in planes $x=a_0$, $y=a_0$ and $z=a_0$ in the positive directions of x, y and z axes, respectively.

A 8-node brick element with reduced integration (C3D8R) in ABAQUS was used for testing the hydrostatic tension problem. The boundary conditions are the same as those in reference [3]. Equal displacement increments were used so that a logarithmic volumetric strain of 0.4 was reached in 10 and 20 increments, respectively. The initial void volume fraction is 0.04, all the other parameters were the same as the plane strain tension problem. The finite element analysis results of three algorithms are compared with the numerically obtained exact results for two different increment sizes in Table 4.8. Similar to the plane strain tension problem, the results of the three algorithms agree very well

with the exact results. It is interesting to note that for the hydrostatic tension problem, in which only the volumetric strain increment is available and the volumetric strain increment is exactly perpendicular to the yield surface (q=0, point B in Fig. 4.6), the accuracy of the generalized mid-point algorithms varies with the change of void volume fraction or the curvature of the yield surface at point B in Fig. 4.6. In the beginning when the void volume fraction is small, the Euler backward algorithm is the most accurate one; however when the void volume fraction exceeds about 0.2, the true mid-point algorithm becomes the most accurate one. For both large and small increment sizes, the algorithm with $\alpha = 0.75$ gives moderate accuracy during the whole history of the analysis.

Table 4.8 Comparison of the hydrostatic pressure between the FE results and the exact results for hydrostatic tension problem. 10 and 20 equal displacement increments were applied in FE solution.

Exact values			UMAT-10 increments			UMAT-20 increments		
ε_v	Exact ($-p$)	Exact f	$\alpha = 0.5$ error (%)	$\alpha = 0.75$ error (%)	$\alpha = 1$ error (%)	$\alpha = 0.5$ error (%)	$\alpha = 0.75$ error (%)	$\alpha = 1$ error (%)
0.042	201.4	0.0728	-6.70	-3.23	-0.65	-2.23	-1.19	-0.35
0.084	172.8	0.1130	-2.60	-1.39	-0.46	-0.93	-0.58	-0.29
0.126	148.7	0.1524	-1.14	-0.54	-0.2	-0.34	-0.20	-0.13
0.166	128.8	0.1911	-0.23	0.00	0.08	-0.08	0.00	0.00
0.207	112.1	0.2287	0.36	0.45	0.45	0.18	0.18	0.18
0.246	98.1	0.2645	0.67	0.72	0.76	0.25	0.31	0.37
0.285	86.3	0.2980	0.75	0.92	1.10	0.27	0.39	0.54
0.324	76.3	0.3290	0.69	1.04	1.40	0.25	0.47	0.72
0.362	67.8	0.3575	0.46	1.02	1.61	0.13	0.47	0.80
0.400	60.4	0.3838	0.26	1.04	1.85	0.08	0.51	0.94

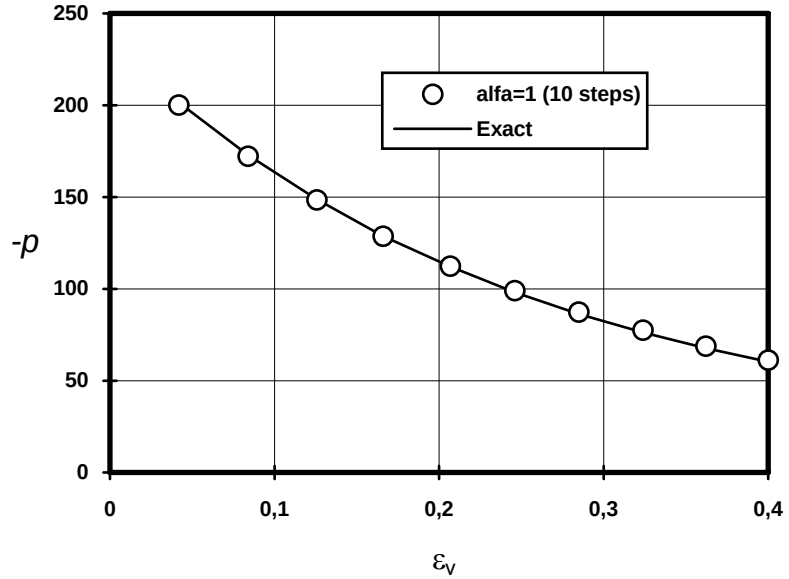

Fig. 4.10 Pressure as a function of ε_v

The finite element analysis results of the hydrostatic stress and void volume fraction for the Euler backward algorithm ($\alpha = 1$) using large increment steps are plotted as a function of ε_v in Fig. 4.10 and Fig. 4.11, respectively. It can be seen that finite element results agree very well with the exact results, even using very large increment steps. Due to the absence of deviatoric stress, the convergence in the global Newton iteration is very fast, only one iteration is needed in every increment, regardless of the algorithm chosen.

Although present implementation has demonstrated that the results are still very accurate when relative large increment sizes are used, it should be noted that the choice of increment size not only depends on the accuracy but also depends on the problem itself. For example, as far as the plastic localization problem is concerned, the increment size shouldn't be very large.

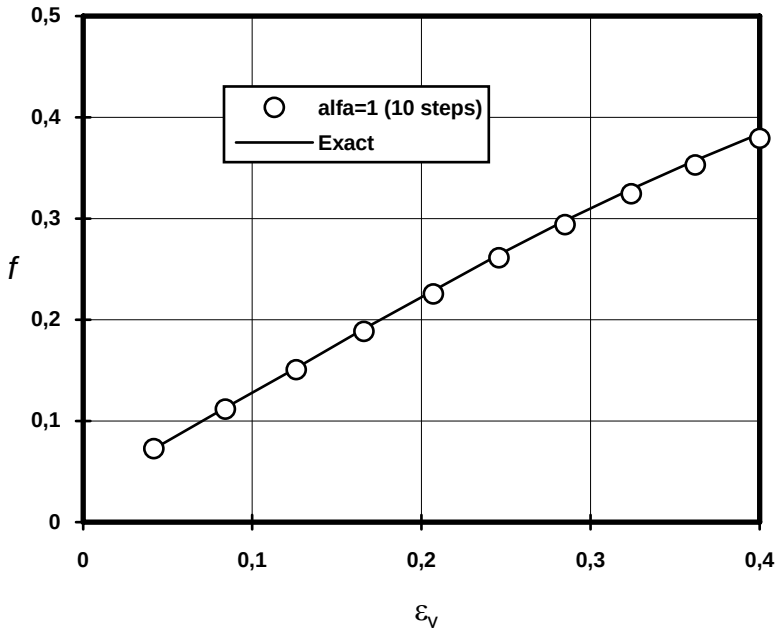

Fig. 4.11 void volume fraction as a function of ε_v

General remarks

From the numerical behaviour of present finite element results and the observation in the previous chapter, it can be concluded that the accuracy of the a numerical algorithm depends on many factors, for example, the location of stress points on the yield surface, the yield surface curvature, the stain increment direction to the yield surface and the strain increment size. The second-order accuracy of the true mid-point algorithm depends strongly on the direction of strain increment to the yield surface. As shown in the analysed plane strain tension case, the second-order accuracy of the true mid-point algorithm is almost insensitive to the strain increment size if the deviatoric strain increment is radial to the yield surface. A similar finding can be seen in the results of von Mises model by Ortiz and Popov [94] and Gratacos et al. [40]. Therefore, it can be

generally concluded that for the loading case, where the deviatoric strain increment is radial to the yield surface, the true mid-point algorithm is the most accurate one, regardless of the increment size. The results in the plane strain tension problem have also shown that the true mid-point algorithm is not only the most accurate, but also the fastest in convergence in global Newton iteration. However, one thing, which it is necessary to pay attention to, is that, although the true mid-point algorithm is the most accurate and efficient one in the plane strain tension problem, an unexpected negative system eigenvalue problem once appeared in the true mid-point algorithm which discontinued the analysis (see Table 4.6). The reason why the negative eigenvalue problem appeared only in the true mid-point algorithm was not clearly known to us, however, it may have something to do with the extra non-symmetry caused by the algorithm, as discussed in section 4.3. We have not tried to enforce the consistent condition at time $t_{n+\alpha}$, i.e. $\phi_{n+\alpha} = 0$, yet, to avoid the extra non-symmetry. Considering this incident of the true mid-point algorithm and the fact that the Euler backward algorithm has no extra non-symmetric term caused by the algorithm and is versatile, reasonably accurate, though not the most accurate, and has been widely used in the von Mises model, the Euler backward algorithm should be recommended for the G-T model.

4.6 Summary

A class of generalized mid-point algorithms for the increasingly popular G-T model has been presented and incorporated into the finite element program ABAQUS via user material subroutine UMAT. By decomposing of the stress into hydrostatic and deviatoric parts, a seven-constant formula for calculating the corresponding CTM with the generalized mid-point algorithms has also been presented, which greatly facilities the computer implementation of the algorithms. The formula presented in the paper is simple and can be regarded as a general form of the CTM. One interesting feature of the formula is that the non-symmetric property of the CTM can be easily identified and studied. The efficiency of the present Euler backward algorithm implemented through UMAT has been compared with normal ABAQUS runs without UMAT. Comparison of the results show that present implementation is as least as efficient as the normal ABAQUS analysis without UMAT for conventional von Mises material. The performance and accuracy of the generalized mid-point algorithms have been assessed by application to two cases, plane strain and hydrostatic tension problems using the G-T model. Results show that in all the cases considered, the class of the generalized mid-point algorithms are reasonably accurate. Furthermore, the accuracy of the algorithms seems to depend on many factors and it has been concluded that for the case where the deviatoric strain increment is radial to the yield surface, the true mid-point algorithm is the most accurate, no matter how large the increment size is. However, considering the extra non-symmetric property of the CTM caused by the algorithms with α<1.0, and the negative eigenvalue problem encountered in this study for the true mid-point algorithm, the Euler backward algorithm (α=1) is perhaps the best choice for the wide application of the G-T model.

Chapter 5

FAILURE CRITERIA FOR THE G-T MODEL

(I) Studies of current failure criteria

The numerical integration problem for the G-T type model has been studied in chapters 3 and 4. In this chapter and the next chapter we shall study the second problem, the failure criteria for the G-T model. The purpose of this chapter is to assess the consistency of present local failure criteria. Three local failure criteria for ductile fracture, including the constant critical void volume fraction criterion based on the G-T constitutive relation, the critical void growth criterion based on the Rice-Tracey void growth equations, and Thomason's plastic limit-load failure criterion, are compared in this chapter against the predictions of ductility with respect to stress triaxility. A calibration for the predictions by the plastic limit-load failure criterion has been made, which yields a modification to the criterion to give more realistic predictions at low stress triaxility than the original criterion. It has been found that there are considerable differences in the predictions made using the three criteria. Finally a method has been introduced which can well correlate the predictions by the three criteria.

5.1 Three Local Failure Criteria

Notched axisymmetric tensile tests have demonstrated that plastic deformation at fracture is highly dependent on the state of stresses [74]. It has been shown that ductile fracture surfaces are formed by the sudden catastrophic coalescence of voids which grow by plastic deformation under the influence of a prevailing triaxial stress system [134]. Once a void has been nucleated in a plastically deforming matrix, the resulting stress-free surface of the void causes a localized stress and strain concentration in the adjacent plastic field. With continuing plastic loading of the matrix, the void will undergo a volumetric growth and shape change.

We mentioned in chapter 1 that Rice and Tracey [106] successfully established a growth model for an isolated spherical void in an infinite non-hardening von Mises matrix in 1969. A local fracture criterion named "critical void growth ratio" based on Rice and

Tracey's work [106] has been formulated and used in the local approach of fracture [109]. As described in chapters 1 and 2, another criterion, the constant critical void volume fraction criterion which simulates the void coalescence in the G-T model is gaining in popularity both in theoretical analyses and practical applications [83,87,127-128]. On the basis of a detailed analysis of the mechanism of ductile fracture by the nucleation, growth and coalescence of voids, Thomason [134] has presented a micromechanical "plastic limit-load or internal necking" failure criterion for ductile fracture.

Although the three criteria are relatively well known, no theoretical assessment on the consistency of the predictions made by the three criteria, especially the predictions with respect to stress triaxility has been found in the literature, with the exception of the comparison of experimental and theoretical ductilities made by Riedel [108]. The purpose of this chapter is not to physically examine whether critical void volume fraction and void growth ratio are material constants and independent of stress states as did by Shi et al. [116], but to show the differences and inconsistencies among the criteria. A simple geometric model which simulates the axisymmetric loading is used for various studies here, see Fig. 5.1. Firstly, a calibration of Thomason's plastic limit-load failure criterion is made which leads to a modification of the criterion to bring realistic predictions at low stress triaxility. Then various comparisons of the criteria are made.

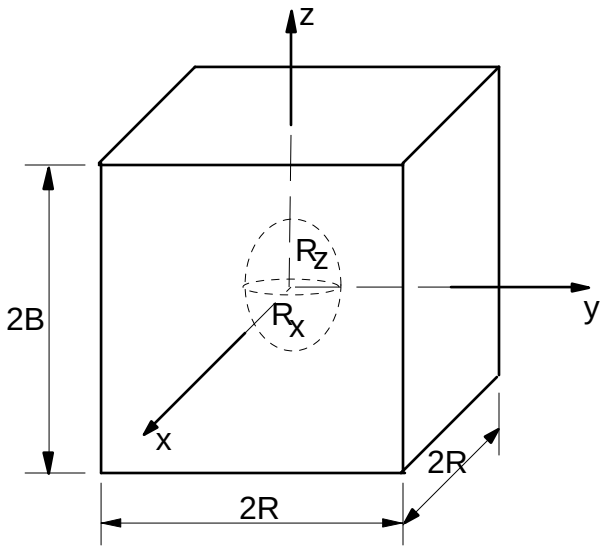

Fig. 5.1 Current void geometry in a plastic matrix unit cell, symmetric tension in z plane ($\sigma_x = \sigma_y$) and ellipsoidal void ($R_x = R_y$) are assumed.

Here and subsequently, in order to simplify the presentation Rc, Fc and Sc are used to identify the critical void growth ratio criterion, constant critical void volume fraction criterion and the original plastic limit-load failure criterion, respectively. The plastic strain in the figures in this chapter means the equivalent plastic strain at failure and "prediction" in this chapter means the prediction of ductility or equivalent plastic strain at failure.

Critical void growth ratio criterion (Rc)

For the axisymmetric case ($\sigma_x = \sigma_y$, Fig. 5.1) and constant stress triaxility (proportional loading), the Rice-Tracey void growth theory can be expressed as [106,134]:

$$\frac{R_{mean}}{R_0} = B_1 \tag{5.1}$$

$$\frac{R_z}{R_0} = B_1 + B_2 \tag{5.2}$$

$$\frac{R_x}{R_0} = \frac{R_y}{R_0} = B_1 - \tfrac{1}{2} B_2 \tag{5.3}$$

where

$$B_1 = \exp(B_3 \bar{\varepsilon}^p),$$

$$B_2 = \frac{1 + B_4}{B_3}(B_1 - 1),$$

$B_4 = \frac{3}{4}\frac{\sigma_m}{\bar{\sigma}}$ for linear hardening material,

$B_3 = 0.283\exp(\frac{3}{2}\frac{\sigma_m}{\bar{\sigma}})$ for non-hardening material,

$1 + B_4 \approx 5/3$ for linear hardening material or lower σ_m with non-hardening material,

$1 + B_4 \approx 2$ for high values of σ_m with non-hardening material.

R_0, R_x R_y and R_{mean} are the initial void radius, current radii in x and y directions and mean radius, respectively, $\bar{\varepsilon}^p$ is the equivalent plastic strain, σ_m is the first invariant of the stress tensor and $\bar{\sigma}$ the flow stress of the matrix surrounding the void, which is equal to the von Mises equivalent stress q. It must be noted that the above equations were derived for a spherical void located inside an infinite perfectly plastic matrix material.

Although the void growth model does not itself constitute a fracture criterion, a general remark concerning the void growth model has been made in [109]: as a first approximation, deformation at fracture in tension is independent of the size of and distance between voids and only depends on void growth ratio. With this observation, a fracture criterion based on the assumption of a critical ratio of void growth $(R_{mean} / R_0)_c$, specific to the material for a given direction of the load, has been formulated and widely used in the local approaches to fracture. In general, the critical void growth criterion modified to take into account the hardening and non-constant stress triaxility case can be written [109,150]:

$$\int_{\varepsilon_n}^{\varepsilon_c} 0.283 \exp\left(\frac{3\sigma_m}{2\bar{\sigma}}\right)_{vonMises} d\varepsilon^p = \ln\left(\frac{R_{mean}}{R_0}\right)_c = R_c \tag{5.4}$$

where ε_n and ε_c are the strains at void nucleation and coalescence, respectively. The value of $(R_{mean} / R_0)_c$ is usually determined through simple uniaxial or axisymmetric tests and then applied to more complex stress cases, for example, notched or cracked specimens.

Constant critical void volume fraction criterion (Fc)

The G-T yield model has been described in detail in Chapter 2. It is easy to see that the material loses the load carrying capacity, if f reaches the limit $1/q_1$, because all the stress components have to vanish in order to satisfy the equation (2.1). However, even if q_1 = 1.5, the void volume fraction, f=$1/q_1$, is still too large to be realistic in practice to simulate the final material failure. Therefore, a modification replacing f in (2.1) by f^* as follows, in order to account for the void coalescence effect on final failure, has been proposed by Tvergaard and Needleman [140]:

$$f^* = \begin{cases} f & for \quad f \le f_c \\ f_c + K_F(f - f_c) & for \quad f > f_c \end{cases}. \tag{2.10}$$

Here, f_c is the critical void volume fraction at which voids coalesce and K_F is a constant determined from the void volume fraction at final failure of the material f_F, which is much smaller than $1/q_1$:

$$K_F = \frac{f_u^* - f_c}{f_F - f_c} \tag{2.11}$$

where f_u^* is the ultimate void volume fraction, f_u^*=$1/q_1$.

In the absence of physical proof and in line with mathematical convenience, this modification has actually induced another fracture criterion, the constant critical void volume fraction criterion, which is perhaps one of the most widely applied criteria [54,83,87,126].

In order to compare the predictions, a theoretical solution of the G-T model described in chapter 2 to the axisymmetric problem is given as follows. For the axisymmetric proportional loading ($\sigma_x = \sigma_y = c\sigma_z$, c is a constant) with no intermediate void nucleation involved, we obtain, after some algebraic manipulations, the following analytical equations:

$$
\begin{aligned}
d\varepsilon^p &= \alpha\omega d\varepsilon_z \\
d\varepsilon_z^p &= G_z\omega d\varepsilon_z \\
d\sigma_z &= E_1(1-G_z\omega)d\varepsilon_z \\
df &= \beta\omega d\varepsilon_z
\end{aligned}
\tag{5.5}
$$

where

$$
\omega = \frac{E_1 G_s}{E_1 G_z G_s - \beta\dfrac{\partial\phi}{\partial f} - \alpha\bar{h}\dfrac{\partial\phi}{\partial\bar{\sigma}}}
$$

$$
G_z = \tfrac{1}{3}\frac{\partial\phi}{\partial\sigma_m} + \frac{2(1-c)}{\bar{\sigma}^2}\sigma_z
$$

$$
G_s = \frac{(1+2c)}{3}\frac{\partial\phi}{\partial\sigma_m} + \frac{2(1-c)^2}{\bar{\sigma}^2}\sigma_z
$$

$$
\alpha = \frac{\sigma_z G_s}{(1-f)\sigma_f}
$$

$$
\beta = (1-f)\frac{\partial\phi}{\partial\sigma_m}
$$

$$
E_1 = \frac{E}{1-2c\nu}
$$

$$
\bar{h} = \frac{d\bar{\sigma}}{d\varepsilon^p}
$$

ε_z^p is the plastic strain in z direction, E is Young's modulus, ν is Poisson's ratio, $\dfrac{\partial\phi}{\partial\sigma_m}, \dfrac{\partial\phi}{\partial f}$ and $\dfrac{\partial\phi}{\partial\bar{\sigma}}$ can be easily calculated from the G-T equation (2.1). In the following calculations, (5.5) is numerically integrated by a Euler forward algorithm using very small time steps.

Plastic limit-load criterion (Sc)

Thomason [16-18] has developed a plastic limit-load failure criterion based on a dual dilational-plastic response theory for the ductile fracture by void coalescence. After a detailed analysis of the mechanics of ductile fracture by void coalescence, Thomason [134] observed that the sudden transformation from a macroscopically homogeneous state of plastic flow, to a highly localized internal necking of the intervoid matrix across a single "weakest" sheet of voids coincides with the attainment of the plastic limit-load condition for localized plastic failure of the intervoid matrix. In more explicit words,

stable void growth is terminated once the applied load (stress) on the ligaments between the voids reaches the plastic limit load. It is very important to understand that here the plastic limit load is not fixed but changing (decreasing) with the change in void-matrix dimensions, or more generally, the applied load. After the limit load has been reached, the strain localizes to the ligament and the material fails with little additional strain outside the ligament. Based on this observation, Thomason [134] has defined two dilational yield surfaces: the weak dilational yield surface, which represents the stable homogenous macroscopic plastic flow field, and the strong dilational surface, which signifies the virtual unstable model of incipient void coalescence. A critical condition for incipient void coalescence by internal necking failure of the intervoid matrix, can therefore be given by [134]:

$$\sigma_1^{strong} = \sigma_1^{weak} \tag{5.6}$$

where σ_1^{weak} is the applied maximum principal stress on the current stable yield surface, the weak constitutive surface. For a real problem, σ_1^{weak} can be calculated by any analytical or numerical method, for example, the finite element method. σ_1^{strong} is the virtual maximum principal stress required to initiate the localized internal necking of the intervoid matrix material, which represents the strong dilational-plastic response.

The critical condition (5.6) for the incipient void coalescence in a unit cell with an ellipsoidal void can be written:

$$\sigma_1^{strong} = \sigma_n A_n = \sigma_1^{weak} \tag{5.7}$$

where A_n is the net area fraction of intervoid matrix perpendicular to the maximum principal stress direction which in the present case is z direction (Fig. 5.1), and σ_n is the mean stress required to initiate the internal necking in the intervoid matrix of a porous solid. It should be noted that the direction of σ_1^{strong} usually coincides with that of σ_1^{weak}. By assuming the initial normalized lengths of the unit cell in three directions are unit (Fig. 5.1), and denoting the current (normalized) lengths of the cell by 2X, 2Y and 2Z and current (normalized) radii of the ellipsoidal void by R_x, R_y and R_z, we can write:

$$A_n = 1 - \frac{\pi R_x^2}{e^{\varepsilon_x^p + \varepsilon_y^p}}. \tag{5.8}$$

where $2X \equiv 2Y \equiv e^{\varepsilon_x^p} \equiv e^{\varepsilon_y^p}$ have been used, because of the assumptions made in Fig. 1 . For von Mises material, $\varepsilon_x^p + \varepsilon_y^p = -\varepsilon_z^p$ and $A_n = 1 - \pi R_x^2 e^{\varepsilon_z^p}$. A "law-of-mixtures" has been used by Thomason [134] to relate the microscopic yield stress of the matrix, $\overline{\sigma}$, and the macroscopic yield stress $\overline{\sigma}_m$:

$$\overline{\sigma}_m = (1 - f_0)\overline{\sigma} \tag{5.9}$$

where f_0 is the initial void volume fraction. Using the above two equations we obtain the following non-dimensionalized equation:

$$\frac{\sigma_1^{strong}}{\overline{\sigma}_m} = \left(\frac{\sigma_n}{\overline{\sigma}}\right)(1-f_0)^{-1} A_n = \frac{\sigma_1^{weak}}{\overline{\sigma}_m} \tag{5.10}$$

for the case where macroscopic yield stress (von Mises material) $\overline{\sigma}_m$ is used and

$$\frac{\sigma_1^{strong}}{\overline{\sigma}} = \left(\frac{\sigma_n}{\overline{\sigma}}\right) A_n = \frac{\sigma_1^{weak}}{\overline{\sigma}} \tag{5.11}$$

for the case where matrix yield stress (such as G-T material) $\overline{\sigma}$ is used. In (5.10) and (5.11) $\frac{\sigma_n}{\overline{\sigma}}$ is called the plastic constraint-factor [134] for the incipient plastic limit-load failure of the intervoid matrix. By approximating the ellipsoidal void by the equivalent square-prismatic void and assuming two kinematically admissible velocity fields, namely parallel and triangular fields in the intervoid matrix of the 3D unit cell, Thomason [134] obtained the following closed-form empirical expression for the constraint factor $\frac{\sigma_n}{\overline{\sigma}}$ which is in close agreement with his upper-bound results:

$$\frac{\sigma_n}{\overline{\sigma}} = \frac{0.1}{\left(\frac{R_z}{X-R_x}\right)^2} + \frac{1.2}{\left(\frac{R_x}{X}\right)^{0.5}} \tag{5.12}$$

where R_x and R_z are calculated from the Rice-Tracey theory, equations (5.1-5.3). By substituting A_n and $\frac{\sigma_n}{\overline{\sigma}}$ into (5.10) the critical void coalescence condition was finally written:

$$\left(\frac{0.1}{\left(\frac{R_z}{X-R_x}\right)^2} + \frac{1.2}{\left(\frac{R_x}{X}\right)^{0.5}}\right)(1-f_0)^{-1}\left(1-\frac{\pi R_x^{\,2}}{e^{\varepsilon_x+\varepsilon_y}}\right) = \frac{\sigma_1^{weak}}{\overline{\sigma}_m} \tag{5.13}$$

It should be noted that, according to the plastic limit-load failure theory, the failure of the material is the result of a "competition" process between the weak but stable and strong but unstable responses and the satisfaction of the condition (5.6). In the beginning of plastic flow the left-hand side of (5.6) (strong dilational response) exceeds the right-hand side (weak dilational response) and ductile fracture is thus prevented. Ductile fracture by

void coalescence only occurs when the equality (5.6) is just satisfied after sufficient void growth strain. If the matrix material is characterized by von Mises model and for the fixed stress triaxility case, (5.6) clearly shows that the plastic strain solely depends on the initial void volume fraction. This demonstrates the significant difference between Sc and the other two criteria, where for a given initial void volume fraction the critical values still have to be calibrated by experiments.

5.2 Comparison of the Predictions by the Three Criteria

Calibration of the plastic limit-load failure criterion (Sc)

Two matrix materials are used in this study, one is rigid-perfectly-plastic, with initial yield stress, $\overline{\sigma}$ = 404.7 MPa; E=2.1E5 Mpa and ν=0.3; another one is linear hardening with the same initial yield stress and a constant plastic tangent modulus 400.6 MPa. Tvergaard's constants $q_1 = 1.5$ and $q_2 = 1.0$ were used in all the analyses concerning the G-T model. In the presentation, stress triaxility is defined by:

$$T = \frac{\sigma_m}{q}. \tag{5.14}$$

T can be determined by uniquely choosing c in the axisymmetric condition, $\sigma_x = \sigma_y = c\sigma_z$. Please note that in the definition (5.14) the von Mises equivalent stress, not the actual material flow stress is used. There is no difference between the two stresses in von Mises material, because $q = \overline{\sigma}$, however, as we will see in the next sub-section, considerable differences exist in the G-T material, especially when the stress triaxility is high. The stress triaxility used in the comparison ranges from 0.7 to 3.0, which is believed to represent most practical cases.

In the original plastic limit-load failure criterion Sc, the real void radius changes calculated from the Rice-Tracey theory (5.1-5.3) were used. The results for two initial void volume fractions based on the original Sc denoted as Case 1 are shown in Fig. 5.2. It was assumed in the calculation that radii R_x and R_y are fixed once they begin to decrease because, otherwise, it will predict very large, sometimes even infinite void coalescence strain. For the case with stress triaxility T=0.7, the Sc predicts equivalent plastic strains 1.722 and 1.272 corresponding to the two initial void volume fractions, f_0=0.005 and 0.01, respectively. Using the G-T model, it can be easily shown that the two plastic strains correspond to f_c =0.322 and 0.224, respectively, which are far from realistic compared with the cases in [87,126]. It, therefore, means that the original Thomason criterion gives too large predictions at low stress triaxility. A modification is tested which uses the mean void radius R_{mean} to replace R_x in (5.8). The results after this modification are shown in Fig. 5.2 as Case 2 for comparison with the original predictions denoted as Case 1. Surprisingly, this modification greatly decreases the prediction at lower stress triaxility, while for the high stress triaxility case, the predictions are nearly the same. For

stress triaxility T=0.7, the new predictions give plastic strain 0.749 and 0.561, which corresponds to f_c = 0.045 and 0.038 by the G-T model, respectively. These two f_c values are very close to the values used by Sun et. al. [126-127], though in Sun et al.'s work void nucleation has been taken into consideration.

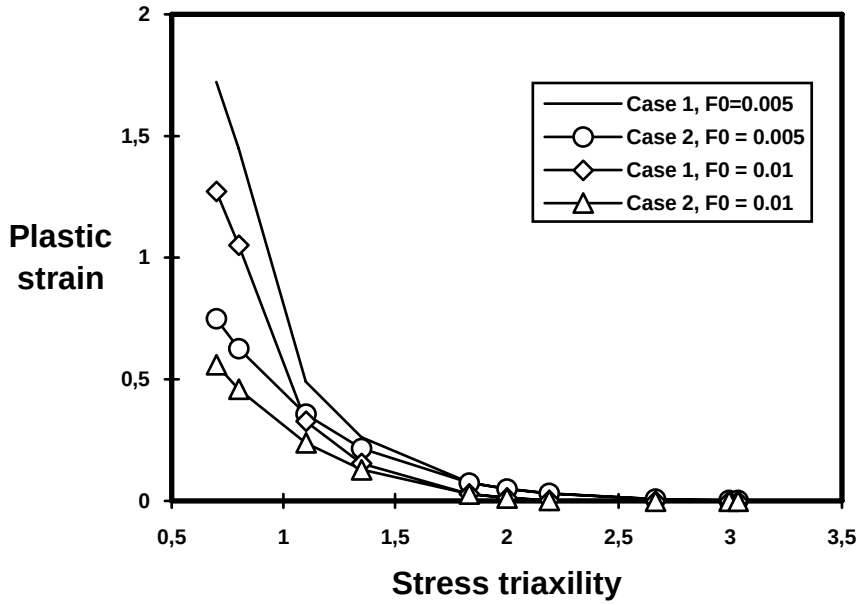

Fig. 5.2 Predictions by the Sc criterion. In Case 1, R_x and R_z were calculated by Rice-Tracey equations (5.1-5.3). In Case 2, the mean void radius was used, $R_x = R_z = R_{mean}$. In the legend, F0 means f_0.

The convergence behaviour of the plastic limit-load failure criterion (5.13) is shown in Fig. 5.3, for the case T=0.7. The horizontal line in Fig. 5.3 represents the right-hand side of (5.13). In the beginning of plastic loading, the left-hand side of the (5.13) is almost four times larger than the right-hand side for the case with f_0=0.005. Void coalescence only occurs when the two lines cross, or the equality of (5.13) is satisfied. It is obvious that according to Sc, small f_0 results in large void growth strain, and vice versa.

Linear hardening matrix material has also been used for the calculation, however, although the absolute values of the stress are different from the non-hardening material, no significant difference has been found concerning Fig. 5.2 and Fig. 5.3. So, subsequently, only non-hardening material is used.

Comparison of the predictions by the Three Criteria

In the following, all the predictions are calibrated at stress triaxility T=0.7, based on the Sc with modification $R_x = R_z = R_{mean}$. This means the plastic strains predicted by the three criteria are the same at stress triaxility T=0.7 and the critical void growth ratio R_c and critical void volume fraction f_c are then obtained from this plastic strain and shown in Table 5.1:

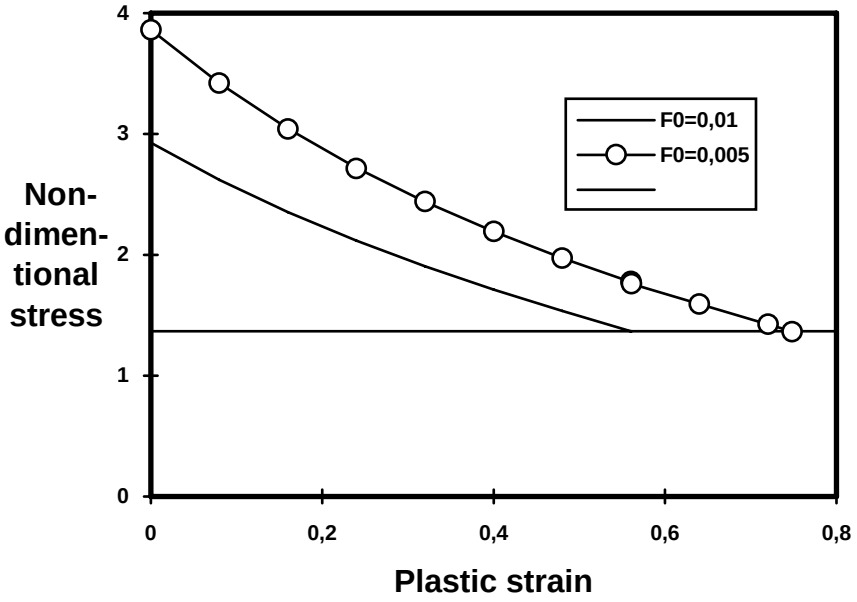

Fig. 5.3 Convergence of the Sc for two initial void volume fractions for the case T=0.7. Horizontal line represents right-hand side of equation (5.13).

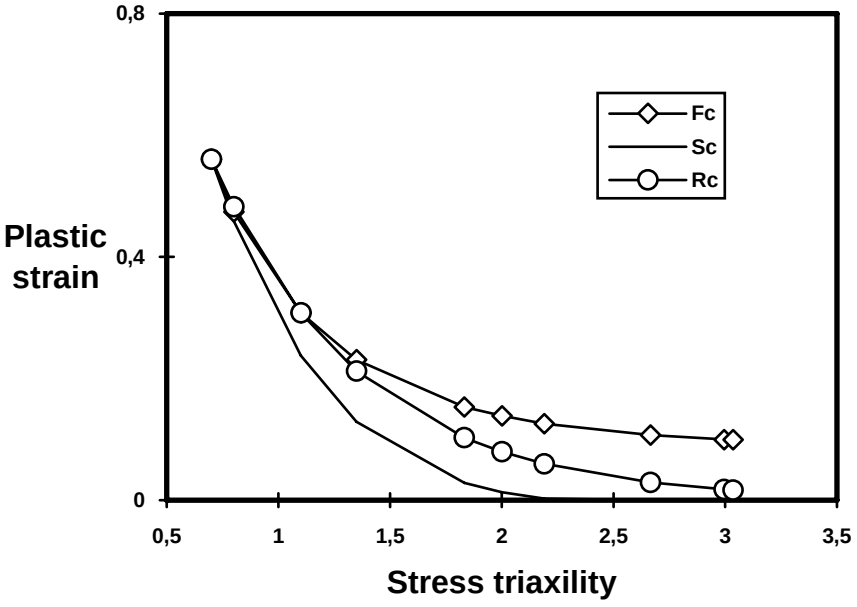

Fig. 5.4 Comparison of the predictions by different criteria for the case of initial void volume fraction 0.01. $R_x = R_z = R_{mean}$ was used in Sc criteria.

Table 5.1 Calibrated critical values for Fc and Rc.

f_0	Plastic strain	f_c	R_c
0.005	0.748	0.045	0.6051
0.01	0.561	0.038	0.4537

Two initial void volume fractions were used for comparison, with results shown in Figs. 5.4 and 5.5, respectively. In Figs. 5.4 and 5.5, predictions are given by the original criteria, except the modification $R_x = R_z = R_{mean}$ which was used in Sc. It can be found that there are large differences in the predictions by the three criteria. Figs. 5.4 and 5.5 show that the predictions by Rc and Fc criteria are very close to each other when the stress triaxility is less than or equal to 1.25. In general, Fc gives the highest prediction and Sc gives the lowest, with Rc in the middle. Although the Rc prediction is close to Fc at low stress triaxility, it is near the Sc prediction at high stress triaxility. Comparing Figs. 5.4 and 5.5, it can be seen that a small initial void volume fraction reduces the difference between Fc and Sc predictions.

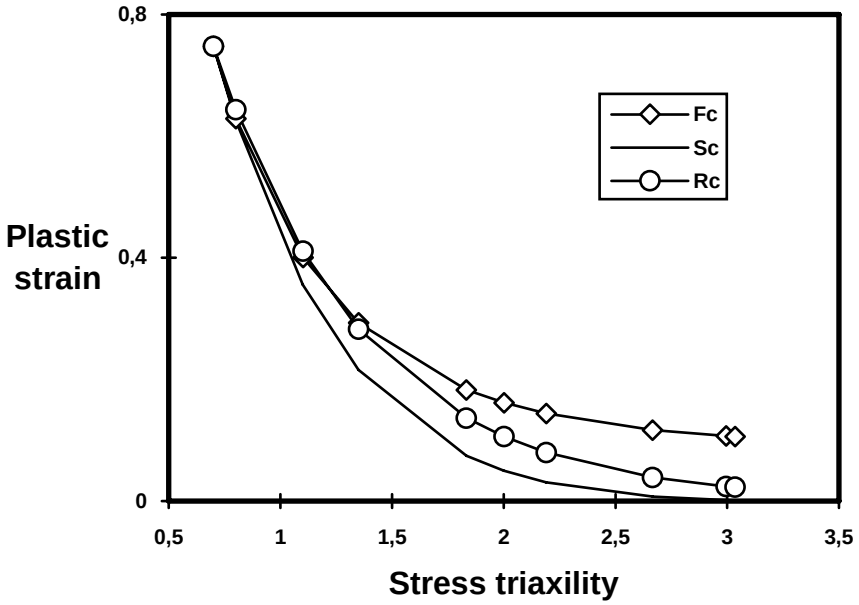

Fig. 5.5 Comparison of the predictions by different criteria for the case of initial void volume fraction 0.005. $R_x = R_z = R_{mean}$ was used in Sc criteria.

Comparison between the predictions by Rc and Fc

It was found above that when the stress triaxility is larger than about 1.25, a very large difference appears in the predictions by Rc and Fc. The difference is caused by the fact that, in the Fc criterion, the effect of void on the flow behaviour has been taken into consideration, and the larger the stress triaxility, the more significant the effect is. With the above understanding, the Rc criterion has been re-calculated using the G-T material and the following equation:

$$\int_{\varepsilon_n}^{\varepsilon_c} 0.283 \mathbf{exp}\left(\frac{3\sigma_m}{2\bar{\sigma}}\right)_{G-T} d\varepsilon^p = \mathbf{ln}\left(\frac{R_{mean}}{R_0}\right)_c . \tag{5.15}$$

Please note the difference between the present equation (5.15) and the original equation (5.4). The results are shown in Fig. 5.6 for two initial void volume fractions and good

consistency at low as well as high stress triaxility are obtained. This finding suggests that as long as the G-T material is used in the calculation, the Rc criterion is virtually equivalent to the Fc criterion. Fig. 5.6 also shows that the initial void volume fraction has less effect on the predictions at high stress triaxility than at low stress triaxility.

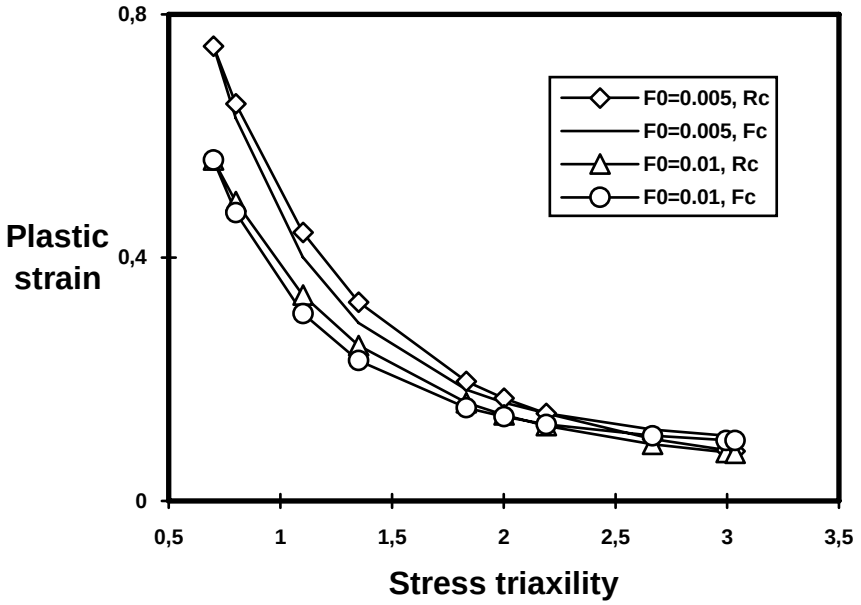

Fig. 5.6 Comparison between predictions by Rc and Fc, where the G-T material was used in Rc calculation.

Predictions by Sc using different methods to calculate void growth

Figs. 5.4 and 5.5 have shown that the original Sc criterion which uses the Rice-Tracey equations (5.1-5.3) to calculate the void growth, even under the modification $R_x = R_z = R_{mean}$, in general gave much lower predictions than both Rc and Fc criteria. In order to see whether the differences between the predictions by Sc, by Fc and by Rc can be narrowed, further modifications to Sc are tried here: (a) use the G-T constitutive model to represent the weak dilational response of the material as once suggested by Thomason [134] as one solution to the problems of the G-T model (for discussions about Thomason's comments on the problems of the G-T model, see two recent publications [107-108]); (b) assume the void grows spherically and use the void volume fraction from the G-T model to calculate the void radius changes. This proposal is put forward for the following reasons:

- The void itself in the G-T model is approximated as spherical [43-44].
- The proposal is backed by Rice-Tracey's work [106] at least at higher stress triaxility, where they found that the spherically symmetric volume changing part of void growth far overwhelms the shape changing part when the mean stress is large.

With the new modification, equation (5.11) is used in Sc. The effect of the modification on Sc predictions is shown in Fig. 5.7 for two initial void volume fractions. Obviously, after this modification the Sc criterion significantly increased its predictions when the stress triaxility is high, while the prediction remains more or less the same at low stress triaxility.

One thing which is worth mentioning is that, after the modification, the convergence behaviour is different, see Fig. 5.8, where the right-hand side of (5.11) is not a horizontal line any more. Instead, it declines with increase of the plastic strain because of the effect of the void volume fraction considered in the G-T model.

Using the modifications (a) and (b) we have just mentioned, we can compare the three criteria again. After a new calibration with the predictions of the equivalent plastic strain at failure by the modified Sc at stress triaxility T=0.7, the critical values of Rc and Fc are obtained. The new results are shown in Figs. 5.9 and 5.10, where in Rc the original von Mises material is used, see (5.4). It is interesting to note that, the modified Sc has made its prediction very close to the original Rc prediction and also narrowed the difference to the Fc prediction. This consistency is even better for small initial void volume fraction. It is interesting to make another comparison for an even smaller initial void volume fraction, 0.0005 which is close to the values used by Sun et al. [126-127]. The results are shown in Fig. 5.11. Surprisingly, the difference nearly disappeared and the three criteria gave almost identical predictions.

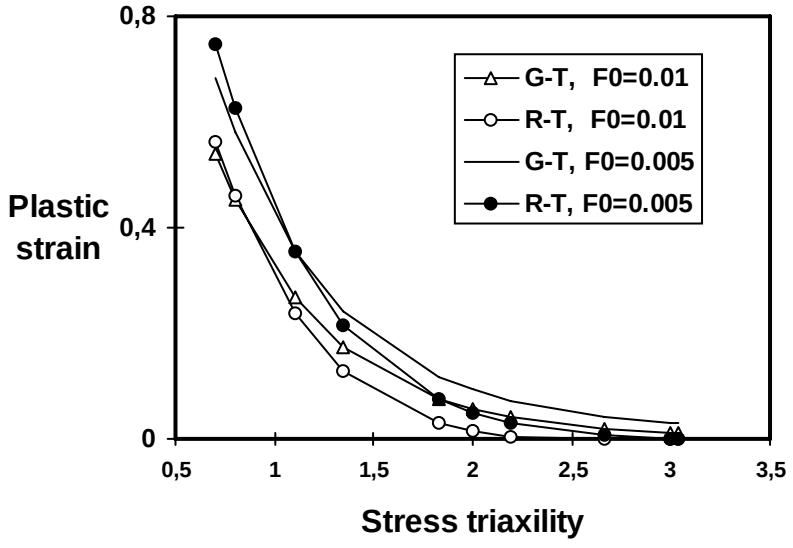

Fig. 5.7 Predictions by Sc criterion using different methods to calculate the void radius change. In the legend, G-T means the void dimensions are calculated from the G-T model; R-T means from the Rice-Tracy theory.

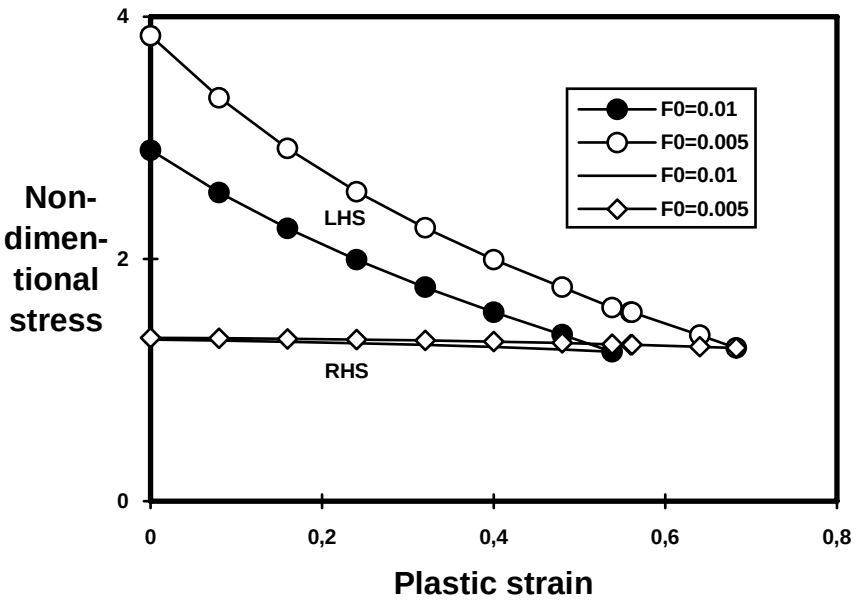

Fig. 5.8 Convergence behaviour of Sc with the new modifications, for the case with T=0.7. RHS means the right-hand-side of (5.11); LHS means the left-hand-side of (5.11).

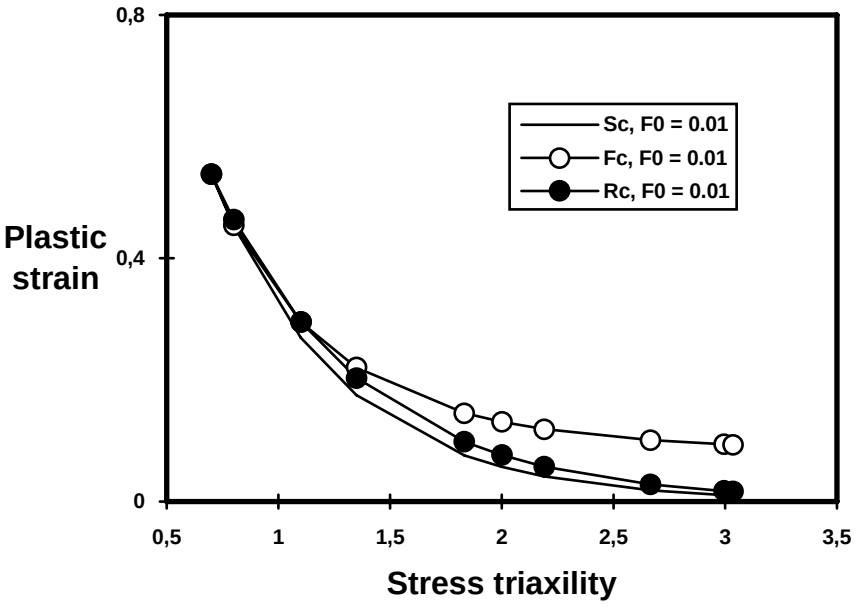

Fig. 5.9 Predictions by different criteria with $f_0 = 0.01$. Sc was modified according to the proposal.

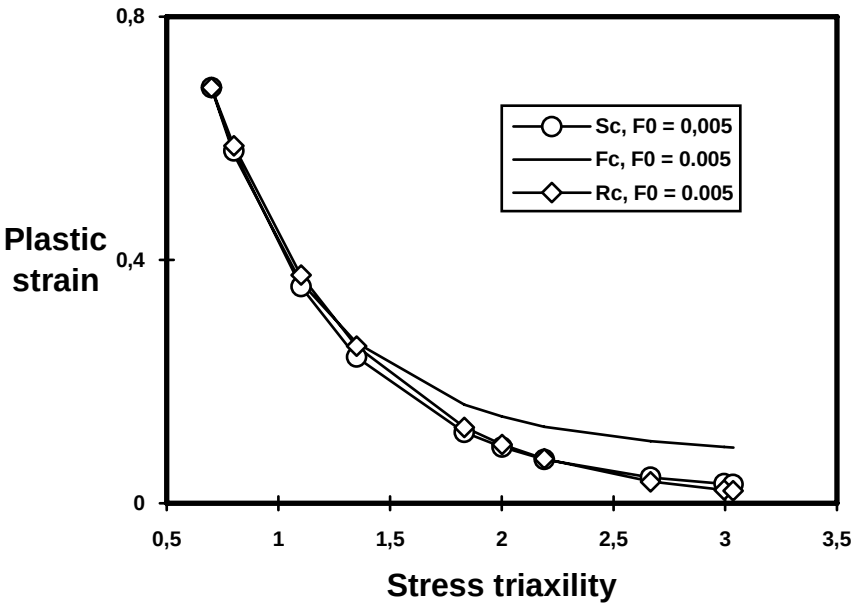

Fig. 5.10 Predictions by different criteria with f_0 = 0.005. Sc was modified according to the proposal.

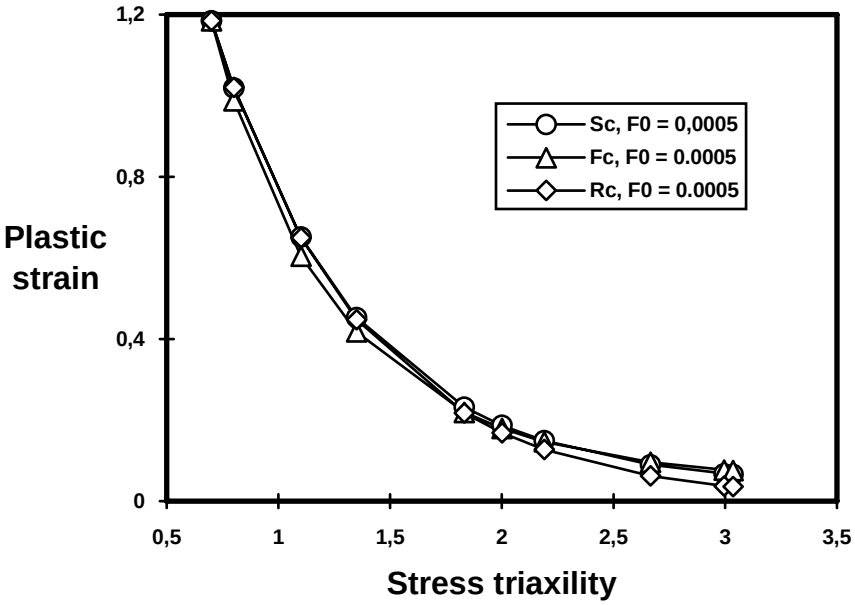

Fig. 5.11 Predictions by different criteria with f_0 = 0.0005. Sc was modified according to the proposal.

5.3 DISCUSSION and SUMMARY

Rc and Fc criteria

In the comparison of the three criteria, the results have demonstrated that there are very large differences in the original predictions. Rc and Fc are generally more widely used than Sc in literature and Rc is usually taken as a criterion for continuum damage mechanics approaches [150]. However, it has been shown that the original criteria compel each other, i.e., if f_c is constant, the prediction shows R_c is not. The difference is mainly attributable to the effect of void. In the original Rc criterion, infinite matrix surrounding the voids is assumed and the remote stress changes caused by the void growth and void-interaction are neglected. While in Fc, although approximate, the effect of void growth is reflected in the constitutive equation. It has been demonstrated that if Rc is calculated using the G-T model, the predictions by Rc and Fc are very close to each other. This implies that if the void effect is taken into consideration by using G-T type material model, the critical void fraction criterion and Rc are identical to a first approximation. In other words, Rc could also be taken as a failure criterion for the G-T model.

Sc and the other criteria

Two kinds of modifications to the Sc criterion have been tried. It was found that the original Sc gave very large predictions, sometimes even infinite, at low stress triaxility, which corresponds to unrealistic f_c in the G-T model. This leads to the first modification which uses the mean radius ($R_x = R_z = R_{mean}$) to calculate the strong dilational yield surface, the left-hand side of (5.13). This modification significantly decreased the predictions at low stress triaxility, while it keeps the predictions at high stress triaxility almost without change, which well reproduced the fact that symmetrical volume growth dominates the shape changing at large stress triaxility [106]. Compared with the predictions by Rc and Fc, it was found that, after the first modification, Sc gave very much smaller predictions than Fc and Rc at high triaxility. Noticing this inconsistency, further modifications have been proposed. In the second kind modification, it is proposed to use the G-T model to represent the weak dilational response as suggested by Thomason [134] and use the void volume fraction from the G-T model to calculate the plastic constraint factor in (5.11). The modifications yield an interesting result in that it has brought the Sc prediction very close to the one by the original Rc and significantly narrowed the difference between Sc and Fc as well. This difference is found to decrease with a smaller initial void volume fraction. Surprisingly, in an extra comparison for a very small initial void fraction (f_0 = 0.0005), the three criteria give virtually the same predictions.

General remarks

As stated in the introduction, the purpose of the work in this investigation was not to ascertain which criterion is physically right, or which one is the best. Actually, until now

experimental studies have not given concrete confirmation for the ductile fracture criteria. In the Rc and Fc criteria considered here no real "mechanics" for void coalescence has been incorporated, but only the "effect" of coalescence was reflected. This explains why the critical values of the two criteria have to be determined from simple tests. The Sc criterion itself is a condition, which represents a mechanism of void coalescence and is a natural result of the plastic deformation. No critical value needs to be obtained from tests, except the initial conditions. Once the initial conditions are given, the fracture strain at material failure is determined. Therefore, the Sc criterion is physically more sound than Fc and Rc. It must be noted, however, that void coalescence is an extremely complicated process, and that there are various approximations and assumptions made in the formulations of Sc, the validity and accuracy of the (modified) Sc must be examined in a more thorough way before its possible application as a failure criterion in the G-T model. The examination will be carried out in the next chapter.

Chapter 6

FAILURE CRITERIA FOR THE G-T MODEL

(II) A new failure criterion

In this chapter, the limitations of the widely known criterion Fc for the G-T model are addressed first. Then the original criterion Sc is examined against the FE void dimension data at failure by Koplik and Needleman, which shows good agreement. Based on the modifications to the criterion Sc introduced in the preceding chapter, a new failure criterion (NSc) which is fully compatible with the G-T model, is presented. The accuracy and validity of the new failure criterion is assessed by comparing the predictions by the new failure criterion and the finite element results of Koplik and Needleman. An important advantage of the new failure criterion as well as other related issues are discussed.

6.1 Limitations of the constant critical void volume fraction criterion (Fc)

In the preceding chapter, it has been shown by pure numerical comparisons that there are considerable differences in the predictions of ductility by the three criteria, and a method has been proposed to correct the predictions. Here, we shall focus on the justification of a new failure criterion for the G-T model. As mentioned in chapters 1 and 2, a criterion of void coalescence which determines a critical void volume fraction, f_c, has to be used in the G-T yield model in order to simulate the material failure by coalescence. How to determine f_c is the main concern of this Chapter.

A constant critical void volume fraction 0.15, was suggested by Tvergaard and Needleman [140] and it has been widely used later in both the theoretical analysis of ductile fracture and the investigation of fracture initiation of real material [54,83,87]. However, a recent numerical study of void coalescence using axisymmetric cell models by Koplik and Needleman [63] has shown that the critical void volume fraction depends on the initial void volume fraction of the material and is generally smaller than the value 0.15. Tvergaard [139] has hence pointed out that the most realistic predictions are obtained by using a critical void volume fraction that depends on the initial void volume fraction.

On the other hand, for the same material with a unique initial void volume fraction, whether the critical void volume fraction is a material constant, or whether the critical void volume fraction is independent of the stress triaxility, is questionable. Experimental studies by Shi et al. [116] and Thomson and Hancock [135] have indicated a variation of the real critical void volume fraction of material as a strong function of stress triaxility. The numerical study by Koplik and Needleman [63] has also indicated that the real critical void volume fraction corresponding to the shift to a uniaxial straining deformation mode (onset of localization) of their model depends slightly on the stress triaxility when the initial void volume fraction is small. However, when the initial void volume fraction is large there is a large spread in the critical void volume fraction observed. The general they trend shown is that the critical void volume fraction decreases with the increase of stress triaxility. Another interesting result found by Koplik and Needleman [63] is that the shift to a uniaxial straining deformation mode of their cell model is very sensitive to the uniformity of void distribution or void-matrix dimensions. In other words, if the distribution of voids is not equal in radial and axial directions in the axisymmetric cell model, the void volume fraction can hardly be taken as a failure criterion. As will be discussed later, it is important to note that there is a difference between the critical void volume fraction in the G-T model, f_c, and the one observed either experimentally [116] or numerically [63], which is denoted here as f_c^*. Nevertheless, despite these findings, in the absence of an appropriate failure criterion and in line with mathematical convenience, the criterion using the constant critical void volume fraction has been almost always used in the analysis using G-T constitutive equation.

Taking the critical void volume fraction f_c, as a constant, there are usually two methods of determining the constant. One is using the cell model by Koplik and Needleman [63]. Because, f_c is not equal to f_c^* which varies with the change of stress triaxility, especially when the initial void volume fraction is large, f_c has to be guessed or obtained by a "trial and error" method to get the best fit. No specific procedure was given by Koplik and Needleman [63] for the choice of f_c. The limitation of this method is that it can only be used to determine the critical volume fraction for a specific initial void volume fraction, because the intermediate void nucleation process which is very important in ductile fracture, is very difficult to incorporate into the cell model. Furthermore, in practical application the critical void volume fraction obtained by this method still has to be re-examined in order to obtain realistic simulation of the global behaviour.

Quite recently, Sun et al. [126-127] have suggested that f_c can be obtained first from smooth axisymmetric tensile tests by numerical simulation and then applied to a general stress status case. The advantage of Sun et al.'s method is that the void nucleation can be taken into account. This method has been verified by simulating tensile bars with different notch radii for a steel with small initial void volume fraction. One thing worth noting is that, in Sun et al.'s method [126-127], the critical void volume fraction is not unique. It depends on the choice of void nucleation model and parameter(s). However, the problem is that there is no sound theory or method at present available in the literature for choosing of the void nucleation model and parameter(s).

Because of the difficulty in measuring the nucleation parameter(s) in practice, usually approximate void nucleation model and parameter(s) are used. There is a possible discrepancy in Fc when void nucleation is involved, which can be shown in the following simple numerical example using the statistical void nucleation model (2.5) by Chu and Needleman [25]. In the numerical example, two sets of parameters shown in Table 6.1 were used. There is only a slight difference in the two sets in ε_N. Case 1 is widely used in the literature.

Table 6.1 Two sets of void nucleation parameters in equation (2.5). The values of f_c are calibrated from the low stress triaxility case, case 1.

	f_0	f_N	ε_N	f_c
case 1	0.0	0.04	0.30	0.104
case 2	0.0	0.04	0.25	0.109

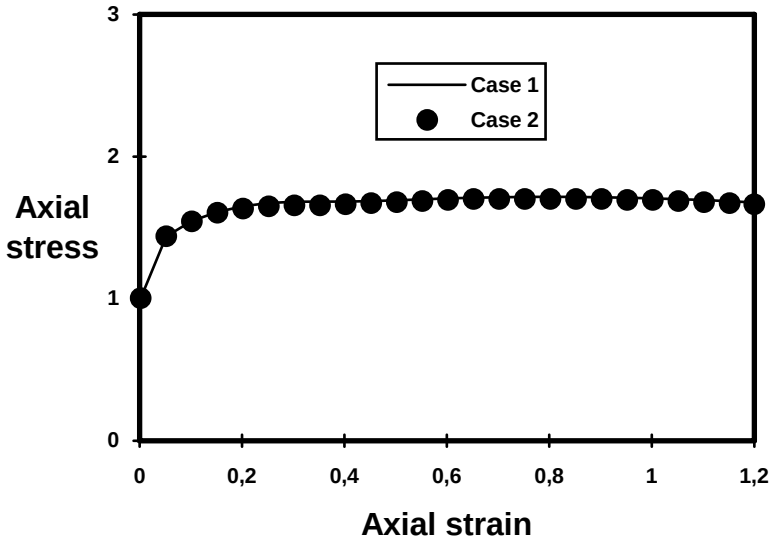

Fig. 6.1 Different sets of parameters yielded almost the same results. Stress-strain in axial direction for the case with stress triaxility T=0.333

The two values of f_c shown in Table 6.1 were calibrated from a smooth axisymmetric tensile specimen approximately simulated by one element with stress triaxility T=0.333 and stopped arbitrarily at an axial strain 1.2. A power-hardening matrix material with power 0.11 was used in the numerical example. Fig. 6.1 shows that the two sets of parameters give virtually identical predictions but different critical void volume fractions which are shown in Table 6.1. Then these two sets of parameters were applied to a high stress triaxility (T=2) case. It was found that in the high stress triaxility case there are considerable differences both in the ductility and load-carrying behaviour, see Fig. 6.2. Therefore, the non-unique nature of Fc could in certain cases yield great differences in practical applications. Here we only slightly changed the value of ε_N; similar or possibly even worse behaviour may be expected if an other parameter(s) is varied.

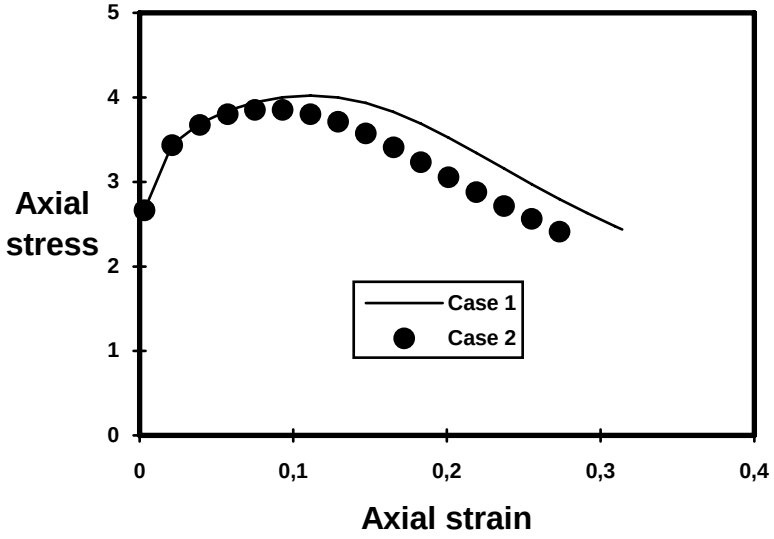

Fig. 6.2 Different sets of parameters yielded different results. Stress-strain in axial direction for the case with stress triaxility T=2.

6.2 Comparison of the predictions by the plastic limit-load failure criterion (Sc) and the FE results

Thomason [16-18] has developed a plastic limit-load failure criterion based on his dual dilational-plastic response theory for the ductile fracture by void coalescence. What is unique in the plastic limit-load failure criterion is that failure is not only related to void volume fraction, but also to the void-matrix geometry and the stress triaxility. It will be seen in this section that the finite element results of the void distribution effect studied by Koplik and Needleman [63] can be well predicted by the original Sc criterion with a modification in the calculation of σ_1^{weak} in equation (5.6).

Axisymmetric cell models shown in Fig. 6.3 have been used by Koplik and Needleman [63] to study the void growth and coalescence in porous plastic solids. Three models with two initial void volume fractions, f_0, are considered: M1 (f_0=0.0013, $B_0 / R_0 = 1.0$), M2 (f_0=0.0013, $B_0 / R_0 = 8.0$) and M3 (f_0=0.0104, $B_0 / R_0 = 1.0$), where B_0 and R_0 are the initial axial and radial dimensions of the model (Fig. 6.3). Koplik and Needleman [63] found that, until the stress drop, the stress-strain response is the same for both calculations with f_0=0.0013 (M1 and M2). However, the void volume fraction f_c, corresponding to the shift to a uniaxial straining state (onset of localization) which is associated with the accelerated void growth accompanying coalescence, for M2 is about one tenth of that for M1. Hence, they concluded that the initial stress-strain response is primarily a function of the void volume fraction while the onset of localization primarily depends on void spacing.

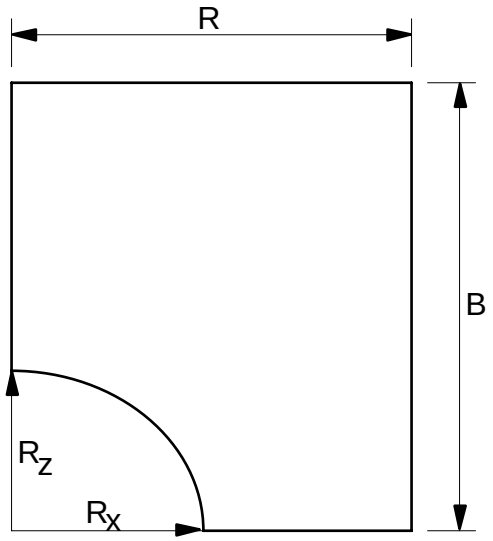

Fig. 6.3 Current dimensions in a plastic axisymmetric cell model [63]. Displacement-controlled loading scheme which adjusts itself to meet the condition that the average macroscopic true stresses acting on the cell follow a proportional history was used.

In the following, we will try to compare the predictions by the Sc and the finite element results by Koplik and Needleman [63]. Table 6.2 shows the void spacing data at which the shift to a uniaxial straining state occurs for two stress triaxility cases. The f_c values in Table 6.2 were suggested in the original paper [63]. The comparison of the predictions by Sc and FE results is shown in Fig. 6.4 for the case with stress triaxility *T*=2 and in Fig. 6.5 with stress triaxility *T*=1. In Figs. 6.4 and 6.5, curves are the void spacing traces at failure predicted by the Sc criterion, equation (5.11), for a specific material constitutive model and a stress state; FE means the FE analysis results from Koplik and Needleman [63]. It should be noted that if the von Mises model is used in Sc, the prediction curves in Figs. 6.4 and 6.5 are only dependent on the stress triaxility. However, the prediction curve is also dependent on the void volume fraction, if the G-T model is used in the calculation of σ_1^{weak}. Fig. 6.4 shows that the von Mises model gives lower predictions compared with the FE results. However, by using the G-T model ($q_1 = 1.25,\ q_2 = 1.0$ in equation (2.1)) to calculate σ_1^{weak} in (5.6) and taking the critical void volume fraction, f_c (see Table 6.2) into account, it can be seen from Fig. 6.4 that the predictions have been improved very much for M1 with little underestimate for M2 and little overestimate for M3. Fig. 6.5 shows that the von Mises model gives rather good predictions for M1 and M2, while the G-T model ($q_1 = 1.25,\ q_2 = 1.0$) improves the prediction for M2 and gives a little worse prediction for M1 than the von Mises model. The good agreement between the predictions by (5.11) and the FE results shown in Figs. 6.4 and 6.5 indicates that the void spacing effect on void coalescence, in which the criterion using constant void volume fraction, Fc, does not work at all can be predicted by the Sc criterion with a reasonable accuracy.

Table 6.2 Void spacing data at the shift to a uniaxial straining (onset of localization) state in the cell models used by Koplik and Needleman [63].

Models	Stress triaxility	f_0	$\frac{R_z}{R - R_x}$	$\frac{R_x}{R_z}$	f_c
M1	2.0	0.0013	0.58*	1.1	0.03
M2	2.0	0.0013	0.49	1.1	0.003
M3	2.0	0.0104	0.49	1.03	0.055
M1	1.0	0.0013	1.06	0.5	0.03
M2	1.0	0.0013	1.08	0.71	0.003**

* The original value of 0.28 in p. 844 of reference [63] is a typographical error, as is evident from Fig. 7 on p. 845. The current value was confirmed by professor A. Needleman in private communication.

** Value was not given in [63]. Same value as M2 was used here. Actually no significant effect can be expected.

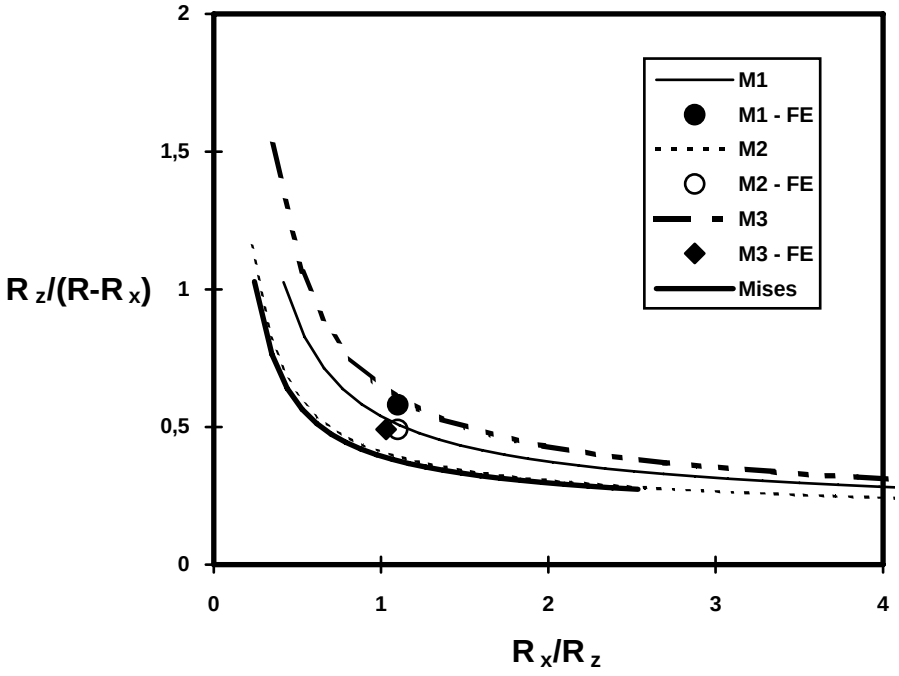

Fig. 6.4 Predictions by the Sc verse FE results by Koplik and Needleman [63], for the case with stress triaxility T=2

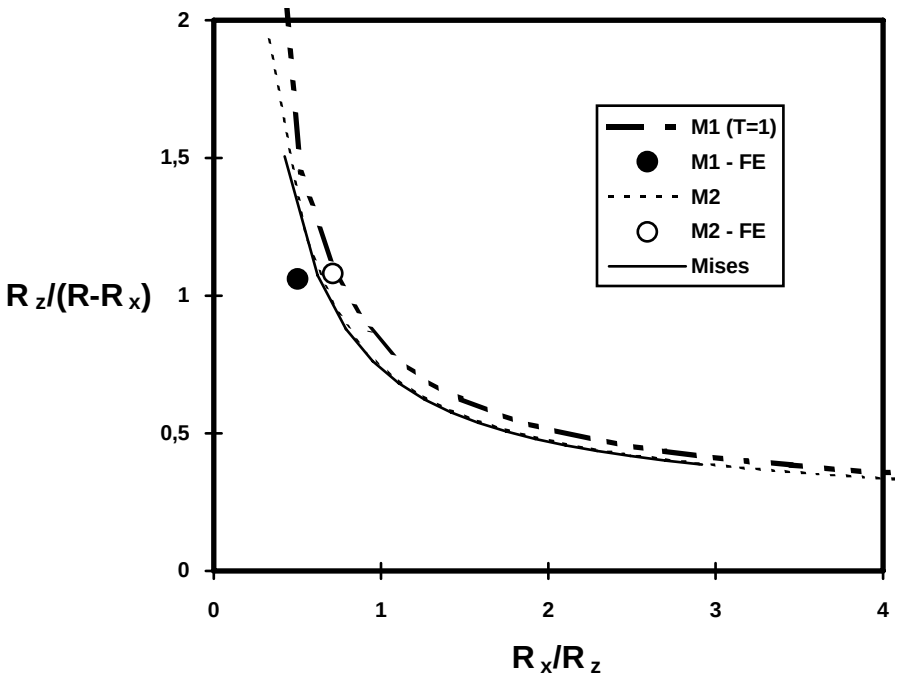

Fig. 6.5 Predictions by the Sc verse FE results by Koplik and Needleman [63], for the case with stress triaxility T=1

6.3 A New Failure Criterion (NSc)

In Thomason's original plastic limit-load failure model using dual dilational constitutive responses theory, which is schematically illustrated in Fig. 6.6, a von Mises material was assumed together with a "law of mixtures" to consider the void effect on material yield behaviour, and the void geometry changes were calculated from the Rice-Tracy void growth theory [106], in which the effect of void growth on the remote stress changes were neglected. It has been shown in the previous chapter that Thomason's original model gives very large, sometimes even infinite, predictions of the equivalent plastic strain which correspond to unrealistic critical void volume fractions in the G-T material, at lower stress triaxility. A modification which uses the mean void radius ($R_x = R_z = R_{mean}$) in Rice-Tracy equations [106] to calculate the strong response σ_1^{strong}, was tried in chapter 5. This modification significantly decreased the predictions at low stress triaxility, while it keeps the predictions at high stress triaxility almost without change, which well reproduced the observation that symmetrical volume growth dominates the shape changing at large stress triaxility [106, 129]. Furthermore, in order to combine the plastic limit-load failure model with the G-T model and to see if the difference between the predictions by Sc and Fc could be narrowed, further modifications have been tested in chapter 5: (a) assume that the void grows *spherically* ($R_z = R_x = R_y$); (b) as once suggested by Thomason [134] as one solution to the problems of the G-T model he mentioned, use the G-T model to characterize the material as the weak but

stable response; (c) furthermore, calculate the void matrix geometry changes using the current strain and void volume fraction from the G-T model

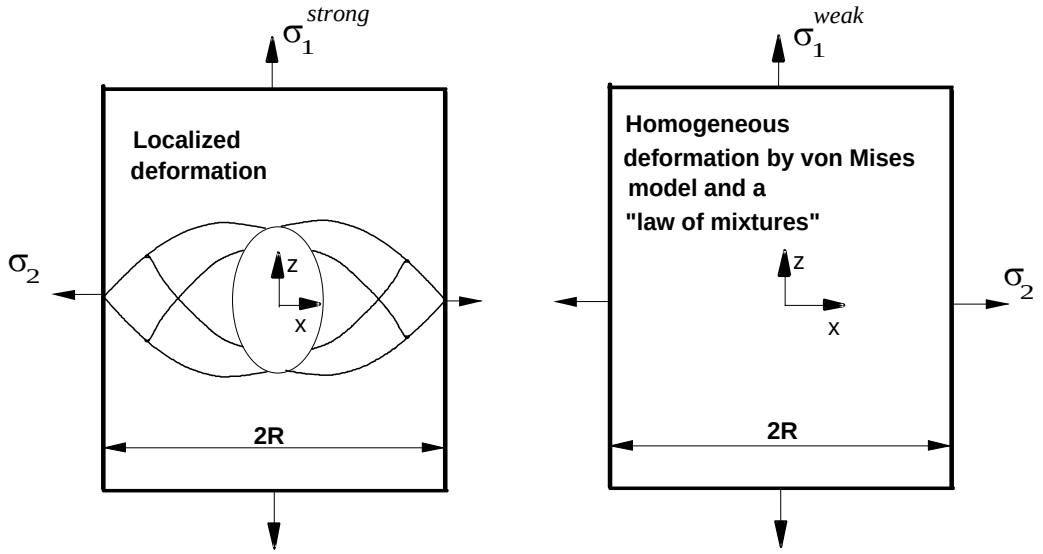

Fig. 6.6 Original 2D plane strain dual dilational constitutive responses introduced by Thomason [134].

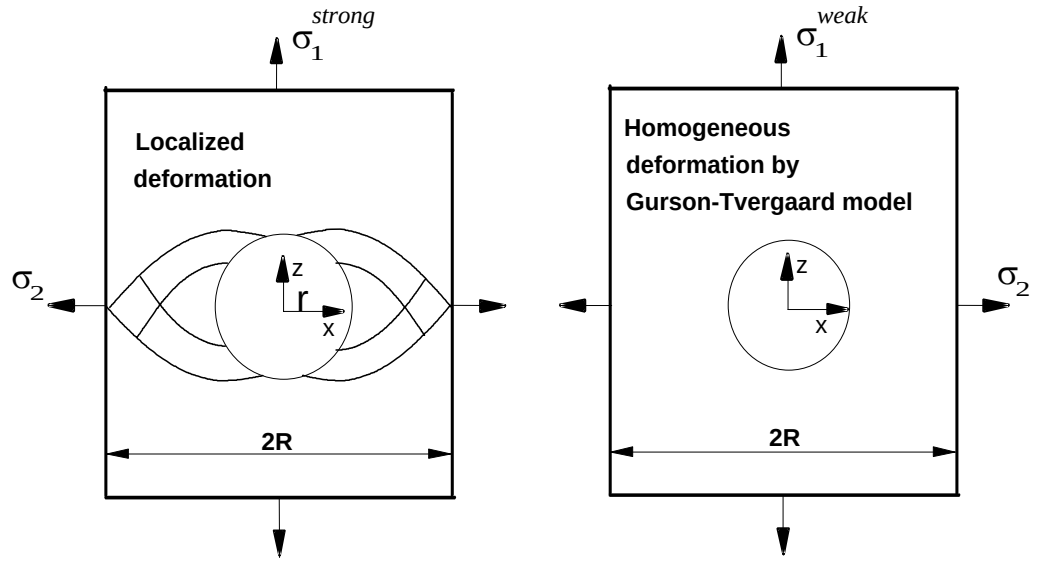

Fig. 6.7 Modified 2D plane strain dual dilational constitutive responses.

After these modifications, the modified dual constitutive responses theory is schematically shown in Fig. 6.7. The modified theory actually incorporated a void coalescence condition into to the G-T model, which essentially functions as a new failure criterion for the G-T model. Here we name it NSc. It is important to note that in the NSc, the void dimension is calculated from the current strain and the void volume fraction output of the G-T model. It should also be noted that no "law of mixtures" approximate relation (5.9) between the macroscopic and microscopic values of the yield stress is

necessary in NSc. This new criterion NSc is fully compatible with the G-T model. It will be discussed later that one advantage of this criterion is that the critical void volume fraction need not be pre-determined. On the other hand, in practical application, the void nucleation parameters, which are difficult to monitor in experiments and are usually "arbitrarily" chosen, can be numerically calibrated from, for example, notched axisymmetric tensile tests. For detailed discussions see the next chapter.

Calculation of void and matrix dimensions in NSc

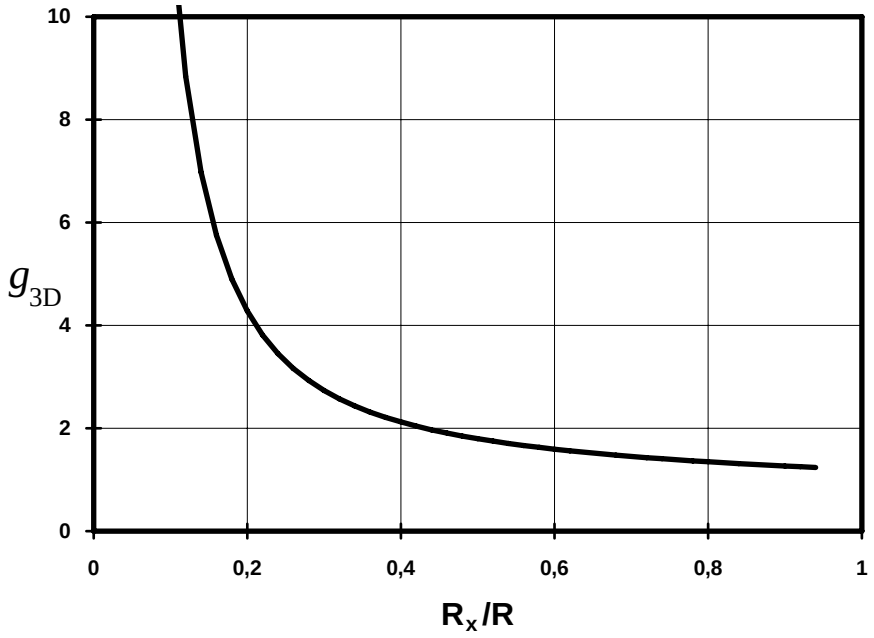

Fig. 6.8 Plastic constraint factor (g_{3D}) as a function of R_x / R

If the initial and current normalized volumes of a unit void containing cell are 1 and V, by modifications (a)-(c), the current void radius R_x for 3D or r for 2D cases, and current half intervoid distance R, in the direction perpendicular to the maximum principal stress, are calculated:

$$R_x = \left(\frac{3f}{4\pi}V\right)^{1/3} \tag{6.1}$$

$$R = R_0 e^{\varepsilon_x} \tag{6.2}$$

for the 3D model shown in Fig. 5.1 and

$$r = \sqrt{\frac{f}{\pi}e^{\varepsilon_x+\varepsilon_z}} \tag{6.3}$$

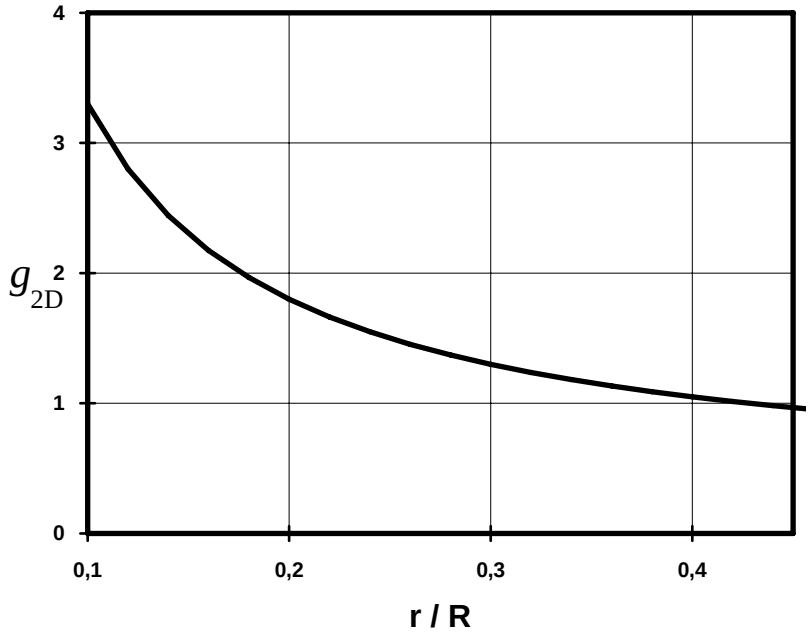

Fig. 6.9 g_{2D} in (6.7) as a function of r/R.

$$R = e^{\varepsilon_x} / 2 \tag{6.4}$$

for the 2D plane strain model shown in Fig. 6.7. In (6.2) and (6.4) ε_x is the strain in x axis which is perpendicular to the maximum principal stress in z axis and f is the current void volume fraction.

After these modifications, the plastic constraint factor for the 3D case is solely determined by R_x / R as

$$\frac{\sigma_n}{\overline{\sigma}} = g_{3D}(\frac{R_x}{R}) \tag{6.5}$$

which was obtained from (5.12) in chapter 5 using the condition $R_x = R_z$, and is plotted in Fig. 6.8. Because A_n in (5.11) can also be determined by R_x / R, so the left-hand-side of (5.11) is only a function of R_x / R. Then the plastic limit-load condition (5.11) after modification can be re-written as

$$g_{3D}(\frac{R_x}{R}) A_n(\frac{R_x}{R}) = \frac{\sigma^{weak}}{\overline{\sigma}}. \tag{6.6}$$

For 2D plane strain problem, by using the above modifications, the plastic limit-load condition (5.11) becomes

$$g_{2D}(\frac{r}{R}) = \frac{\sigma^{weak}}{\overline{\sigma}}. \tag{6.7}$$

Thomason [134] has obtained an approximate formula for the 2D plane strain constraint equation g_{2D} through slip-line analysis:

$$g_{2D}(\frac{r}{R}) = \frac{\sigma_n}{\overline{\sigma}} A_n = \frac{0.3}{r/(R-r)} + 0.6 \tag{6.8}$$

which is plotted in Fig. 6.9. Please note that there is a slight difference in the definition of g_{2D} and g_{3D} in that g_{2D} already includes A_n.

Procedures for using NSc in the Gurson-Tvergaard model

With the above formulations, NSc can now be incorporated into the G-T model by the following steps:

- Calculate the maximum principal stress and the principal strains in the directions perpendicular to the maximum principal stress from the output of the Gurson-Tvergaard model.

- Calculate the current void and matrix dimensions and plastic limit-load factor according to (6.1)-(6.2) or (6.3)-(6.4) from the output of the Gurson-Tvergaard model.

- Evaluate the plastic limit-load condition (6.6) or (6.7).

- Once the condition (6.6) or (6.7) is satisfied, the void coalescence starts to occur and the void volume fraction at this point is the critical void volume fraction, f_c, in the G-T model.

It should be mentioned that the modifications (a)-(c) used in this study make the plastic limit-load model fully compatible with the G-T model. From (6.1)-(6.4), it can be seen that g_{2D} or g_{3D} is a function of *f*, ε_x and *V*.

6.4 Verification of the New Failure Criterion (NSc)

In this section, we will compare the ductility as a function of stress triaxility, predicted by using the G-T model and NSc with the finite element analysis results by Koplik and Needleman [63]. Consistent with the results in [63], here the ductility means the effective strain at the onset of localization. The constitutive equation of the G-T model for the axisymmetric problem (5.5) was solved for various proportional stressing histories using an Euler forward integration scheme with very small increment steps. The material

properties are the same as those used in [63]: $E/\sigma_0 = 500, \nu = 0.3$. Both hardening and non-hardening materials are considered in [63], here we only compare the results of the non-hardening material. Two pairs of Tvergaard's q parameters in (2.1): $q_1 = 1.5$, $q_2 = 1.0$ and $q_1 = 1.25$, $q_2 = 1.0$ were tested by Koplik and Needleman [63]. They found that the last pair of parameters gave better results. In this verification $q_1 = 1.25$, $q_2 = 1.0$ is used in (2.1).

In should be mentioned that in our predictions, the net area fraction of the intervoid matrix and the volume of the void containing cell model are calculated according to the cell model in Fig. 6.3 as $A_n = 1 - (R_x / R)^2$ and $V = 2\pi R^2 B$. The comparison for the case with a small initial void volume fraction, f_0=0.0013 (see Table 6.2) is shown in Fig. 6.10. It is surprising to find that a very good fit to the finite element results [63] has been given by the predictions using the new criterion, NSc. In Fig. 6.10, the predictions of Fc using constant values, f_c=0.03 proposed by Koplik and Needleman [63] for the case f_0=0.0013, and two f_c^* which correspond to cases with stress triaxility T=1 and T=3, are also presented. The three predictions are indicated in the legend as Fc, Fc(T=1) and Fc(T=3), respectively. f_c^* of the case with T=2 is very close to f_c, so its prediction is not presented. Because the values of f_c and f_c^* are near each other in this small initial void volume fraction case, no large difference in the predictions has been observed. From Fig. 6.10, it can also be seen that, for this small initial void volume fraction case, predictions using both NSc and Fc can well correlate the trend of effective strain at failure (onset of localization) as a function of stress triaxility.

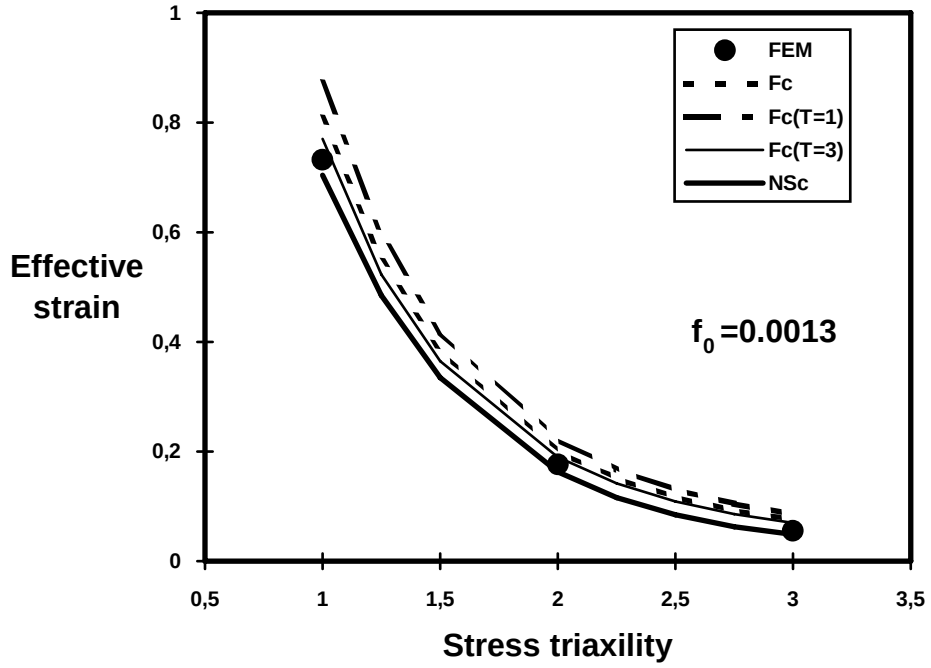

Fig. 6.10 Effective strain at failure as a function of stress triaxility for the case with f_0=0.0013.

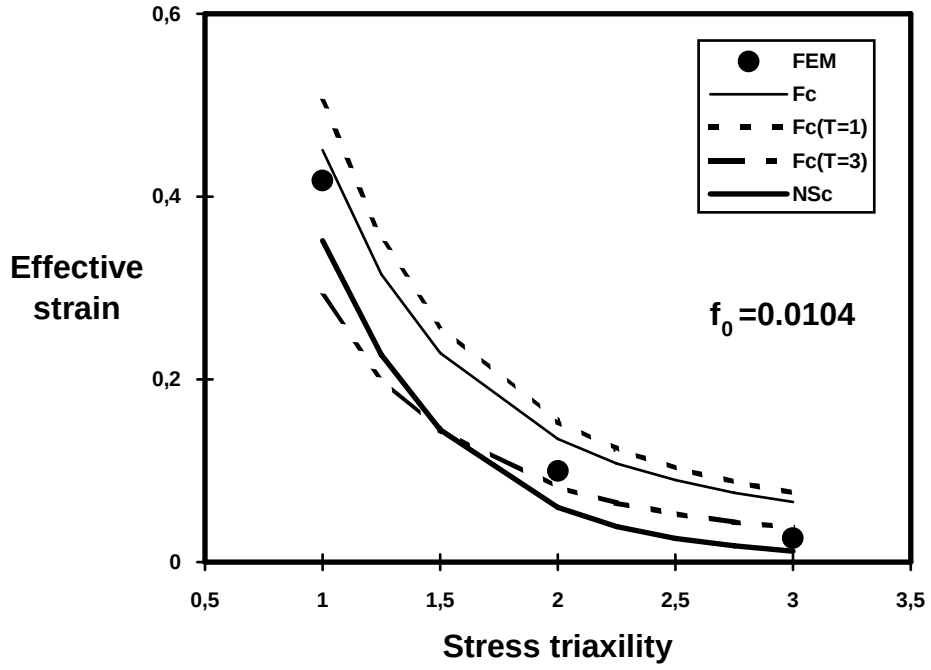

Fig. 6.11 Effective strain at failure as a function of stress triaxility for the case with f_0=0.0104.

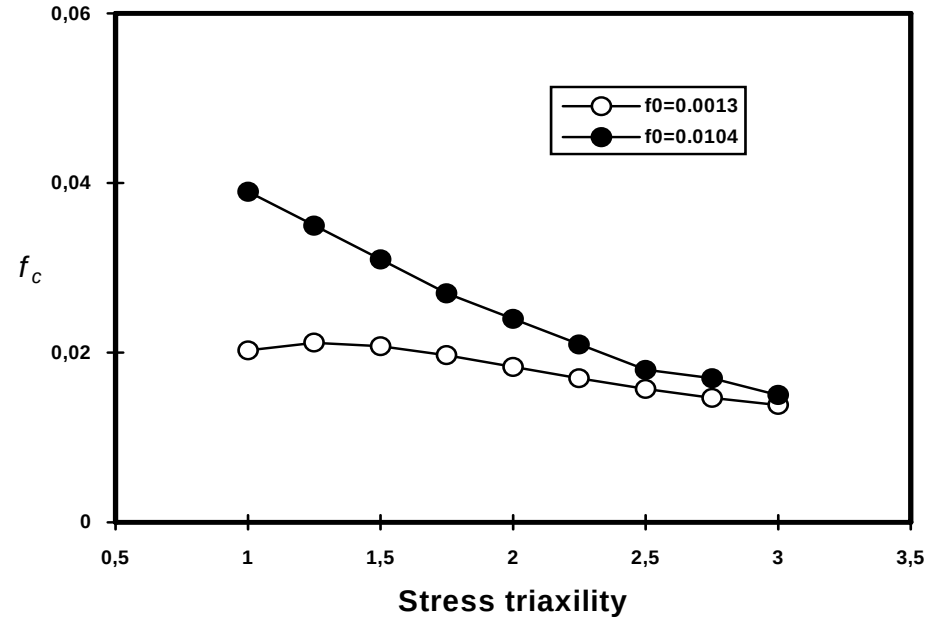

Fig. 6.12 f_c obtained in NSc as a function of stress triaxility

Figure 6.11 shows the same comparison as in Fig. 6.10 but for a large initial void volume fraction, f_0=0.0104. In this case, f_c^* corresponds to T=2 is also quite close to f_c=0.055

proposed in [63], so its prediction is not shown. It can be seen from Fig. 6.11 that there is a reasonably good agreement between the prediction with NSc and the finite element results [63]. Fig. 6.11 also shows that the predictions by NSc provide a lower bound to the finite element results, while the predictions by Fc using f_c=0.055 provide an upper bound to the finite element results. A large scatter between the predictions of Fc and the finite element results [63] can be seen in Fig. 6.11. Fig. 6.11 also indicates the difficulty in choosing f_c from f_c^*. A general trend can be observed from Fig. 6.11 that the predictions of Fc usually overestimate the ductility at high stress triaxility for the case with a large initial void volume fraction. Compared with Fig. 6.10, it can be found that this trend diminishes when the initial void volume fraction is small.

The critical void volume fractions obtained in the new criterion versus stress triaxility are shown in Fig. 6.12 for the two initial void volume fractions. Obviously f_c is not exactly a constant but generally decreases as the stress triaxility increases. From Figs. 6.10 and 6.12, it can be concluded that, only for a small f_0 case, as a first approximation can, f_c be taken as a constant.

6.5 Discussion

Conditions for the use of NSc

In this study, a failure criterion, NSc, was introduced and verified with the finite element results of non-hardening matrix material [63]. Rather good agreement has been observed. However, it should be mentioned that various assumptions and approximations have been made in obtaining the plastic constraint factor (6.6) and (6.7). Thomason [134] has pointed out that the plastic constraint factor is only expected to be accurate when the void volume fraction is less than 0.2. Due to the assumptions made in Fig. 1, it can also be expected that NSc is accurate only when the loading conditions are similar to the assumptions shown in Fig. 1. In fact, the order of 0.2 does not lead to any serious limitation in the application of NSc, because the critical void volume fraction is usually less than or equal to 0.15.

It should be noted that the G-T model was originally based on rigid non-hardening matrix material and was extended to hardening matrix material by regarding $\bar{\sigma}$ in (9) as a measure of the effective (in an appropriate average sense) flow stress of the matrix material in the current state [53]. Like the G-T model, the Sc criterion could be readily applied, in principal, to incorporate the effect of work-hardening of the matrix material, as argued by Thomason [134]. However, how sensitive the NSc is to work- hardening and especially the strain-rate sensitivity of NSc remains to be seen in our future work.

f_c and f_c^*

It is essential to point out the difference between the critical void volume fraction in the G-T model, f_c, and the real critical void volume fraction observed either experimentally [116] or numerically [63], f_c^*. Unlike the yield stress and other material constitutive

constants, f_c is an indirect material parameter which depends on the mathematical form of the material model and can not be determined directly. Studies [63,116] show that f_c^* is not a material constant but depends strongly on stress triaxility. f_c is usually different to f_c^*, because of the inability of the current material model to describe the material behaviour very accurately. If a more accurate and reasonable model appears, f_c should be closer to f_c^*. So, strictly speaking, f_c is not a material constant. Figs. 6.10 and 6.12 show that according to the results of NSc, for the small initial void volume fraction case, as a first approximation, f_c can be taken as a constant. In such a case, f_c should not be determined experimentally, but numerically.

The potential advantages of Sc

In section 6.1, we mentioned two weakness in Fc: 1) it is difficult to determine f_c even when void nucleation is not present; 2) no sound theory or method is available for the choice of void nucleation model and parameters. Furthermore, for an assumed nucleation model, a small variation in the selected void nucleation parameters which produces very little differences in global behaviour as well as ductility in a low stress triaxility case, could possibly yield very large differences in a high stress triaxility case. It is interesting to note that these weaknesses could be partially overcome by the use of NSc, if an assumed nucleation model can be used. Similar to the G-T model, with no extra effort, the void nucleation process can be taken into account in NSc. By NSc, the failure is a natural result of the competition between the stable plastic flow mechanism and unstable void coalescence mechanism, and f_c is determined once the unstable response prevails. Therefore, if the initial void volume fraction is fixed, which usually can be deduced from the initial void volume fraction of inclusions, the primary void nucleation parameter(s) can be calibrated based on the assumed nucleation model, from experimental results, for example, notched tensile specimens. Here we prefer the notched round tensile specimen, rather than the smooth specimen, because the stress triaxility in a notched specimen is higher than in a smooth specimen and is more suitable for the application of the G-T model. Furthermore, the assumed nucleation model itself could be studied and its validity could be assessed by NSc.

In summary, the significant difference between Fc and NSc is that, in Fc, the void coalescence parameter f_c usually has to be fitted or pre-determined based on the initial material state and an assumed void nucleation model and some assumed parameter(s); in contrast, not the void coalescence parameter f_c, but the void nucleation parameter(s) can be fitted in NSc. It is thus obvious that the proposed criterion NSc is not only rather accurate in the cases assessed but also make the calibration of nucleation parameter(s) possible and physically sound. The later feature is very desirable in the micro-mechanical modelling of ductile fracture.

Chapter 7

APPLICATION TO WELDED T-JOINTS

The two main problems, namely the numerical integration and the failure criterion have been studied in detail in the previous four chapters. Therefore, a local approach methodology based on the solutions to these two problems is built up. In this chapter, in order to verify its applicability, application of this methodology is made to welded T-joints where non-homogenous materials are involved. The numerical procedure of the methodology is discussed first. Then we focus on the determination of damage parameters of both base and simulated HAZ materials for the welded T-joint from smooth and notched simple round tension specimens. The fracture behaviour of the T-joint is analyzed using these parameters. Finally, some critical issues in the analysis of ductile fracture are discussed.

7.1 Numerical Procedures of the Methodology

Based on the studies of the two problems described in chapters 3 to 6, a G-T model based local approach methodology is thus built up in the commercial finite element program ABAQUS via the user material subroutine UMAT. In ABAQUS, the non-linear equations are solved using the Newton method. In the present implementation, the numerical integration is efficiently performed using the generalized mid-point algorithms and its explicit seven-constant CTM for pressure-dependent material models proposed in chapters 3 and 4. It has been found in chapter 4 that for the G-T model, the true mid-point algorithm is usually the most accurate one, and the one-step Euler forward algorithm has the poorest accuracy. However, considering the extra non-symmetric property of the CTM for the true mid-point algorithm and the numerical problems encountered in chapter 4, in general the Euler backward algorithm is recommended and actually used in the following analyses, except when otherwise mentioned. The numerical procedures of the methodology in ABAQUS UMAT are:

(1) Stress is updated first, using the Euler backward algorithm.
(2) During the stress updating, the maximum principal stress and strains are evaluated.

(3) After the stress has been updated, the void and matrix dimensions are calculated according to equations (6.1)-(6.4) and then the plastic limit-load failure condition (5.11) was evaluated.
(4) Once the failure condition is satisfied, the modification to account for the void coalescence effect (2.11) is taken into action.
(5) If the equation (2.11) is already used, check if $q_1 f_u^* < 0.9$, otherwise, hold the void volume fraction and flow stress constant so that the material becomes pressure-dependent perfectly-plastic.
(6) Finally, the CTM is computed.

It should be noted that the value of the ultimate void volume fraction f_u^* has no physical meaning but the product $q_1 f_u^*$ in the yield function may not be equal to 1, in order to keep numerical stability. For this reason, $q_1 f_u^* \approx 0.9$ is used in step (5) in the analyses below where the G-T model is used.

7.2 Procedures for the Study of Welded T-Joints

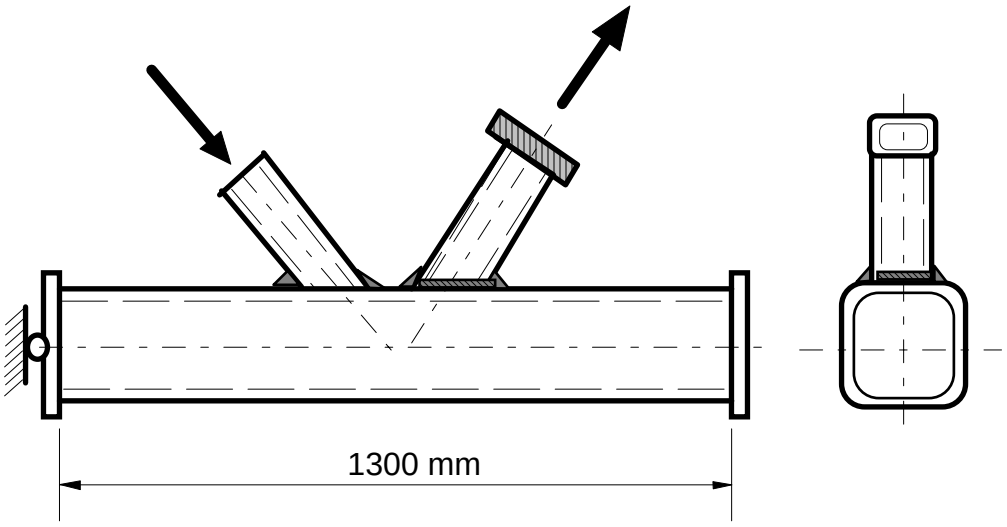

Fig. 7.1 Gapped K-joint tested in reference [123]. The dimensions of the chord member were $150 \times 150 \times 7.9$ *mm. Two kinds of brace members were used, one with dimensions* $100 \times 100 \times 6.1$ *mm and another one with* $70 \times 70 \times 5$ *mm.*

Recently a series of experimental studies on the fracture behaviour of gapped (cold-formed) rectangular hollow section K-joints schematically shown in Fig. 7.1 have been conducted in this university [123]. The experimental study has revealed that ductile fracture is a very important failure mode. It is well known that conventional elastoplastic analyses using the commercial program ABAQUS is unable to treat the ductile fracture problem. So, the purpose of this study was to develop a realistic, but simple enough tool for the analysis of the fracture behaviour of welded joints. Because the real K-joint shown in Fig. 7.1 is too difficult to tackle in this study, a simple welded T-joint suggested

by Niemi [90] was adopted as a first step in the study of a real rectangular hollow section K-joint.

The adopted T-joint schematically shown in Fig. 7.2 was welded together (full penetration) by two plate strips with thickness 7.9 mm. The welding parameters used in the T-joint are shown in Table 7.1. The plate strips were cut from the chord member of a tested K-joint at the region far away from the deformed area. The width of the plate strip is 40 mm, which can be regarded as large enough to simulate the plane strain behaviour. The rectangular hollow section was made of a Finnish steel, Fe510. The main chemical composition of the steel is shown in Table 7.2.

Table 7.1 Welding parameters

	welding current	welding voltage	welding speed
MAG-welding	150 A	22 V	18 cm/sec

Table 7.2 Main chemical composition (wt. %)

	C	Mn	Si	S	P
Fe510	0.136	1.47	0.15	0.0065	0.016

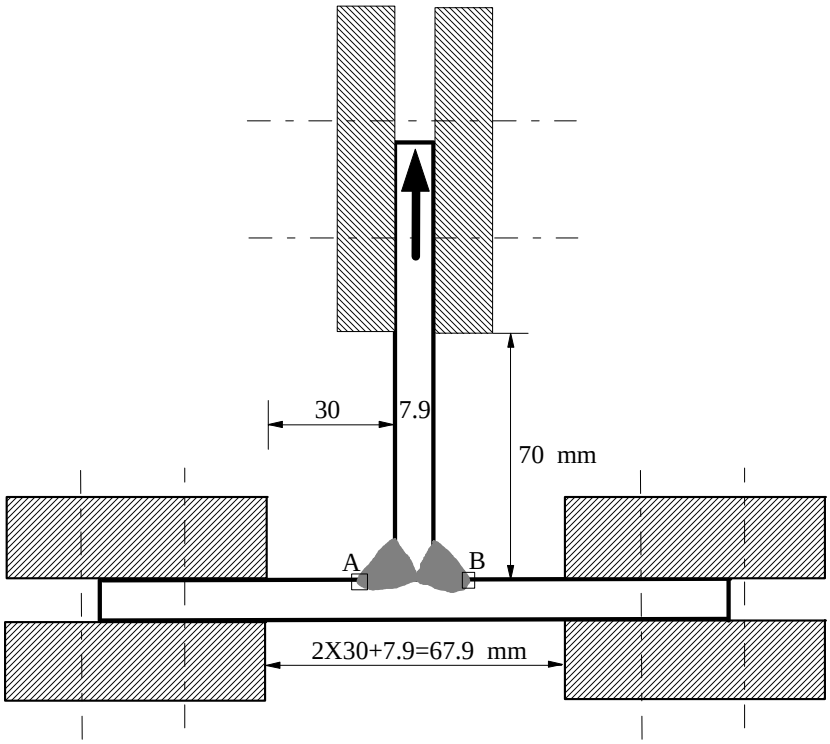

Fig. 7.2 Welded T-joint for this study. The material was cut from the chord of a tested K-joint (Fig. 7.1) at the region far away from the deformed area. The plate thickness is the same as that of the chord member of K-joint , 7.9 mm.

In order to apply present methodology to the welded T-joint, besides the normal elastic and plastic material constants, damage parameters should be determined beforehand. In this methodology, the damage parameters include initial void volume fraction and void nucleation parameters. Because the crack in a welded joint usually initiates at the heat affected zone (HAZ), both base and simulated HAZ materials have to be studied. The procedure for the study of the welded T-joints is:

- Test smooth and notched axisymmetric tensile specimens and use the present methodology to calibrate the damage parameters, here in this study, the void nucleation parameters for the base material.

- Test notched axisymmetric tensile specimens made of simulated HAZ material to calibrate the void nucleation parameters for the HAZ material.

- Test welded T-joints and use the parameters calibrated from both base and simulated HAZ materials to predict and compare the fracture behaviour of welded T-joints.

In the next section we determine the damage parameters for the base material first. 5 groups of tests were conducted in total in order to guarantee that at least one group data is valid for this study. Because the material for this study was cut from tested K-joints, although care has been taken to cut the materials far away from the deformed area, the pre-strain-hardening and residual stresses were usually not the same. Here we only report the results of group D4, of which the material was cut from the K-joint D4 in reference [123].

7.3 Damage Parameters for the Base Material

Specimens and finite element meshes

Table 7.3 Details of the FE meshes

Specimens	Minimum diameter [mm]	Maximum diameter [mm]	Notch radius [mm]	Coarse mesh name	Fine mesh name
Smooth	3.99	4.0		AX0	
Notched 1	4.0	7.0	1.75	AX1	FAX1
Notched 2	4.0	7.0	0.785	AX2*	FAX2*

* Notch opening at the edge is 1.95 mm.

Because the raw base material was not available, the material for the tensile specimens was cut also from the undeformed area of the tested rectangular hollow section. One kind of smooth specimen and two kinds of notched specimens were tested. The details of the specimens are shown in Table 7.3. Fig. 7.3 shows the FE meshes for the smooth and notched specimens used in this study. In all the analyses, top displacement-controlled loading was used in ABAQUS. In order to test the mesh size effect, very fine meshes for

the two notched specimens were also created, with typical mesh FAX1 shown in Fig. 7.3 for comparison purpose.

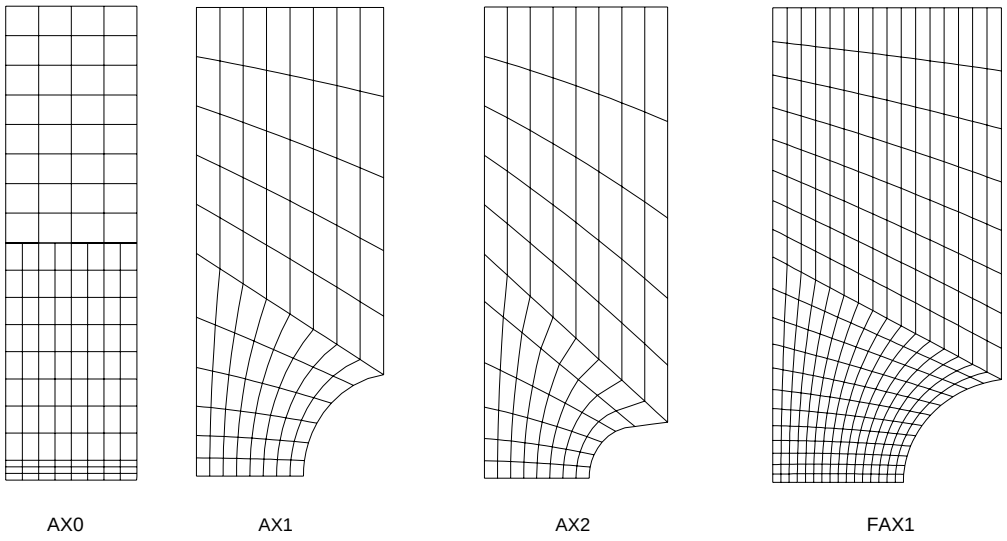

Fig. 7.3 Finite element meshes for the smooth and notched specimens

Elastic constants and other constants

An important step in the analysis of a smooth bar is the simulation of the necking which usually occurs at the maximum load during the displacement-controlled test. The use of the Bridgman-corrected true stress-strain relation [48,134] is very important in the simulation of necking [126]. In all the analyses below, the Bridgman corrected true stress-strain relation was used. The elastic parameters used were Young's modulus E=2.06E5 MPa and Poisson's ratio ν=0.3. The initial yield stress of the base material is 480 MPa. Below 0.195 strain, the true stress-true strain is approximated by multi-linear curves. No hardening was available after the strain 0.5. Between 0.195 and 0.5, an extrapolation $\overline{\sigma} = 685\overline{\varepsilon}^{0.085}$ was used. The true-stress and strain relation is plotted in Fig. 7.4. In the following analyses, $f_u^* = 0.605$ in equation (2.11) was used, except when otherwise mentioned. As is normal practice, $q_1 = 1.5$ and $q_2 = 1.0$ proposed by Tvergaard [136-137] were used. Another constant which should be chosen is f_F, in equation (2.11).

Table 7.4 A small survey on the values of f_F chosen in the literature

f_F	References	Comments
0.15	[128]	Determined by quantitative metallography from experiment
0.25	[83,139,140]	
0.13	[63]	chosen to obtain a good approximation to the void volume fraction vs. strain curves of $f > f_c$
0.18-0.2	[62]	known from experiment

A small survey shown in Table 7.4 has shown that there is large variation in the value of f_F chosen in the literature. In this study, quantitative metallographical data for f_F is not available, so two values of f_F, 0.125 and 0.20 are chosen in order to show its effect on the fitted values of damage parameters. Because the value of 0.2 is the mean value of those appeared in the literature as shown in Table 7.4, so 0.2 is adopted in the final simulation of welded T-joint.

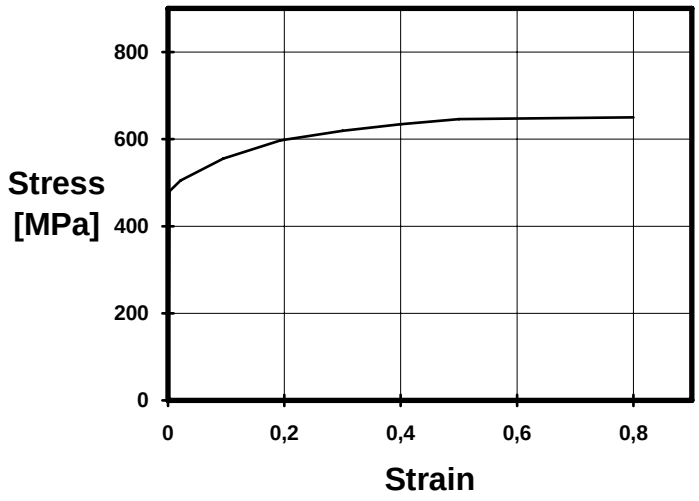

Fig. 7.4 Bridgman corrected true stress-strain for the base material

Initial void volume fraction

There are usually two families of voids in steel corresponding to large inclusions and to small carbides. Void nucleation at MnS or Al_2O_3 inclusions occurs much earlier than at small carbides [108]. The main chemical composition of the present steel is similar to the steel used in [11]. A metallographic analysis of the inclusions, mainly manganese sulphides MnS, gave that the average size in length direction is 5.7 μm, with minimum size 2.8 μm and maximum 42.5 μm. The metallographic data for the area or volume fraction of the inclusions was not available. However, the inclusion dimensions of present material is very close to those of the material studied in [14]. Both references 11 and 14, where metallographic data for inclusion volume fraction was available, have shown that an approximate formula by Franklin [37] can well estimate the volume fraction of MnS inclusions. So, as a first approximation, the initial void volume fraction is taken to be the volume fraction of MnS inclusions [11,14] estimated from the formula by Franklin [37]

$$f_v = 0.054\left(S(\%) - \frac{0.001}{Mn(\%)} \right) \tag{7.1}$$

For the present base material S=0.0065% and Mn=1.47% and so $f_0 = f_v$=0.00031, which is reasonable compared with the values of [11,14,126-127]. We will as usual assume that

the initial void volume fraction is to be present at the very beginning of plastic loading, However, nothing prohibits the introduction of a nucleation criterion for the initial voids.

Void nucleation parameters

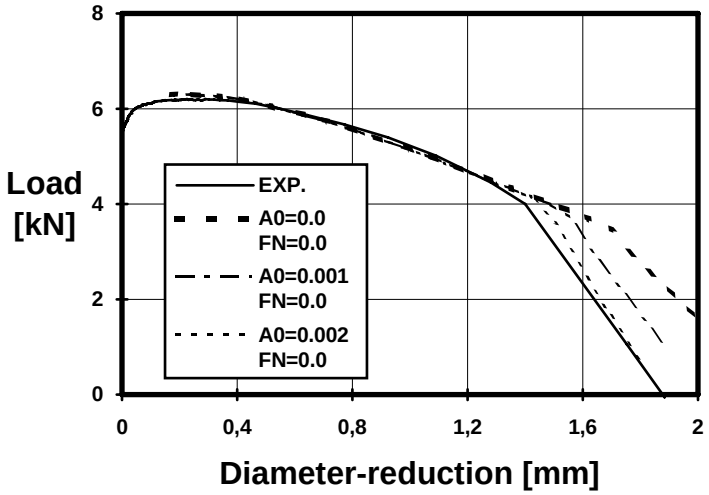

Fig. 7.5 Load-diameter reduction curves of the smooth specimen, mesh AX0, f_F =0.125.

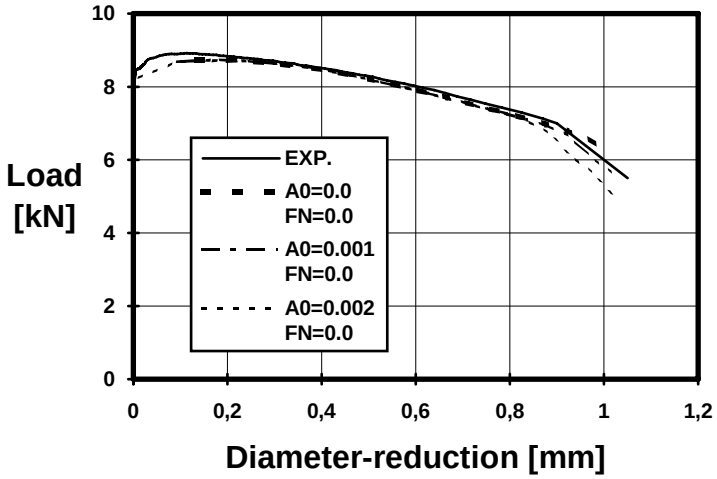

Fig. 7.6 Load-diameter reduction curves of notched specimen 1, mesh AX1, f_F =0.125.

Here nucleation parameters mean the parameters for the nucleation of small secondary particles or carbides. In order to see whether void nucleation modelling is necessary in the present steel, we first assume that there is only an initial void volume fraction and no intermediate void nucleation available ($A_0 \equiv A_1 \equiv 0$ in equation (2.6) and $A \equiv 0$ in (2.4)) in all the three specimens. The numerical results with f_F=0.125 are compared with experimental ones in Figs. 7.5-7.7 represented by A0=0 and FN=0, where A0 is A_0 and FN is f_N. Here and subsequently, diameter reduction denotes the reduction of the

diameter of the smallest cross section. It is clearly shown that with f_0 alone, the predicted diameter-reductions corresponding to fracture initiation defined as the sudden drop of the load [126-127] are too large in all the three specimens compared with the experimental ones. Therefore it means that the nucleation of new voids during the loading should be taken into account in the analyses.

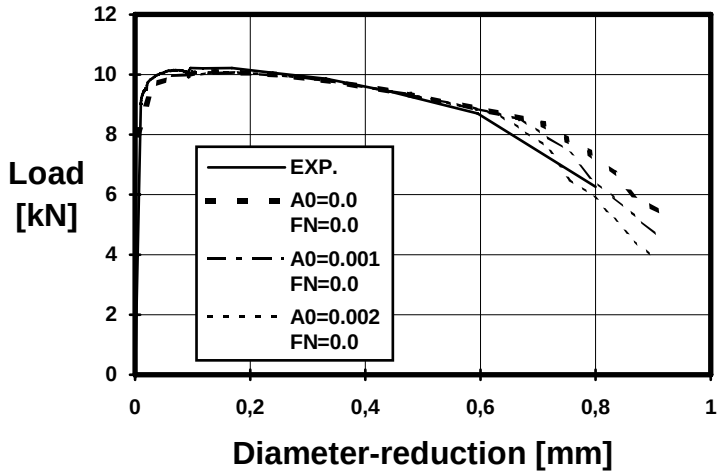

Fig. 7.7 Load-diameter reduction curves of notched specimen 2, mesh AX2, f_F =0.125.

The two void nucleation models introduced in chapter 2 were tested. The typical shapes of the two models are shown in Fig. 7.8. As described in chapter 6, one main feature of the present methodology using NSc is that the critical void volume fraction corresponding to void coalescence need not be determined beforehand and the nucleation intensity parameters A_0 or A_1 in (2.6) can be fitted from experimental results. In the following, we shall try to fit the void nucleation parameters.

At first, the continuous void nucleation model was adopted. Three values of A_0, 0.0, 0.001 and 0.002 were tested. The predicted results are compared with experimental ones for the three specimens in Figs. 7.5-7.7. It can be seen that the difference in crack initiation caused by the difference of A_0 is larger for the smooth specimen than for the notched specimens. On average, the value A_0=0.002 gives the best predictions with f_F=0.125 for the three cases.

Then the void nucleation model by Chu and Needleman (2.5) with $\varepsilon_N = 0.3$ and $S_N = 0.1$ was tried. Also three values of f_N, 0.0, 0.001 and 0.002 were tested. The predicted results are shown in Figs. 7.9-7.11. Although the nucleation intensity of this model is very different to that of the continuous model (see Fig. 7.8), it is interesting to find that the predictions by this model are quite similar to those by the continuous model. Similar to the continuous model, the value 0.002 of f_N gives the best fit to these experimental results in general.

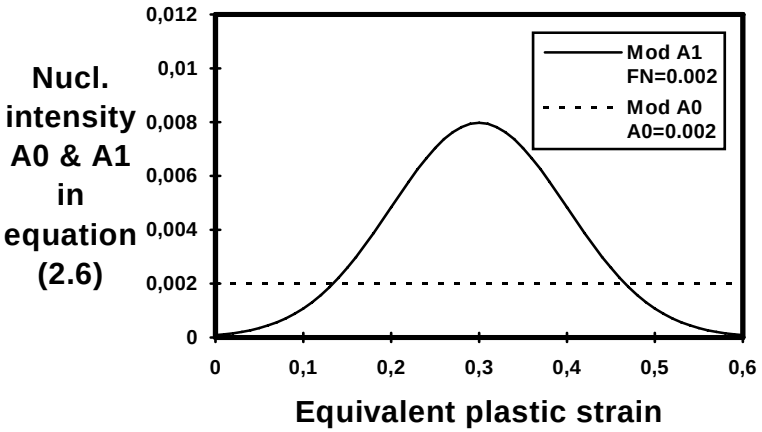

Fig. 7.8 Void nucleation intensities as a function of equivalent plastic strain for two void nucleation models. Mod A0 is the continuous void nucleation model and Mod A1 denotes the nucleation model by Chu and Needleman (2.5).

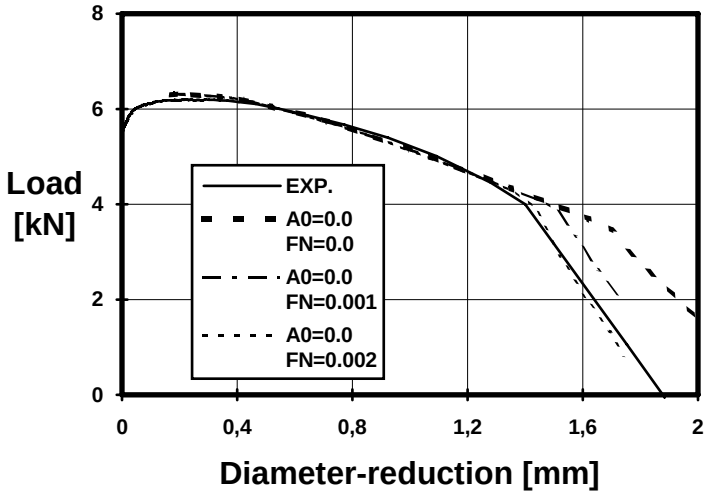

Fig 7.9 Load-diameter reduction curves of the smooth specimen, mesh AX0, f_F =0.125.

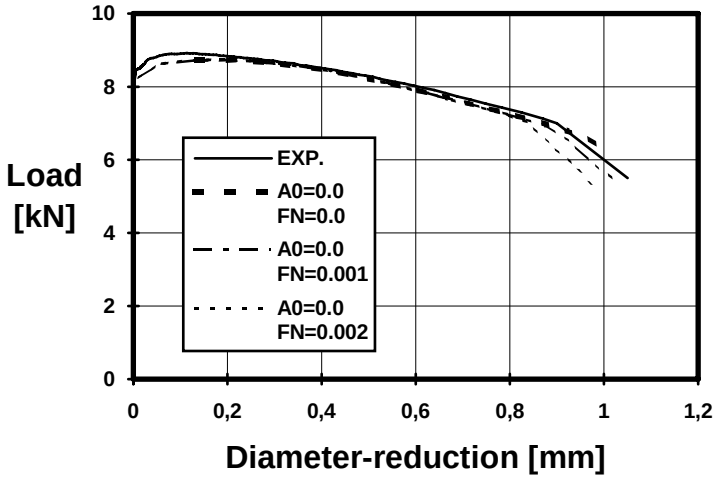

Fig 7.10 Load-diameter reduction curves of notched specimen 1, mesh AX1, f_F =0.125.

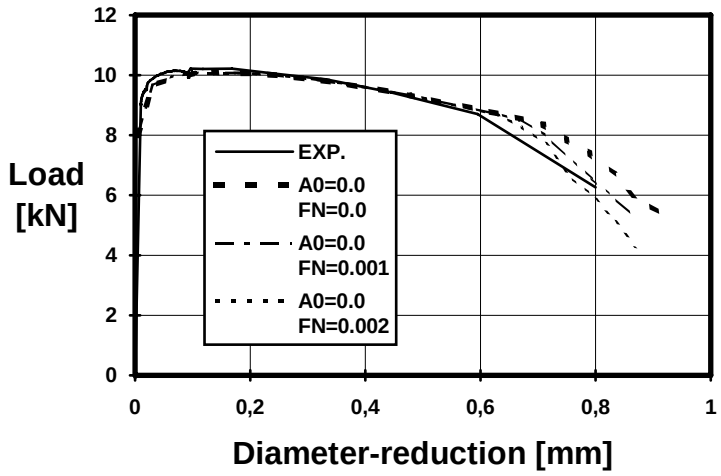

Fig 7.11 Load-diameter reduction curves of notched specimen 2, mesh AX2, f_F =0.125.

The same analyses as above have been repeated using f_F=0.2, with results shown in Figs. 7.12-7.17. By comparing the new results with the previous ones in Figs. 7.5, 7.7 and 7.8-7.11, it can be seen that the fitted void nucleation parameters A_0 and f_N, which give the best fit in general to the experimental results are slightly different (larger than) from the previous ones, although the critical void volume fractions determined by NSc in both cases are the same. The fitted void nucleation parameters for both void nucleation models can be approximately taken as A_0=0.0025 and f_N=0.0025.

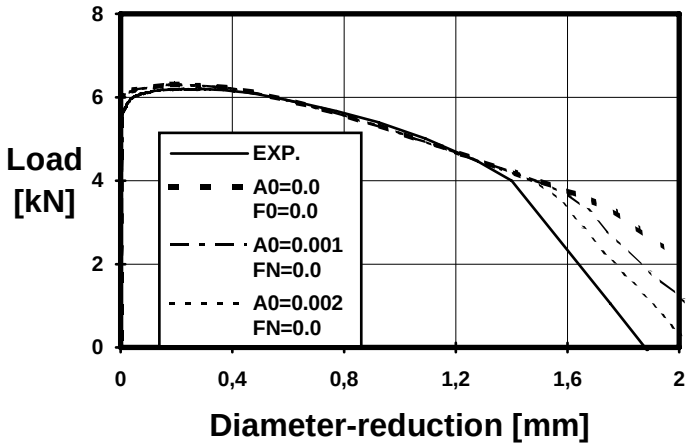

Fig. 7.12 Load-diameter reduction curves of smooth specimen, mesh AX0 and f_F =0.2.

From the studies of the two void nucleation models which are very different in void nucleation intensity distribution, it can be concluded that the simple continuous void nucleation model is as effective and useful as the more sophisticated model by Chu and Needleman (2.5), at least in the cases studied. So, in the calibration of nucleation parameters for the HAZ material described in section 7.4, only the continuous void nucleation model is adopted.

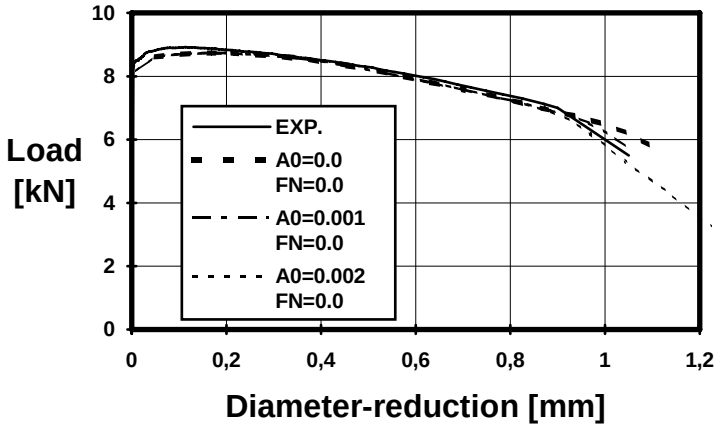

Fig. 7.13 Load-diameter reduction curves of notched specimen 1, mesh AX1, f_F =0.2.

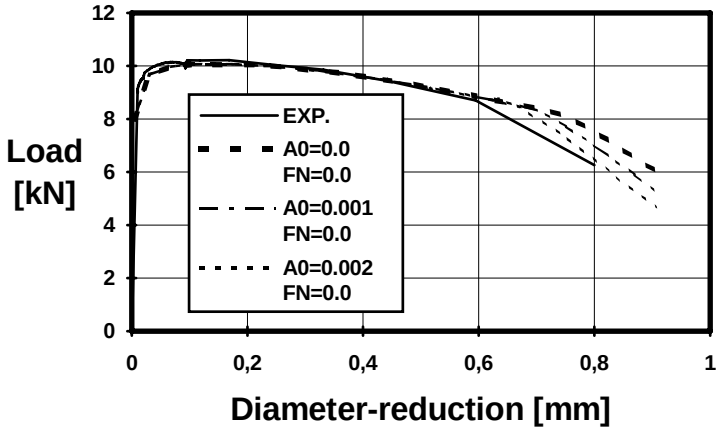

Fig. 7.14 Load-diameter reduction curves of notched specimen 2, mesh AX2, f_F =0.2.

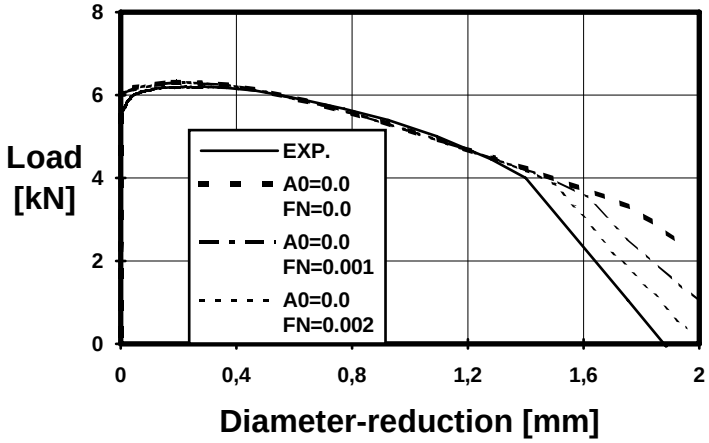

Fig 7.15 Load-diameter reduction curves of smooth specimen, mesh AX0, f_F =0.2.

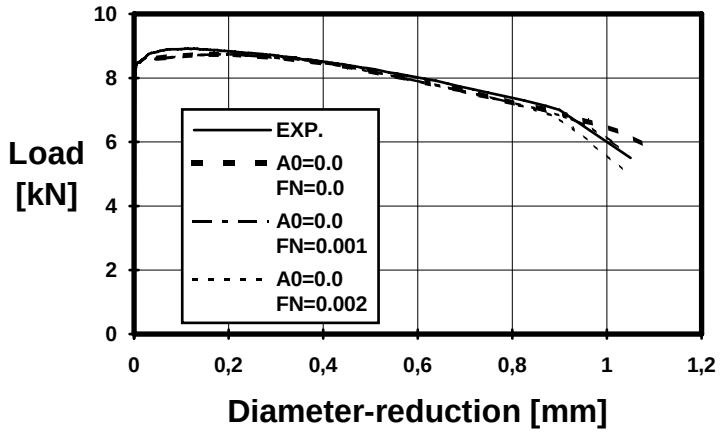

Fig 7.16 Load-diameter reduction curves of notched specimen 1, mesh AX1, f_F =0.2.

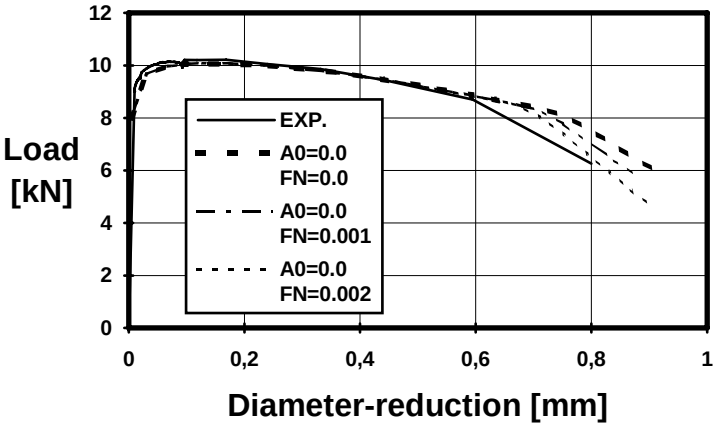

Fig 7.17 Load-diameter reduction curves of notched specimen 2, mesh AX2 , f_F =0.2.

Crack development in notched specimen 1

Fig. 7.18 shows that distribution of the computed void volume fraction, f (after f has locally exceeded f_c (by NSc) at the centre of the smallest section of the specimen) over the smallest cross section as a function of several load levels. The load level is characterized by the different diameter reduction values indicated in the legend. The distribution of the computed von Mises stress in the smallest cross section of the specimen at the same load levels as in Fig 7.18 is shown in Fig. 7.19. It can be seen from Fig. 7.19 that as soon as the critical void coalescence condition is satisfied ($f > f_c$), the equivalent stress nearly approaches zero. The length of the damaged zone where f has reached f_F can be used to define the numerical crack growth [128]. According to this idea, the numerical crack extension as a function of load levels can be obtained. However, it should be mentioned that, because the stress distribution in the neck region is fairly uniform before the fracture initiation, the time from initiation to final failure of the specimen is very short. So, practically the crack growth in the present tension specimen is not meaningful.

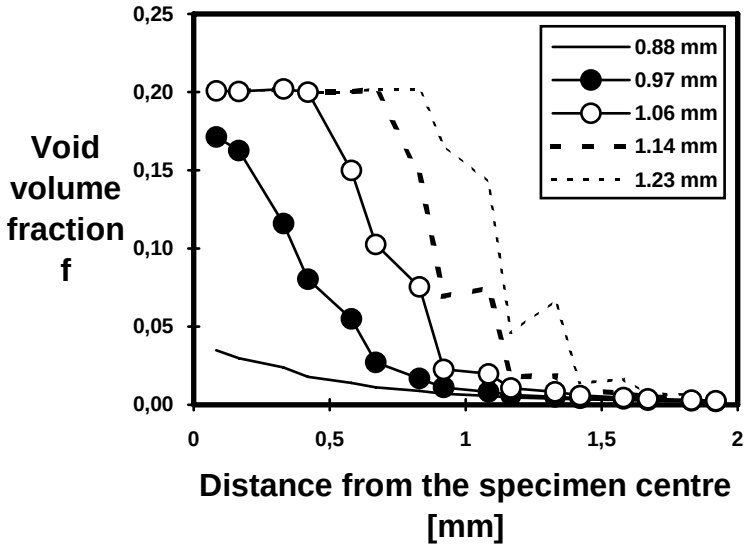

Fig. 7.18 Distribution of the void volume fraction in notched specimen No. 1, f_F =0.2.

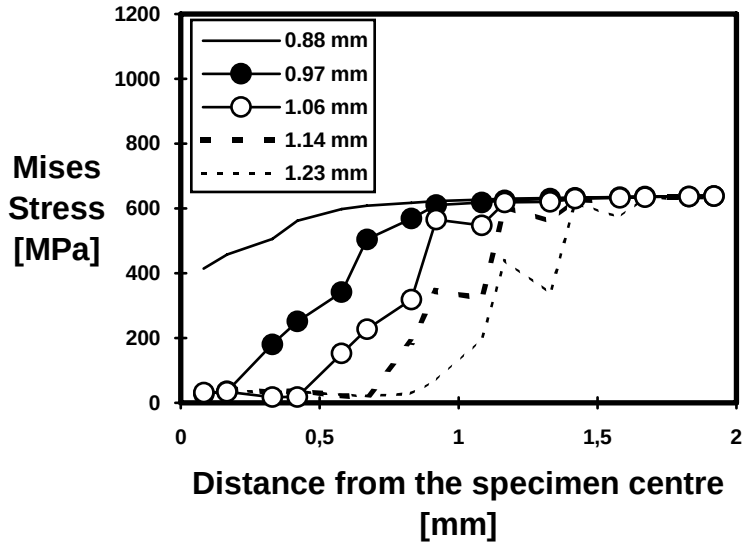

Fig. 7.19 Distribution of Mises equivalent stress in notched specimen No.1, f_F =0.2.

7.4 Damage Parameters for the HAZ Material

A weld is a highly heterogeneous medium of several zones with significantly different microstructures, different strengths and ductilities. The HAZ is localized between the base metal and weld metal, and includes a narrow zone of base metal affected by the welding thermal cycle, shown in Fig. 7.20. Depending on the peak temperature of the weld thermal cycle, HAZ can be divided into a coarse grained region, a fine grained region, an intercritical region and a subcritical region. It is well known that the coarse

grained HAZ (CGHAZ) has the lowest toughness. The rupture of the welded structure and joint usually initiates from this small region, which therefore plays a very important role in controlling the damage and fracture behaviour of welded joints [29,142-143]. The crack initiation in the welded T-joint is clearly shown in Fig. 7.20. So, it is necessary to study the damage and fracture behaviour of the CGHAZ for the prediction of welded joints.

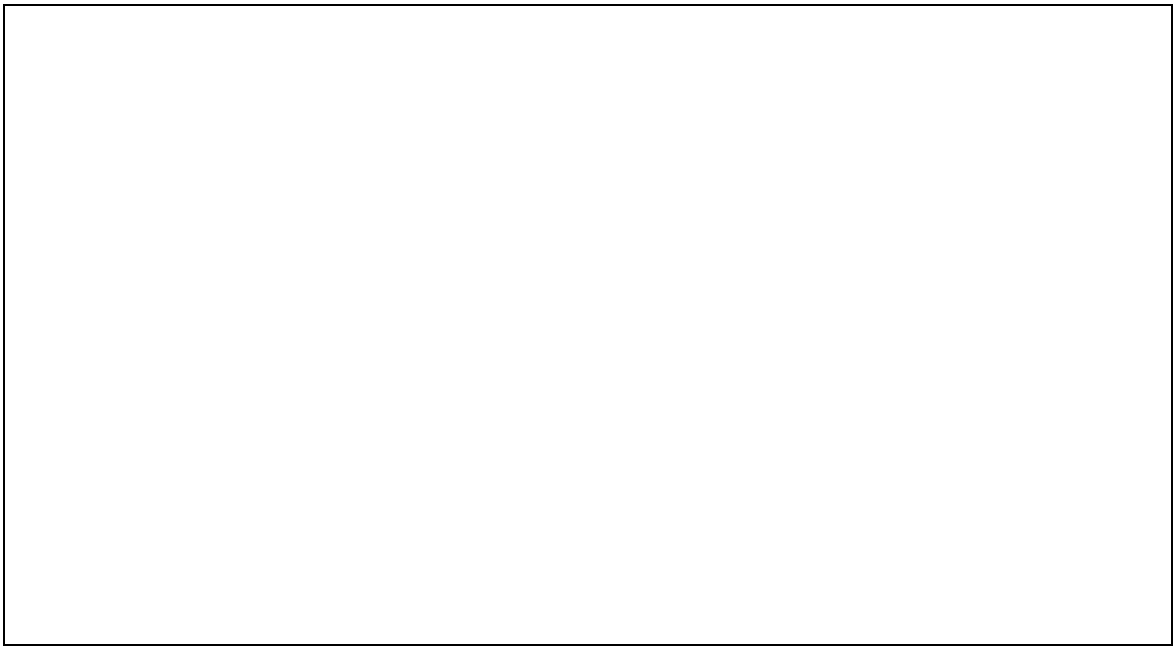

Fig. 7.20 Photo showing the HAZ and crack initiation location in welded T-joint. HAZ is the small region between weld metal and base metal illustrated by slightly white colour.

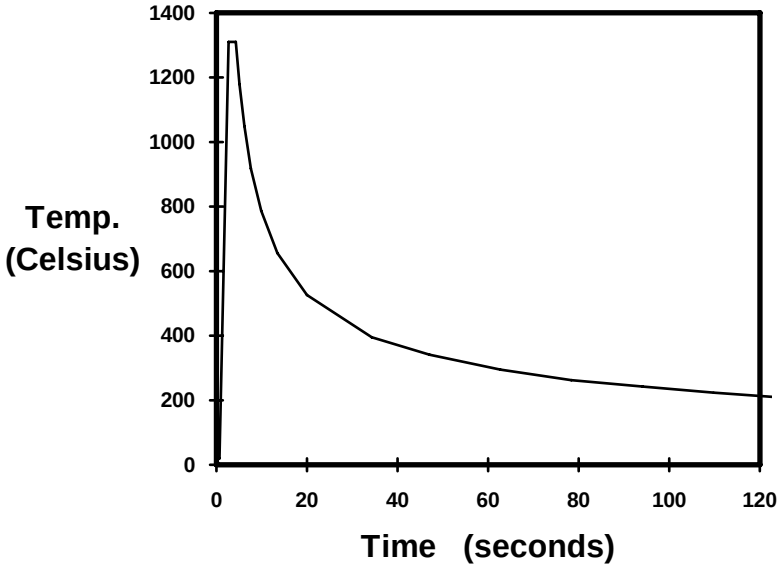

Fig. 7.21 Thermal cycle of the CGHAZ

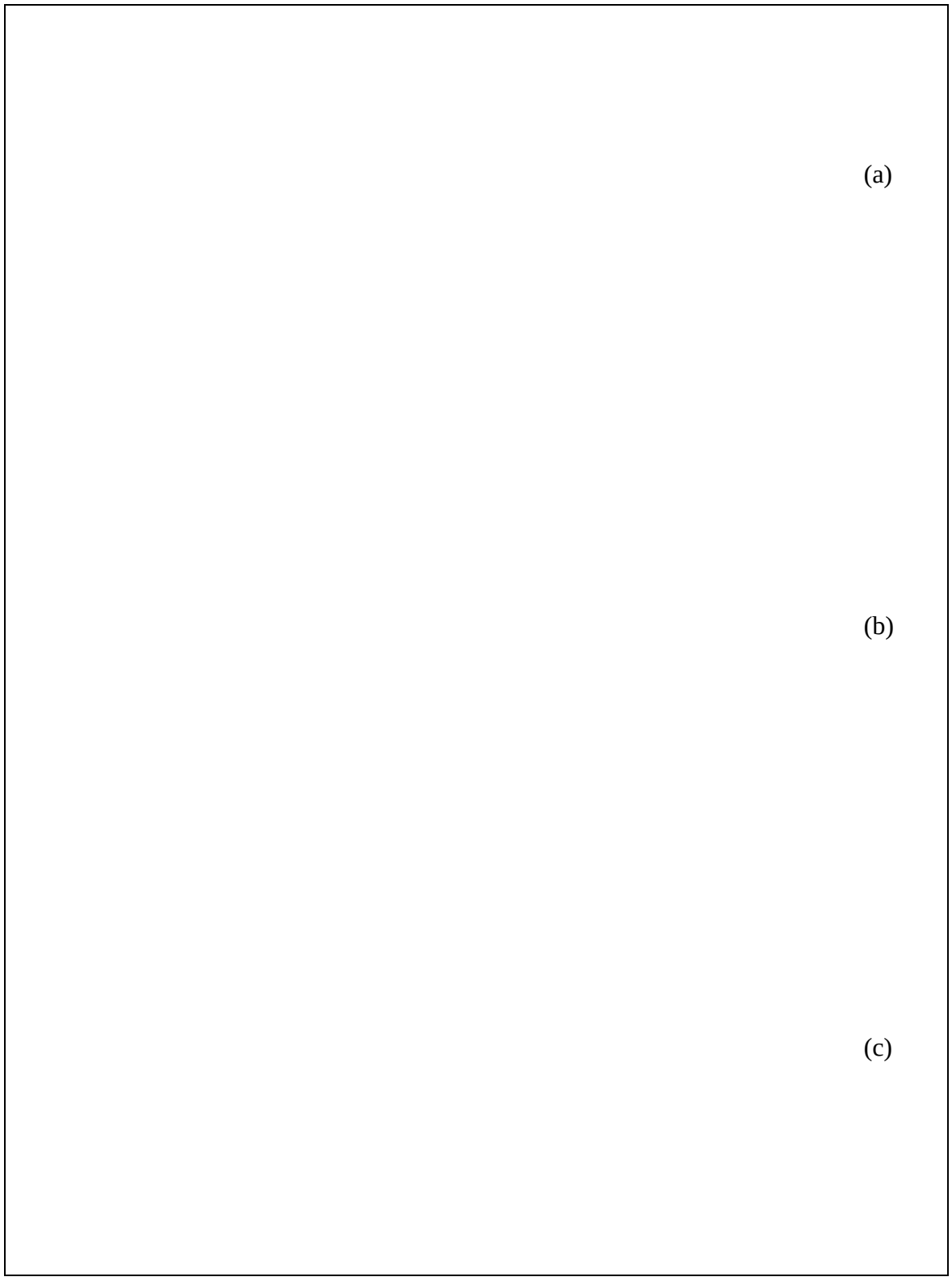

Fig. 7.22 Micrographs showing the microstructures of (a) base material, (b) real CGHAZ and (c) simulated CGHAZ. The scale in the three photos is 500:1.

Simulation of CGHAZ

Because CGHAZ usually is a very narrow area, in order to study the damage behaviour of CGHAZ, the weld thermal simulation technique is used to enlarge this small region. The simulation was performed in the university of Oulu by Gleeble-simulator. The material for the simulation is the base material with the main chemical composition shown in Table 7.2. Round bar specimens with diameter 7 mm were used for the simulation. The length of the simulated area was limited to 15 mm. The thermal cycle used in the simulation is shown in Fig. 7.21. The simulation parameters include the heating rate characterized by the heating time of 2 sec from room temperature to the peak temperature, 1310 $^{\circ}$C, and cooling rate of the cooling time $t_{8/5}$ of 3.5 sec from 800 to 500 $^{\circ}$C.

Microstructures of the real CGHAZ in T-joint and the simulated CGHAZ

In order to examine the simulation results, the microstructures of the real CGHAZ in the welded T-joint taken from areas A and B in Fig. 7.2 are compared with the microstructures of the simulated ones. The typical results are shown in Fig. 7.22, in which the microstructure of the base material is also included for comparison purposes. It can be seen that the microstructure of the simulated CGHAZ is very similar to the real one in the welded T-joint. In other words, the present simulation of CGHAZ can be regarded as valid

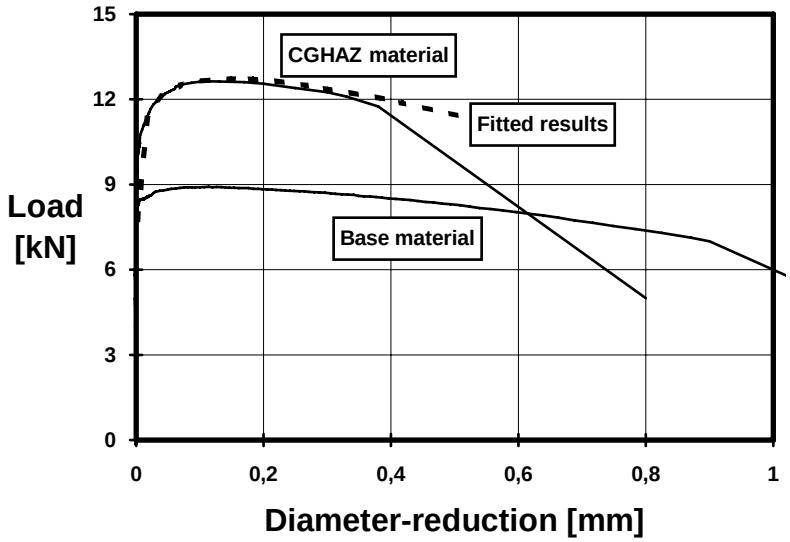

Fig. 7.23 Comparison of the experimental results between HAZ material and base material. Mesh AX1 was used. Fitted results mean the results of fitting the true stress-strain relation. No damage is involved in this fitting.

Specimen and finite element mesh

Because the length of the simulated CGHAZ is only 15 mm, which is not long enough to make a smooth tension specimen so that the necking could appear at the CGHAZ material, only one kind of notched specimen was prepared and tested. The geometry of the notched specimen made of CGHAZ is the same as the notched specimen 1 of the base material. Therefore, the mesh AX1 in Fig. 7.3 was used for the analysis of CGHAZ. The comparison of the experimental results of the CGHAZ material with those of the base material is shown in Fig. 7.23, which shows a certain degree of strain softening characterics of the CGHAZ material.

Fitting of true stress and strain relation for the CGHAZ material

As we stated above, the length of 15 mm is not long enough to conduct smooth tension tests for CGHAZ, so the true stress-strain for the CGHAZ material has to be fitted from the experimental results of a notched tension specimen. The fitted stress-strain relation and fitted load-diameter reduction curve are shown in Figs. 7.24 and 7.23, respectively. In Fig. 24, the true stress-strain relation of the base material is also included for comparison which indicates that there is significant difference in the initial yield stresses between these two materials.

Initial void volume fraction

Damage and fracture in CGHAZ is a progressive process with void initiation, growth and coalescence [143]. The real micro-mechanisms (usually multi-mechanisms) for the nucleation of intermediate as well as initial voids are very complicated. Here, as evidenced in [143], we can assume that the initial void volume fraction of CGHAZ is taken to be the volume fraction of MnS inclusions, which is equal to that of the base material, $f_0 = f_v$=0.00031. In the following, we use the same method as for the base material to calibrate the void nucleation parameters for the CGHAZ material.

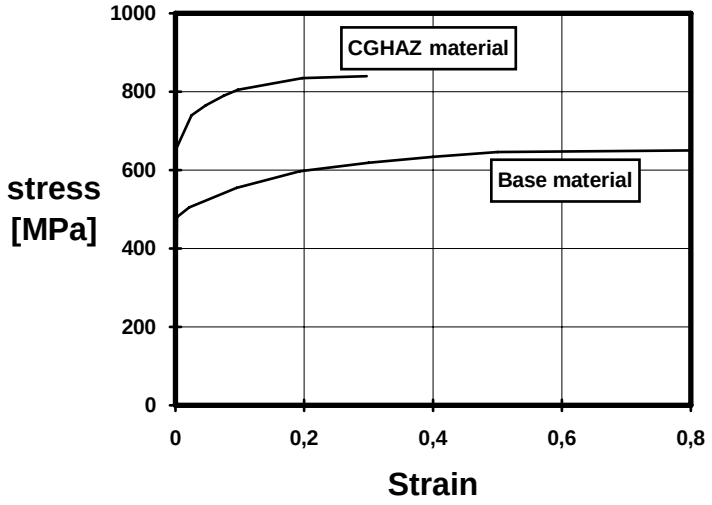

Fig. 7.24 Fitted true stress-strain relation of the CGHAZ material. The true stress-strain relation for the base material in Fig. 7.4 is reproduced here for comparison.

Void nucleation parameters

At first, we analyze the CGHAZ notched specimen with only the initial void volume fraction, by assuming no void nucleation is available during the loading process. The result is shown in Fig. 7.25. The same situation as in the base material can be observed in Fig. 7.25, which indicates that the void nucleation modelling during the loading process is very necessary and important in the damage and fracture of CGHAZ material, because with the initial void volume fraction alone, no void coalescence appeared even up to nearly 0.6 mm of the diameter reduction.

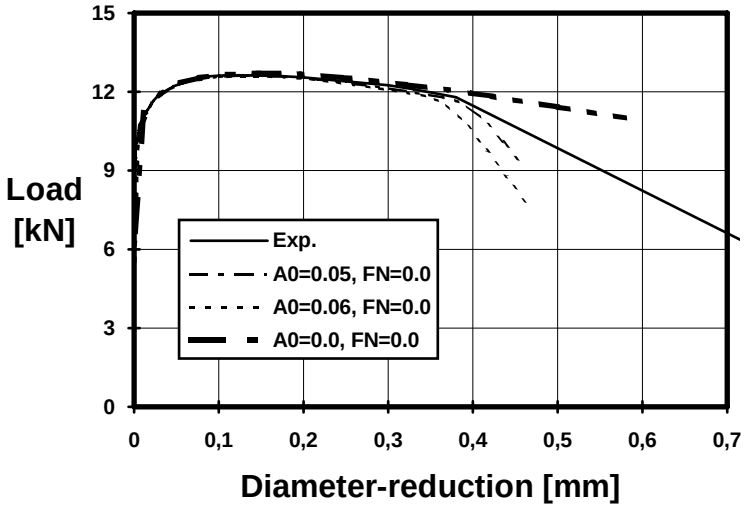

Fig 7.25 Load-diameter reduction curves of CGHAZ material, mesh AX1, f_F =0.2.

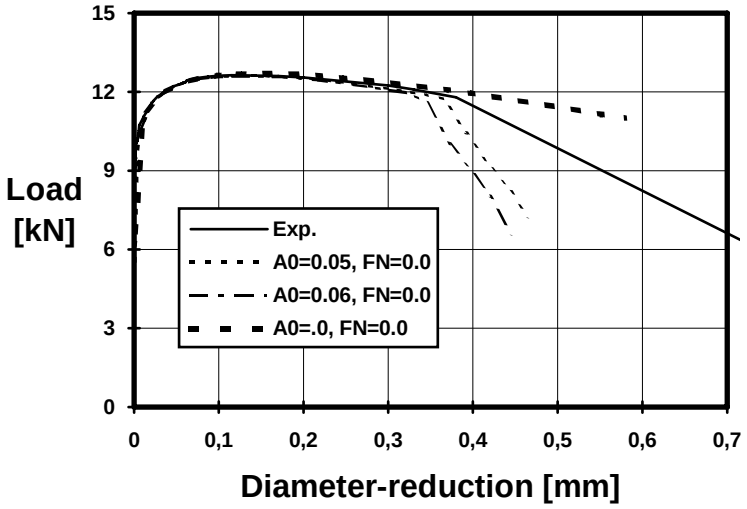

Fig 7.26 Load-diameter reduction curves of CGHAZ material, mesh AX1, f_F =0.125.

As mentioned in the previous section, only the simple continuous void nucleation model is considered in the CGHAZ material. Two extra values of the continuous void nucleation parameter A_0, 0.05 and 0.06 were tested. The numerical results are compared with experimental results in Fig. 7.25 for f_F =0.2 and in 7.26 for f_F =0.125. From these

two figures, it can be seen that the stress decrease rate for the case f_F=0.125 is larger than that for the case f_F=0.2. Because the total diameter reduction for the CGHAZ material is very small compared with the base material, the difference in void nucleation parameter A_0 caused by different f_F is not very large. In both cases f_F=0.125 and f_F=0.2, A_0=0.05 gives a reasonably good fit to the experimental results. So, A_0=0.05 is used for CGHAZ material in the following simulation of a welded T-joint.

7.5 Simulation of the Ductile Fracture of Welded Joints

Experimental results

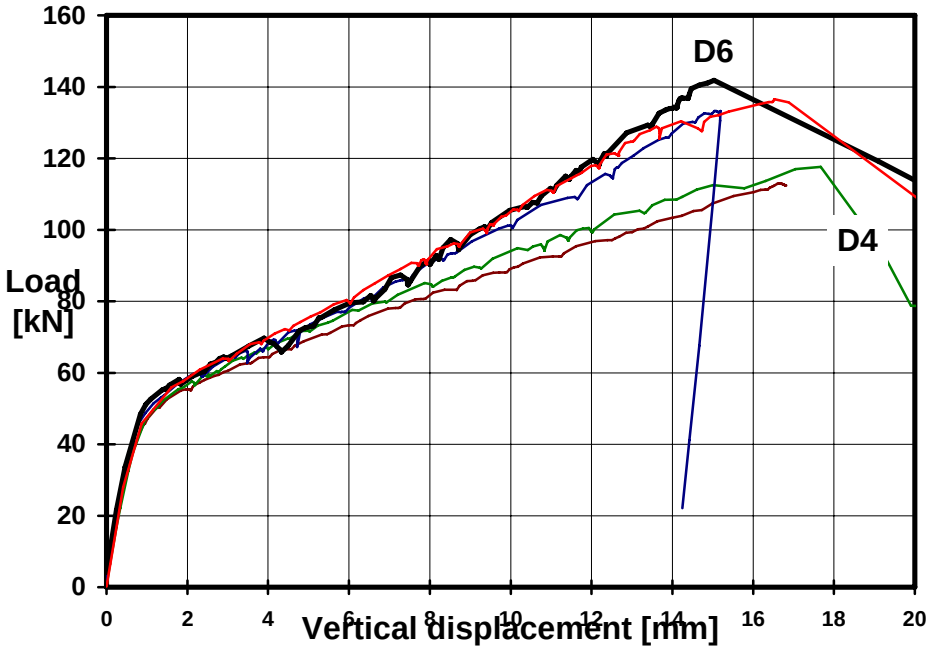

Fig. 7.27 Experimental results of the welded T-joints. The displacement was measured at the top of the T-joint which is 70 mm above the horizontal plate, see Fig. 7.2.

A schematic drawing of the loading arrangement is shown in Fig. 7.2. The two ends of the horizontal plate of the T-joint were clamped with pre-compression force. The vertical plate was fixed to the piston of a servo-hydrostatic actuator via a load cell. The applied load was measured by the test machine load cell. After the welding, there was considerable residual deformation both in the horizontal and vertical plates of the welded T-joint caused by the welding residual stress. Before and during fixing the T-joint into the test rig, some "cold forming" was made. The load-versus-deformation data of the tests are plotted in Fig. 7.27. The crack initiation load visually observed was between 80.0-90.0 kN, with 84 kN for joint D4 and 80 kN for joint D6. Because it was very difficult to clamp the ends fully, some joints including joint D4 with which the base and simulated CGHAZ materials have been studied in previous sections slipped quite considerably from the clamped ends. This can be observed from the experimental results shown in Fig. 7.27.

Fig. 7.27 also shows that for these joints which did not slip significantly, the variation in the global behaviour is not very significant. So, in the following, the numerical predictions are compared with typical experimental results of joint D6.

Preliminary analyses without damage

Before we go to analyze the fracture behaviour, a 2D plane strain analysis without damage was performed. Only two materials, the base and the CGHAZ materials, were considered. The finite element mesh and CGHAZ (about 0.49 mm in thickness) in the finite element model are shown in Fig. 7.28. In the FE mesh there were 258 8-node plane strain finite elements (CPE8R) and 911 nodes. Very fine mesh was used in the regions where the stress triaxility was expected high and crack initiation was suspected. Due to the symmetric loading and geometry, only half of the joint was considered. The loading was applied to the joint as a prescribed displacement of the nodes at the end of vertical plate in the finite element models. The analysis results are compared with the experimental ones in Fig. 7.29.

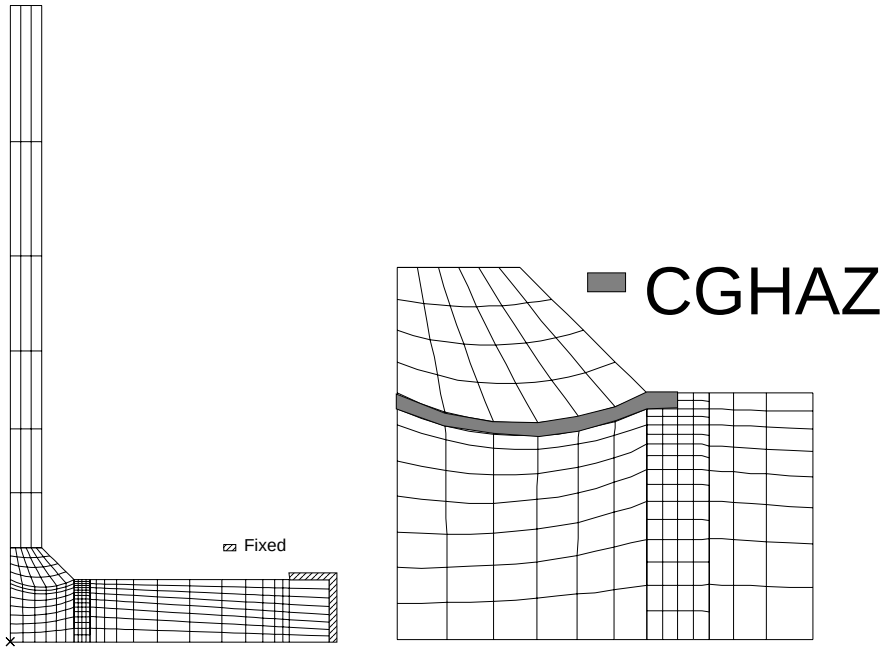

Fig. 7.28 (a) 2D plane strain finite element mesh and boundary conditions at the end of horizontal plate (b) CGHAZ in the finite element model

Fig. 7.29 shows that there is large difference in the stiffness, with FE analysis predicting less deformation than measured, although both analyzed and experimental load-displacement shapes are similar to each other, especially in the early loading stage. The reasons causing this difference are: the residual stress due to the welding and the subsequent "cold forming" which are expected to decrease the stiffness of the joint have not been taken into account in the analysis. Another reason which is obvious is that in test, there was always slipping at the ends of horizontal plate and this slipping has not

been considered in the analysis. Though, by using friction elements in ABAQUS, the slipping could be taken into account to a certain extent, considering that the main purpose of this study is not to accurately study the global behaviour, but the fracture behaviour, the friction elements have not been used.

It can be seen from Fig. 7.29 that the normal analysis predicts no failure at all for the present T-joint under tension load. This limitations of the conventional finite element analysis, which were the main deriving force of this study, reveals the importance of developing a practical approach which is capable of predicting crack initiation, propagation and final failure of welded joint and structure.

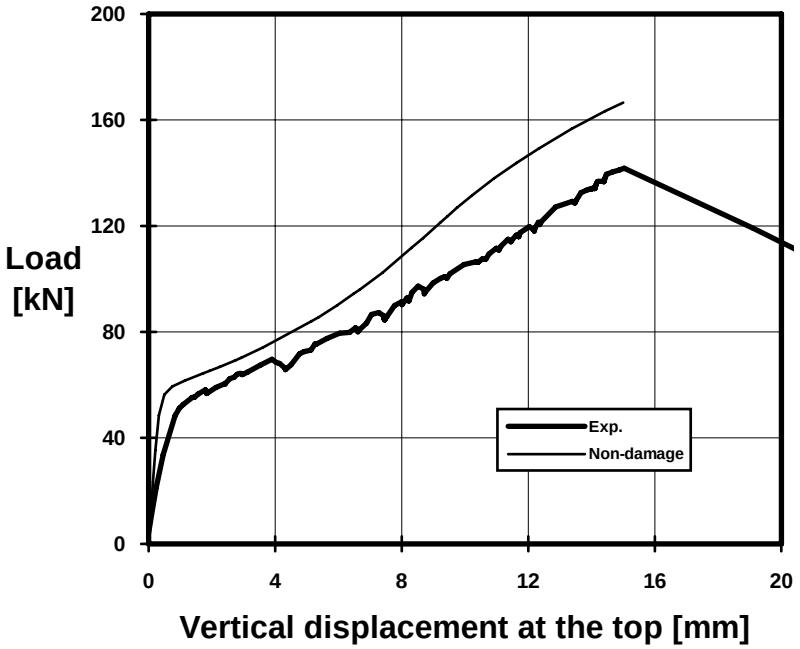

Fig. 7.29 Comparison of the preliminary analysis results without damage and the experimental results.

Damage analyses

The same mesh and boundary conditions as shown in Fig. 7.28 were used in the damage analysis. In the damage analysis, the joint was loaded in a stepwise fashion (about 200 increments). Three sets of void nucleation parameters were tested:

Case (a) A_0=0.002 for base material and A_0=0.002 for CGHAZ material;

Case (b) A_0=0.002 for base material and A_0=0.05 for CGHAZ material;

Case (c) A_0=0.0025 for base material and A_0=0.05 for CGHAZ material.

The purpose of case (a), is to see the importance of CGHAZ material in the fracture of a welded T-joint. The predicted load-displacement curves using the above sets of parameters are plotted in Fig. 7.30, where the non-damage analysis results in Fig. 7.29

were reproduced for comparison purpose. The following observations can be made from the results in Fig. 7.30:

- The predicted ultimate failure load in the damage analyses case (b) and (c) is about 120 kN, which is a reasonable approximation to the experimental ultimate failure load, observed between 115-140 kN, shown in Fig. 7.27.

- The predicted joint stiffness in the damage analyses case (c) and (b) obviously deviates from the one predicted by non-damage analysis at the middle way of loading and the predicted stiffness is then close to the experimental one. In other words, the macroscopic damage effect has been predicted by the current approach.

- There is a large difference in both the ultimate failure load and stiffness in the prediction of case (a) and the predictions by case (b) and (c). The predicted ultimate failure load of case (a) is too large compared with the experimental results. This finding highlights the importance of incorporation of CGHAZ material into the analysis of welded joints.

- The difference between the predictions by case (b) and (c) is negligible, which means that CGHAZ material perhaps plays a more significant role in the fracture behaviour of welded joint.

These results show that the current approach is indeed very effective and that meaningful results could not be obtained otherwise.

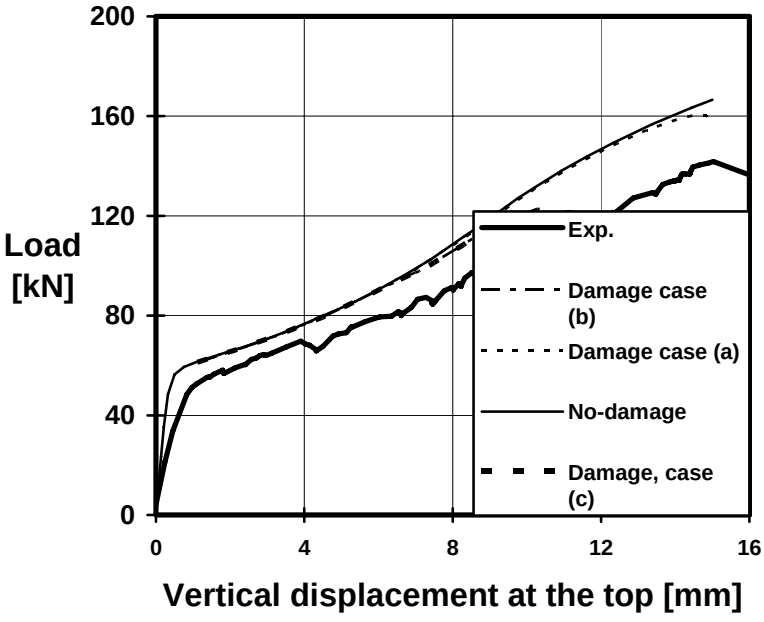

Fig. 7.30 Comparison of numerical solutions

Crack initiation and propagation

The crack initiation and propagation in the welded T-joint can be studied according to the definition of a numerical crack mentioned in section 7.3. A part of FE mesh around the weld toe where the crack is supposed to initiate, has been cut out for detailed observation. Fig. 7.31 shows the dimensions of that part of the mesh. In the damage analysis case (b), the failure sequence paralleled that observed experimentally and it may be summarized as follows:

Crack-initiation A macro numerical crack ($f = f_F$) initiated in the CGHAZ material at the weld toe, shown in Fig. 7.32 (a) for an approximate applied load of 95 kN corresponding to a vertical displacement 7 mm, which is slightly higher than the experimentally observed load, between 80-90 kN. The difference is most likely due to the discrepancies between the definition of a numerical crack and that of the experiment. For example, here the numerical crack is defined at the integration points within the finite elements, while in the experiment, the crack is checked by examining the surface for its appearance. The equivalent plastic strain and void volume fraction at crack initiation are plotted in Fig. 7.33.

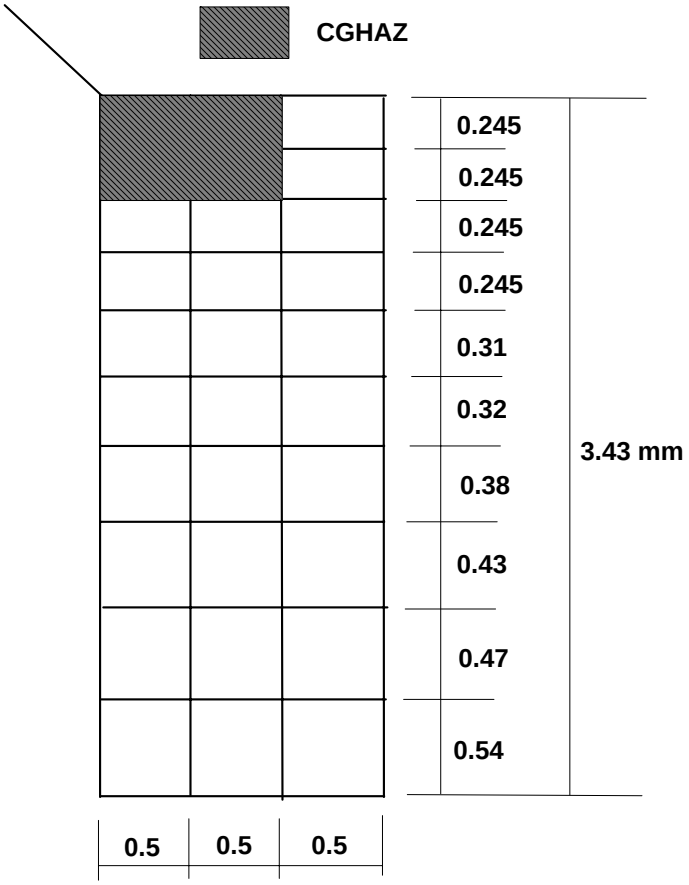

Fig. 7.31 Dimensions of part of the mesh around the crack initiation location.

Crack propagation direction The crack then expanded in the plate thickness direction to the next CGHAZ element and then to the next base material element. After that, the crack propagated in a zigzag fashion to the depth of the plate thickness. The crack propagation profile at the vertical displacement 12 mm is shown in Fig. 7.32 (b). The equivalent plastic strain and void volume fraction at displacement 12 mm are plotted in Fig. 7.34 on the deformed geometry, which clearly show the real crack propagation direction. The crack growth direction observed from the experiment is shown in Fig. 7.35. It can be seen that the predicted crack propagation is very similar to that observed from the experiment. The deformed shape of the whole joint at displacement 12 mm is shown in Fig. 7.36.

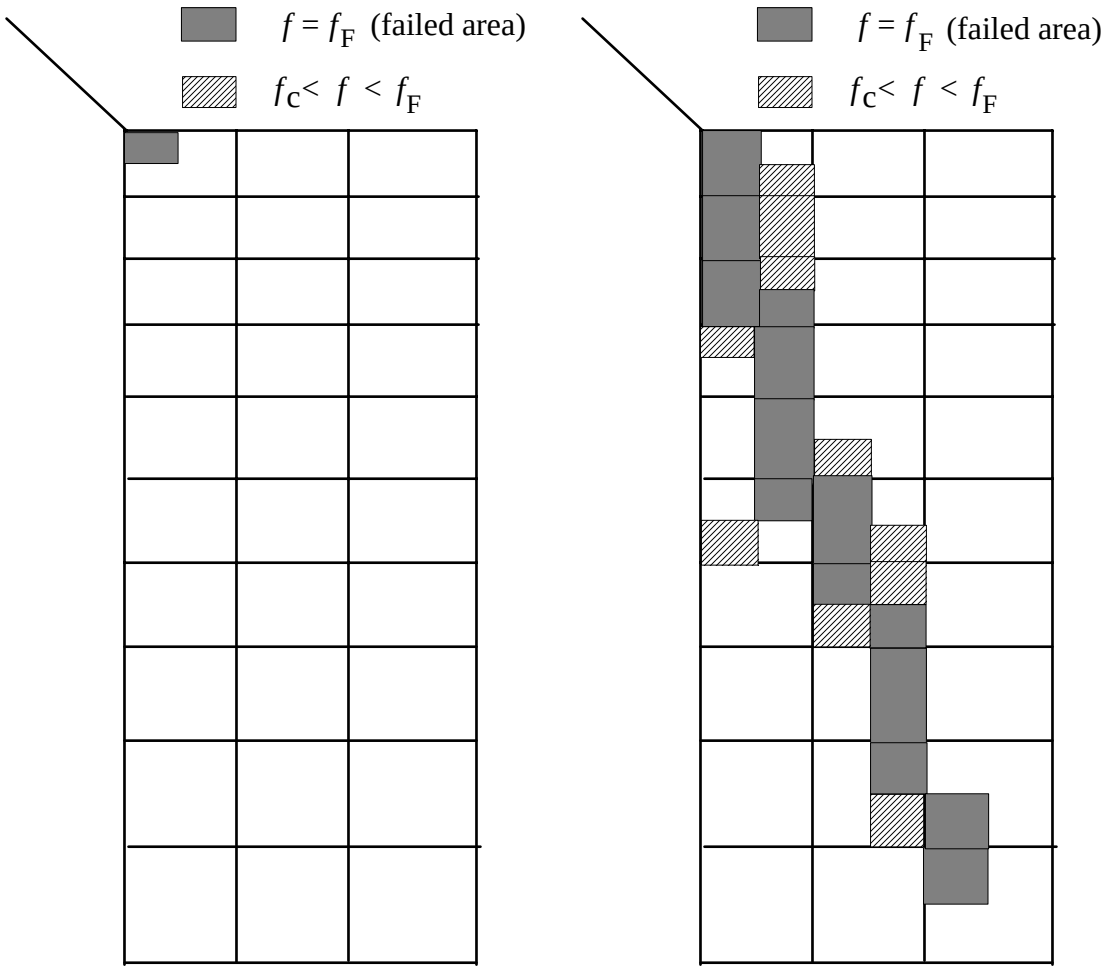

Fig. 7.32 (a) Crack initiation position at the vertical displacement about 7 mm, and (b) crack propagation profile at displacement 12 mm. One element is divided into four sub-areas for each integration point.

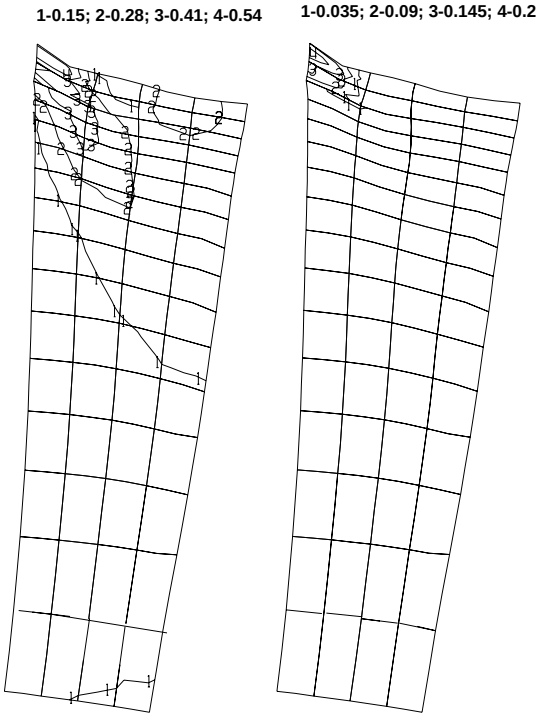

(a) (b)

Fig. 7.33 Equivalent plastic strain (a) and void volume fraction distribution (b) at crack initiation, which corresponds to the vertical displacement 7 mm.

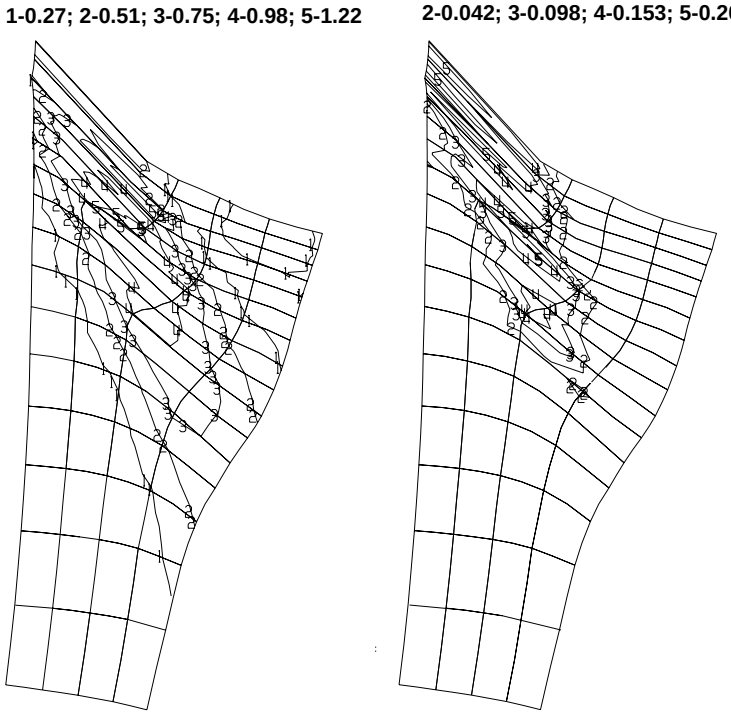

(a) *(b)*

Fig. 7.34 Equivalent plastic strain (a) and void volume fraction distribution (b) at a vertical displacement 12 mm.

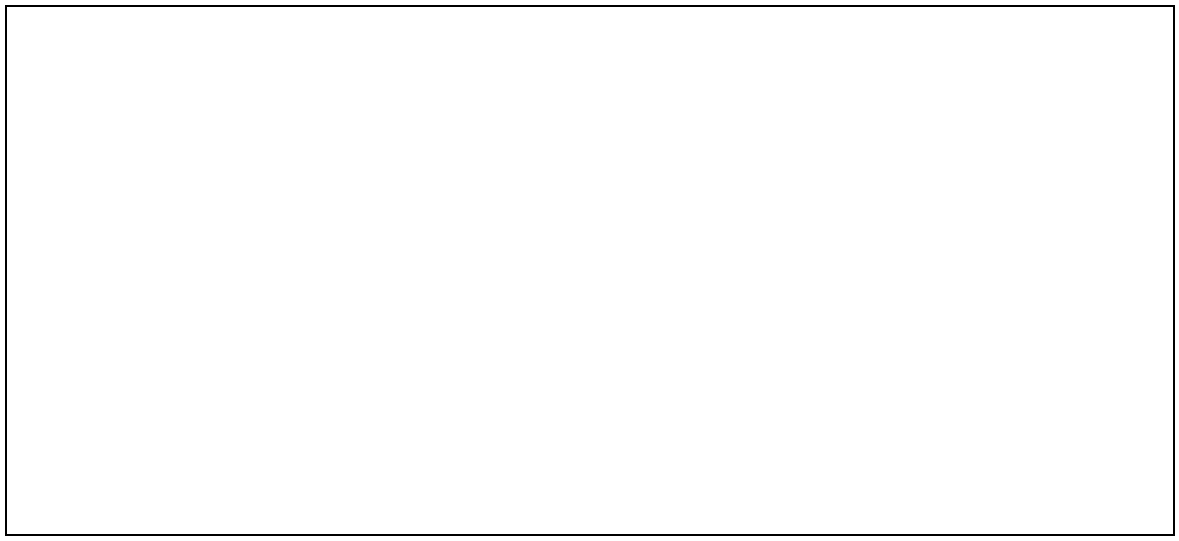

Fig. 7.35 Photo showing crack propagation direction in welded T-joint observed from experiment

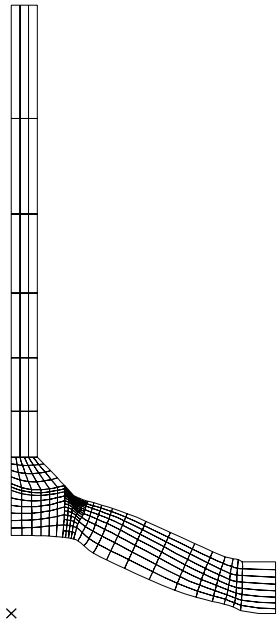

Fig. 7.36 Deformed mesh of the T-joint at displacement 12 mm.

Crack growth The numerical crack growth in the plate thickness has been calculated from the analysis results of case (b) and is shown in Fig. 7.37 as a function of vertical displacement of the joint. From Fig. 7.30, it can be observed that the ultimate load appears at a displacement of about 10 mm. Fig. 7.37 also shows that before reaching the displacement 10 mm, the crack growth increases slowly as the displacement increases. However, after the displacement 10 mm, the crack grows very rapidly, which suggests that the final failure is approaching. These findings suggest that there is a considerable stable crack growth in the welded T-joint before the ultimate failure. In the analysis case

(b), the stable crack from initiation to ultimate load can be computed from Fig. 7.37 and is about 1.1 mm.

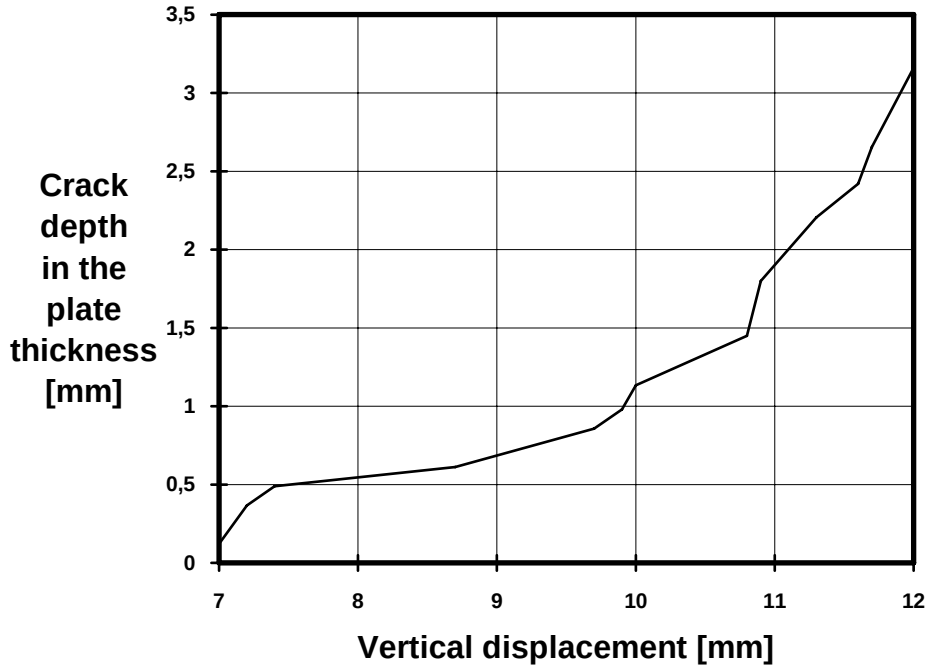

Fig. 7.37 Predicted crack growth in the plate thickness direction as a function of vertical displacement.

7.6 Discussion and Summary

Void nucleation modelling

There are two kinds of void nucleation in the Gurson-Tvergaard model: the initial void nucleation of large inclusions, for example MnS, and the intermediate void nucleation of secondary particles or small carbides. As mentioned earlier, in line with convenience, it is usually assumed that the initial voids nucleate at the beginning of plastic deformation, although nothing prohibits the introduction of a nucleation criterion for the initial voids. It has been shown that the modelling of the intermediate nucleation is necessary and important in the analysis using the G-T model. The use of a strain-controlled nucleation model has several advantages: it is easy to handle and there is no extra term to the asymmetry of tangent moduli. In practice, it is very difficult to determine the void nucleation model and its parameters. In failure criterion Fc, the nucleation parameter(s) is usually selected beforehand and the critical void volume fraction is determined later, or vice versa. Because there is no mechanism for void coalescence available in Fc, for any strain-controlled nucleation model, either the nucleation parameter(s) or the critical void volume fraction can be taken as an independent variable. Hence, the non-consistency problem described earlier appears in Fc. However, in the new criterion NSc, a void coalescence criterion which is fully compatible with the G-T model has been installed

into the G-T model. The void coalescence in NSc is a natural result of the development of the stable and unstable responses. In contrast with Fc, in NSc void nucleation parameter(s) is the only independent variable which can be fitted from experimental results. In nature, however, the discrepancy problem has not been absolutely eliminated in NSc. This is because of the inability to determine accurately the void nucleation model and select its parameters, for example, the values of ε_N and S_N. However, for a simple nucleation model such as the continuous void nucleation model, the nucleation parameter is determined without any ambiguity. Two nucleation models have been compared in the previous section. It was interesting to find that the simple continuous nucleation model works equally as well as the more complicated model by Chu and Needleman (2.5) for the present steel. This finding may suggest that by using the simple nucleation model and the new failure criterion, the risk of non-consistency problems could be reduced to as small as possible, at least for the cases studied.

Effect of mesh size on the fitted nucleation parameters

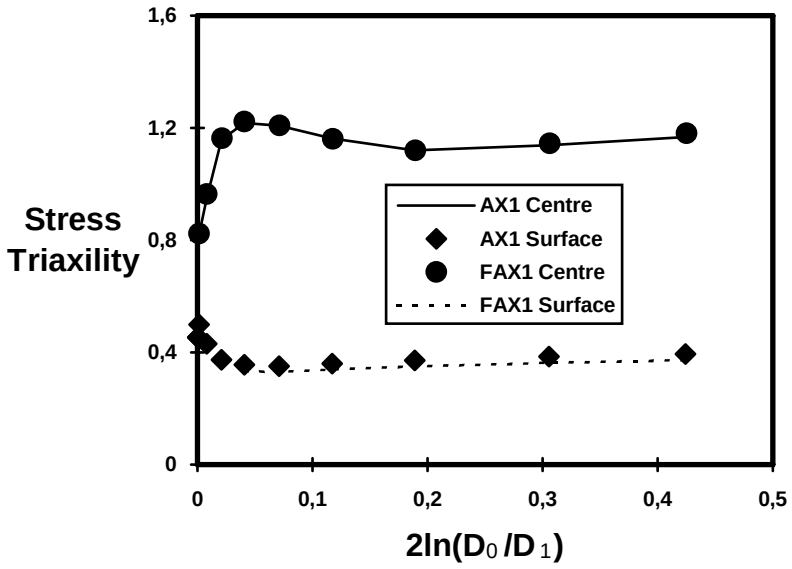

Fig. 7.38 Stress triaxility as a function of the macroscopic equivalent strain for notched specimen 1, where D0 and D1 are the initial and current minimum diameters, von Mises material was used.

One of the important aspects in local approaches is the so-called critical length effect. Because the finite element method is usually involved in the local approaches, so the critical length is directly related to the finite element mesh size. It is essential to note that the mesh size effect is effective only when the stress distribution is uneven. Two meshes, FAX1 (shown in Fig. 7.3) and FAX2 which use nearly half of the mesh size of AX1 and AX2 were created in order to study the mesh size effect on the fitted nucleation parameters. Figs. 7.38 and 7.39 show the stress triaxility results near the minimum cross section at the nearest integration point to the centre and at the nearest integration point to

the surface as a function of the macroscopic equivalent strain, $2ln(D_0/D_1)$, where D_0 and D_1 are the initial and current diameters at the notch. It should be mentioned that in Figs. 7.38 and 7.39, von Mises yield model was used. It can be seen that in both cases studied the mesh size has a negligible effect on the stress triaxility, especially at the centre. Besides the mesh size effect on stress triaxility, the effect on the fracture behaviour has also been studied, which is shown in Fig. 7.40. It can be observed that the crack initiation in the fine mesh, FAX1, happened just slightly earlier than that in AX1. The only significant effect of the mesh size is the post initiation load diameter-reduction behaviour, which is not very important in the calibration of nucleation parameters. A similar finding has been reported by Batisse et al. [11,62]. In conclusion, the mesh size effect in the notched tension specimens studied is not significant and the finite element meshes used in this study are accurate enough for void nucleation parameter fitting. In other words, stress distribution in the notched specimens is smooth enough so that the effect of mesh size on the void nucleation parameters calibrated may be neglected.

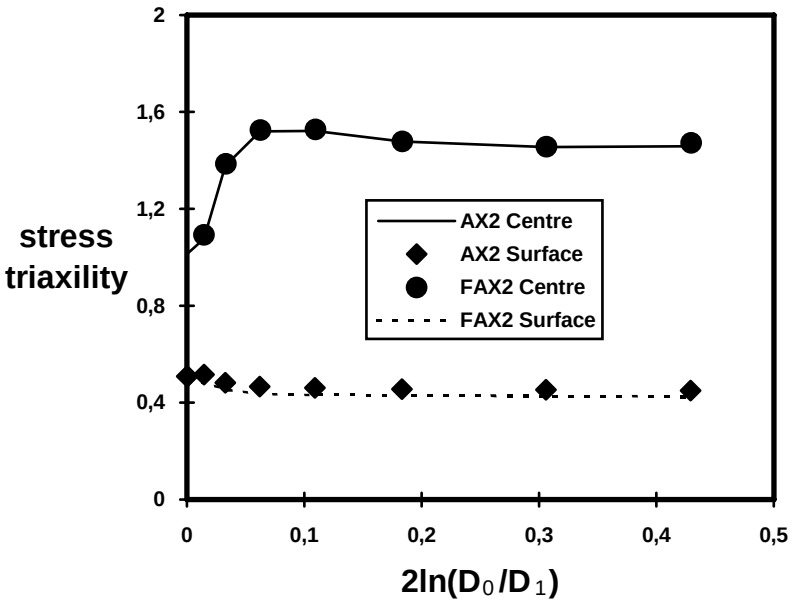

Fig. 7.39 Stress triaxility as a function of the macroscopic equivalent strain for notched specimen 2, where D0 and D1 are the initial and current minimum diameters, von Mises material was used.

2D and 3D failure criteria

It should be mentioned that in this study a 2D plane strain failure criterion has been applied to the analysis of axisymmetric fracture problem. Strictly speaking this is an approximation. The situation is similar to the Gurson model. The original Gurson model was constructed from a 2D plane strain yield field where a cylindrical void was assumed and a 3D yield field which contains a spherical void, where an axisymmetric void is involved. Nevertheless, the Gurson model has been applied to axisymmetric problems. In order to assess the validity of 2D criterion on axisymmetric problems, the 3D criterion in

chapter 6 has been also applied in one case. The results using the 3D criterion are compared with the results using the 2D criterion in Fig. 7.41. The comparison shows that the initiations predicted by 2D and 3D criteria are in very close agreement, with 3D criterion predicting slightly late crack initiation. Thomason [134] has compared the critical void growth strains from his original 2D and 3D ductile fracture criteria. For the same initial void volume fraction, he found that the critical 'limit load' stress by 2D and 3D criteria were quite near each other, even though the intervoid matrix geometries of the 2D and 3D models differ substantially. The actual solution for axisymmetric problems must be near or between the 2D and 3D solution, so the above findings suggest that 2D or 3D criterion may be used for axisymmetric problems as a first approximation.

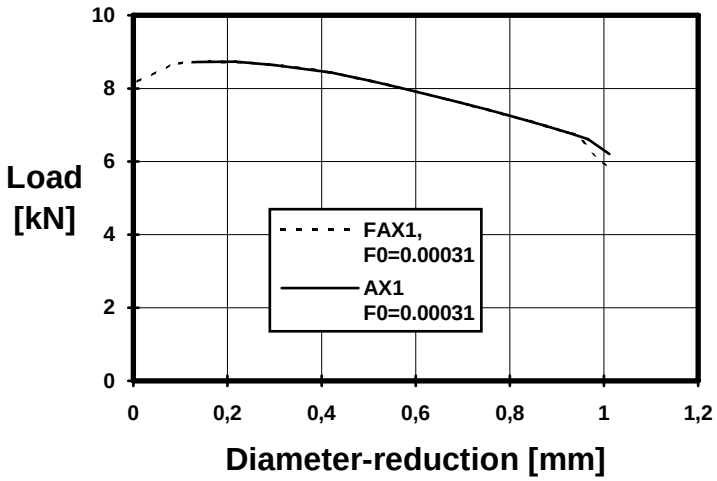

Fig. 7.40 Load-diameter reduction curves of notched specimen 1 with mesh AX1 and FAX1, $A_0 = 0$ $f_N = 0,$ $f_F = 0.125.$

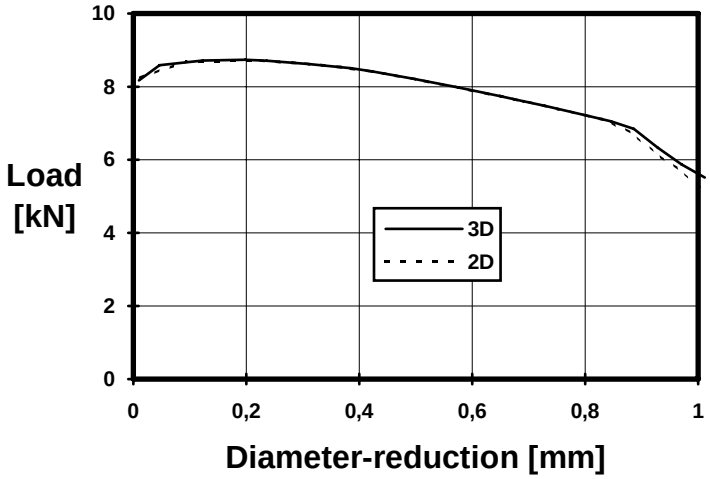

Fig. 7.41 Predictions using 2D and 3D failure criteria, mesh AX1, $A_0 = 0.002,$ $f_N = 0,$ $f_F = 0.125,$ $f_0 = 0.00031.$

2D plane strain FE model and 3D FE model for the T-joint

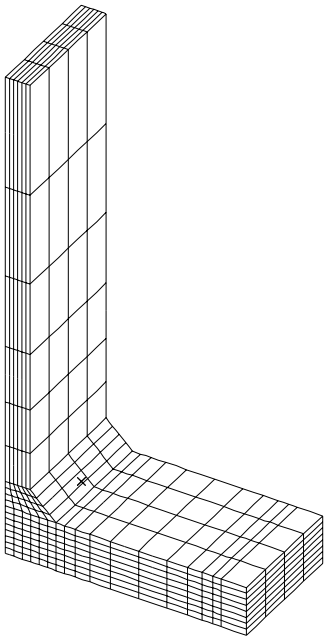

Fig. 7.42 3D FE model (1/4) for the T-joint. Same boundary conditions as 2D plane strain model were used. No HAZ material was considered.

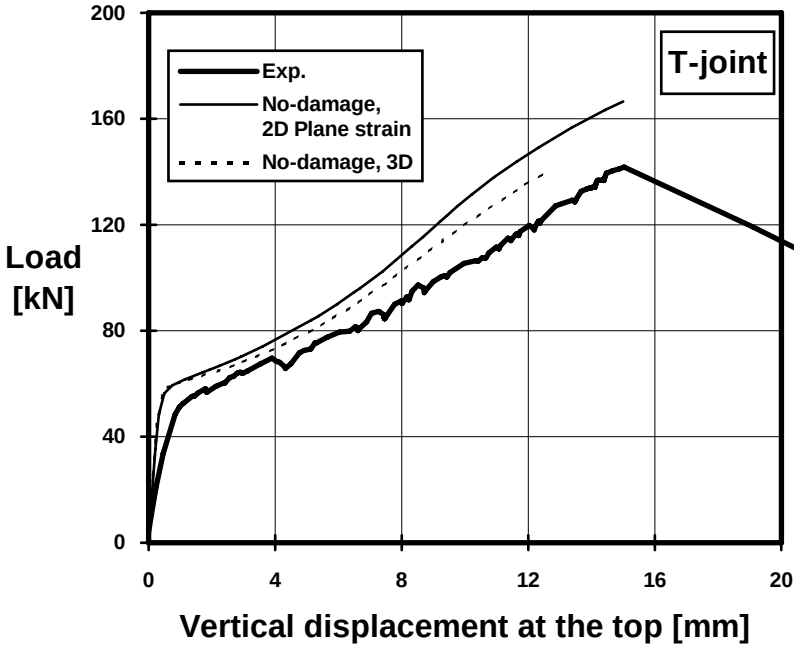

Fig. 4.43 Comparison of 2D plane strain and 3D finite element analysis results. von Mises material was used in both analyses.

Finally, a 3D FE model (1/4 of the joint) shown in Fig. 7.42 for the T-joint with coarse mesh was created and analyzed in order to compare the results of the previous 2D plane strain analysis. In the 3D elastoplastic analysis, no HAZ material has been considered. However, it is expected that the very thin layer of HAZ material has no significant effect on the global behaviour of the T-joint. The comparison is shown in Fig. 7.43. It can be seen that the actual behaviour of the T-joint is not exactly plane strain and if a 3D model is used in the damage analysis, better results than the reported plane strain analysis results can be expected. However, a 3D model is very time consuming, so the damage analysis was not performed in this thesis study.

Summary

In this chapter, the local approach methodology developed in this study has been applied to the simulation of ductile fracture of the welded T-joint. The damage parameters for both base and CGHAZ materials have been fitted from the experimental results of smooth and notched axisymmetric tension specimens by using the local approach methodology. Although the predicted global load-displacement curve of the T-joint is stiffer than the experimental one, partly due to the residual stress and strain which have not been considered in the analyses and partly due to the slipping of the ends of the horizontal plate in the tests, the crack initiation time, location and propagation pattern as well as the ultimate failure load have been predicted very well, compared with experimental results. It has been predicted that there is a considerable stable crack growth in the present welded T-joint before final failure. This prediction is fully in accordance with the observation in experiments, though no quantitative data of crack growth for comparison was available. This study has also revealed the importance and necessity of incorporating the CGHAZ material properties into the welded joint.

Chapter 8

FINAL CONCLUSIONS

Firstly, the main contributions and findings in this investigation are briefly summarized. Then follows a proposal for the possible engineering application of present methodology. Recommendations for future work are presented at the end of the chapter.

8.1 Summary

In this thesis, based on the solutions to two important problems, namely the numerical integration and the failure criterion problems, a practical local approach methodology using the Gurson-Tvergaard material model has been built up in ABAQUS via the user material subroutine UMAT for the analysis of ductile fracture. In this methodology, the ductile fracture mechanisms by void nucleation, growth and coalescence have been taken into account in the material constitutive equation. Unlike the classical fracture mechanics methods where a pre-crack must be assumed, this methodology can be applied to both cracked and non-cracked bodies. Application of this methodology has been made to a welded T-joint. Based on the void nucleation parameters established from the base and the simulated coarse grained heat affected zone (CGHAZ) materials, the fracture behaviour, including the crack initiation time and location, crack propagation direction, stable crack growth as well as the ultimate failure load, have been well predicted, compared with the experimental results.

In general, the original contributions made to ductile fracture can be classified in the following three aspects:

a. The presentation of a class of efficient and accurate numerical integration algorithms for the increasingly popular pressure-dependent and damage-coupled Gurson-Tvergaard model, and a systematic assessment of the accuracy and performance of various numerical algorithms for the first time for the Gurson-Tvergaard model.

b. An assessment of the consistency of three current local failure criteria and the presentation of a new failure criterion for the Gurson-Tvergaard model. The desired advantage of the new failure criterion is that the void nucleation

parameter(s), not the critical void volume fraction, can be numerically fitted from experimental results. This salient feature makes the calibration of the void nucleation parameter(s) possible and physically sound.

c. Application of the local approach methodology based on the above two contributions to a practical problem, the welded T-joint. Examples have shown how the damage parameters in practical application can be obtained in a step-by-step manner and how useful and capable the local approach methodology is in the analysis of fracture behaviour and crack development as well as structural integrity assessment of practical problems.

Besides the general contributions, in this investigation we have the following new findings which are worth mentioning.

Numerical integration

1. Ortiz and Popov [94] have theoretically proved that for a class of generalized mid-point algorithms, the choice of the true mid-point algorithm ($\alpha = 0.5$ in equations (3.22)-(3.25)) leads to optimal accuracy for *small* strain increments. However, we have found that, from both present results (Fig. 3.4-3.6 and Table 4.6 and 4.8) and the results in [40,94], that the true mid-point algorithm is the most accurate one no matter how large the strain increment is, as long as under the condition that the deviatoric strain increment is radial or nearly radial to the yield surface.

2. Compared with the implicit algorithms formulated in this study, the widely used one-step Euler forward algorithm for the Gurson-Tvergaard model has the poorest accuracy. Within the generalized mid-point algorithms, the recommended Euler backward algorithm in any sense is not the most accurate one. On average, for both radial and tangential strain increments, the errors of the one-step Euler forward algorithm are more than 8 times those of the algorithm with α=0.75, and more than 2.5 times those of the Euler backward algorithm (α=1).

3. In ABAQUS, where the Newton iteration method is used and during the increment the reference state is kept fixed to the configuration at the beginning of the increment (see section 4.1), it has been shown that the widely used continuum tangent moduli (section 4.2) associated with the Euler forward algorithm for the Gurson-Tvergaard model will lose the quadratic rate of asymptotic convergence as demonstrated by the consistent tangent moduli associated with the generalized mid-point algorithms. It has also been found that although in general the matrix of consistent tangent moduli is not symmetric, the approximation of consistent tangent moduli by its symmetric part does not significantly affect its convergence behaviour.

4. Based on the approach adopted and experience of this study and the results of reference [71], it may be concluded that for the class of generalized mid-point algorithms, an explicit formula for its consistent tangent moduli can always be found, no matter whether the isotropic hardening rule or mixed-hardening rule is used.

Failure criterion

5. A considerable difference has been found in the prediction of ductility as a function of stress triaxility by the three failure criteria assessed. It has been shown that the original criteria compel each other, i.e., if the critical void volume fraction is a constant, critical void growth is not and vice versa. However, we found that if the calculation of void growth is based on the Gurson-Tvergaard material, rather than the von Mises material, then the predictions of ductility by the first two criteria are very similar. This finding suggests that if the void effect of the Gurson-Tvergaard material is taken into consideration, the critical void growth criterion and critical void volume fraction criterion are identical to a first approximation.

6. It has been shown that the original plastic limit-load or internal necking failure criterion by Thomason gives too large prediction of ductility, which corresponds to unrealistic critical void volume fractions at low stress triaxility. Compared with predictions by the critical void growth criterion and the critical void volume fraction criterion, it was found that Thomason's plastic limit-load model gives very much smaller predictions at high stress triaxility.

7. By the modifications to the original Thomason model proposed in chapter 6, a new failure criterion for the Gurson-Tvergaard model is obtained. It has been shown that there is a large difference between the predictions by the conventional critical void volume fraction criterion and the new failure criterion when the initial void volume fraction is large. However, it was also found that this difference becomes small when the initial void volume fraction decreases. For a very small initial void volume fraction ($f_0 \leq 0.0005$), the predictions by the new failure criterion and the conventional critical void volume fraction are nearly the same (see Fig. 5.11).

8. By verification with the finite element results by Koplik and Needleman [63], it has been shown that the new failure criterion is indeed fairly accurate. Besides the accuracy, a salient feature of the new failure criterion is its role in the damage parameter calibration. In the conventional critical void volume fraction criterion where no physical mechanism for void coalescence is available, the critical void volume fraction is closely related to the void nucleation parameter assumed (see section 6.1). However, in the new failure criterion, a mechanism for void coalescence is incorporated in the constitutive model. Hence, the material failure is a natural result of the development of macroscopic plastic flow and the microscopic internal necking mechanism.

So, in this regard, the initial material status (mainly the initial void volume fraction) and the intermediate parameters (void nucleation) uniquely determine the material failure. In normal practice, the initial void volume fraction can usually be selected beforehand, which means the only unknown left is the void nucleation parameter(s). In other words, if the void nucleation model (distribution) is known or can be selected, the key void nucleation parameter(s) (value) can be numerically calibrated from the experiment. This feature is desirable and helps to make the practical application of the Gurson-Tvergaard based approach possible and physically sound for quantitative prediction.

Before ending this sub-section, it should be cautioned that, in fully understanding the above findings, one should be aware that material failure by void nucleation, growth and coalescence is an extremely complicated process; very limited knowledge is available on the mechanism and numerical modelling of void nucleation; both the Gurson-Tvergaard model and the Thomason plastic limit-load model are approximate and idealized to a certain extent and some further assumptions have been introduced in the present formulation of the new failure criterion. However, it is believed that the new failure criterion does provide one good solution to the problem involved and application described in chapter 7 has proved its effectiveness and usefulness.

Application of the present methodology

9. It was found that the modelling of secondary particles or small carbides is necessary and very important in the fracture analysis of present steel Fe510. The continuous void nucleation model and the model by Chu and Needleman [25] were then studied. It was interesting to find that, despite the very different distribution of the void nucleation intensity of the two models, the simple continuous model is as effective as the Chu and Needleman model [25], at least in the cases studied.

10. CGHAZ material plays a decisive role in the fracture of welded joints and it is very important to study the behaviour of CGHAZ material and incorporate it into the analysis of a welded joint.

11. The present methodology can well predict the fracture behaviour of the welded T-joint tested, including crack formation and propagation and stable development. The effectiveness and usefulness of present methodology in the assessment of structural integrity are thus obvious.

8.2 A proposal for possible engineering application of the present methodology

A step by step procedure proposed for possible application of the present methodology to practical problems can be summarized as follows.

- Determine the material constants, the Young's modulus, Poisson ratio, Bridgman corrected true stress-strain relation and the initial void volume fraction for each material, for example, the base material and heat affected zone (HAZ) material. Be aware that the Bridgman corrected true stress-strain relation is essential in the ductile fracture where large deformation is often associated.

- Select the void nucleation model. The simplest model available perhaps is the continuous void nucleation model, which as a first approximation, could be tried first. If necessary, the statistical model by Chu and Needleman (equation 2.5) or other models, for example, stress-controlled models can be used.

- Calibrate the key void nucleation parameter (value) from smooth and notched axisymmetric tension specimens. In order to vary the stress triaxility, normally two or more notched specimens are needed in the parameter calibration. Make sure that the finite element mesh is fine enough for the calibration.

- Apply the calibrated parameters to the analysis of practical problems. In a complicated problem, a preliminary run may be necessary to locate the most stressed region where crack initiation is suspected. Construct a fine mesh on the crack initiation region (it is preferred that the mesh is as fine as those used in the parameter calibration) and run the analysis. The methodology will automatically perform the damage analysis.

- According to the definition of a numerical crack, the crack initiation location and time can be determined and crack development results can be obtained.

8.3 Future work

Listed below are some possible directions in which the present research work can be extended:

- Application of present methodology to study the real fracture in full size joints, including the effect of material, geometry and temperature on the crack initiation load and ultimate failure load as well as fracture pattern of the joint under tension or bending loading. How to incorporate effectively the local failure analysis to the global structural analysis is perhaps an important

problem to be solved. At present, the Gurson-Tvergaard is overwhelmingly used in 2D, axisymmetric and 3D solid element analysis. From the point of view of engineering, study on how to incorporate the Gurson-Tvergaard model into plate element analysis is meaningful. Very recently, Shi and Voyiadjis [115] has presented a computational model to incorporate the ductile plastic damage model by Lemaitre [73] to the plate bending.

- Considering the importance of the Gurson-Tvergaard model and its non-trivial nature, it might be beneficial to conduct a further study to compare the behaviours of numerical algorithms for the Gurson-Tvergaard model, including the cutting plane algorithm [95] which has been installed into NIKE2D program [31] and the Runge-Kutta algorithm installed into ABAQUS by Dr. Klingbeil [62]. Such study could provide a very helpful guideline to the Gurson-Tvergaard model community.

- The limitations of the plastic limit-load failure model, especially the strain-hardening effect on the validity of the new failure criterion, as suggested by Prof. A Needleman [85], need further verification and clarification.

- Investigation in this thesis is mainly concentrated on non-pre-cracked body where results have shown that the effect of length scale [88,128] is not very serious. When application of the Gurson-Tvergaard model is made to physically pre-cracked body where the variation of the stress-strain field at the crack tip is very large, the length scale effect is expected to be strong [128]. So, in this case, how to incorporate the length scale in a suitable way needs further research effort.

- The relation between the local approach and classical fracture mechanics methods is certainly worth study. Local approach emerged as a remedy to the classical approaches, however, as Prof. F. M. Burdekin once said to the author, it should finally come back to the classical approaches with one or more extra parameters. Applying the present methodology to the study of geometry and constraint effect on ductile fracture could be fruitful.

Bibliography

1. ABAQUS User & Theory Manuals (1992). Hibbitt, Karlsson & Sorensen, Version 5.1.

2. Anderson T. L. (1989) Crack tip parameters for large scale yielding and low constrain configurations. *Int. J. Fract.* **41**, 79-104.

3. Aravas N. (1987) On the numerical integration of a class of pressure-dependent plasticity models. *Int. J. Numer. Meth. Engng.* **24**, 1395-1416.

4. Arif A. F. M. (1991) Computational Aspects of an Implicit Finite Element Procedure for Elasto-Viscoplastic Large Deformation Problems. Ph.D thesis, University of Minnesota, U.S.A.

5. Arif A. F. M. & Zabaras N. (1992) On the performance of two tangent operators for the finite element analysis of large deformation inelastic problems. *Int. J. Numer. Meth. Engng.* **35**, 369-389.

6. Atluri S. N & Nishioka T. On some recent advances in computational methods in the mechanics of fracture. Proceedings of the 7th Int. conference on Fracture (ICF7), Houston, Texas, 20-24 March, 1989. Ed. K. Salama, K. Ravi-Chandar, D. M. R. Taplin, P. Rama Rao, pp. 1923-1969.

7. Bakker A. (1990) Influence of material flow curve modelling on fracture. Proceedings of the 5th Int. Conference on Numerical Methods in Fracture Mechanics, April, 1990. Ed. A. R. Luxmoore & D. R. J. Owen, Pineridge Press, 433-449.

8. Bains R. (1992) Boundary Element Analysis of 3-D Crack Problems: Weight Function Techniques. Ph.D disseration, Wessez Institute of Technology, U.K.

9. Bains R., Aliabadi M. H. & Rooke D. P. (1992) Fracture mechanics weight functions in three dimension: subtraction of fundamental fields. *Int. J. Numer. Meth. Engng.* **35**, 179-202.

10. Bains R., Aliabadi M. H. & Rooke D. P. (1993) Weight functions for curved crack fronts using BEM. *J. Strain Analysis.* **28**, 67-78.

11. Batisse R., Bethmont M., Devesa G. & Rousslier G. (1987) Ductile fracture of A508 CL3 steel in relation with inclusion content: The benefit of the local approach of fracture and continuum damage mechanics. *Nucl. Engng. Design* **105,** 113-120.

12. Becker R., Needleman A., Richmond O. & Tvergaard V. (1988) Void growth and failure in notched bars. *J. Mech. Phys. Solids* **36**, 317-351.

13. Belie R. G. & Reddy J. N. (1980) Direct prediction of fracture for two-dimensional plane stress structures. *Comp. Struct*. **11**, 49-53.

14. Bilby B. A., Howard I. C. & Li Z. H. (1992) Predicition of the first spinning cylinder test using ductile damage theory. *Fatigue Fract. Engng. Mater. Struct*. **16**, 1-20.

15. Billardon R. & Moret-Bailly (1987) Fully coupled strain and damage finite element analysis of ductile fracture. *Nucl. Engng. Design* **105**, 43-49.

16. Braudel H. J., Abouaf M. & Chenot J. L. (1986) An implicit and incremental formulation for the solution of elastoplastic problems by the finite element method. *Comp. Struct*. **22**, 801-814.

17. Bueckner H. F. (1970) A novel principal for the computation of stress intensity factors. *ZAMM*, **50**, 529-546.

18. Bueckner H. F. (1987) Weight functions and fundamental fields for the penny-shaped and the half-plane crack in three-space. *Int. J. Solids Struct.* **23**, 57-93.

19. Burdekin F. M., Saket H. K., Thurlbeck S.D. & Frodin J. G. (1991) Aspects of assessment of defects in welded joints and related reliability analysis treatments. Defect Assessment in Components-Fundamentals and Applications, ESIS/EGF9, Ed. by J. G. Blauel and K.-H. Schwalbe, Mechanical Engineering Publications, London, 1051-1071.

20. Chen W. F. & Han D. J. (1988) Plasticity for Structural Engineering, Springer Verlag, New York.

21. Chow C. L. & Lu T. J. (1992) A comparative study of continuum damage models for crack propagation under gross yielding. *Int. J. Fracture.* **53**, R43-75.

22. Chow C. L. & Wang J. (1987) An anisotropic theory of continuum damage mechanics for ductile fracture. *Engng. Fract. Mec*h. **27**, 547-558.

23. Chow C. L. & Wang J. (1988) A finite element analysis of continuum damage mechanics. *Int. J. Fract* **38**, 83-108.

24. Chow C. L. & Wang J. (1991) A continuum damage mechanics model for crack initiation in mixed mode ductile fracture. *Int. J. Fract.* **47**, 145-160.6

25. Chu C. C. & Needleman A. (1980) Void nucleation effects in biaxially stretched sheets. *J. Engng. Mater. Tech.* **102**, 249-256.

26. Cofer W. F. (1992) Washington State Unversity. Private communication, July.

27. Cofer W. F. & Jubran J. S. (1992) Analysis of welded tubular connections using continuum damage mechanics. *J. Struct. Engng*. ASCE **118**, 828-845.

28. Delmotte J. ; Roelandt J. M. and Abisror A. (1990) A numerical analysis to assess ductile tearing in thin plates using local approach-application to R curve simulation. Proceedings of the 5th Int. Conference on Numerical Methods in Fracture Mechanics, April, 1990. Ed. A. R. Luxmoore & D. R. J. Owen, Pineridge, press. 631-643.

29. Denys R. M. & Dhooge A. (1988) Mechanical tensile properties of weld simulated HAZ microstructures in normalized, quenched-tempered and TMCP low carbon mangnese steels. Presented at the Seventh Int. Conference on Offshore Mechanics and Arctic Engineering, Houston, Texas - February 7-12, 1988.

30. Du Z.-Z. & Hancock J. W. (1989) Stress intensity factors of semi-elliptical cracks in a tubular welded joint using line springs and 3d finite elements. *J. Press. Vessel Tech*. ASME **111**, 247-251.

31. Engelmann B. E. & Whirley R. G. (1992) Recent development in NIKE2D for metalforming analysis and low rate impact. *Nucl. Engng. Design* **138**, 23-35.

32. Finch D. M. (1992) Effects of welding residual stresses on significance of effects in various types of welded joint --II. *Engng. Fract. Mech.* V **42**, 479-500

33. Finch D. M. & Burdekin F. M. (1992) Effects of welding residual stresses on significance of effects in various types of welded joint. *Engng. Fract. Mech.* **41**, 721-735

34. Finch D. M & Burdekin F. M (1992) Finite element validation studies of the revised PD6493/CEGB R6. Part 1-failure assessment methodologies applied to welded flat plates and pipe/plates joints. *Int. J. Press. Vessels Pipings* **49**, 187-211.

35. Finch D. M & Burdekin F. M (1992) Finite Element Validation Studies of the Revised PD6493/CEGB R6. Part 2-Failure Assessment Methodologies Applied to Welded Tubular Joints. *Int. J. Press. Vessels Pipings* **49**, 213-229.

36. Francois D. (1993) A review of methods for fitness for purpose evaluation of defected parts in the field of extended plasticity. *Welding in the world*, **32**, 197-206.

37. Franklin A. G. (1969) Comparison between a quantitative microscopic and chemical methods for assessment on non-metallic inclusions. *J. Iron and Steel Inst*. **207**, 181-186.

38. Ghassemieh M., Ali M. S. & Kukreti A. R. (1992) Procedure to predict ultimate fracture failure history for plane stress plasticity problems. *Engng. Fract. Mech.* **41**, 919-933.

39. Goan J. M., Sutton M. A. & Chao Y. J. (1990) A study of J-controlled crack tip deformation fields. *Int. J. Fract.* **45**, R17-R22.

40. Gratacos P., Montmitonnet P. & Chenot J. L. (1992) An integration scheme for Prandtl-Reuss elastoplastic constutive equations. *Int. J. Numer. Meth. Engng.* **33**, 943-961.

41. Gueninnouni T. & Francois D. (1987) Constitutive equations for rigid plastic or viscoplastic materials containing voids. *Fatigue Fract. Engng. Mater. Struct.* **10**, 399-418.

42. Gurland J. (1972) Observations on the fracture of cementite particles in a spheroidized 1.05C steel deformed at room temperature. *Acta Metall.* **20,** 735-741.

43. Gurson A. L. (1975) Plastic Flow and Fracture Behaviour of Ductile Materials Incorporating Void Nucleation,Growth and Interaction. Ph.D Disseration, Brown University.

44. Gurson A. L. (1977) Continuum theory of ductile rupture by void nucleation and growth: part I-yield criteria and flow rules for porous ductile media. *J. Engng. Mater. Tech.* **January**, 2-15.

45. Haswell J. (1991) Simple models for predicting stress intensity factors for tubular joints. *Fatigue Fract. Engng. Mater. Struct.* **14**, 499-513.

46. Haswell J. & Hopkins P. (1991) A review of fracture mechanics models of tubular joints. *Fatigue Fract. Engng. Mater. Struct.* **14**, 483-497.

47. Heinstein M. W. & Yang H. T. Y. (1992) Plane strain finite element simulation of shear band formation during metal forming. *Int. J. Numer. Meth. Engng.* **33**, 719-737.

48. Hill R. (1971) The Mathematical Theory of Plasticity. Oxford Press.

49. Hom C. L. & McMeeking R. M. (1989) Void growth in elastic-plastic materials. *J. Appl. Mech.* **56**, 309-317.

50. Hom C. L. & McMeeking R. M. (1989) Three-dimensional void growth before a blunting crack tip. *J. Mech. Phys. Solids* **37**, 395-415.

51. Hu J. M. (1989) Analysis of Ductile Crack Extension in Plastic Fracture. Ph.D thesis, University of Maryland.

52. Hutchinson J. W. (1968) Singular behaviour at the end of a tensile crack in a hardening material. *J. Mech. Phys. Solids* **16** 13-31.

53. Hutchinson J. (1987) Micro-Mechanics of Damage in Deformation and Fracture. The Technical University of Denmark.

54. Jha M. & Narasimhan R. (1992) A finite element analysis of dynamic fracture initiation by ductile failure mechanisms in a 4340 steel. *Int. J. Fract.* **56**, 209-231.

55. Jubran J. S. & Cofer W. F.(1991) Ultimate strength analysis of structural components using the continuum damage mechanics approach. *Comp. Struct.* **39**, 741-752.

56. Kachanov L. M. (1986) Introduction to Continuum Damage Mechanics, Kluwer Academic Publishers, Printed in the Netherlands

57. Kanninen M. F. & Popelar C. H. (1985) Advanced Fracture Mechanics. Oxford University Press, New York.

58. Khan A. S. & Yuan S. (1989) A three-dimensional finite element program for prediction of crack initiation and growth. *Comp. Struct.* **31**, 439-444.

59. Kim D. S.(1989) Analysis of Fatigue Crack Propagation Behaviour of a Surface Crack of Fillet Toe of Tubular Joints. Ph.D Disseration, Ohio State University.

60. Kleiber M. (1984) Numerical study of necking-type bifurcations in void-containing elastic-plastic material. *Int. J. Solids Struct.* **20**, 191-210.

61. Kleiber M. (1986) On plastic localization and failure in plane strain and round void containing tensile bars. *Int. J. Plasticity* **2**, 205-221.

62. Klingbeil D., Kunecke G., Schicker J. (1993) On the application of Gurson's model to various fracture mechanics specimens. Lecture notes on the course, Modern Approaches to Fracture, Sophia Antipolis, France.

63. Koplik J. & Needleman A. (1988) Void growth and coalescence in porous plastic solids. *Int. J. Solids Struct.* **24**, 835-853.

64. Kordish H. and Sommer E. (1988) Three-dimensional effects affecting the precision of lifetime predictions. Fracture Mechanics: Nineteenth Symposium, ASTM STP 969, Ed. T. A. Cruse, American Society for Testing and Materials, Philadelphia, 73-87.

65. Krieg R. D. & Krieg B. D. (1977) Accuracies of numerical solution methods for the elastic-perfectly plastic model. *J. Press. Vessels Tech*. **99**, 510-515.

66. Kukreti A. R., Khan A. S. & Kumar A. (1989) A three-dimensional finite element program to predict ultimate fracture failure load. *Comp. Struct.* **32**, 1325-1345.

67. Kukreti A. R. & Shammaa A. H. (1990) Fracture failure prediction using a moving finite element mesh refinement scheme. *Comp. Struct.* **35**, 23-40.

68. Le Roy G., Embury J. D., Edward G. & Ashby M. F. (1981) A model of ductile fracture based on the nucleation and growth of voids. *Acta Metall.* **29,** 1509-1522.

69. Lee H., Peng K. & Wang J. (1985) An anisotropic damage criterion for deformation instability and its application to forming limit analysis of metal plates. *Engng. Fract. Mech.* **21**, 1031-1054.

70. Lee J. H. (1988) Accuracies of numerical solution methods for the pressure-modified von Mises model. *Int. J. Numer. Meth. Engng.* **26**, 453-465.

71. Lee J. H. & Zhang Y. (1991) On the numerical integration of a class of pressure-dependent plasticity models with mixed hardening. *Int. J. Numer. Meth. Engng.* 32, 419-438.

72. Lemaitre J. (1984) How to use damage mechanics. *Nucl. Engng. Design* **84**, 233-245.

73. Lemaitre J. (1985) A continuous damage mechanics model for ductile fracture. *J. Engng. Mater. Tech.* **107**, 83-89.

74. Lemaitre J. (1990) Micro-Mechanics of Crack Initiation. *Int. J.Fract*. **42**, 87-99.

75. Mackenzie A. C., Hancock J. W. & Brown D. K. (1977) On the influence of state of stress on ductile failure initiation in high strength steels. *Engng. Fract. Mech.* **9**, 167-188.

76. McClintock F. A. (1968) A criterion for ductile fracture by the growth of holes. *J. Appl. Mech.* **35**, 363-371.

77. Mear M. E. (1990) On the plastic yielding of porous metals. Mechanics of Materials **9**, 33-48.

78. Mear M. E. & Hutchison J. W. (1985) Influence of yield surface curvature on flow localization in dilatant plasticity. *Mech. Mater.* **4**, 395-407.

79. Mudry F. (1993) Classical Approach. Lecture notes on the course, Modern Approaches to Fracture, Sophia Antipolis, France.

80. Murakami S. (1988) Mechanical modelling of material damage. *J. Appl. Mech*. **55**, 280-286.

81. Nagaki S., Sowerby R. & Goya M. (1991) An anisotropic yield function for porous metal. *Mater. Sci. Engng.* **A142**, 163-168.

82. Nagtegaal J. C. & De Jong J. E. (1981) Some computational aspects of elastic-plastic large strain analysis. *Int. J. Numer. Meth. Engng.* **17**, 15-41.

83. Narasimhan R., Rosakis A. J. & Moran B. (1992) A three-dimensional numerical investigation of fracture initiation by ductile mechanism in a 4340 steel. *Int. J. Fract.* **56**, 1-24.

84. Needleman A. (1990) Numerical studies of ductile fracture processes. Proceedings of the 5th Int. Conference on Numerical Methods in fracture mechanics, April, 1990. Ed. A. R. Luxmoore & D. R. J. Owen, Pineridge, press. 259-274.

85. Needleman (1993) private communication.

86. Needleman A. & Rice J. R. (1978) Limits to ductility set by plastic flow localization, in Koistinen D. P. & Wang N. M. (eds), Mechanics of Sheet Metal Forming, Plenum, New York, p.237.

87. Needleman A. & Tvergaard V. (1987) An analysis of ductile rupture modes at a crack tip. *J. Mech. Phys. Solids* **35**, 151-183.

88. Needleman A. & Tvergaard V. (1992) Analysis of plastic flow localization in metals. *Appl. Mech. Rev.* **45**, s3-s18.

89. Nemat-Nasser S. (1992) Phenomenological theories of elastoplasticity and strain localization at high strain rates. *Appl. Mech. Rev.* **45**, s18-s45.

90. Niemi E. (1992) Lappeenranta University of Technology. Private communication, January.

91. Nykänen T. (1993) M_k-Factor Equations and Crack Growth Simulations for Fatigue of Fillet-Welded T-joints. Ph.D disseration, Lappeenranta University, Finland.

92. Nyssen C. (1981) An efficient and accurate iterative method, allowing large incremental steps, to solve elasto-plastic problems. *Comp. Struct*. **13**, 63-71

93. Ortiz M. & Martin J. B.(1989) Symmetry-preserving return mapping algorithms and incrementally external paths: a unification of concepts *Int. J. Numer. Meth. Engng*. **28**, 1839-1853.

94. Ortiz M. & Popov E. P. (1985) Accuracy and stability of integration algorithms for elastoplastic constutive relations. *Int. J. Numer. Meth. Engng.* **21**, 1561-1576.

95. Ortiz M. & Simo J. C. (1986) An analysis of a new class of integration algorithm for elastoplastic constutive relations. *Int. J. Numer. Meth. Engng.* **23**, 353-366.

96. Owen D. R. J. & Hinton E. (1986) Finite Element in Plasticity: Theory and Practice. Pineridge Press, Swansea, U. K.

97. Peirce D., Shih C. F. & Needleman A. (1984) A tangent modulus method for rate dependent solids. *Comp. Struct.* **18**, 875-887.

98. Perrin J. D. & Leblond J. B. (1990) Analytical study of a hollow sphere made of platic porous material and subject to hydrostatic tension-application to some problems in ductile fracture of metals. *Int. J. of Plasticity* **6**, 677-679.

99. Qiu Y. P. & Weng G. J. (1992) A Theory of plasticity for porous materials and particle-reinforced composites. *J. of Appl. Mech.* **59**, 261-268.

100. Reddy B. D. & Martin J. B. (1991) Algorithms for the solution of internal variable problems in plasticity. *Comp. Meth. Appl. Mech. Engng.* **93**, 253-273.

101. Rencontre L. J., Caddemi S. & Martin J. B. (1992) The relationship between the generalised mid-point and trapezoidal rules in incremental elasto-plasticity. *Comp. Meth. Appl. Mech. Engng.* **96**, 201-212.

102. Rhee H. C. (1989) Fatigue crack growth analysis of offshore structural tubular joints. *Engng. Fract. Mech.* **34**, 1231-1239.

103. Rhee H. C. and Salama M. M. (1988) Mixed-mode stress-intensity factor solutions for offshore structural tubular joints. Fracture Mechanics: Nineteenth Symposium, ASTM STP 969, Ed. T. A. Cruse, American Society for Testing and Materials, Philadelphia, 1988, 669-676.

104. Rice J. R. (1968) A path independent integral and the approximate analysis of strain concentrations by notches and cracks. *J. Appl. Mech.* 1968, **35**, 379-386.

105. Rice J. R. & Rosengren G. F. (1968) Plane strain deformation near a crack tip in a power-law hardening material. *J. Mech. Phys. Solids* **16** 1-12.

106. Rice J. R. & Tracey D. M. (1969) On the ductile enlargement of voids in triaxial stress fields. *J. Mech. Phys. Solids* **17**, 201-207.

107. Richelsen A. B. & Tvergaard V. (1993) Dilatant plasticity or upper bound estimates for porous ductile solids. Depart of Solid Mechanics, The Technical University of Denmark.

108. Riedel H. (1992) Fracture Mechanics, *FhG/IWM* publication W 3/92.

109. Rousselier G. (1987) Ductile fracture models and their potential in local approach of fracture. *Nucl. Engng. Design* **105,** 97-111.

110. Roy S., Dexter R. J. & Fossum A. F. (1993) A computational procedure for the simulation of ductile fracture with large plastic deformation. *Engng. Fract. Mech.* **45**, 277-293.

111. Saje M., Pan J. & Needleman A. (1982) Void nucleation effects on shear localization in porous plastic solids. *Int. J.Fract*. **19**, 163-182.

112. Schreyer H. L., Kulak R. L. & Kramer J. M. (1979) Accurate numerical solutions for elastic-plastic models *J. Press. Vessels Tech*. **101**, 226-234.

113. Sham T. L. (1987) A united finite element method for determining weight functions in two and three dimensions. *Int. J. Solids Struct.* **23**, 1357-1372.

114. Sham T. L. & Zhou Y. (1989) Computation of three-dimensional weight functions for circular and elliptical cracks. *Int. J. Fract.* **41**, 51-75.

115. Shi G. & Voyiadjis G. Z. (1993) A computational model for FE ductile plastic damage analysis of plate bending. *J. of applied Mechanics* **60**, 749-758.

116. Shi Y. W.; Barnby J. T. and Nadkarni A. S.(1991) Void growth at ductile crack initiation of a structural steel. *Engng. Fract. Mech.* **39**, 37-44.

117. Shima S. & Oyane M. (1976) Plasticity theory for porous metals. *Int. J. Mech. Sci.* **18**, 285-291.

118. Simo J. C. (1992) Algorithms for static and dynamic multiplicative plasticity that preserve the classical return mapping schemes of the infinitesimal theory. *Comp. Meth. Appl. Mech. Engng.* **99**, 61-112.

119. Simo J. C. & Govindjee S. (1991) Non-linear b-stability and symmetry preserving return mapping algorithms for plasticity and viscoplascity. *Int. J. Numer. Meth. Engng.* **31**, 151-176.

120. Simo J. C. & Ortiz M. (1985) A unified approach to finite deformation elastoplastic analysis based on the use of hyperelastic constutive equations. *Comp. Meth. Appl. Mech. Engng.* **49**, 221-245.

121. Simo J. C. & Taylor R. L. (1985) Consistent tangent operators for rate-independent elastoplasticity. *Comp. Meth. Appl. Mech. Engng.* **48**, 101-118.

122. Simo J. C. & Taylor R. L. (1986) A return mapping algorithm for plane stress elastoplasticity. *Int. J. Numer. Meth. Engng.* **22**, 649-670.

123. Soininen R., Niemi E. & Zhang Z. L. Studies of the fracture behaviour of RHS K-joints at low temperatures, to be published.

124. *Steenkamp P. S. (1986) Investigation into the validity of J-Based methods for the prediction of ductile tearing and Fracture. Ph.D thesis, Delft University of Technology, Delft, The Netherlands,.

125. Sun D.-Z. (1993) *FhG/IWM*. Private communication, September.

126. Sun D.-Z., Kienzler R., Voss B. & Schmitt W. (1990) Application of micro-mechanical models to the prediction of ductile fracture. Presented in the 22nd national Symposium on Fracture Mechanics, Atlanta, Georgia, USA, June 26-28, 1990.

127. Sun D. Z.; Siegele D.; Voss B. and Schmitt W. (1989) Application of local damage models to the numerical analysis of ductile rupture. *Fatigue Fract. Engng. Mater. Struct*. **12**, 210-212.

128. Sun D.-Z., Voss B. & Schmitt W. (1989) Numerical prediction of ductile fracture resistance behaviour based on micromechanical models. Proceedings of Europe Symposium on Elastic-Plastic Fracture Mechanics, Freiburg, FRG, Oct., 1989.

129. Sun J. (1991) Effect of stress triaxiality on micro-mechanisms of void coalesence and micro-fracture ductility of materials. *Engng. Fract. Mech.* **39**, 799-805.

130. *Sun Y. (1989) The microscopic constitutive theory of ductility damaged metals and its application to instability and fracture analysis. Ph.D thesis, Harbin Institute of Technology, China.

131. Thomason P. F. (1981) Ductile fracture and the stability of incompressible plasticity in the presence of microvoids. *Acta Metall.* **29**, 763-777.

132. Thomason P. F. (1985) Three-dimensional models for the plastic limit-loads at incipient failure of the intervoid matrix in ductile porous solids. *Acta Metall.* **33**, 1079-1085.

133. Thomason P. F. (1985) A three-dimentional model for ductile fracture by the growth and coalescence of microvoids. *Acta Metall.* **33**, 1087-1095.

134. Thomason P. F. (1990) Ductile Fracture of Metals. Pergamon Press, U.K.

135. Thomson R. D. & Hancock J. W. (1984) Ductile failure and void nucleation, growth and coalescence. *Int. J. Fract.* **26**, 99-112.

136. Tvergaard V. (1981) Influence of voids on shear band instabilities under plane strain conditions. *Int. J. Fract.* **17**, 389-407.

137. Tvergaard V. (1982) On localization in ductile materials containing spherical voids. *Int. J. Fract.* **18**, 237-252.

138. Tvergaard V. (1987) Effect of yield surface curvature and void nucleation on plastic flow localization. *J. Mech. Phys. Solids* **35**, 43-60.

139. Tvergaard V. (1990) Material failure by void growth to coalescence. *Advances in Applied Mechanics*. eds. J. W. Hutchinson & T. Y. Wu, 83-151, Academic Press.

140. Tvergaard V. & Needleman A. (1984) Analysis of the cup-cone fracture in a round tensile bar. *Acta Metall*. **32**,157-169.

141. Voyiadjis G. Z. & Kattan P. I. (1992) Finite element plasticity and damage in constitutive modelling of metals with spin tensors. *Appl. Mech. Rev*. **45**, S95-S109.

142. Wang T.-J (1991) A continuum damage model for ductile fracture of weld heat affected zone. *Engng. Fract. Mech.* **40**, 1075-1082.

143. Wang T.-J (1993) Micro and Macroscopic damage and fracture behaviour of welding coarse grained heat affected zone of a low alloy steel: Mechanisms and modelling. *Engng. Fract. Mech.* **45**, 799-812.

144. Worswick M. J. & Pick R. J. (1991) Void growth in plastically deformed free-cutting brass. *J. Appl. Mech.* **58**, 631-638.

145. Yamada K. & Agerskov H. (1990) Fatigue Life Prediction of Welded Joints Using Fracture Mechanics. The Technical University of Denmark.

146. Yamamoto H. (1978) Conditions for shear localization in the ductile fracture of void-containing materials. *Int. J. of Fracture* **14**, 347-465.

147. Yan X. Q. (1992) Effect of yield surface curvature on local necking in biaxially stretched sheets in porous materials. *J. Engng. Mater. Tech.* **114,** 196-200.

148. Yoder P. J. & Whirley R. G. (1984) On the numerical implementation of elastoplastic models. *J. Appl. Mech.* **51**, 283-288.

149. Zhang Z. L. & Mikkola T. P. J. (1992) A simple path-independent integral for calculating mixed-model stress intensity factors. *Fatigue Fract. Engng. Mater. Struct.* **15**, 1041-1049.

150. Zheng M.; Luo Z. J. and Zheng X. (1992) A new damage model for ductile materials. *Engng. Fract. Mech*. **41**, 103-110.

* References were not directly available to the author.

APPENDIX A

Coefficients in equation (3.45)

Treating $\Delta\varepsilon_p$ and $\Delta\varepsilon_q$ as the two indenpendent unknowns and all other variables as a function of $\Delta\varepsilon_p$ and $\Delta\varepsilon_q$, and using Newton's method to solve (3.40) and (3.41), we obtain the following coefficients in (3.45):

$$A_{11} = P + \alpha\Delta\varepsilon_p\left[\frac{\partial P}{\partial p_{n+\alpha}}\frac{\partial p_{n+1}}{\partial\Delta\varepsilon_p} + \frac{\partial P}{\partial \mathbf{H}_{n+\alpha}} : \frac{\partial \mathbf{H}_{n+1}}{\partial\Delta\varepsilon_p}\right] + \alpha\Delta\varepsilon_q\left[\frac{\partial Q}{\partial p_{n+\alpha}}\frac{\partial p_{n+1}}{\partial\Delta\varepsilon_p} + \frac{\partial Q}{\partial \mathbf{H}_{n+\alpha}} : \frac{\partial \mathbf{H}_{n+1}}{\partial\Delta\varepsilon_p}\right]$$

$$A_{12} = Q + \alpha\Delta\varepsilon_p\left[\frac{\partial P}{\partial q_{n+\alpha}}\frac{3}{2}\frac{\mathbf{S}_{n+\alpha}}{q_{n+\alpha}} : \frac{\partial \mathbf{S}_{n+1}}{\partial\Delta\varepsilon_q} + \frac{\partial P}{\partial \mathbf{H}_{n+\alpha}} : \frac{\partial \mathbf{H}_{n+1}}{\partial\Delta\varepsilon_q}\right] + \alpha\Delta\varepsilon_q\left[\frac{\partial Q}{\partial q_{n+\alpha}}\frac{3}{2}\frac{\mathbf{S}_{n+\alpha}}{q_{n+\alpha}} : \frac{\partial \mathbf{S}_{n+1}}{\partial\Delta\varepsilon_q} + \frac{\partial Q}{\partial \mathbf{H}_{n+\alpha}} : \frac{\partial \mathbf{H}_{n+1}}{\partial\Delta\varepsilon_q}\right]$$

$$A_{21} = \frac{\partial\phi_{n+1}}{\partial p_{n+1}}\frac{\partial p_{n+1}}{\partial\Delta\varepsilon_p} + \frac{\partial\phi_{n+1}}{\partial \mathbf{H}_{n+1}} : \frac{\partial \mathbf{H}_{n+1}}{\partial\Delta\varepsilon_p}$$

$$A_{22} = \frac{\partial\phi_{n+1}}{\partial q_{n+1}}\frac{\partial q_{n+1}}{\partial\Delta\varepsilon_q} + \frac{\partial\phi_{n+1}}{\partial \mathbf{H}_{n+1}} : \frac{\partial \mathbf{H}_{n+1}}{\partial\Delta\varepsilon_q}$$

$$b_1 = -\Delta\varepsilon_p P - \Delta\varepsilon_q Q$$

$$b_2 = -\phi_{n+1}$$

where we have

$$\frac{\partial H^i_{n+1}}{\partial\Delta\varepsilon_p} = w_{ij}\left(\frac{\partial h^j_{n+\alpha}}{\partial\Delta\varepsilon_p} + \frac{\partial h^j_{n+\alpha}}{\partial p_{n+\alpha}}\frac{\partial p_{n+\alpha}}{\partial\Delta\varepsilon_p}\right)$$

$$\frac{\partial H^i_{n+1}}{\partial\Delta\varepsilon_q} = w_{ij}\left(\frac{\partial h^j_{n+\alpha}}{\partial\Delta\varepsilon_q} + \frac{\partial h^j_{n+\alpha}}{\partial q_{n+\alpha}}\frac{\partial q_{n+\alpha}}{\partial\Delta\varepsilon_q}\right)$$

Here w_{ij} is the inverse of

$$\delta_{ij} - \alpha\frac{\partial h^i_{n+\alpha}}{\partial H^j_{n+\alpha}}$$

and for the Gurson-Tvergarrd model applied in the paper, $2 \geq i, j \geq 1$.

APPENDIX B

Coefficients in equation (4.32)

$$C_{11} = \left[(A_{22} + 3GB_{22}) * B_{11} - (A_{12} + 3GB_{12}) * B_{21}\right] / \Delta$$
$$C_{21} = \left[(A_{11} + 3KB_{11}) * B_{21} - (A_{21} + 3KB_{21}) * B_{11}\right] / \Delta$$
$$C_{12} = \left[(A_{22} + 3GB_{22}) * B_{12} - (A_{12} + 3GB_{12}) * B_{22}\right] / \Delta$$
$$C_{22} = \left[(A_{11} + 3KB_{11}) * B_{22} - (A_{21} + 3KB_{21}) * B_{12}\right] / \Delta$$

$$\Delta = (A_{11} + 3KB_{11}) * (A_{22} + 3GB_{22}) - (A_{12} + 3GB_{12}) * (A_{21} + 3KB_{21})$$

APPENDIX C

Coefficients in equation (4.49)

$$A_{11} = P + \left[\Delta\varepsilon_p \frac{\partial P}{\partial \mathbf{H}_{n+\alpha}} + \Delta\varepsilon_q \frac{\partial Q}{\partial \mathbf{H}_{n+\alpha}} \right] \alpha \frac{\partial \mathbf{H}_{n+1}}{\partial \Delta\varepsilon_p}$$

$$A_{12} = Q + \left[\Delta\varepsilon_p \frac{\partial P}{\partial \mathbf{H}_{n+\alpha}} + \Delta\varepsilon_q \frac{\partial Q}{\partial \mathbf{H}_{n+\alpha}} \right] \alpha \frac{\partial \mathbf{H}_{n+1}}{\partial \Delta\varepsilon_q}$$

$$B_{11} = \frac{\alpha}{3} \Delta\varepsilon_p \left[\frac{\partial P}{\partial p_{n+\alpha}} + \frac{\partial P}{\partial \mathbf{H}_{n+\alpha}} \frac{\partial \mathbf{H}_{n+1}}{\partial p_{n+\alpha}} \alpha \right] + \frac{\alpha}{3} \Delta\varepsilon_q \left[\frac{\partial Q}{\partial p_{n+\alpha}} + \frac{\partial Q}{\partial \mathbf{H}_{n+\alpha}} \frac{\partial \mathbf{H}_{n+1}}{\partial p_{n+\alpha}} \alpha \right]$$

$$B_{12} = -\alpha\Delta\varepsilon_p \left[\frac{\partial P}{\partial q_{n+\alpha}} + \frac{\partial P}{\partial \mathbf{H}_{n+\alpha}} \frac{\partial \mathbf{H}_{n+1}}{\partial q_{n+\alpha}} \alpha \right] - \alpha\Delta\varepsilon_q \left[\frac{\partial Q}{\partial q_{n+\alpha}} + \frac{\partial Q}{\partial \mathbf{H}_{n+\alpha}} \frac{\partial \mathbf{H}_{n+1}}{\partial q_{n+\alpha}} \alpha \right]$$

$$A_{21} = \frac{\partial \phi_{n+1}}{\partial \mathbf{H}_{n+1}} : \frac{\partial \mathbf{H}_{n+1}}{\partial \Delta\varepsilon_p}$$

$$A_{22} = \frac{\partial \phi_{n+1}}{\partial \mathbf{H}_{n+1}} : \frac{\partial \mathbf{H}_{n+1}}{\partial \Delta\varepsilon_q}$$

$$B_{21} = \tfrac{1}{3} \left[\frac{\partial \phi_{n+1}}{\partial p_{n+1}} + \frac{\partial \phi_{n+1}}{\partial \mathbf{H}_{n+1}} : \frac{\partial \mathbf{H}_{n+1}}{\partial p_{n+1}} \right]$$

$$B_{22} = -\left[\frac{\partial \phi_{n+1}}{\partial q_{n+1}} + \frac{\partial \phi_{n+1}}{\partial \mathbf{H}_{n+1}} : \frac{\partial \mathbf{H}_{n+1}}{\partial q_{n+1}} \right]$$

where we have

$$\frac{\partial H^i_{n+1}}{\partial \Delta\varepsilon_p} = w_{ij} \frac{\partial h^j_{n+\alpha}}{\partial \Delta\varepsilon_p}$$

$$\frac{\partial H^i_{n+1}}{\partial \Delta\varepsilon_q} = w_{ij} \frac{\partial h^j_{n+\alpha}}{\partial \Delta\varepsilon_q}$$

$$\frac{\partial H^i_{n+1}}{\partial p_{n+\alpha}} = w_{ij} \frac{\partial h^j_{n+\alpha}}{\partial p_{n+\alpha}}$$

$$\frac{\partial H^i_{n+1}}{\partial q_{n+\alpha}} = w_{ij} \frac{\partial h^j_{n+\alpha}}{\partial q_{n+\alpha}}$$

and for the Gurson-Tvergarrd model applied in the paper, $2 \geq i, j \geq 1$. In the derivation, $\frac{\partial q_{n+\alpha}}{\partial \boldsymbol{\sigma}_{n+1}} = \alpha \mathbf{n}_{n+\alpha}$ has been used.

APPENDIX D

Coefficients in equation (4.50)

$$D_{11} = \left[(A_{22} + 3\overline{G} * B_{22}) * B_{11} - (A_{12} + 3\overline{G} * B_{12}) * B_{21}\right] / \Omega$$
$$D_{12} = \left[(A_{22} + 3\overline{G} * B_{22}) * B_{12}\right] / \Omega$$
$$D_{13} = \left[-(A_{12} + 3\overline{G} * B_{12}) * B_{22}\right] / \Omega$$
$$D_{21} = \left[(A_{11} + 3K * B_{11}) * B_{21} - (A_{21} + 3K * B_{21}) * B_{11}\right] / \Omega$$
$$D_{22} = \left[-(A_{21} + 3K * B_{21}) * B_{12}\right] / \Omega$$
$$D_{23} = \left[(A_{11} + 3K * B_{11}) * B_{22}\right] / \Omega$$

where

$$\Omega = (A_{11} + 3KB_{11}) * (A_{22} + 3\overline{G}B_{22}) - (A_{21} + 3KB_{21}) * (A_{12} + 3\overline{G}B_{12})$$
$$\overline{G} = \frac{2G/3}{(1 + 3G\alpha\Delta\varepsilon_q / q_n)} \frac{q_{n+\alpha}}{q_n} \mathbf{n}_{n+\alpha} : \mathbf{n}_{n+1}$$

G is the shear modulus.